Improving Passive Magnetic Inspection for Reinforced Concrete Condition Assessment

by

Milad Mosharafi

A thesis

presented to University of Waterloo

in fulfillment of the

thesis requirement for the degree of

Doctor of Philosophy

in

Mechanical and Mechatronics Engineering

Waterloo, Ontario, Canada, 2020

Examining Committee Membership

The following served on the Examining Committee for this thesis. The decision of the Examining Committee is by majority vote.

External Examiner   Professor J. Carlos Santamarina

Supervisors   Professor Roydon Fraser; Professor Maurice B. Dusseault

Internal Members   Professor Adrian Gerlich; Professor Kevin Musselman

Internal-external Member   Professor Giovanni Cascante

Author's declaration

I hereby declare that I am the sole author of this thesis. This is a true copy of the thesis, including any required final revisions, as accepted by my examiners. I understand that my thesis may be made electronically available to the public.

Abstract

Life quality, industrial productivity, and community safety can be assured by the reliability and the safety of infrastructure such as highways, bridges, and energy-supply systems. Reinforced concrete is the most-commonly used massive construction material in urban, road and industrial infrastructure because of its mechanical properties, durability, and mouldability. Concrete has acceptable compressive strength but relatively low tensile strength, so steel reinforcement rods (rebar) are usually added to concrete to enhance its tensile strength. However, steel rebar is subject to the serious and costly problem of corrosion, which eventually can significantly degrade the mechanical properties of concrete. Quantifying the corrosion condition of reinforcing steel can help manage associated risks arising from the unexpected function failure of reinforced concrete structures. In efforts to avoid such failures, engineers rely on quantitative time-history condition monitoring of reinforcing steel to help make decisions on rehabilitation, decommissioning, or replacement of concrete infrastructure.

The self-magnetic behaviour of ferromagnetic materials can be used for quantitative condition assessment. Inspection of reinforced concrete structures by a method based on this concept is under development. Improving the data recording, mathematical simulation and interpretation so as to obtain more-reliable outcomes from this novel NDT technology (Passive Magnetic Inspection (PMI)) is the main aim of this research project. This thesis, consisting of eight chapters, investigates various experiments and simulations, and delineates future work: Chapter 1 includes the introduction, theoretical background, and research objectives; Chapter 2 consists of numerical simulations and experimental results on the passive magnetic behavior of a rebar with pitting; Chapter 3 represents the simulations and experimental results of the investigations on rebars with local longitudinal defects; Chapter 4 investigates the self-magnetic behaviour of rebars with different sizes of crack; Chapter 5 covers numerical simulations and experimental results of passive magnetic behavior of an intact rebar and a rebar with general corrosion; Chapter 6 compares the magnetic flux density values generated from rebars with different degrees of general corrosion; Chapter 7 describes a successful fieldwork project; Chapter 8 outlines a general conclusion and future works that can help the further improvement of the inspection technology.

To explain the content of the thesis in more detail, through the analysis of magnetic data, Chapters 2, 3, and 4 cover methods for identifying the local defects in steel reinforcements, and Chapters 5

and 6 focus on realizing the general corrosion of steel rebars. Applicable findings generated from Chapter 2 to Chapter 6 are used in detecting and categorizing the local defects and general corrosion in steel rebars. For instance, it is shown that a certain percentile threshold can be applied on magnetic data to accurately detect longitudinal defects. It is also demonstrated that medium and large cracks are detected by magnetic values' absolute gradients of greater than 0.87 ($\mu T/mm$) and 0.95 ($\mu T/mm$), respectively. In addition, it is shown that the average of standard deviations calculated for a magnetic data set decreases when the degree of general corrosion increases. The findings in the first six chapters are implemented to establish the data gathering, data analysis, and interpretation approaches used in the field work described in Chapter 7.

In the field work, the condition of culvert C072's reinforced concrete (RC) bridge structure (located in the north of Markham, Ontario, Canada) is inspected. The inspection, supervised by the Corporation of the City of Markham, uses PMI technology. The inspection outcomes demonstrate that the sections close to the south and north ends of the bridge display the most-severe reinforcement anomalies: roughly, maximums of 20% and 14% of the reinforcement's cross-sectional area loss are detected close to the bridging structure's south and north ends, respectively. Additionally, an area in the middle of the bridge is found to have a noticeable anomaly in the reinforcement. The results generated from the magnetic data, collected using a PMI scanner, are in good agreement with visual-investigation results and the culvert's historical information, such as the concrete's chloride content and compressive strength values, as well as information from a half-cell potential survey. Culvert C072's condition is considered moderately deteriorated and corrective actions are recommended.

Acknowledgements

Dedication

To my wonderful parents who have supported me in every chapter of my life.

Table of contents

List of figures

xiii

xv

xvii

List of tables

Chapter 1: Reinforced concrete assessment

1.1. Importance of reinforced concrete corrosion assessment

Reinforced concrete as a composite infrastructure material is widely used in construction because of its excellent properties (Babaei and Tavassolian, 2015) and construction ease. Three factors control the behavioural responses of reinforced concrete: the reinforcing steel (generically referred to as **rebar**) which has a noticeable ductile nature, the concrete itself which has a noticeable brittle nature (low tensile strength but high compressive strength), and the condition of the rebar-concrete bonding (to achieve reliable stress transfer) (Hameed *et al*., 2017).

Reinforced concrete is commonly used in infrastructure such as buildings, bridges and highway construction (Boyle and Karbhari, 1995). The quality of a country's transportation system is mostly based on the conditions of its highway bridges, all of which contain steel. At the present time, apparently, approximately 28% of concrete bridge decks in the US and 33% of highway bridges in Canada can actually be considered operationally deficient or in a condition warranting cessation of active service, mainly because of rebar corrosion (Abouhamad *et al*., 2017).

Rebar corrosion is a common reason for reducing the service life and load capacity of environmentally exposed structures (Li and Ye, 2017). It appears that the major reason for concrete structures' failure is rebar corrosion, which can become more serious under aggressive environmental conditions such as de-icing by salts (during winters) or being in coastal locations (Zhao *et al.*, 2011). The mechanical properties of steel rebars are remarkably influenced by corrosion, hence investigation of corrosion conditions can help in determining the local and global safety levels of reinforced structures. Corrosion reduces the nominal cross-section area, which results in non-uniforms stress distribution and stress concentrations at notch tips (Fernandez *et al.*, 2015), increasing the risk of catastrophic rupture.

Various studies have been performed to represent the influence of the corrosion degree (percentage of mass reduction due to the corrosion) of rebars on their mechanical properties. For instance, Figure 1.1a and Figure 1.1b show the results of static and dynamic loading (with a 200 MPa stress range) of several steel-rebar specimens with 12 mm diameter and 310 mm to 320 mm length. It is shown that increasing the corrosion degree causes the yield strength and resisting cycles to decrease for monotonic tensile tests and high cycle load tests, respectively (Fernandez *et al.*, 2015).

Tolerating operational loads requires an appropriate bond between concrete and rebar (Kearsley and Joyce, 2014), and bond deterioration leaves structures more vulnerable to vibrations related to daily usage or large short loads such as those caused by earthquakes (Shi *et al.*, 2009). Rebar corrosion degrades bonding quality and can create cracks in the structure from volumetric expansion (Mahbaz, 2016). Figure 1.1c shows the results of pull-out tests of several corroded rebars with a length of 355 mm and diameter of 10 mm. At the initial period of corrosion (until the 2% corrosion degree), the confinement of the rebar in the concrete is increased due to the formation of adhesive corrosion products, so the bond strength increases. However, a further increase in the corrosion degree leads to more interfacial pressure and concrete cracking, which can reduce bond strength to less than 75% of its original value (Kearsley and Joyce, 2014).
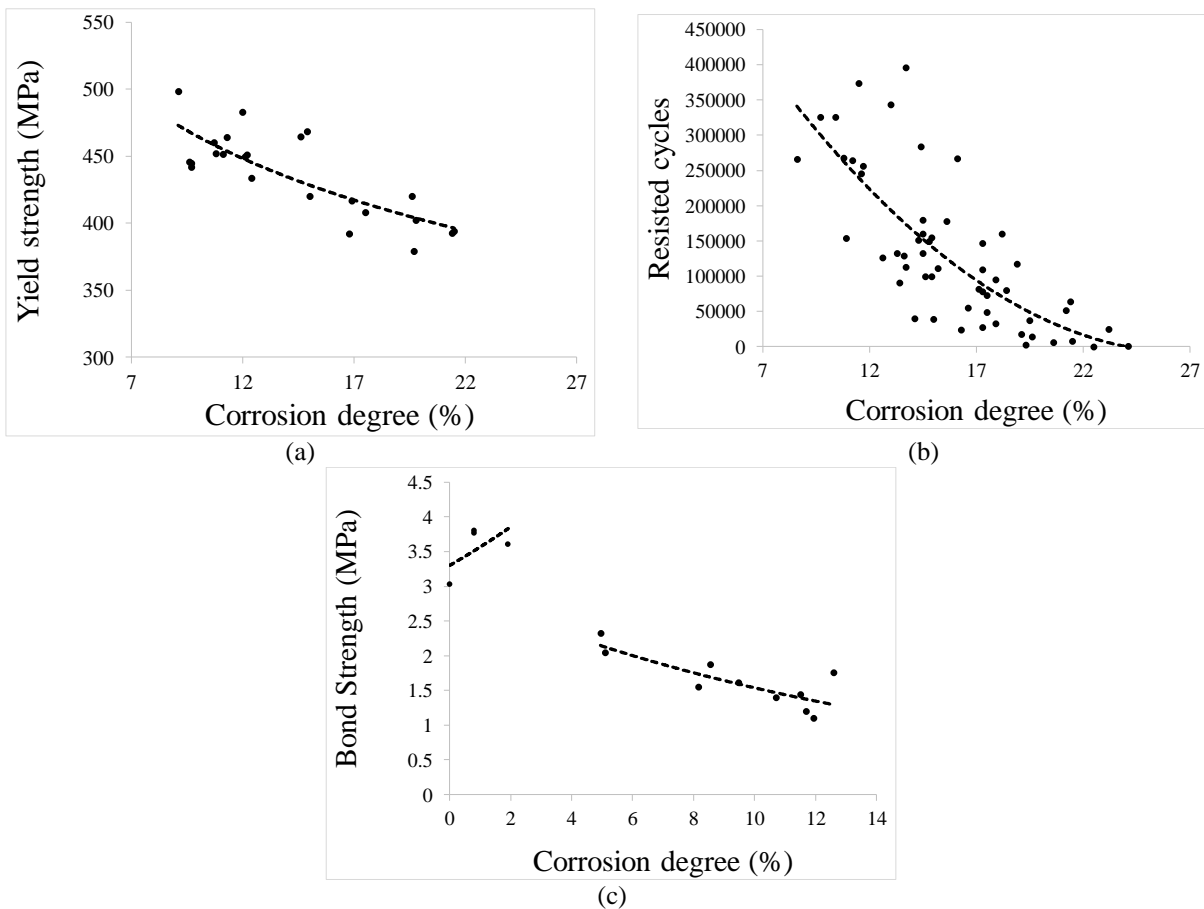
Figure 1.1. Relation between the corrosion degree and mechanical properties of steel rebars: (a) Yield strength under static loading (Fernandez *et al.*, 2015), (b) Resisted cycles under dynamic loading (Fernandez *et al.*, 2015), (c) Bond strength under pull-out test (Kearsley and Joyce, 2014).

The corrosion of steel rebar embedded in concrete falls into two categories: one is related to the specifications of the rebar and the concrete, the other includes the environmental conditions

(temperature, humidity, pH, salinity, etc.) to which the structure is exposed (Valipour *et al*., 2014). Exposure to chloride ions, usually from environmental exposure, is the most significant reason for rebar corrosion (Montemor *et al*., 2003). Long-term exposure to chloride ions deteriorates the passive layer of oxide on the steel rebar, causing significant deterioration or structural failure, which can carry substantial economic loss (Valipour *et al*., 2014). To reduce safety threats and financial impact, the condition of corrosion-threatened rebar should be monitored so that risks can be quantitatively managed (repair, replace, restore) (Muchaidze *et al*., 2011).

1.2. Reinforced concrete inspection methods

Non-Destructive Testing (NDT) is defined as techniques capable of detecting flaws and anomalies in or at the surfaces of structures without destroying or changing their original features (Gholizadeh, 2016). Several NDT methods are commonly used for monitoring the condition of composite materials from different aspects (Table 1-1). Visual Inspection (VI) remains the most-common NDT approach used for assessing the corrosion condition of reinforced concrete structures (Alcantara Jr *et al.*, 2016). VI evaluates the external surface of the structure without directly assessing the internal conditions (Takahashi *et al.*, 2015), and features such as external cracks and spalling are marked as signs of active corrosion (Alcantara Jr *et al.*, 2016). Even with detailed rubrics and photo imagery, VI methods are weak and semiquantitative, and must be supported by other non-destructive methods (Concu *et al.*, 2011).

Table 1-1. Some common reinforced concrete assessment methods (Clifton *et al.*, 1982; Zaki *et al.*, 2015; Verma *et al.*, 2013; Zhang *et al.*, 2016).

Inspection purpose	NDT method	Advantages	Limitations
Concrete quality, defects, and voids	Visual inspection (VI)	• Inexpensive • Large area coverage	• Strongly subjective • Only superficial anomalies can be detected
	Infrared thermography	• Easy interpretation • Safe (no radiation) • Portable • Relatively inexpensive	• Results affected by environmental conditions • No quantitative information about corrosion conditions
	Radiography	• Appropriate detection of composition and thickness • Locates the rebars	• Expensive • Hazardous (radiation)

Table 1-1 (continued).

Inspection purpose	NDT method	Advantages	Limitations
Surface hardness and compressive strength of concrete	Rebound hammer	• Inexpensive • Simple procedure	• Results affected by geometry and mass of test object
	Ultrasonic pulse velocity (UPV)	• Efficient cost • Quick • Portable	• Results affected by moisture and presence of rebars • Requires coupling
Corrosion rate and location	Half-cell potential	• Easy • Inexpensive	• Not quantitative • Requires preparations • Time consuming
	Linear polarization resistance (LPR)	• Quick procedure	• Results affected by temperature and humidity
	Galvanostatic pulse method	• Measures the half-cell potential and electrical resistance at the same time	• Not quantitative • Requires preparations • Time consuming • Results affected by humidity
	Ground Penetrating Radar (GPR)	• Portable • Inexpensive • Effective for Large area coverage	• Complex outcomes • Requires difficult interpretations
	Eddy Current Testing (ETC)	• Relatively inexpensive • Good resolution • Portable	• Sensitive to geometry of rebars • Limited depth of inspection
	Magnetic Flux Leakage (MFL)	• Detecting various types of rebar defects • high sensitivity	• Time consuming • Expensive • Requires a strong external magnetic field

Reinforced concrete can be inspected for different types of defects using various types of NDT methods (Szymanik *et al*., 2016); some identify corrosion through implementing electrochemical measurements. For instance, anodic and cathodic regions can be located through surface potential measurements, and corrosion rates can be estimated by linear polarization resistance measurements. Other methods assess the extent of corrosion based on the electromagnetic phenomena; ECT and GPR are two well-known reinforced concrete NDT techniques based on low-frequency and high-frequency electromagnetic fields, respectively (Alcantara Jr *et al.*, 2016). Each NDT method has limitations (Hussain and Akhtar, 2017); for instance, the macro-current measurement is complicated to interpret since its results are influenced by the distance between anode and cathode and by humidity (Xu *et al*., 2013). GPR results are influenced by the existence of voids and variable internal moisture conditions (Evans and Rahman, 2012) which can confound

4

interpretation in many ways, such as confusion with background structures, shadowing, or false identification of gaps or previously repaired sites as being corrosion sites (Type I errors). (Abouhamad *et al*., 2017). Half-cell potential surveys can only mark corrosion locations; they give no information about the corrosion extent (Twumasi *et al*., 2016). Ultrasonic pulse velocity (UPV) or Schmidt hammer techniques assess the mechanical properties of concrete with no information directly related to rebar corrosion (Verma *et al*., 2013). Similarly, radiographic and acoustic inspections are used to assess concrete conditions, but give no direct information related to rebar conditions (Perin and Göktepe, 2012). Additionally, radiography is rarely used these days due to challenges such as high costs, special safety requirements, and the need to access the other side of a structure (Alcantara Jr *et al.*, 2016).

Magnetic based NDTs are also used widely for assessing rebar condition. Such methods are based on the changes of magnetic domains and magnetic properties of ferromagnetic materials due to the existence of defects, and can be categorized into active and passive approaches. Active magnetic approaches need actuators and receivers (Wang *et al.*, 2012). Such methods need an external source such as electromagnets to properly magnetize objects during inspection (Daniel *et al.*, 2017), increasing assessment time and energy costs. Active magnetic-based methods such as magnetic flux leakage (MFL) can provide information directly related to the corrosion conditions of pre-magnetized ferromagnetic rebars (Makar and Desnoyers, 2001).

In 1997 Dubov introduced a passive magnetic approach with only receivers, without magnetic actuation of the structures (Dubov, 1997). Passive magnetic methods inspect the ferromagnetic structures under the effect of the Earth's magnetic field (Dubov and Kolokolnikov, 2008; Dubov, 2012). Such methods require no special preliminary actions (Ahmad *et al.*, 2015) or any expensive complicated artificial magnetic source (Gontarz *et al*., 2015), and use passive magnetic flux density to locate defects (Miya, 2002).

1.3. Passive magnetic inspection theoretical background

The Earth's internal magnetic field is caused by liquid iron motion in the planetary core (Hughes and Cattaneo, 2016; Davies and Constable, 2017) plus contributions from other sources such as mantle movements, the nature of the lithosphere, etc. (Bezděk *et al*., 2017). The magnetic field is a three-dimensional vector (Taylor *et al*., 2017) with a harmonic pattern due to the globe's rotational movement (Zagorski *et al*., 2017). The vector field originates from the surface of the

Earth and extends beyond the atmosphere, and its magnitude and orientation are also functions of location (Taylor *et al*., 2017) and time (Bezděk *et al*., 2017).

Natural magnetic fields and other influential local magnetic sources (Mahbaz *et al*., 2017), combined with the effect of internal and external stresses, can change the scattered stray magnetic field of ferromagnetic materials (Mironov *et al*., 2016). Internal domain-wall displacement and magnetic-moment rotation in ferromagnetic materials happen under the influence of external magnetic fields (Guo *et al*., 2016), and there are relationships between the micro-magnetic characteristics of these materials and their mechanical response (Gupta and Szielasko, 2016). For example, if a steel rebar is deformed significantly in the presence of a magnetic field during manufacture, the magnetization of the domains and their orientation within the steel are affected. Self-Magnetic Flux Leakage (SMFL) is assumed to take place in the stress concentration areas of ferromagnetic materials affected by mechanical load under the Earth's magnetic field (Huang and Qian, 2017), and this condition can remain even after removing the load, creating detectable magnetic leakage at the material surface (Yuan and Zhang, 2010). Measuring SMFL at the surface of the materials helps in estimating their stress-strain state (SSS), an important parameter in determining a structure's reliability (Dubov, 2012). Therefore, the relation between localized stress and oriented magnetic domains is useful for detecting defects in ferromagnetic materials within the background magnetic field of the Earth (Jarram, 2016).

Magnetic field parameters at a point in space are represented by magnetic flux density (*B*) and external magnetic field (*H*). Magnetic flux density (*B*) represents the closeness of the magnetic field lines and shows the strength of the magnetic field (Tauxe, 2010). Also, Gauss's magnetic field law states that $\nabla B = 0$ (Hu *et al*., 2017). *H* and *B* may have a complex relation in magnetic materials (Tabrizi, 1987), but engineers usually invoke the relation established by Faraday and Maxwell which demonstrates that *B* is produced in magnetisable material due to the existence of a primary magnetic field (*H*) (Tanel and Erol, 2008).

Numerical simulation of the PMI method is performed based on the stray magnetic field (H_d) and the stray magnetic field energy (E_d) (Mahbaz *et al.*, 2017). Hubert and Schäfer (1998) presented the relation for calculating the stray magnetic field (Eq. 1-1), based on summarizing Gauss's magnetic field law. In Eq. 1-2, magnetic polarisation (J) is the product of "Volume-normalized magnetization" *M,* multiplied by "Vacuum magnetic permeability of free space" μ_0 (Ahrens,

1995). Additionally, a relation suggested for estimating the stray magnetic field energy uses the magnetic charges' balance and integration over the volume of a ferromagnetic material (Eq. 1-2).

$$divH_d = -div \left(J/\mu_0 \right) \tag{1-1}$$

$$E_d = \frac{1}{2}\mu_0 \int_{all\ space} H_d^2 dV \rightarrow E_d = -\frac{1}{2}\mu_0 \int_{sample} H_d \cdot J dV \tag{1-2}$$

Based on potential theory, volume charge density (λ_V) – Eq. 1-3 – and surface charge density (σ_S) – Eq. 1-4 and Eq. 1-5 – are other parameters related to Magnetization (M) – Eq. 1-6 – and can be implemented for computing stray fields. Surface charge density is calculated by Eq. 1-4 when there is just one magnetic medium; Eq. 1-5 is applied when there are two varied different media with their own magnetization values and a specific vector perpendicular to the separation plane of those materials (n).

$$\lambda_V = -divM \tag{1-3}$$

$$\sigma_S = M \cdot n \tag{1-4}$$

$$\sigma_S = (M_1 - M_2) \cdot n \tag{1-5}$$

$$M(r) = J(r)/J_s \tag{1-6}$$

According to Eq. 1-7, the stray field energy at a position (r) can be also calculated through the negative gradient of the potential of the stray field energy at a place ($\Phi_d(r)$) (Kronmuller, 1987), where $\Phi_d(r)$ – Eq. 1-8 – is a function of magnetization saturation (J_s), volume charge density (λ_V), surface charge density (σ_S) and the derivative of the position vector (r'). Next, the magnetic field energy is obtained from Eq. 1-9 through the integration of surface charge density and volume charge density over the volume and surface, respectively.

$$H_d(r) = -grad\Phi_d(r) \tag{1-7}$$

$$\Phi_d(r) = \frac{J_s}{4\pi\mu_0} \left[\int \frac{\lambda_V(r')}{|r - r'|} dV' + \int \frac{\sigma_S(r')}{|r - r'|} dS' \right] \tag{1-8}$$

$$E_d = J_s \left[\int \lambda_V(r) \Phi_d(r) dV + \int \sigma_S(r) \Phi_d(r) dS \right] \tag{1-9}$$

The passive magnetic method can detect not only defects in rebar such as corrosion or cracks (Ahmad *et al.*, 2015) but also stress changes arising from mechanical loads in ferromagnetic materials because of alterations in crystalline structure (Witos *et al.*, 2014).

Steel reinforcement commonly used for transferring tensile stresses in different parts of industrial structures such as bridges (Kopas *et al*., 2016). The main reasons for structural failure are associated with steel reinforcement failure linked to micro-defects and stress-concentration regions that intensify the destructive effects of corrosion, fatigue, and creeping (Xin *et al*., 2012). Stress measurements help in monitoring the safety of structures that contain steel parts. Stress values (changes) can be measured using strain gauges but this is generally considered a destructive method unless the sensors are all pre-installed. Hence, magnetic non-destructive techniques have been developed to evaluate the stress behaviour of ferromagnetic steel structures, even under operating conditions (Sakai *et al*., 2004).

Previous investigations have demonstrated the relationship between the magnetic properties and the stress behaviour of ferromagnetic materials. For instance, it has been shown that materials with residual stress have different magnetic behaviour (Luming *et al*., 2003). Additionally, studying the magnetic behaviour of ferromagnetic specimens during their elastic phase can predict rupture locations with an acceptable accuracy. This latter quality motivates efforts to predict places prone to failure (micro-defects) using the passive magnetic method (Da-wei *et al*., 2005). Moreover, it is understood that ferromagnetic materials have distinguishable magnetic properties at elastic and plastic phases of their mechanical stress-strain behavior, which can help in finding micro and macro scale defects by passive magnetic methods (Leng *et al*., 2010).

The evaluation of ferromagnetic structures by magnetic non-destructive techniques works based on the magneto-mechanical coupling. Ferromagnetic materials are composed of many magnetic domains that can be influenced by internal and external stresses. Such mechanical loads can displace the domain walls, which changes the macro-magnetic properties of ferromagnetic structures. Some magnetic non-destructive techniques work by using artificial (external) magnetic sources to pre-magnetize the steel structures to be inspected (Yao *et al*., 2012). However, mechanical loads can change the magnetic behaviour of ferromagnetic materials even under the ambient geomagnetic field (Li and Xu, 2012).

Mechanical loading in the presence of the Earth's magnetic field causes reversible and irreversible effects on the magnetic domains. To illustrate, the domains' dislocations density is at its highest state in the middle of the stress concentration zones. Additionally, the self-magnetic flux leakage (SMFL) behaviour is clearly detectable around the stress concentration zones. It is assumed that

the tangential SMFL component is at its highest value when the polarity of its normal component is changed at the middle of the stress concentration zone (Figure 1.2) (Wang *et al.*, 2010).

(a)   (b)
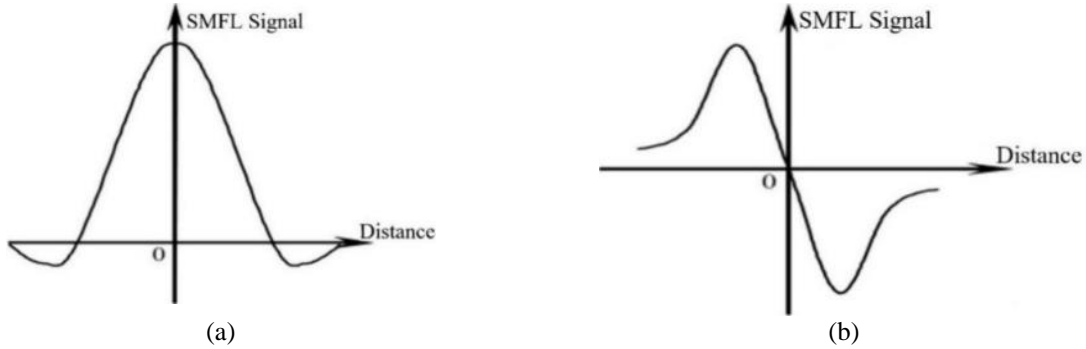
Figure 1.2. SMFL behaviour around stress concentration zone: (a) Tangential component of SMFL, (b) Normal component of SMFL.

The relation between stress and magnetic behaviour can be expressed by the Magnetostriction phenomena, which defines the effects of the magnetization in the changes of the dimensions of a material (Wilson *et al.*, 2007). However, the magnetic behaviour of materials depends on their atomic structure, and stress changes can move the atoms and change the atomic arrangement, leading to different magnetic properties (Bulte and Langman, 2002). The magneto-mechanical effect is the reverse of the Magnetostriction phenomena and describes the changes in the magnetic properties of a material due to applied stresses (Wilson *et al.*, 2007). Jiles (1995) stated that the relation between stress values (σ) and magnetization (M) can be expressed as in Eq. 1-10, where M is a function of anhysteretic magnetization (M_{an}), and irreversible magnetization (M_{irr}).

$$\frac{dM}{d\sigma} = \frac{1}{\varepsilon^2}\sigma(1-c)(M_{an} - M_{irr}) + \frac{dM_{an}}{d\sigma} \tag{1-10}$$

Two other parameters also affect the above relation: ε, a constant coefficient that is related to the elasticity modulus of the material; and c, a dimensionless constant coefficient that expresses the domains walls' flexibilities. Eq. 1-10. shows that the magnetization values resulting from stress can differ according to the magnetic properties of the ferromagnetic materials (Jiles, 1995). Additionally, the Magnetostriction phenomena can be explained by energy equations. A material's energy state is stable under the conditions of not being affected by either an external load or magnetic field, as in Eq. 1-11, where the total energy (E) is equal to the summations of magnetic anisotropy energy (E_k), magnetoelastic energy (E_{ms}), and elastic energy (E_{el}) (Ren *et al.*, 2001).

$$E = E_k + E_{ms} + E_{el} \tag{1-11}$$

If a material is subjected to an external force, the energy related to that applied stress (E_σ) should be added to Eq. 1-11, leading to a new equation (Eq. 1-12). The magnetoelastic stress energy can be represented according to Eq. 1-13, where θ is the angle between the applied stress vector and the magnetising field, and λ_s is the saturation magnetostriction coefficient (Ren *et al.*, 2001).

$$E = E_k + E_{ms} + E_{el} + E_\sigma \tag{1-12}$$

$$E_\sigma = -\frac{3}{2}\lambda_s \sigma \cos^2\theta \tag{1-13}$$

1.4. Research methodology

The Passive Magnetic Inspection (PMI) method, an NDT approach, was developed at the University of Waterloo for use in inspecting the corrosion conditions of rebar through scanning from the external surface of concrete (Mahbaz, 2016). Investigations have since been successfully conducted on PMI to enhance the interpretation quality of the recorded data (Mahbaz *et al.*, 2017). However, additional studies on the magnetic behavior of ferromagnetic materials are required to achieve more accurate and better calibrated outcomes for engineering applications. Several specific steps are followed in this project to improve PMI's data gathering and data interpretation processes for assessing the condition of the rebar in reinforced concrete.

The magnetic flux density values of ferromagnetic rebars with different types and extents of local defects (considered as point sources affecting the stray magnetic field around rebars) and general corrosion (considered as linear sources affecting the stray magnetic field around rebars), are simulated numerically with the finite element method using COMSOL® software. The results of the simulations are compared with the experimental results for verification and calibration. Next, the experimental and simulation results are implemented in a real case study involving the inspection of a bridge structure, and successful outcomes obtained (Figure 1.3).
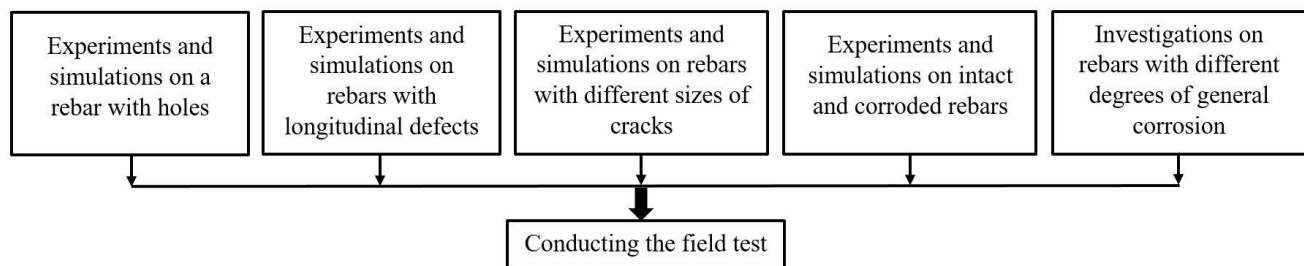
Figure 1.3. General flow of the thesis.

In experiments, every data-gathering session is conducted by moving the PMI's scanner on a defined path along the length of a rebar (the sensor array is centered above the rebar). Every scan along a specific path is repeated several times to statistically confirm the reliability of data recording. Data are recorded as a text file easily opened by different software products for interpretation. The distinct and diagnostic magnetic properties of rebar under different conditions (intact, with local corrosion, and with general corrosion) are recorded, while the linear density of data points collected is controlled through an appropriate scanning speed. Furthermore, various data-processing approaches are conducted in order to obtain more-accurate interpretations. The processes of data recording, data analysis, and interpretation can be generally represented in a flow chart (Figure 1.4).
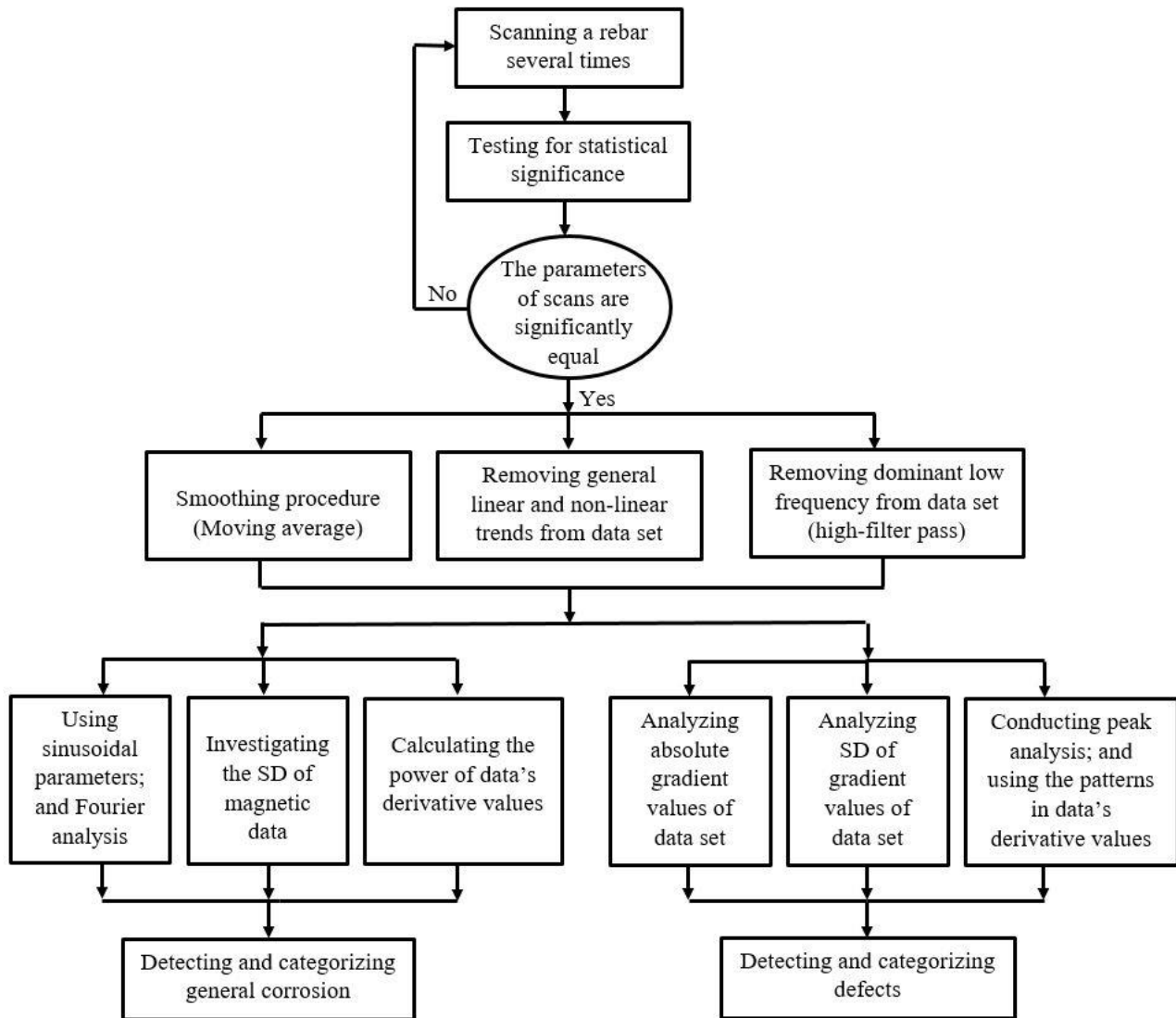
Figure 1.4. Flowchart showing the general process from data recording to data analysis and interpretation.

For confirming the quality of experiments, every scan is conducted several times (Cochran and Gertrude, 1957). This replication gives a more accurate measurement of the rebar's magnetic flux density values and reduces the effects of systematic errors on data caused by "technical or procedural factors" (Malo *et al*., 2006) so as to establish the PMI data recording's precision. Means, and standard deviations are calculated for every scanning episode. Next, statistical tests such as Analysis of Variance (ANOVAs) (Kaur *et al*., 2014) and T- tests (Xu *et al*., 2017) are carried out to verify that there is no statistically significant difference between the data recorded in different scans.

The data processing procedures include Fourier transform, use of sinusoidal parameters, statistical analysis, peak analysis, data smoothing procedures, normalizing, and using the gradient and SD values of data. Fourier transform, the conventional method for data analysis, can be used for decomposing the magnetic data into its amplitude and phase components (Mahbaz, 2016). Then, the recorded data can be investigated based on associated frequencies, so various data processing activities can be conducted. The signal-to-noise ratio of the recorded data can be increased using high frequency smoothing (Lam *et al*., 1981). Data also can be categorized based on their frequencies through high- and low-pass filtration (Costa-García *et al*., 2018) and be reviewed separately.

Sinusoidal parameters can help better interpret the data, and these parameters can be estimated through a Fourier spectrum (Mosharafi *et al*., 2020). However, a Fourier transform represents the function based on sine and cosine waves approaching infinity (Modi *et al*., 2004); it also has difficulties in describing occasional or transient odd signals (Zhao *et al*., 2000). The shortcomings of Fourier transform can be compensated for by using peak analysis, and by investigating the SD and gradient values of magnetic data so as to more-easily determine local and abrupt signal changes due to local defects (Mosharafi *et al*., 2020).

Statistical approaches are also considered in data processing procedures. It was demonstrated that the probability distributions and histogram frequencies of magnetic data can help in assessing the conditions of rebars (Mosharafi *et al*., 2018). On the other hand, magnetic data processing is performed through moving average smoothing procedures to identify trends in a signal without much affecting the signal, and thus reduce the effects of random errors on data. The goal of smoothing is to remove roughness (fast-changing components) to more easily recognize trends

(Guiñón *et al*., 2007). Next, the patterns of magnetic flux density values, or the amounts of their gradient over distance, are investigated to identify anomalies and defects in the rebars (Dubov and Kolokolnikov, 2012; Dubov *et al*., 2010). Furthermore, for better comparison, the ranges of values in simulation and experiment results will be modified to an equal range by normalization techniques such as Z-score and Min-Max normalization (Saranya and Manikandan, 2013).

1.5. Research Objectives

PMI technology is a novel NDT method for inspection of reinforced concrete developed at the University of Waterloo; many technical improvements are still needed to the method, most of which are investigated in this research project. Accordingly, this research project was planned to meet the following objectives:

- Review the theory and fundamental equations;
- Investigate the magnetic parameters of rebar with defects (e.g., holes, cracks, longitudinal defects);

- Investigate the magnetic parameters of rebar with different degrees of general corrosion;
- Study the influential parameters during inspections, such as defects' clock positions in rebars and vertical distance of data recording;
- Improve data-recording, data analysis, and data-interpretation procedures;
- Investigate the reliability of the inspection method under the real conditions of a fieldwork.

1.6. Contribution

The experiments in a study by Mahbaz *et al.* (2017) explored defective rebar in conjunction with simulations, using solid rebar sketched in COMSOL® based on a real rebar's geometry. The rebar was then magnetized, assuming a certain value of the magnetic field. Next, the passive magnetic behavior was investigated at a fixed distance from the rebar. To continue the technical development of PMI, the current research project focuses on complementary experiments on the same ferromagnetic steel rebar with artificial defects. In addition, the defective rebar will be scanned with a 3D laser scanner to generate a detailed point cloud of the structure. This point cloud data will be used in the finite element method software COMSOL® as the geometric basis for studying its magnetic behaviour under the influence of the Earth's magnetic field. Different

magnetic properties of the object will be extracted and interpreted at several distances from the rebar. Additionally, a statistical detection method will be presented as a new development in passive magnetic data processing and interpretation.

Furthermore, as a new investigation subject, the patterns of magnetic values at different local defects in steel rebars are studied. Novel approaches for data analysis of magnetic data are introduced to identify the defective sites in steel rebars. Additionally, certain innovative criteria are presented for categorizing the magnetic values based on the severity of the defects in rebars. Another new investigation subject in this thesis is the comparison of the self magnetic behaviour of an intact rebar and a rebar with general corrosion through simulations and experiments. Additionally, innovative data processing approaches are introduced for comparing the magnetic properties recorded over rebars with different degrees of general corrosion. Novel data gathering and data processing procedures, have been established, along with new interpretation approaches. This material has been incorporated in the first real case study, conducted on a reinforced concrete bridging structure.

1.7. Thesis organization

This thesis is divided into two main parts: laboratory investigations and field work. The former investigates the self-magnetic properties of rebars with local defects, and rebars with different degrees of general corrosion. To ensure the reliability of the investigations, the magnetic data sets are subjected to different methods of statistical analysis. Additionally, the self-magnetic behaviors of similar defective rebars are subsequently simulated under the effect of Earth's magnetic field, using a finite-element based software. The recorded data sets are interpreted using different data-processing approaches, and noticeable relations are observed between the magnetic properties and the rebars' physical conditions. The findings obtained from these investigations are implemented in a case study to detect and categorize corrosion sites in the steel reinforcements embedded in the deck of a bridging structure located in the north of Markham city (Ontario, Canada). The thesis has eight chapters:

Chapter 1: Introduction to nondestructive testing methods and the methodology used in this thesis, and organization of the thesis;

Chapter 2: Review of self-magnetic behavior of a rebar with forged holes;

Chapter 3: Investigation of the magnetic properties of rebars with similar longitudinal defects;

Chapter 4: Study of the magnetic response of rebars with different sizes of cracks;

Chapter 5: Comparison the self-magnetic behaviour of an intact reinforcement with a generally corroded one;

Chapter 6: Assessment of magnetic properties recorded over reinforcements with different degrees of general corrosion;

Chapter 7: Case study on reinforced concrete bridging structure assessment using the findings from previous chapters;

Chapter 8: Conclusion and recommendations.

Chapter 2: Detection of forged hole on reinforcement using PMI technology

The contents of this chapter are reflective of an original manuscript published in the journal of   Applied Sciences.

Author Contributions: Conceptualization, M.M., S.M., and M.B.D.; Data curation, M.M.; Formal analysis, M.M.; Funding acquisition, M.B.D.; Investigation, M.M.; Methodology, M.M., and S.M.; Supervision, M.B.D.; Writing—original draft, M.M.; Writing—review & editing, M.M., S.M., and M.B.D.

2.1. Introduction

Corrosion initiation in reinforcement steel happens mainly due to the existence of chloride ions in the surrounding area. Subsequently, corrosion can progress, forming more corrosion products, and applying force on the concrete covering (Zhao *et al*., 2011), leading to cracking, which facilitates access to more corrosion-inducing agents. Rebar corrosion in concrete (as an electrolyte) is an electrochemical process, categorizable into two groups based on the mechanical changes of the rebar and concrete: local corrosion (pitting) and general corrosion (Perkins, 2000). Both pitting and general corrosion are considered threats to the reliability of reinforced concrete structures, and their adverse consequences can be predicted based on parameters such as cover depth, moisture content, stray currents, and microbial activities (Mackechnie and Alexander, 2001). To continue the technical development of PMI with respect to local corrosion, for this chapter, a ferromagnetic steel rebar with artificial defects (holes) is scanned with a 3D laser scanner to generate a detailed point cloud of the structure. The point cloud data set is then served as the geometric basis for finite element method software (COMSOL®), with the Earth's magnetic field as an input. Different magnetic properties of the object are extracted and interpreted, and the parameters influencing them are investigated.

2.2. Numerical simulation procedure and results

The surface of a ferromagnetic rebar (low carbon steel) with a length of 373.87 mm, diameter of 16 mm, and two artificial defects (Table 2-1) (Mahbaz *et al.*, 2017) was scanned using a high resolution 3D laser scanner (FARO LS 840 HE) (Figure 2.1.a) (Nahangi and Haas, 2014). The shape of the rebar was created with cloud points (Figure 2.1.b) which were modified and converted to a mesh by Mesh Lab V1.3.2 ("Meshlab", 2017). Subsequently, the produced mesh was imported to COMSOL® software and converted to a discretized surface and solid, respectively (Figure 2.1.c).
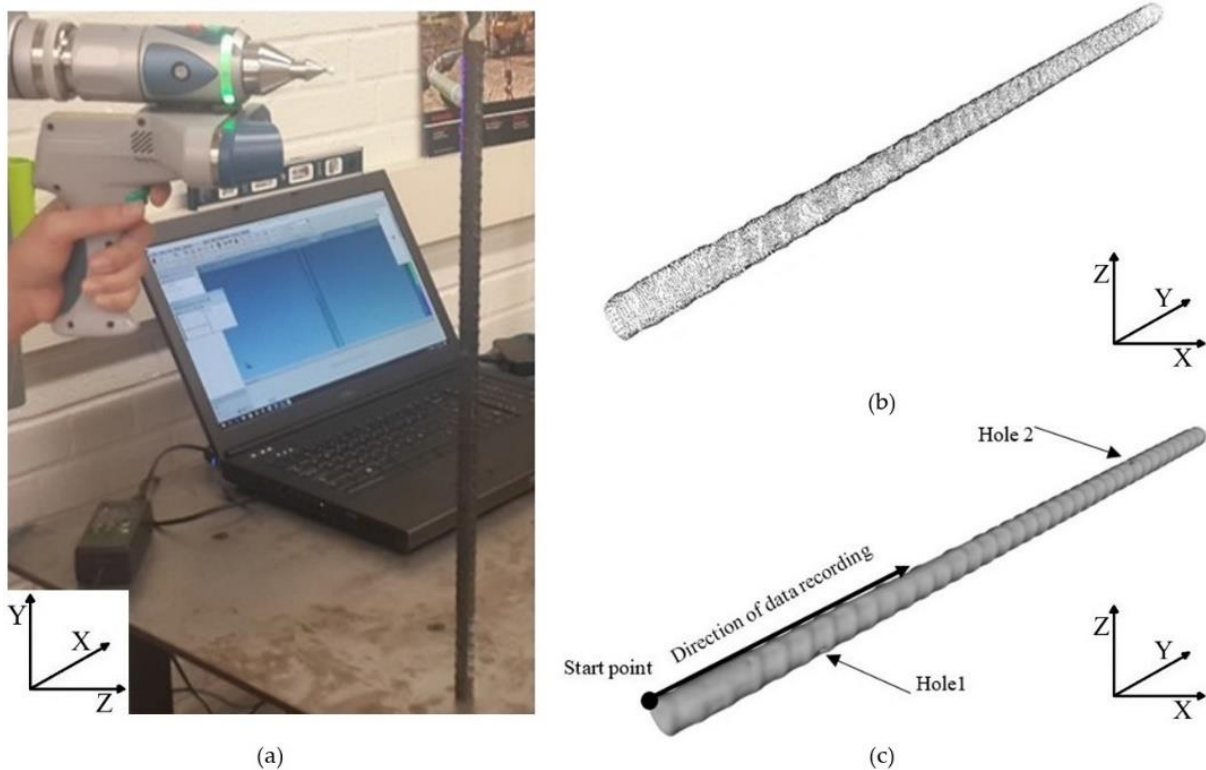
Figure 2.1. Process of converting the geometry of real rebar in to a solid model: (a) Scanning the rebar with 3D laser scanner, (b) Cloud points of rebar, presented in MeshLab, (c) Solid illustration of rebar.

The solid rebar was simulated via COMSOL® software with regard to the magnetic field of the Earth. As the Earth's magnetic field varies somewhat in time and location, to obtain consistent and realistic results, the average (within a year) of the different components of the magnetic field for the Waterloo, Ontario region (the location of the experiments) was adopted for the simulations (Table 2-2). Moreover, since the unitless relative magnetic permeability of low carbon steels (ASTM 1020) ranges from 50 to 100 (Rose *et al.*, 1995; Ribichini, 2011), a relative magnetic permeability of 75 (Mahbaz, 2016) was selected for this study.

The duration of being affected by an external magnetic field will affect the magnetic behavior of ferromagnetic materials. In reality, ferromagnetic materials are affected by the magnetic field of the Earth from the beginning of their production process. There may also be some unknown external magnetic sources in the surrounding environment which affect the magnetic behaviour of ferromagnetic objects (Li *et al.*, 2017). However, as accurately as possible, we can apply the magnetic field of the Earth to the object and simulate its magnetic behaviour, though some divergence will exist between the simulation and the experimental results.

Table 2-1. Specifications of the two holes in the rebar.

Hole name	Diameter (mm)	Depth (mm)	Y- Location from the rebar's start point (mm)
Hole 1	0.58	1.24	57.91
Hole 2	0.68	0.57	282.67

Table 2-2. Background magnetic field (magnetic field of the Earth): from August 2016 to August 2017 ("Natural Resources Canada," 2017).

Background magnetic field (X component)	18 µT
Background magnetic field (Y component)	-3 µT
Background magnetic field (Z component)	50 µT

To consider the Earth's magnetic field in the simulation, the rebar was located in a regular space with dimensions of 100 mm × 150 mm × 410 mm that included the magnetic field specified in Table 2-2 (Figure 2.2). To have better control of simulation parameters, the box and rebar were meshed separately with tetrahedral meshes according to the specifications of rebar mesh #1 and box mesh #1 in Appendix A. Then, the rebar and box were jointly subjected to the simulation process as a single system (Figure 2.3).
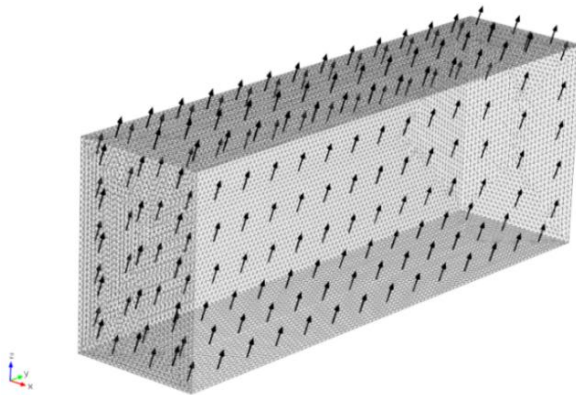
Figure 2.2. Box used in analysis; arrows show the resultant vector for X, Y and Z components of the Earth's magnetic field.
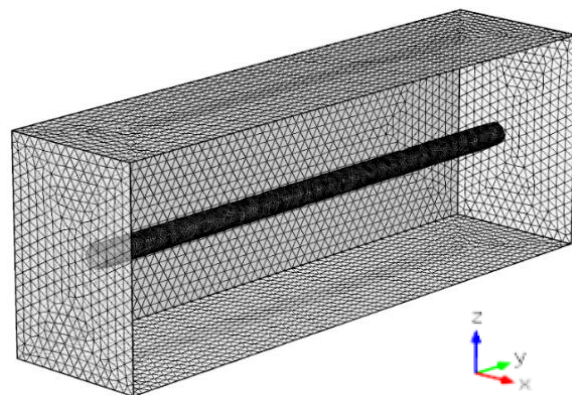
Figure 2.3. Initial meshes of the system (front face of the box is removed for better visualisation).

2.2.1. Defect detection

After applying the rebar and box in the simulation process as a combined system, the values of the different components (X, Y, and Z) of the magnetic flux densities were recorded for the Y direction of the rebar (i.e., the path parallel to the rebar's length). This path is at the surface of the rebar and extends from one side (Edge A) to the other side (Edge B) of the box (Figure 2.4).
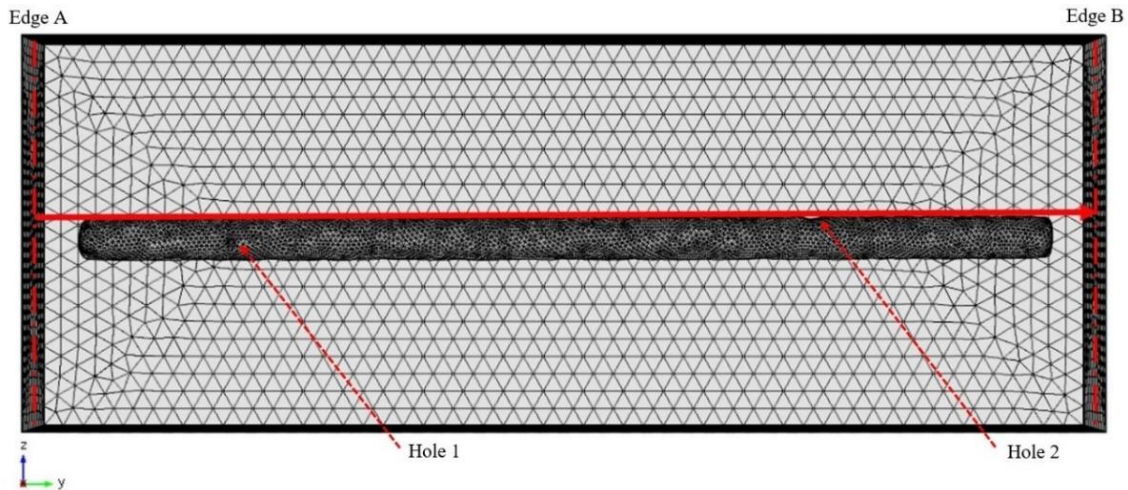
Figure 2.4. Path of the data recording (at the surface of the rebar in Y direction).

As observed in Figure 2.5, at first the values of all the components of magnetic flux densities are equal to the background magnetic flux (the magnetic field of the Earth). When the Y distance reaches about 18.065 mm, at the end of the rebar, the values of all the components are changed based on the magnetic properties of the ferromagnetic rebar. The values of all of the components have a harmonic variation because of the corrugated rebar shape. When the Y distance reaches the end of the rebar, all the components of magnetic flux densities revert to the magnitudes of the background magnetic field. However, there is a distinguishable irregularity in the direction and values of all of the components at the location of Hole 2 (~301 mm from the Edge A of the box). This irregularity is in the form of a minimum peak in the values of the Z and X magnetic flux densities and in the form of a sudden change in the gradient of the Y component of the magnetic flux density (a spike above the zero line, followed by a sudden dip below the zero line, then a sharp jump back to the zero line).
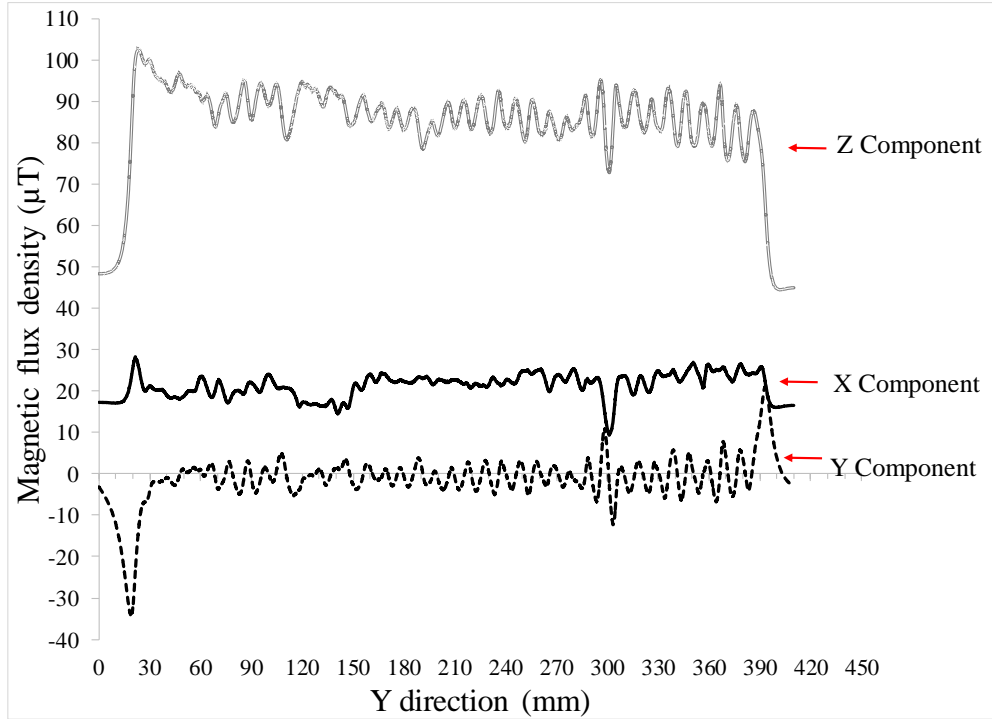
Figure 2.5. Values of different components (X, Y and Z) of the magnetic flux densities in Y direction at the surface of the rebar (initial mesh of the rebar and box).

There are some outlier values in the different components of magnetic flux densities, related to the specifications of the elements used in this simulation. In order to have mesh element independent results, more accurate element specifications were implemented on the rebar (Appendix A). Then, the minimum values of the Z component magnetic flux density (as a representative metric) from 295.0592 mm to 307.0592 mm (values symmetric about Hole 2) were extracted. As seen in Figure 2.6, values of the minimum magnetic flux densities become stable at rebar mesh #8 (Appendix A). Hence, the result of rebar mesh #8 was used for continuing the simulations. The magnetic flux density values for mesh #8 have no out-of-range or disorder trend, compared to the trend of rebar mesh #1, the initial simulation at the surface of the rebar (Figure 2.7).
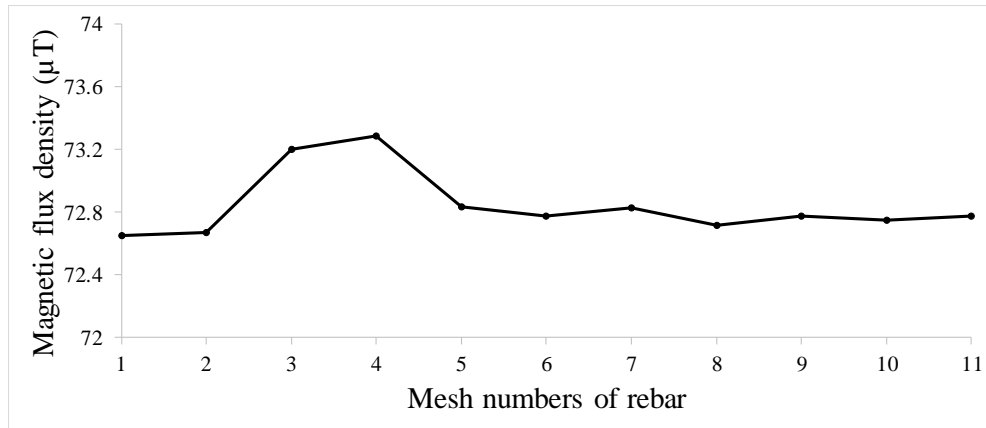
Figure 2.6. Minimum values of Z component magnetic flux density, from 295.0592 mm to 307.0592 mm (values related to Hole 2, for different mesh specifications of rebar with fixed box mesh #1).
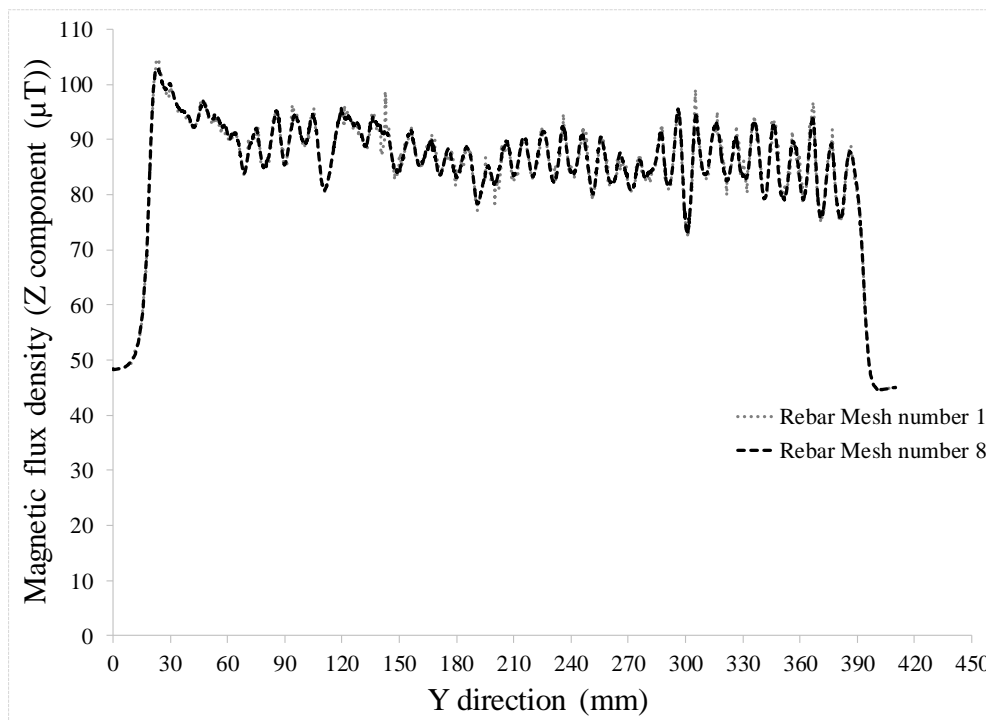
Figure 2.7. Comparison between the values of Z component magnetic flux density of rebar mesh #8 with fixed box mesh #1.

It was understood that increasing the spacing between the rebar and the recording point would result in some outliers in the trend of the Z component magnetic flux density, related to the specifications of the elements used in the box. To make the results of the simulation independent of the mesh, some more accurate element specifications were applied to the box (Appendix A). As a representative result, the magnetic flux density for the Z component at a distance of 16 mm was extracted (Figure 2.8). The minimum values from 295.0592 mm to 307.0592 mm (values related to Hole 2) became stable in the box mesh #5 (Figure 2.9).

21
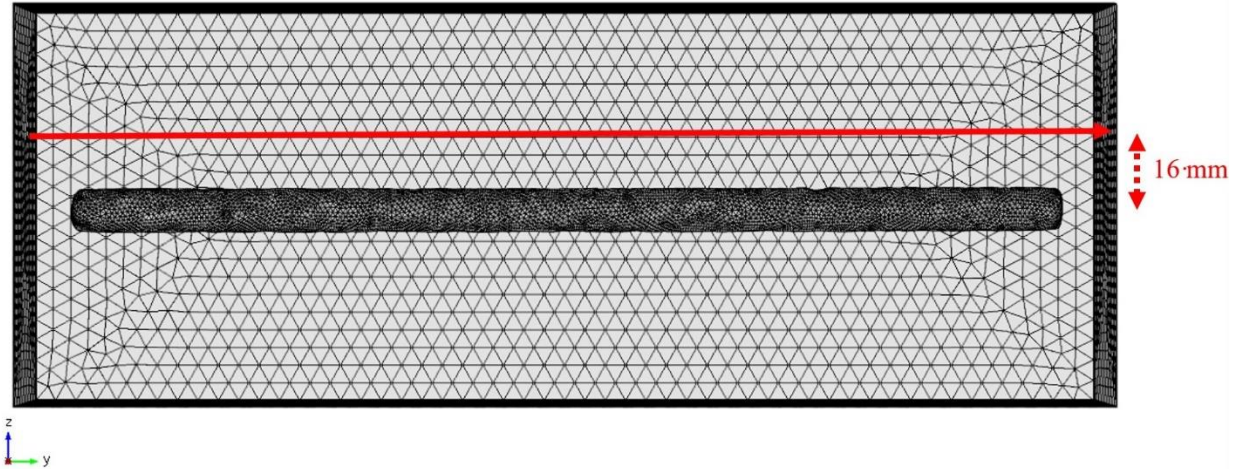
Figure 2.8. Path of data recording (with distance 16 mm from center of the rebar).
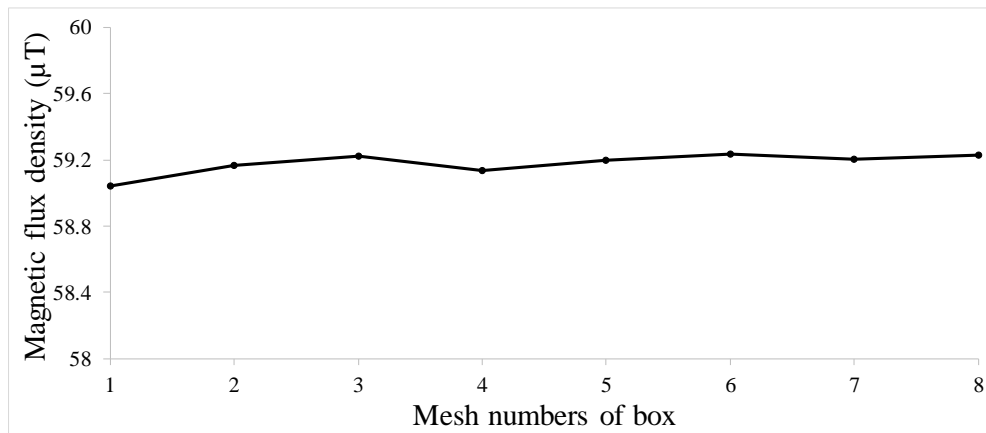
Figure 2.9. Minimum values of Z component magnetic flux density, from 295.0592 mm to 307.0592 mm (values related to Hole 2), for different box mesh specifications with a fixed rebar mesh #8.

Outcomes from the simulation of the rebar with mesh #8 and the box with mesh #5 were chosen for the rest of the investigations. Carrying out simulations with these specifications led to a graphical representation (Figure 2.10), which shows the behaviour of the Z component magnetic flux density at the location of Hole 2. Also, a planar slice of the magnetic field under the rebar (with the distance of 17 mm) shows the conditions of the stray magnetic field around the rebar. As the distance from the rebar increases, the stray magnetic field around the rebar decreases relatively uniformly and symmetrically.
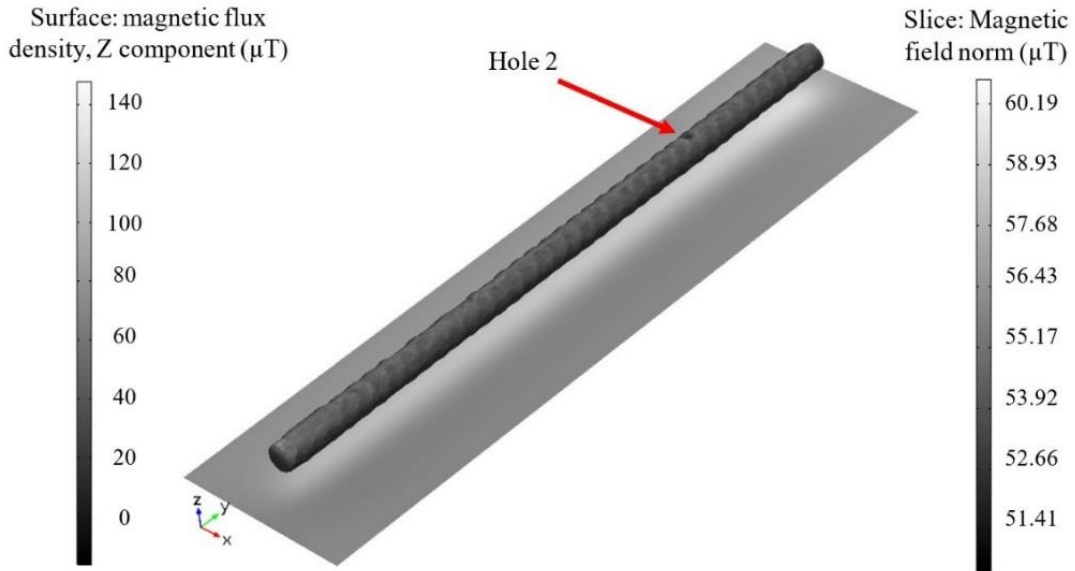
Figure 2.10. Behaviour of Z component magnetic flux density and normal magnetic field around the rebar (rebar mesh #8 & box mesh #5).

2.2.2. Parameter analysis

Figure 2.11 shows the values of magnetic flux densities of rebar with optimum mesh specifications at different spacings from the center of the rebar. The behaviour of the Z component magnetic flux density is distinguishable at Hole 2 at a maximum 16 mm from the center (Figure 2.11). For further investigation, the data-recording distance was increased to the maximum possible distance from the rebar, aligning with the inside edge of the box. At larger distances, the magnetic flux density trend becomes smoother and straighter and approaches the background magnetic field.

The minimum values of Z component magnetic flux density, from 295.0592 mm to 307.0592 mm (values related to Hole 2), were considered for different distances. Increasing the vertical distance (in the Z direction) of the data recording line logarithmically decreased the minimum value of Z component magnetic flux density until this value reached an approximately constant value. The trend line showing the relation between minimum values of the Z component magnetic flux density and data recorded at various distances is a 4th-order polynomial equation (Figure 2.12).

23
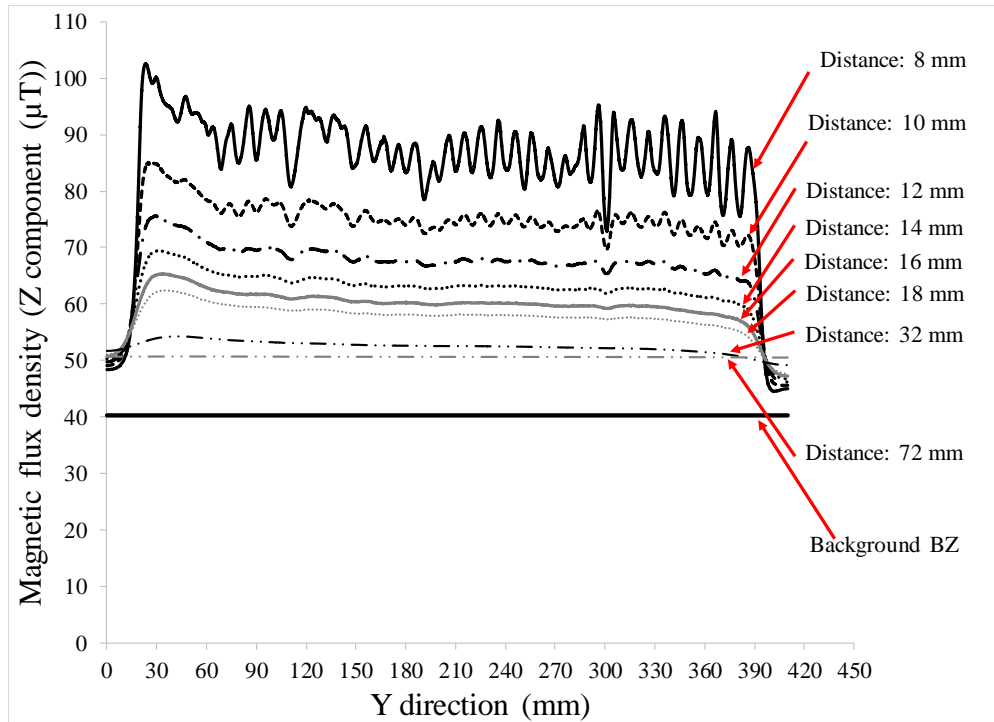
Figure 2.11. Values of magnetic flux densities of rebar mesh #8 and box mesh #5 at different vertical distances from the center of the rebar.
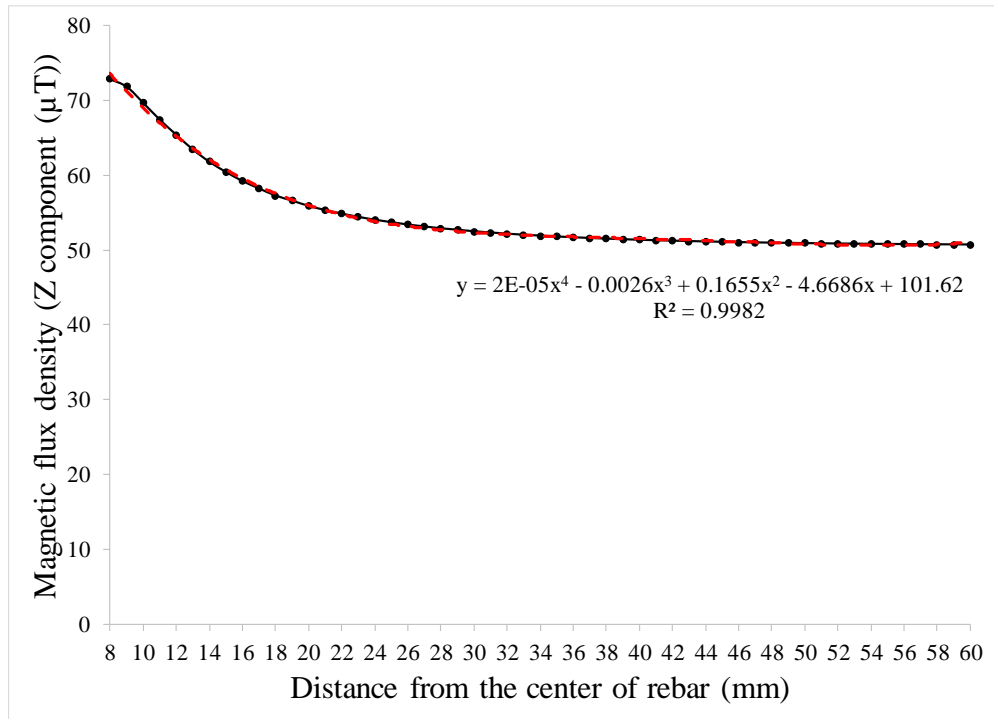
Figure 2.12. Behaviour of the minimum values of Z component magnetic flux density, from 295.0592 mm to 307.0592 mm (values related to Hole 2), of rebar mesh #8 and box mesh #5, recorded at different vertical distances.

24

2.2.3. Statistical analysis of the magnetic data

Assuming that the magnetic flux densities of different locations on the rebar are independent of one another, the probability graph method was used for fitting magnetic flux values to a probability distribution. The magnetic-flux-density data were plotted against various probability distributions (normal, log-normal, Weibull, and Gamma distributions); a Gamma distribution was chosen based on the method of least-squared error (Figure 2.13). This distribution is based on a flexible function of two parameters: α and β (Eq. 2-1), calculated by the mean and standard deviations (SD), which are 87.8 µT and 25.6 µT, respectively. As observed in Figure 2.14, the Gamma function correlates well with the histogram frequency of data, and this approximation may be useful for estimation in practical cases.

$$f(x) = \frac{1}{\beta^{\alpha}\Gamma(\alpha)}\ x^{\alpha-1}e^{-\frac{x}{\beta}} \tag{2-1}$$
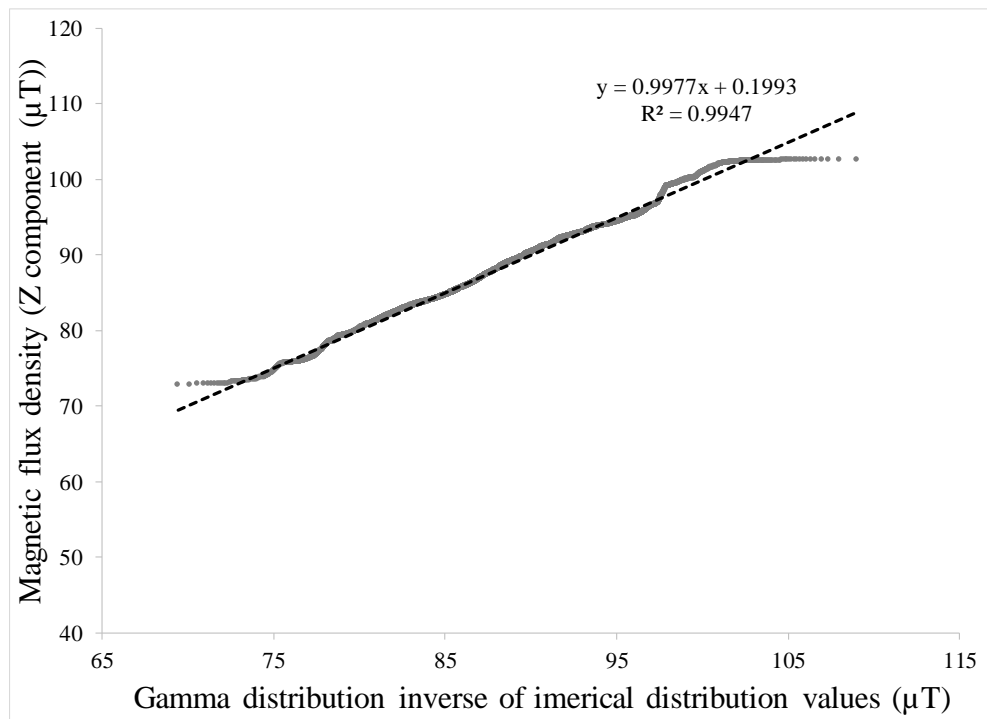
Figure 2.13. Probability plot used to investigate the correlation of simulation data with a Gamma distribution.
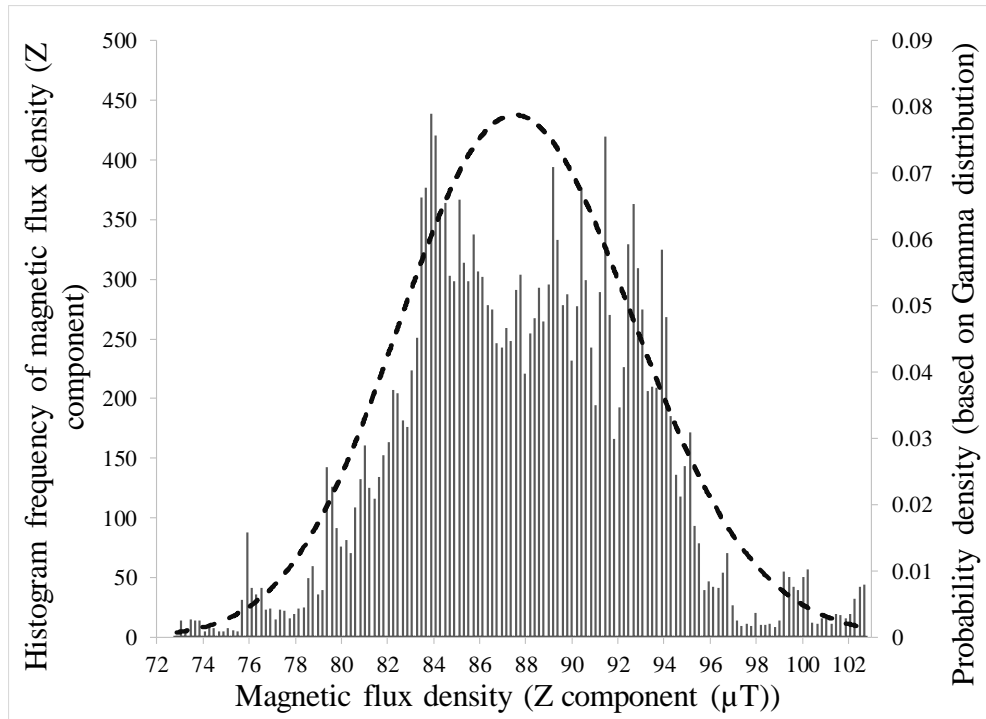
Figure 2.14. Histogram frequency of simulation data along with gamma distribution probability density.

According to Figure 2.11, a Z component magnetic flux density less than 76 µT (without considering the edge effect and background magnetic field) corresponds to the location of Hole 2. Importing this value into the obtained CDF shows that 0.76% of data is related to the defective locations. In other words, 0.76 percent of the rebar surface (at the scanned section) can be considered imperfect. This result can be verified by the Monte Carlo simulation method (based on inverse values of the obtained gamma distribution function). Figure 2.15 presents the probability of defects considering the mean, SD, and limit state, showing that the probability of defectiveness fluctuates until the first 300 trails are completed, then stabilizes at the value of ~0.75%.

For our statistical investigations, we considered the magnetic data as independent variables. Those independent variables were described by the chosen probability distribution with its particular distribution parameters. Knowing that distribution allowed us to estimate an interval over which the unknown future values may lie (with a certain amount of confidence). Using the above-mentioned CDF of the gamma distribution, about 98% of all of the data are from 76 µT to 100 µT (Eq. 2-2). Hence, regarding the recorded magnetic data of the rebar, it can be predicted with 98% confidence that if the rebar was longer (by how much is irrelevant), the next values indicating flawless rebar would be somewhere between 76 µT and 100 µT. Values outside this range should be reviewed as suspected defect locations.

$$GAMMADIS(100\ \mu T) - \ GAMMADIS(76\ \mu T) = 0.98 \hspace{3cm} (2\text{-}2)$$
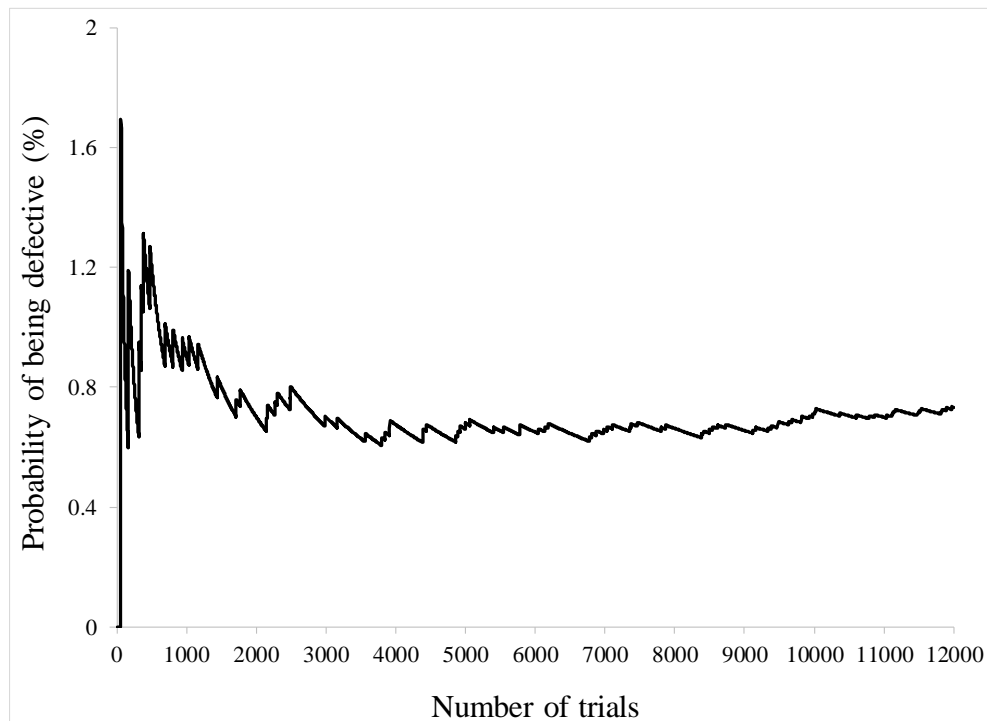
Figure 2.15. Defectiveness probability for inspected rebar based on Monte Carlo simulation method (based on simulation outcomes).

2.3. Comparison of the simulation results with previous experimental outcomes

Figure 2.16 shows different components of magnetic flux densities at the surface of the rebar, extracted from the optimum mesh specifications (for rebar mesh #8, and box mesh #5). The noise and out-of-range values were at their minimum and results correlate well with experimental outcomes reported previously (Figure 2.17) (Mahbaz *et al.*, 2017). The patterns of laboratory and simulated outputs at the holes' locations are reasonably similar, and the top hole, at ~301 mm from the Edge A of the box (Figure 2.16), ~282 mm of rebar's start point (Figure 2.17), is substantially easier to detect than the hole in the side of the rebar.
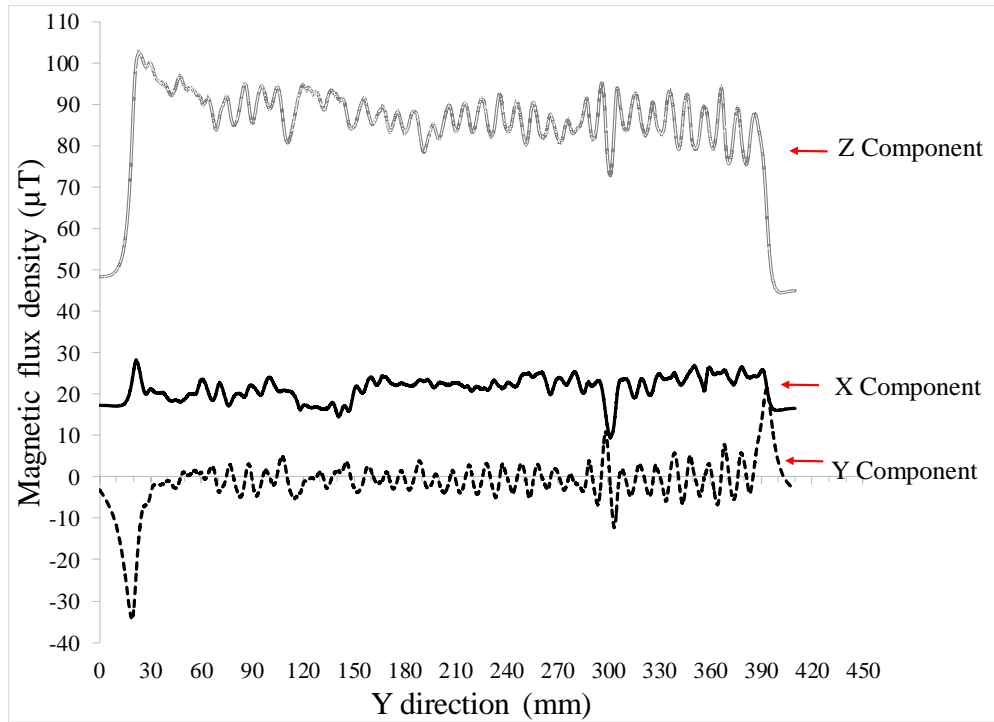
Figure 2.16. Magnetic flux density values at different axes (X, Y and Z) in Y direction at the surface of the rebar (rebar mesh #8 and box mesh #5), resulting from simulation.
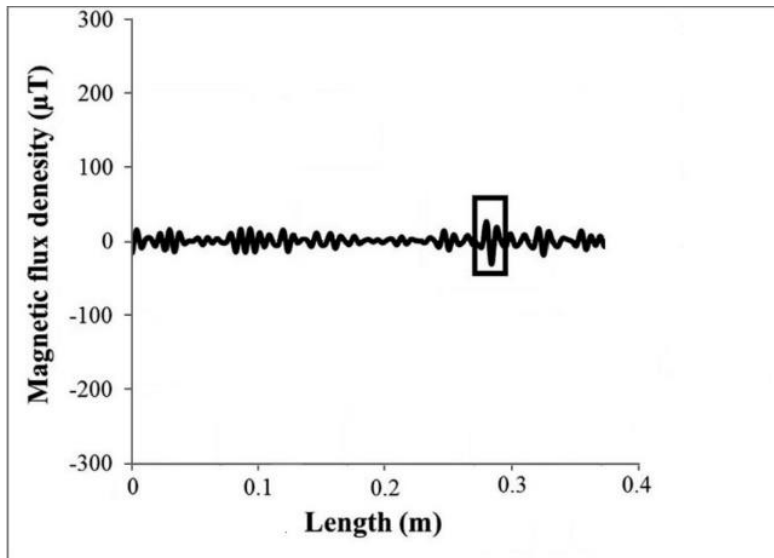
Figure 2.17. X-component of magnetic flux density resulted from the previous experiments, square shows the Hole 2 location (Mahbaz *et al.*, 2017).

2.4. Conclusion

Robust defect detection in steel infrastructure elements would contribute substantially to risk management and condition evaluation over time. To this end, mathematical simulations were carried out on a pre-flawed specimen that was laser-scanned to generate a point cloud surface map

that served as the basis for model development. The intent was to establish detectability limits for very small flaws in order to reduce false positive and false negative errors in anomaly detection. The magnetic behaviour of the ferromagnetic rebar specimen was simulated with a finite-element-based software considering the background magnetic field. Different components of magnetic flux densities on the surface showed consistent harmonic trends because of the corrugated shape of the rebar. However, there were specific irregularities in the direction and values for different components of magnetic flux densities at the location of Hole 2. Simulated patterns can be correlated with the experimental data at the holes' locations, so the top hole (Hole 2) was easily located, but not Hole 1 because of its orientation in the magnetic field and because the point cloud model did not replicate its true depth. The Gamma probability distribution was chosen to statistically assess the magnetic flux density behaviour of the rebar. Two main outcomes were extracted: 0.76 percent of the scanned section of the rebar was considered defective; and, if the rebar specimen was longer, the Z-component magnetic flux density values indicating flawless rebar would be predicted to lie between 76 µT and 100 µT with 98% confidence.

The values of the different components of magnetic flux densities at different distances from the rebar were reviewed. Increasing the vertical distance of the data recording line led to a logarithmic reduction of magnetic flux density values. As this distance is increased, the magnetic flux density values became approximately constant and close to the background magnetic field. In conclusion:

- The pattern of the simulation results at defect locations were similar to the outputs of previous physical experiments;
- The background magnetic field had a significant effect on the trend and values of different components of the magnetic flux density;
- All magnetic flux density components displayed correctly located anomalies corresponding to the defect on the top surface of the rebar;
- Increasing the distance from the rebar changed the trend and values of the magnetic flux densities such that at some distance the anomaly became undetectable;
- To detect various shapes and sizes of defects at different places along a rebar specimen, additional magnetic parameters should be considered. For instance, the Z component of the magnetic flux density was totally constant on the sides of the rebar, and could not detect the anomaly arising from Hole 1;

- The stray magnetic field around the rebar decreased relatively symmetrically by increasing the distance from the rebar

- The choice of the gamma distribution to model the Z-component magnetic flux density values of the numerical simulation resulted in valuable interpretations.

Chapter 3: Longitudinal defect detection in three similar rebars using PMI technology

Most portions of this chapter are reflective of an original manuscript submitted by the Ph.D. candidate (Milad Mosharafi) to the journal of Nondestructive Evaluation in September 2019.

3.1. Introduction

Steel rebar corrosion, the major reason for concrete structures' failure (Zhao *et al.*, 2011), can appear in different forms, including general or local corrosion (Perkins, 2000). One of the most common forms of local corrosion on the surface of steel reinforcement is pitting, which non-uniformly reduces the effective cross-sectional area and causes stress concentration zones (Ma *et al.*, 2017). Pitting-corrosion shapes can be circular (Jiang *et al.*, 2017), semicircular (Ma *et al.*, 2017), or longitudinal (Tahershamsi *et al.*, 2017). This type of corrosion may be non-uniformly distributed along a rebar, and its position may be related to the concrete's properties (such as permeability and thickness of cover), steel impurities, and small-scale environmental conditions (Stewart, 2009). In the previous chapter, investigations were conducted on the magnetic properties recorded over a rebar with circular pittings (holes). To achieve more-accurate and better-calibrated outcomes, additional studies are necessary to improve the analysis and interpretation approaches conducted on the magnetic data. The study described in this chapter focuses on experiments and simulations that investigate ferromagnetic steel rebars with artificial longitudinal defects.

In this chapter, self-magnetic flux leakage (SMFL) data are recorded by running a PMI scanner over three similarly defective rebars, each with three similar-sized longitudinal defects. The data are recorded at different vertical distances from a rebar with the defects at various clock positions. The magnetic data is analysed to identify the data patterns at the defect locations. A data value threshold is then defined, based on the magnetic data, for identifying the locations of the longitudinal defects. Next, the self-magnetic behavior of a solid defective rebar, similar to the rebars used in the experiments, is simulated using a finite-element-based software (COMSOL® software version 5.3a (COMSOL Group, Stockholm, Sweden)). The simulation is conducted under the influence of Earth's magnetic field, in a manner similar to the investigations conducted by Mosharafi *et al.* (2018). Subsequently, SMFL data recorded through the experiments are compared with the simulation outcomes, and the robustness of the thresholding values is assessed.

3.2. Sample preparation and experimental setup

For investigating the PMI device's accuracy in detecting longitudinal defects, three 20 mm diameter steel rebars were cut to approximately the same lengths of 600 mm. One by one, the rebars were tightened into a milling machine's vise, and suitable positions were found for creating three similar longitudinal defects spaced at even distances apart in a line along each rebar using an edge finder (Figure 3.1.a). The longitudinal defects then were created in rebars using a face drill bit (Figure 3.1.b). Next, the sharp edges and attached swarf resulting from machining were removed using a file to finalize the specimens' preparation (Figure 3.2).

(a)	(b)
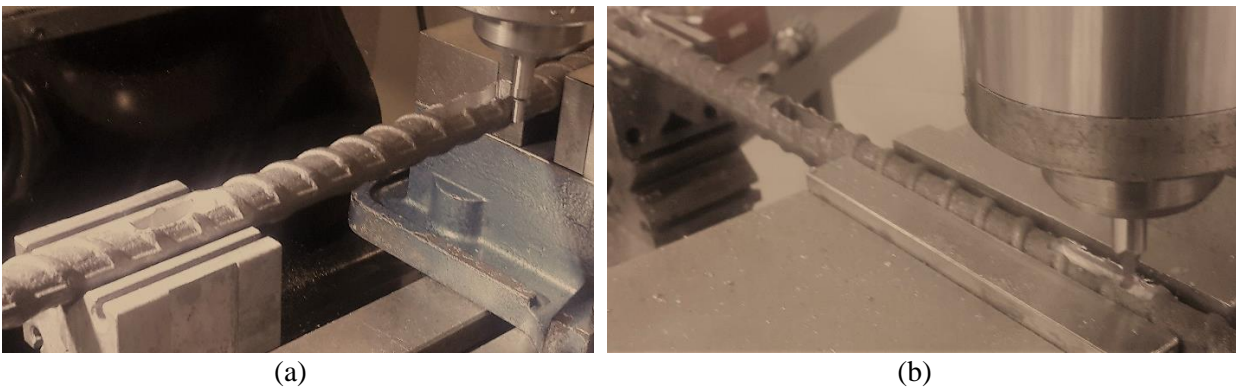
Figure 3.1. The process of creating the defects in rebar: (a) Identifying the desirable position of defects using an edge finder, (b) Creating the defect using a face drill bit.
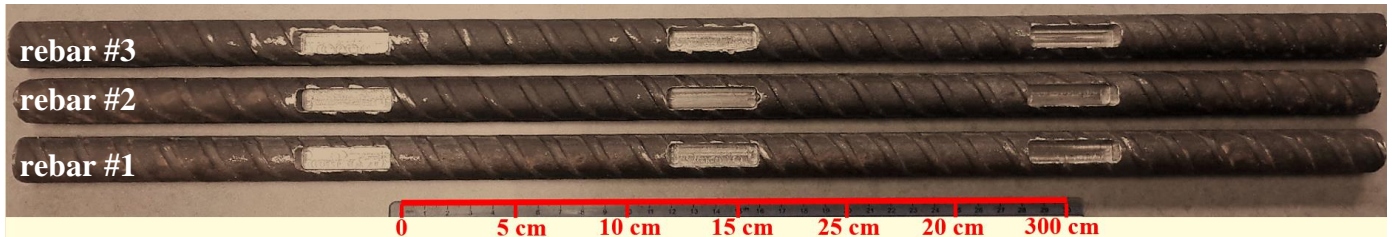
Figure 3.2. Prepared rebars with three symmetrically-located and similar longitudinal defects.

Measurements were then conducted on the rebars (Figure 3.3) to find the dimensions of the rebars and the longitudinal defects. A schematic drawing of the samples was subsequently prepared (Figure 3.4) to better study the relationships between the rebars' magnetic and physical (i.e., dimensional) properties. According to Table 3-1, all 9 longitudinal defects have the same dimensions within a tolerance of about $\mp 0.1 \ mm$ except for the defect #2 of rebar #2. The length of this defect (40.1 mm) has a deviation of about 1.2 mm from the mean value of the length of the other defects.
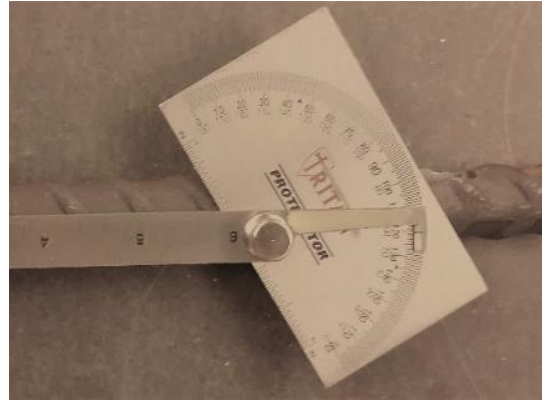
(a)   (b)

(c)

Figure 3.3. Measuring the rebars to provide an accurate schematic drawing.

Isometric view

Top view

Left view

defect #1   defect #2   defect #3
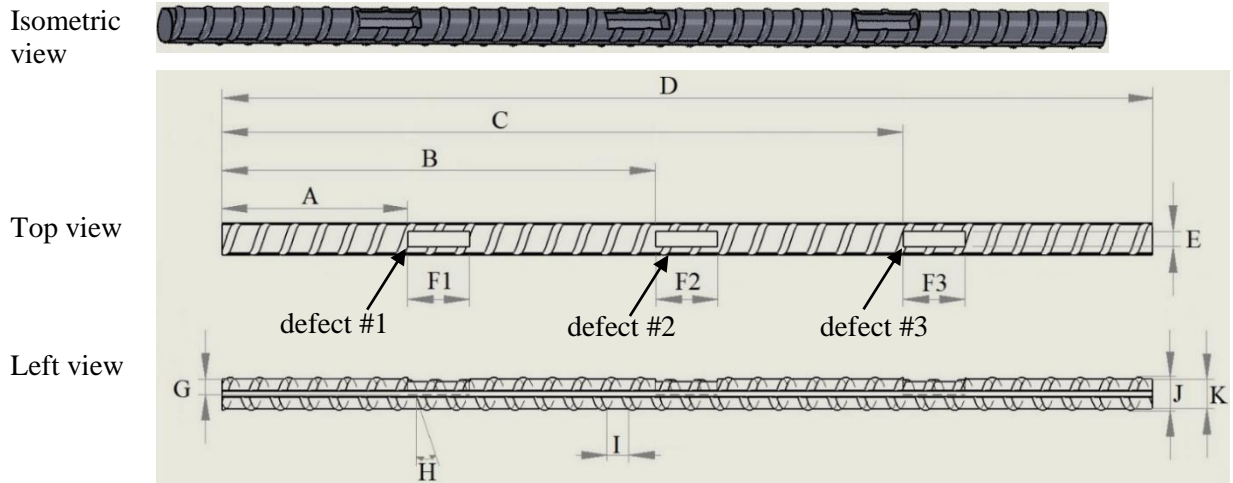
Figure 3.4. Schematic drawing of prepared samples.

Table 3-1. Values for the parameters shown in Figure 3.4.

Parameter's name	Rebar NO.			Parameter's name	Rebar NO.		
	1	2	3		1	2	3
A (mm)	120.09	119.04	121.38	G (mm)	10±0.1	10±0.1	10±0.1
B (mm)	279.91	278.08	281.75	H (Deg.)	30	30	30
C (mm)	439.89	438.99	443.01	I (mm)	12.7	12.7	12.7
D (mm)	599.81	598.29	604.5	J (mm)	19	19	19
E (mm)	10±0.1	10±0.1	10±0.1	K (mm)	20.03	20.03	20.03
F1 (mm)	39.99	40.08	40.03				
F2 (mm)	40.13	41.44	40.01				
F3 (mm)	40.03	40.05	39.99				

3.3. Investigating the rebar with its defects at 12 clock position

3.3.1. Scanning procedure

The prepared defective rebars were located one by one at a non-magnetic location (remote from other ferromagnetic materials) and were scanned along their whole length using the PMI scanner. The PMI device consists of two main parts: a scanner and a data logger. SMFL arising from ferromagnetic rebars is scanned by sensors embedded in the PMI scanner (Mosharafi *et al.*, 2018), and the corresponding distances of each magnetic data value along the linear tracking line are measured using an encoder attached to one of the scanner's wheels. The resulting magnetic data sets are collected and stored in a memory card placed in the data logger for subsequent analyses and interpretations.

The magnetic flux densities of the fixed rebars were measured at three dimensions (X, Y, and Z) at the vertical distance of 10 mm from their surfaces (the minimum vertical distance that can be applied with the PMI device) in order to record more-accurate magnetic data (Figure 3.5). To ensure accuracy, every rebar was scanned along the same path and direction ten times, with statistical T-tests conducted between every two scans (Eq. 3-1) (Montgomery, 2014). Next, the scan that was most significantly equal to the greatest number of other scans was chosen for use in the rest of the study. As an example, Figure 3.6 shows the ten scans' magnetic X component over rebar #2 from the distance of 100 mm to 500 mm of its length. Scan #3 was identified as the best candidate for the rest of the studies on that rebar, being significantly (at a level of 0.002) equal to eight other scans (Table 3-2). The procedure was then conducted for two other rebars to again choose the most-consistent scans. This procedure also allows evaluation of the repeatability of the measurement method, which at the present time is hand-held scanning, and therefore might be expected to have some variability from scan to scan.

$$T_{probe} = \frac{(\bar{X}_{scan\ \#i} - \bar{X}_{scan\ \#j})}{S_P \sqrt{\dfrac{1}{n_{scan\ \#i}} + \dfrac{1}{n_{scan\ \#j}}}}$$

$$(3\text{-}1)$$

$$S_P = \sqrt{\frac{(n_{scan\ \#i} - 1)S^2_{scan\ \#i} + \left(n_{scan\ \#j} - 1\right)S^2_{scan\ \#j}}{n_{scan\ \#i} + n_{scan\ \#j} - 2}}$$

$i\ and\ j : number\ of\ scans$

$S: Standard\ deviation$

$n: total\ number\ of\ data$

$Null\ hypothesis: H_o: \mu_i - \mu_j = 0$

$Alternative\ hypothesis: H_1: \mu_i - \mu_j \neq 0$
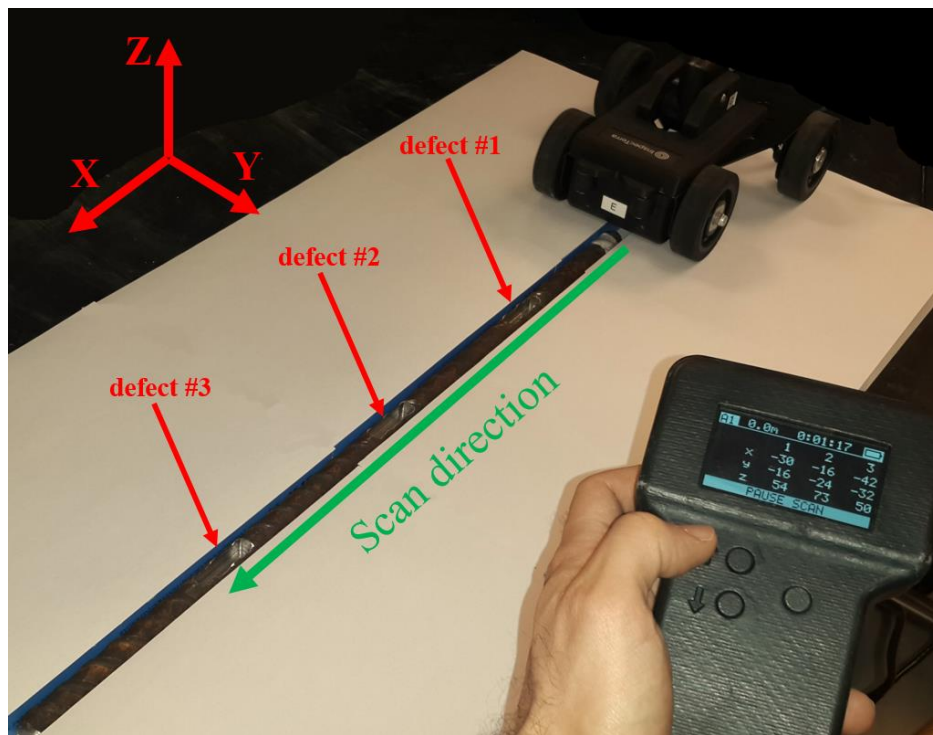
Figure 3.5. Experimental data recording process.
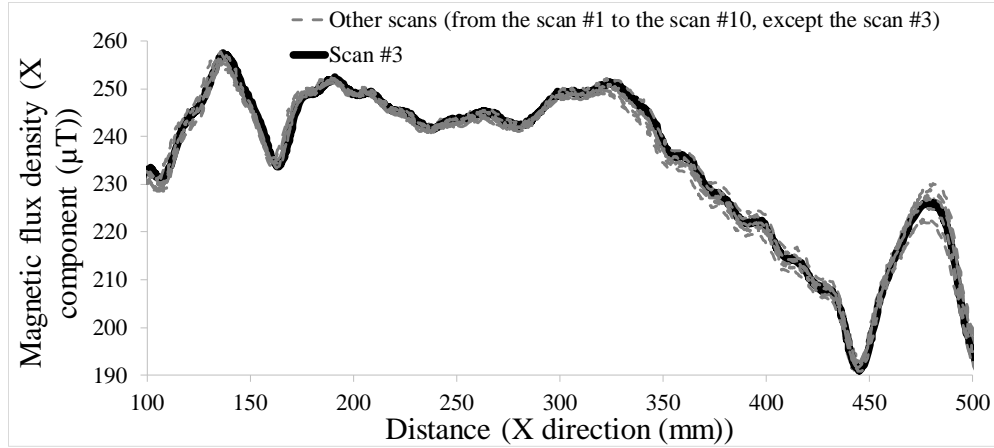
Figure 3.6. X component magnetic flux density values recorded by ten separate scans of the same rebar (rebar #2), moving along a similar path and direction.

Table 3- 2. One-by-one mean value comparisons of scan #3 to the other scans (from scan #1 to scan #2 and from scan #4 to scan #10); green color shows that $\mu_i=\mu_j$ and red color shows that $\mu_i\neq\mu_j$.

Null hypothesis	T_{probe}	$T_{critical}$ (with a significance level of 0.002)	Result of the hypothesis test
$\mu_3 = \mu_1$	0.30929	3.09	$\left\|T_{probe}\right\| < \left\|T_{critical}\right\| \rightarrow$ fail to reject the null hypothesis
$\mu_3 = \mu_2$	0.192412	3.09	$\left\|T_{probe}\right\| < \left\|T_{critical}\right\| \rightarrow$ fail to reject the null hypothesis
$\mu_3 = \mu_4$	0.254363	3.09	$\left\|T_{probe}\right\| < \left\|T_{critical}\right\| \rightarrow$ fail to reject the null hypothesis
$\mu_3 = \mu_5$	1.539648	3.09	$\left\|T_{probe}\right\| < \left\|T_{critical}\right\| \rightarrow$ fail to reject the null hypothesis
$\mu_3 = \mu_6$	0.47967	3.09	$\left\|T_{probe}\right\| < \left\|T_{critical}\right\| \rightarrow$ fail to reject the null hypothesis
$\mu_3 = \mu_7$	7.36928	3.09	$\left\|T_{probe}\right\| > \left\|T_{critical}\right\| \rightarrow$ reject the null hypothesis
$\mu_3 = \mu_8$	0.07102	3.09	$\left\|T_{probe}\right\| < \left\|T_{critical}\right\| \rightarrow$ fail to reject the null hypothesis
$\mu_3 = \mu_9$	3.294002	3.09	$\left\|T_{probe}\right\| > \left\|T_{critical}\right\| \rightarrow$ reject the null hypothesis
$\mu_3 = \mu_{10}$	0.454853	3.09	$\left\|T_{probe}\right\| < \left\|T_{critical}\right\| \rightarrow$ fail to reject the null hypothesis

Data analysis were conducted through various approaches on PMI-recorded magnetic flux density values. The three main approaches that detected the defects more precisely are as follows:

- Marking the minimum values after overall detrending;
- Peak analysis (without overall detrending) with a minimum distance restriction;
- Marking the minimum values after removing the dominate low frequency using the magnitude and power spectrum graphs;
- Using the derivative patterns of the data.

3.3.2. Data-processing Approaches

3.3.2.1. Approach #1: marking the main local minimum values after overall detrending

This approach was carried out for the selected scans (using the T-testing) over each of the three rebars. The first and last 20 mm of the scans were deleted to remove edge effects. Next, a moving

average smoothing technique was used to smooth out short-range fluctuations and highlight longer-range trends. The magnetic data thus obtained showed overall patterns that were not desirable in finding the defect sites. Those overall trends, related to the inherent magnetic properties of the materials, can hinder data analysis and must be removed. Linear and non-linear detrendings algorithms were used to eliminate the overall patterns from the data, and a simple filter was used to identify values below a defined threshold. In this approach, the process of data analysis included the following steps (using MATLAB software):

1. Instead of every magnetic value, a mean value was located. The means were taken from an equal number of data on either side of a central value (with a period of about 1.5 mm);
2. The overall linear trend was removed by subtracting the best fitted straight-line from the magnetic data;
3. The overall non-linear trend was removed by subtracting the best-fitted polynomial or Fourier function from the magnetic data;
4. Main local minimum values of the obtained curves were marked and identified as the locations showing the places of the longitudinal defects.

Figure 3.7 shows the complete details of the data processing approach conducted on the three rebars. The data resulting from rebars #1, #2, and #3 are respectively shown in Figures 3.7a1, 3.7b1, and 3.7c1 before and after removing the linear trend. Additionally, Figures 3.7a2, 3.7b2, and 3.7c2 show the non-linear curves fitted for the overall non-linear trends (Appendix B) of data, respectively taken from Figures 3.7a1, 3.7b1, and 3.7c1. The data (after removing the linear trends) was subtracted from the fitted non-linear curves, and the residual plots, related to rebar #1, #2, and #3 are respectively shown in Figures 3.7a3, 3.7b3, and 3.7c3.

All the defects can be detected through the presence of local minimums shown by red solid-line arrows in the residual plots. However, defect #2 of the rebar #2 cannot be clearly distinguished in Figures 3.7b3 (the red dashed-line arrow), since there are other local minimums with lower values in the non-defective sections. Differences between the magnetic behaviour of different defects may happen because of their slight angular deviation on the top of the rebar, since the magnetic sensors of PMI scanner are sensitive to small geometric effects, particularly sharp edges at different angles. To detect defect #2, after the magnetic data of rebar #2 was processed for a shorter span, a non-linear curve was fitted to cover the data's overall non-linear pattern (Figure 3.8a). The residual

plot, resulting from subtracting the data (after eliminating the linear trend) and the non-linear fitted curve, showed the defect #2 of the rebar #2 as a main local minimum point (Figure 3.8b). Hence, the last residual plot (Figure 3.8b) was used in the rest of the investigations related to rebar #2.

(a1)   (a2)   (a3)

(b1)   (b2)   (b3)

(c1)   (c2)   (c3)
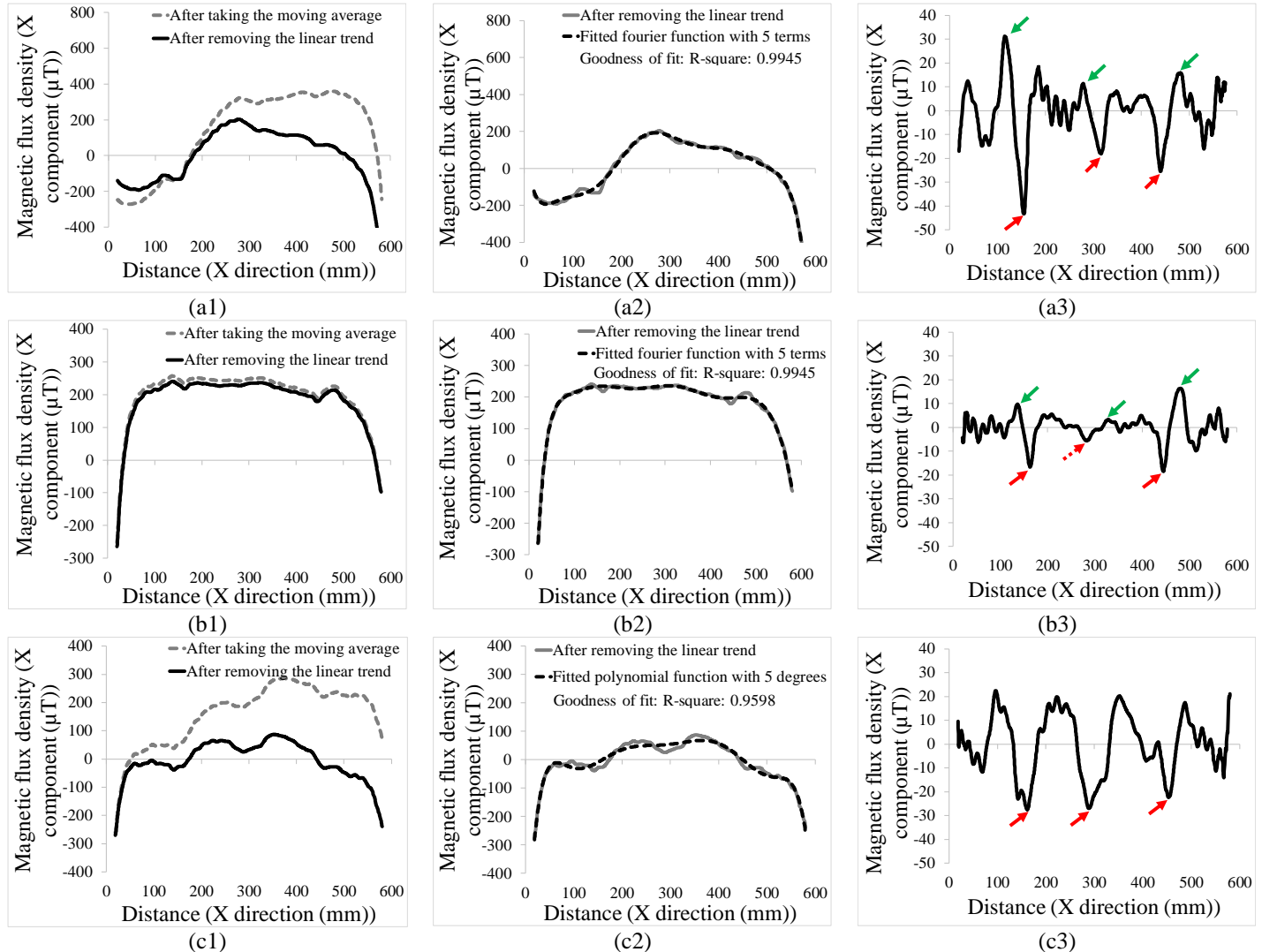
Figure 3.7. Signal analysis of the three rebars: (a1) Removing linear trend from rebar #1's magnetic data, (a2) Fitting a non-linear curve on a1's solid line, (a3) Residual plot after subtracting the non-linear fitted curve from a1's solid line; (b1) Removing linear trend from rebar #2's magnetic data, (b2) Fitting a non-linear curve on b1's solid line, (b3) Residual plot after subtracting the non-linear fitted curve from b1's solid line; (c1) Removing linear trend from rebar #3's magnetic data, (c2) Fitting a non-linear curve on c1's solid line, (c3) Residual plot after subtracting the non-linear fitted curve from c1's solid line.
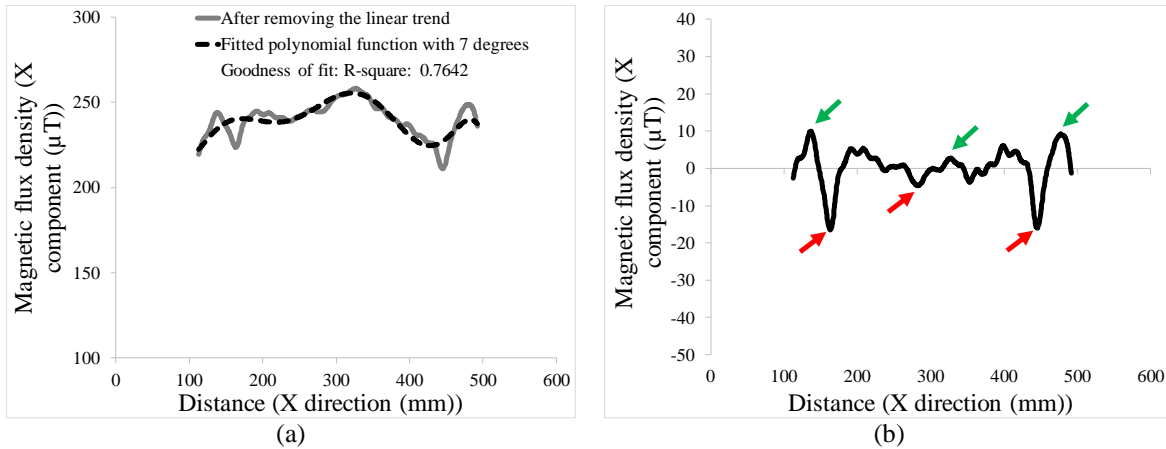
Figure 3.8. Processing the magnetic data resulting from rebar #2, over a shorter distance: (a) Fitting a non-linear curve on the data (after removing its linear trend), (b) Residual plot after subtracting the non-linear fitted curve from the data post removal of the linear trend.

The residual plots representing rebar #1 (Figure 3.7a3) and rebar #2 (Figure 3.8b), at the locations of the longitudinal defects, show relatively similar behaviour. There is a local minimum point (concave upward) close to one of the ends of the defects (the red solid-line arrows). These local minimum points are followed by two local maximum points (concave downward), and the higher maximum point (the green solid-line arrows) is close to the other edge of the defects. Additionally, an inflection point, where a concave upward line transitions to a concave downward line, represents a point close to the middle of the defects. This finding can help in estimating the defects lengths. Figure 3.9 shows a stem-and-leaf diagram of the difference between the locations of the main local minimums and their related local maximum points. Based on this diagram, the median is calculated to be equal to 38.55 mm, which is close to the length of the longitudinal defects. Additionally, using the values in the stem-and-leaf diagram in Figure 3.9, the confidence interval was calculated with an 80% confidence level (Eq. 3-2). Regarding the calculated confidence interval, the difference between the locations of the main local minimums and their related local maximum points is expressed by $37 \pm 4 \, \mu T$ (considering a significance level of 0.2). The calculated interval includes the mean value for the length of the defects computed by the values in Table 3-1 (by parameters F1, F2, and F3) to be equal to 40.2.

Stem	Leaf			Frequency
2	6.45 mm			1
3	2.18 mm	7.28 mm	9.83 mm	3
4	2.38 mm	4.61 mm		2

Figure 3.9. Stem-and-leaf diagram of the difference between the locations of the main local minimums and their related local maximum points for rebars #1 and #2 (leaf unit = 1).

$$\bar{X} \mp T_{\frac{\alpha}{2},(n-1)} \frac{S}{\sqrt{n}}$$

<div align="right">(3-2)</div>

$\bar{X}$: best estimate (features' mean value)

n: sample size

S: sample's standard deviation

α: significance level (considered to be 0.05)

The residual plot for rebar #3 shows different behaviour than those for rebar #1 and rebar #2. In rebar #3's residual plot (Figure 3.7c3), the main local minimum points are found somewhere within the length of the longitudinal defects, and no related local maximum point can be found for estimating the length of the defects. This difference may result from residual stresses from the machining that created the defects (stresses that may appear as strong up and down trends at the defect locations (Figure 3.7c2)). It may also result from certain rebars being stored under different conditions to the others, previous to the study. However, the locations of all nine defects (from all three rebars) can be detected by the main local minimum values.

To ensure the reliability of the main minimum values, their absolute differences from the mean values in every graph (Figure 3.7a3, Figure 3.7c3, and Figure 3.8b) were calculated using a box-and-whisker plot in conjunction with a stem-and-leaf diagram (Figure 3.10). Using the data in Figure 3.10a, the Interquartile Range (IQR) and the maximum and minimum ranges for determining the outliers are calculated in (Eq. 3-3). Although some values (from Figure 3.10b) are close to the IQR limitations, all of them are still within the range. Hence, there are no outliers in the local minimum values, and all of them are reliable.

Stem	Leaf		
0	4.92 µT		
1	6.36 µT	6.78 µT	8.06 µT
2	2.35 µT	6.94 µT	7.49 µT
3	3.33 µT		
4	3.29 µT		

Leaf unit=1

(a)   (b)
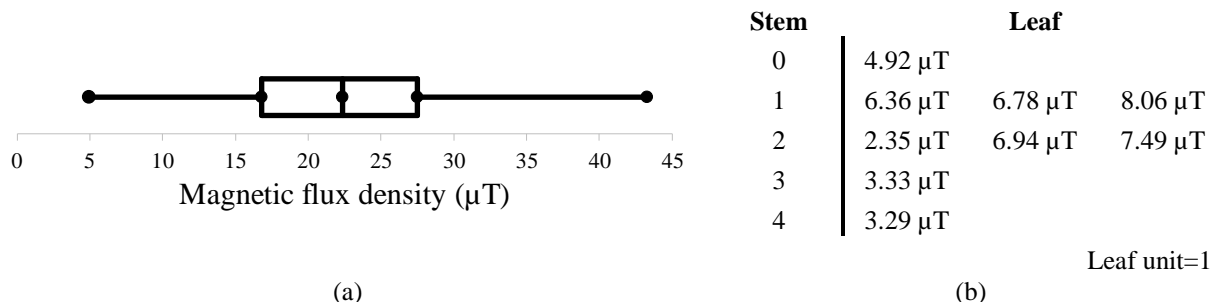
Figure 3.10. Differences between the main local minimum values and mean values for every residual graph shown in Figure 3.7a3, Figure 3.7c3, and Figure 3.8b: (a) Box and whisker plot (b) Stem-and-leaf diagram.

$$IQR = Q_3 - Q_1 \rightarrow IQR = 27.497 \ \mu\text{T} - 16.789 \ \mu\text{T} \rightarrow IQR = \ 10.707 \ \mu\text{T} \tag{3-3}$$

$$Max \ (outlier \ limitation) = Q_3 + 1.5(IQR) \rightarrow Max \ (outlier \ limitation) = 43.559 \ \mu\text{T}$$

$$Min \ (outlier \ limitation) = Q_1 - 1.5(IQR) \rightarrow Min \ (outlier \ limitation) = 0.727 \ \mu\text{T}$$

Q_1: *First quartile*

Q_3: *Third quartile*

Assuming that the magnetic flux densities of different locations on the rebars are independent of one another, the probability paper method was implemented to fit the magnetic data (resulting from residual plots (Figures 3.7a3, 3.7c3, and 3.8b) into probability distributions. The magnetic-flux-density data of the three rebars were plotted against various probability distributions (Normal, Log-normal, Weibull, and Gamma). Next, Normal (with R2 = 0.96), Weibull (R2 = 0.93), and Normal (with R2 = 0.96) distributions were respectively chosen to represent the magnetic data recorded over rebar #1, rebar #2, and rebar #3 (Figure 3.11a, Figure 3.11c, and Figure 3.11e). It should be noted that for plotting Figure 3.11c, a constant value of 50 µT was added to data to eliminate the negative values enable plotting against Weibull distribution. After conducting the paper probability plot, the values were returned to their original state for accurate results. Figures 3.11b, 3.11d, and 3.11f show strong correlations between the histogram frequency of data and the chosen cumulative distributions. These probability distributions guide us in defining a reliable threshold for finding the minimum values of the magnetic data representing the defective locations.
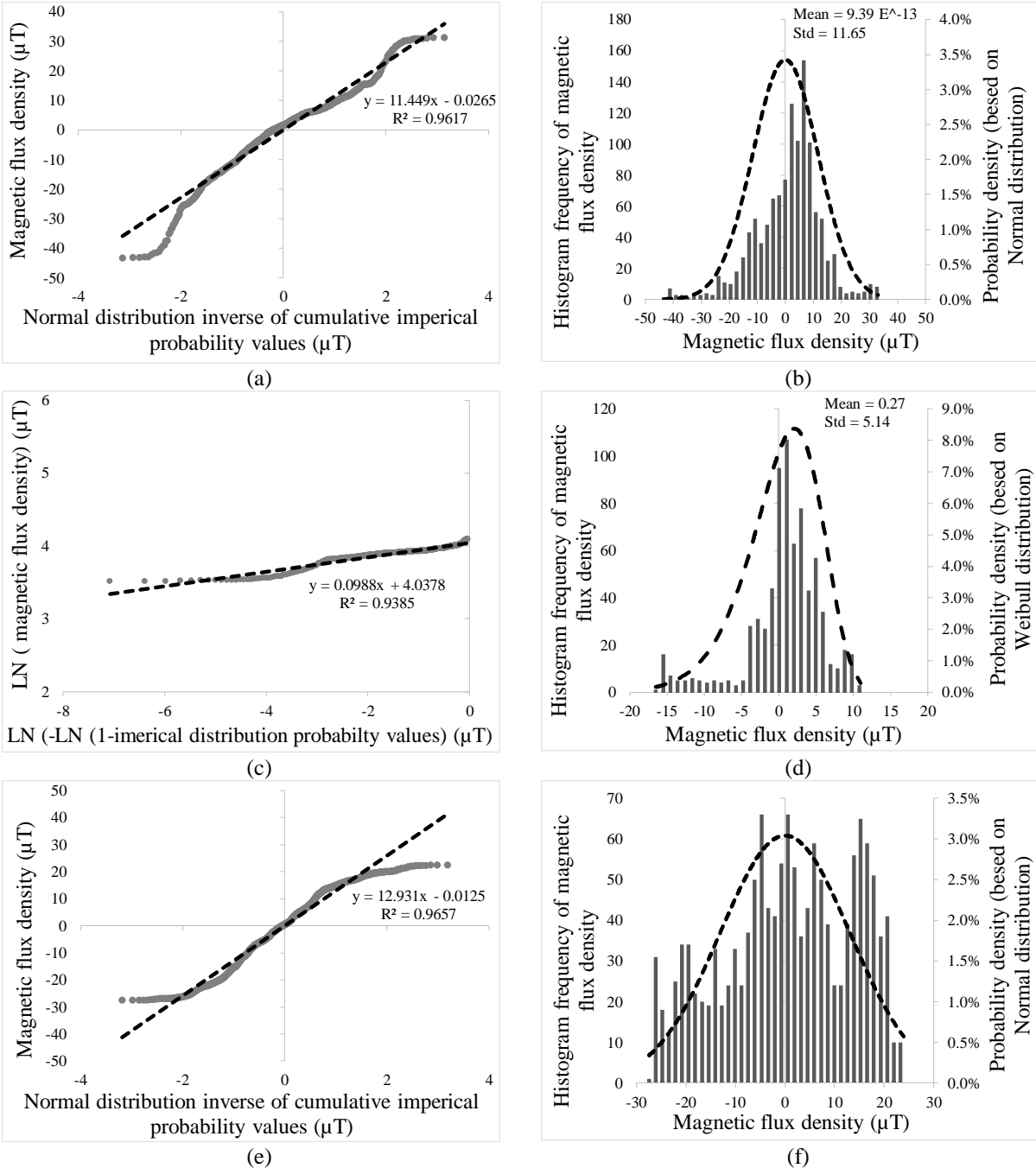
Figure 3.11. Data processing approach on the three rebars: (a) Normal probability plot for rebar #1's residual plot data, (b) Histogram frequency of rebar #1's residual plot data in conjunction with probability density of a Normal distribution; (c) Probability plot investigating the correlation of rebar #2's residual plot data with a Weibull distribution, (d) Histogram frequency of rebar #2's residual plot data in conjunction with probability density of the Weibull distribution; (e) Normal probability plot for rebar #3's residual plot data, (f) Histogram frequency of rebar #3's residual plot data in conjunction with the probability density of a Normal distribution.

Figure 3.7a3 shows that a value of less than or equal to -18.1 µT in the main local minimum magnetic data indicates a defect. This value can be considered as the 6.04th percentile of rebar #1's magnetic data, based on the fitted Normal probability distribution (Figure 3.11b). Figures 3.8b and

3.7c3 respectively demonstrate that values less than or equal to -4.65 µT and -22.4 µT in the main local minimums indicate the positions of longitudinal defects. Placing the two obtained magnetic values resulting from scanning rebar #2 and rebar #3 in their cumulative fitted Weibull and Normal probability distributions respectively shows the 4.41[th] and 16.12[th] percentiles. The percentile value calculated for rebar #2 is relatively different from percentiles calculated for the two other rebars, because of the different behaviour of its defect #2. However, the mean value of the percentiles calculated from the magnetic data of the three rebars (8.88[th] percentile) can be considered a reasonable threshold for subsequent studies.

3.3.2.2. Approach #2: peak analysis with a minimum distance restriction

This approach was carried out for the selected scans (based on T-hypothesis testing) over each of the three rebars. At first, to remove the edge effects, 20 mm of data from both ends of every scan were deleted, and the rest of the data was subjected to moving average smoothing technique (i.e., Smoothing produces better peak analysis by flattening the sudden up-and-downs generated by probable noises). Subsequently, positions with values larger than their neighbors (local peaks) were detected. Those points can be considered as the local maximum positions. The data was reversed, and the same procedure was performed to find the local peaks (local minimum locations of the not-reversed data). Then the local maximum and minimum locations were marked on the original (not-reversed) data. Although the defects were clearly indicated by the detected local extrema, many local extrema also occurred at non-defective places. To decrease the percentage of Type I errors (if H_o : the rebar is non-defective), a constraint was applied for eliminating any peaks closer to each other than a selected distance (minimum peak distance constraint). Using this constraint enabled us to choose the tallest peak in the signal and eliminate all other peaks within a certain distance. The optimum constraint was chosen by applying various minimum peak distance restrictions to find the highest true positive and the lowest false positive. The data analysis in this approach included the following steps:

1. The means of the magnetic data taken from an equal number of data on either side of a central value (with a period of about 4.5 mm), replaced the magnetic data values. The period for taking the moving average was 3 times greater than that used in approach #1 to flatten the meaningless sudden up-and-downs that impede efficient peak analysis.

2. Local peak locations were identified on both the original and the inverted data. The detected positions were then marked on the original data (to show the local extrema).

3. Minimum peak distance restrictions were applied to find the peaks that are separated by certain distances, and the optimum distance was selected based on the true positive and false positive percentages.

4. The local extrema were marked on the original data regarding the selected value for the minimum peak distance restriction.

Figure 3.12 shows all the details of the data processing conducted on rebar #1. Finding the peak locations on both the original and the inverted data is shown in Figure 3.12a. All the detected peaks are then marked on the original data in Figure 3.12b. Additionally, Figure 3.12c shows the detectability percentages, demonstrating that the highest true positive and lowest false positive percentages are obtained by a minimum peak distance restriction of greater than 75 mm. The obtained distance restriction was then used to find the peak positions on the original data (Figure 3.12d). Figure 3.13 and Figure 3.14 also show the last two steps of the same procedure for rebars #2 and #3, respectively. Figure 3.13a and Figure 3.14a demonstrate that the highest true positive and lowest false negative detectability percentages can be respectively obtained using 70 mm and 55 mm minimum peak distance restrictions for rebar #2 and rebar #3.
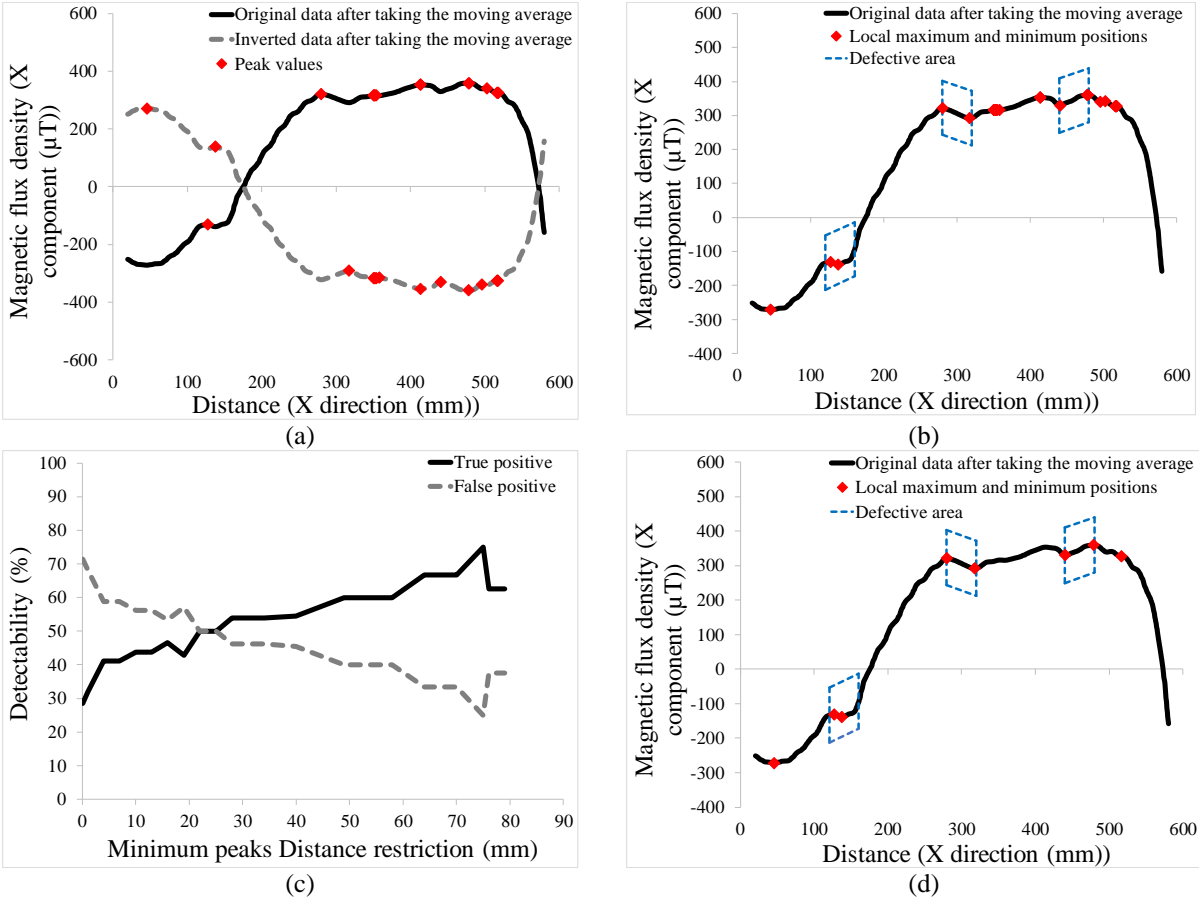
Figure 3.12. The whole peak analysis process for rebar #1: (a) Peaks on the original and the inverted data, (b) Local extrema on the original data, (c) Finding the optimum value for minimum peak distance restriction based on the true and false detectability percentages, (d) Local extrema points for the selected minimum peak distance restriction.
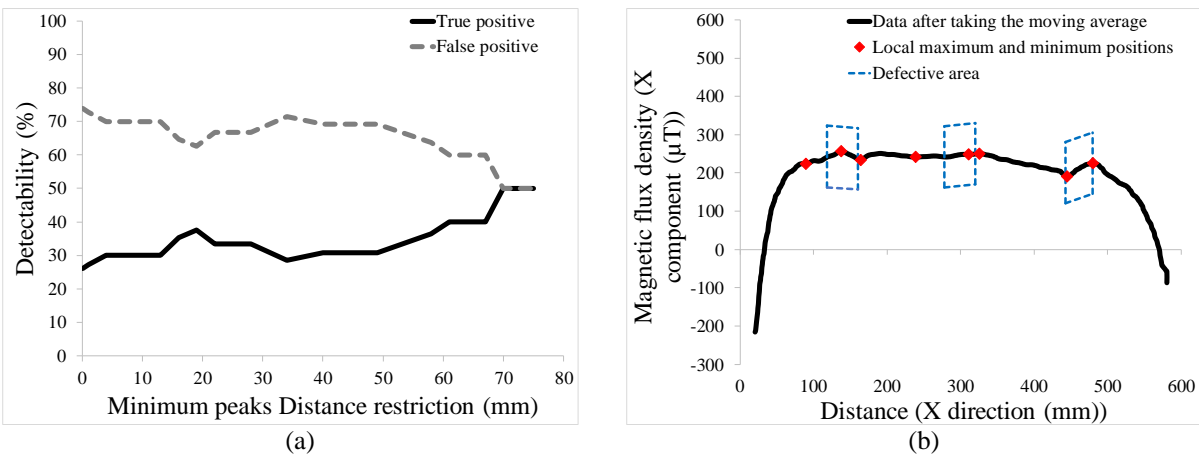
Figure 3.13. The last two peak-analysis steps for rebar #2: (a) Finding the optimum value for minimum peak distance restriction based on the true and false detectability percentages, (b) Local extrema points for the selected minimum peak distance restriction.
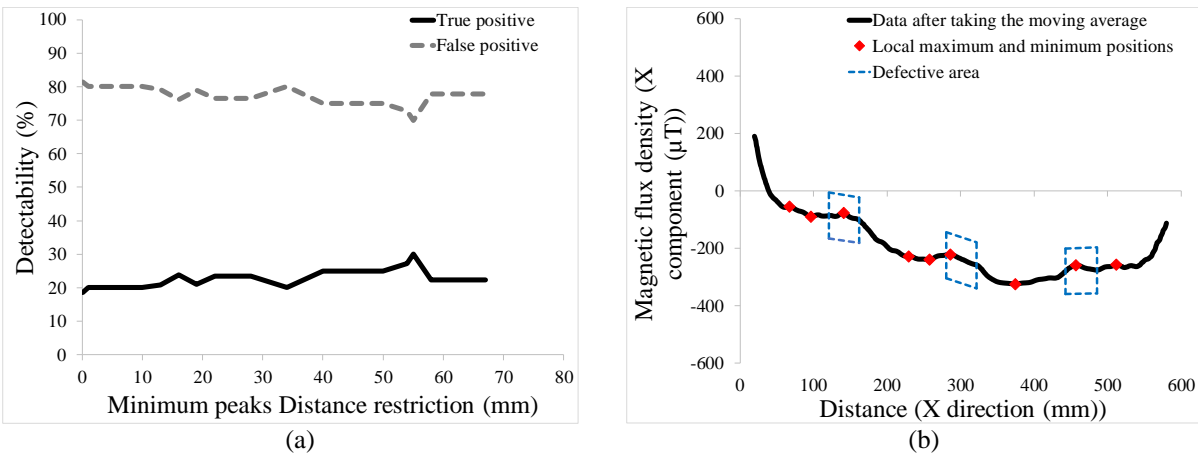
Figure 3.14. The last two peak-analysis steps for rebar #2: (a) Finding the optimum value for minimum peak distance restriction based on the true and false detectability percentages, (b) Local extrema points for the selected minimum peak distance restriction.

According to the results obtained for the three rebars using the peak analysis procedure, there is always an extremum point within the distance range of the defects. These extrema points are mostly marked at one end or both ends of the longitudinal defects. However, other extrema points also occur for non-defective sections and can be reduced by selecting an appropriate minimum peak distance restriction. Figures 3.12a, 3.13a and 3.14a show that a reasonable minimum peak distance in this case (longitudinal defects by the specifications shown in Figure 3.4 and Table 3-1) can be calculated by taking the average among 70 mm, 75 mm, and 55 mm, which is equal to 66.6 mm.

3.3.2.3. Approach #3: marking the minimum values after removing the dominant-low frequency

This approach was carried out for the selected scan (based on T-hypothesis testing) over only the rebar #1. At first, to remove the sharp changes due to edge effects, 20 mm of data at either end of the scan was ignored, and moving average data smoothing technique was carried out on the remained data. Subsequently, for quantifying the overall pattern of the magnetic data, single-sided magnitude spectrum and the power spectrum density (PSD) graphs were generated. Regarding the PSD graph, the dominant -low frequency affecting the data was deleted, and a new set of data was produced. A simple filter was then used for finding those values less or greater than a defined threshold. The data processing steps were as follows:

1. Instead of using every magnetic value, a mean value was determined, by using an equal number of data on either side of a central value (with a period of about 1.5 mm);

2. Magnitude spectrum and PSD graphs of the data were generated;

3. The dominate-low frequency was deleted;

4. A new set of data was generated, and some regions were marked based on a pre-defined threshold (obtained with approach #1).

Figure 3.15 shows the initial magnitude spectrum and PSD graphs for the data obtained by scanning rebar #1. The single-sided magnitude spectrum (Figure 3.15a) was provided using MATLAB 2018 b, after eliminating the offset by subtracting the mean. For obtaining accurate magnitude values, the magnitude spectrum was generated through appending 99000 zero to distance domain magnetic data and using a Hanning window function. A PSD graph of the same data was also prepared (Figure 3.15b). The PSD and the magnitude spectrum have similar behaviour, both showing a considerable peak at the frequency of 0.001 mm^{-1}, which is the dominant-low frequency. To remove the overall pattern, the data's lower frequencies, with a power of greater than 2.15E+05 $\frac{\mu T^2}{m^{-1}}$ were selected and then deleted. Next, a new PSD graph (Figure 3.16a) and a set of data (Figure 3.16b) were generated.
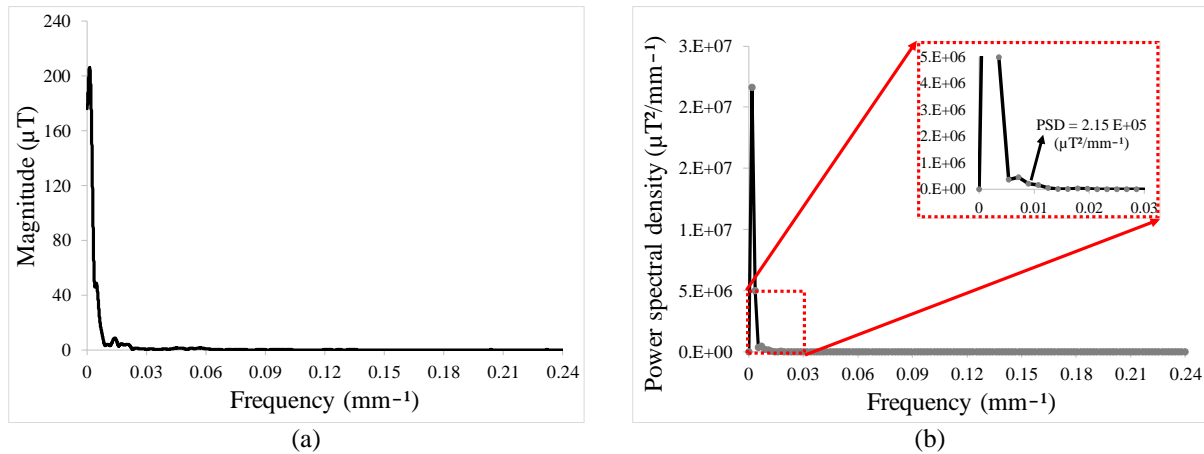
Figure 3.15. The power and magnitudes of the frequencies affecting the data: (a) Single-sided magnitude spectrum, (b) Power spectrum density.
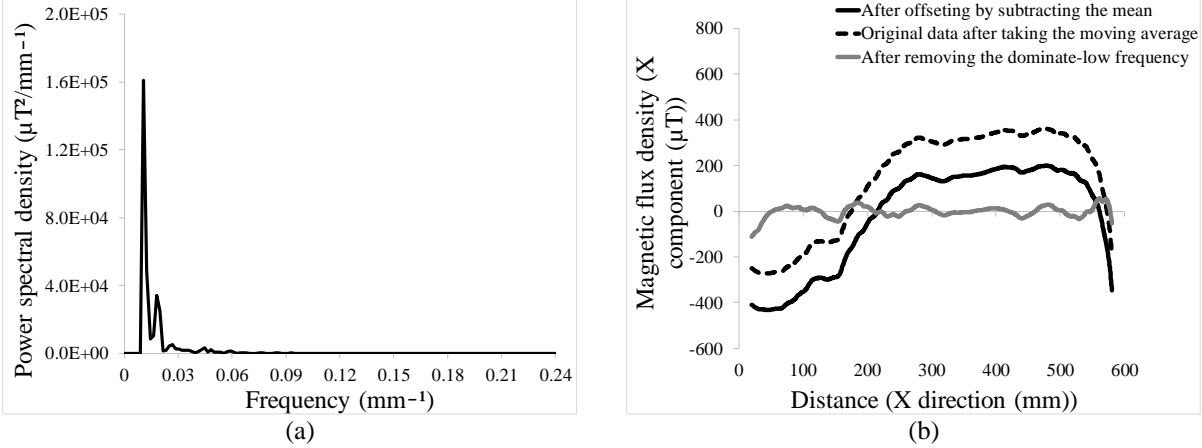
Figure 3.16. Data specifications after removing the dominant-low frequency: (a) Power spectrum density after removing the dominate-low frequency, (b) All changes of data, from the original state to post removal of dominant-low frequency.

The data shown in Figure 3.16b (after the dominate-low frequency is removed) is expected to be similar to the data after detrending (Figure 3.7a3). It was demonstrated that the data after detrending can be appropriately presented by the Normal distribution (Figure 3.11a). An acceptable normality behaviour can also be observed in the data obtained by removing the dominant-low frequency, based on the created Normal Probability Plot (Figure 3.17a). Because of their normality behaviour, these two sets of data (after removing the dominate-low frequency and after detrending) can be compared using Z-score normalization technique (Eq. 3-4). Z-score normalization was used to rescale the two sets of data to give both respectively a mean and a standard deviation value of around 0 μT and 1 μT (Figure 3.17b).

$$Normalized\ (magnetic\ value_i) = \frac{magnetic\ value_i - mean(data\ set_j)}{Std\ (data\ set_j)} \tag{3-4}$$

i: number of data
j: number of data set

48
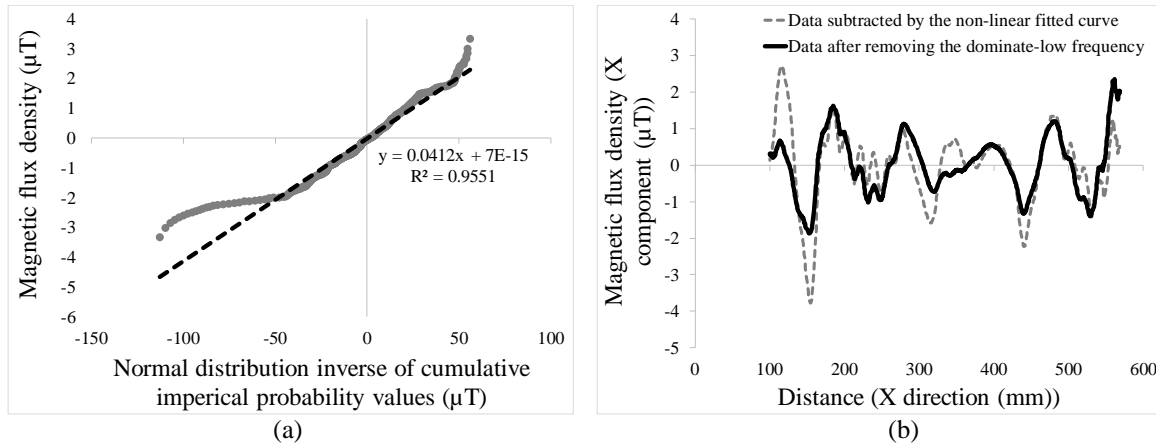
Figure 3.17. Normalizing the data by Z-score technique, considering their normality: (a) Normal Probability Plot for the data after removing the dominant-low frequency, (b) Both sets of data (after removing the non-linear trend and after removing the dominant-low frequency) after normalization by the Z-score technique.

A regression model investigated the compatibility of the normalized form of both data sets from 100 mm to the end of the rebar (Figure 3.17b) (Eq. 3-5), resulting in a coefficient of determination $R^2 = 50.94\%$. Although the obtained R-squared coefficient is not high enough to demonstrate that two data sets follow accurately the same values, it does indicate compatibility between the two sets of data. Hence, the threshold obtained in the statistical analysis conducted for approach #1 is used to detect the defect-location data after removing the dominant-low frequency. According to the statistical studies in approach #1, the values below the 8.88th percentile can represent the defects. The 8.88th percentile of the normalized data after removing the dominant-low frequency (the red boundary in Figure 3.18a) is presented by the Z value of -1.07 μT (the lower limit in Figure 3.18b).

Using the lower boundary can guide the detection of two of the total three defects of the rebar. Although the data can be represented by the Normal probability distribution with a coefficient of determination of $R^2 = 95\%$ (Figure 3.17a), it is not completely symmetric. Hence, adding an upper limit may help better evaluate the data. An upper limit taken from the top 8.88% of values was considered (the green boundary in Figure 3.18a). This upper boundary probability is the same probability used for defining the lower limit, but from the other tail of the distribution. Next, the areas falling outside of the upper and lower limits represent the defective locations. This approach results in detecting all three defects of the rebar, but along with Type I and Type Π errors. These errors in the data may cause some challenges in making appropriate decisions based on the data-processing results.

$$R^2 = 1 - \frac{\text{Error Sum of Squares}}{\text{Total Sum of Squares}} \rightarrow R^2 = 1 - \frac{530.3461\ \mu T^2}{1081.055\ \mu T^2} \rightarrow R^2 = 50.94\% \qquad (3\text{-}5)$$
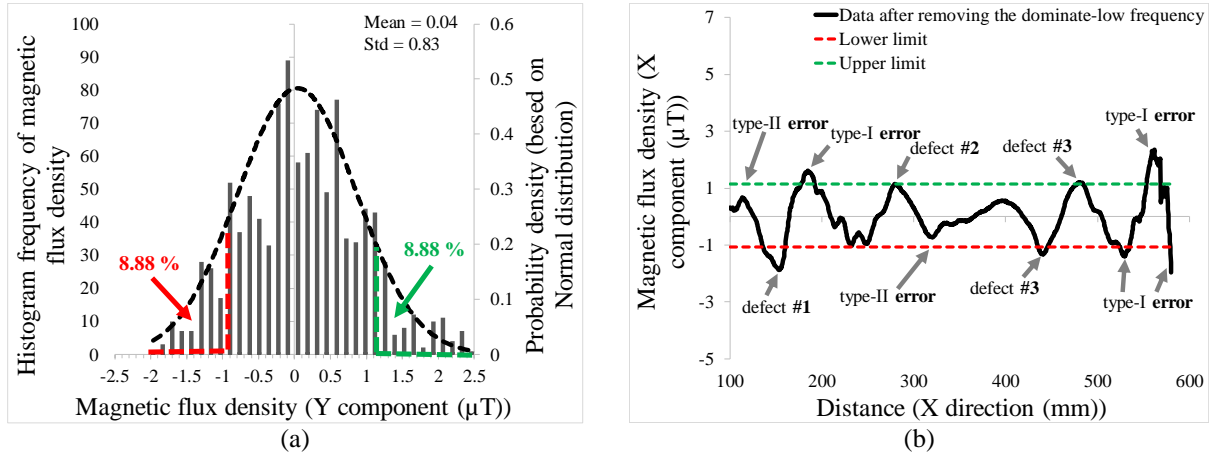
Figure 3.18. Detecting defects based on upper and lower limits: (a) Upper and lower limits defined on the fitted Normal probability distribution function, (b) Locations of defects and errors based on pre-defined upper and lower limits (Considering the null hypothesis, H_o : the rebar is non-defective).

3.3.2.4. Approach #4: using the derivative patterns of the data

According to the results of approaches #1 to #3, the magnetic data (recorded on the path shown in Figure 3.19), after removing its linear and non-linear trends, is expected to have regular peaks and troughs due to the corrugated surface of the rebars. Additionally, there should be obviously more intense non-repeating peaks and troughs, which occur due to defects on the path (cyclic pattern). This intense up-and-down pattern can show up in two ways: first, the magnetic data's values slightly increase for a short distance, followed by a sharp decrease for a longer distance, and again a slight increase for a short distance (defect I in Figure 2.15a); second, the magnetic data's values slightly decrease for a short distance, followed by a sharp increase for a longer distance, and again a slight decrease for a short distance (defect Π in Figure 2.15a). The derivative of the magnetic data can then result in two extrema of shorter duration in one half (the lower or upper half) of the graph (A1 and A2 in Figure 3.19b) and one extremum of a longer duration in the other half (B in Figure 3.19b). The difference between the magnetic values of A1 and B, A2 and B, and the space between A1 and A2 where B occurs are considered for quantifying the magnetic data behaviour at the defective area.

50
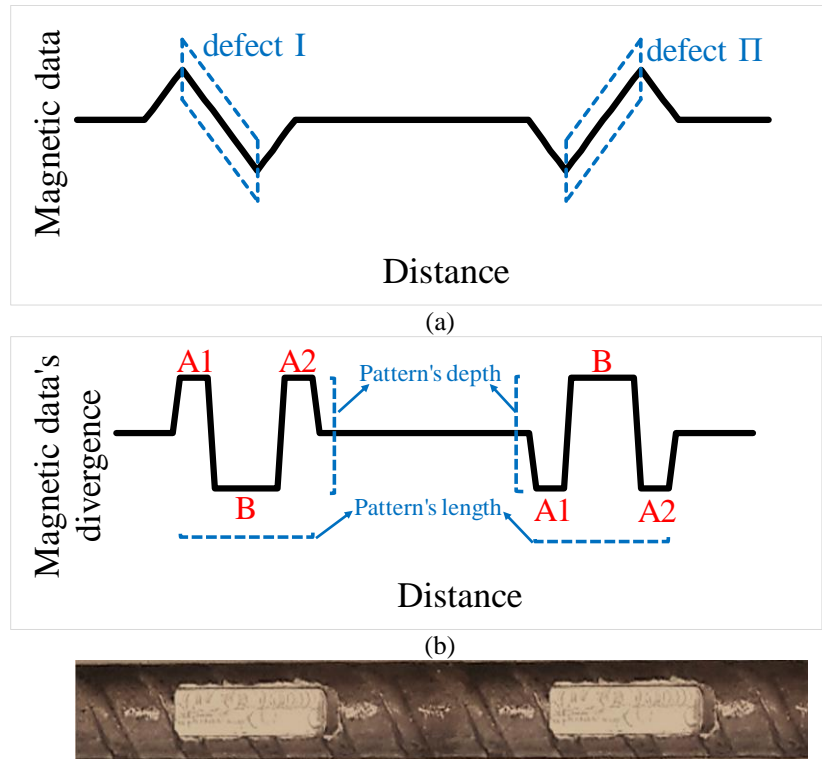
Figure 3.19. Ideal pattern of the magnetic data without considering the seasonal trend due to rebars' bumps: (a) Magnetic data's behaviour at the defective area, (b) Behaviour of magnetic data's derivative at the defective area.

This approach was carried out for the selected scans (using the T test) over each of the three rebars. To remove the edge effects affecting the data's slope, the first and last 50 mm of the scans were deleted. The data obtained from each rebar were split up into three sections. The derivative values were computed by MATLAB 2018 b for every section separately. After removing the linear trend from the graph, a moving average smoothing technique was applied and the defect areas were detected based on the expected patterns shown in Figure 3.19b, and the places representing A1, A2, and B were marked. The steps for data processing using approach #4 were as follows:

1. The first and last 50 mm of the selected scans were deleted;
2. The remained data were split into three parts;
3. The derivative of every part was computed using MATLAB 2018 b;
4. The secular linear trend was removed (separately for every section) from the values of the magnetic data's derivatives by subtracting the best fitted straight-line from the magnetic data;
5. A mean value was used instead of the individual values (in the graphs of magnetic data's derivatives). The mean values were taken from an equal number of data on either side of a central value (with a period of about 3 mm);

51

6. The expected patterns shown in Figure 3.19b were identified as the defective areas, and the points representing A1, A2, and B were marked.

Figure 3.20 shows the magnetic data's derivative values for all sections of the three rebars, with clear cyclic variation because of the rebar's corrugation. However, there is an unpredictable behaviour (non-cyclical or distorted cyclical behaviour) at the defective areas. When the X distance reaches the defective areas the derivative values noticeably increase (or decrease). The data derivatives continue at relatively constant values until they pass the defective area. The defective area can be detected through distinguishing the expected patterns (shown in Figure 3.19b) for all sections of the three rebars (except for section #1 of rebar #3), so the A1, A2, and B features can be identified on all the graphs. The magnetic data's derivative values representing the B feature can be easily labeled, since they have the highest or the lowest values in the graph (except for section #2 of rebar #3). Although section #1 of rebar #3 is not following the exact pattern shown in Figure 3.19b, it does clearly indicate the defective area by its minimum value. This minimum value was considered to represent the B feature, and the A1 and A2 features were identified considering the neighbouring local maximums and the defective area.

To quantify the outcomes, the distances between A1 and A2 (the pattern lengths) were extracted from all the graphs shown in Figure 3.20 (Table 3-3). The distance values were represented using a box-and-whisker plot, which showed no outliers (Figure 3.21a), enabling all the distances values to be used in further studies. Next, the maximum and minimum values between the third and the fourth columns of Table 3-2 were extracted, respectively representing the maximum and minimum depths of the patterns. The box-and-whisker plots were applied to the extracted data (Figures 3.21b & 3.21c), and the outliers were ignored in subsequent studies. The uncertainty values of the patterns' parameters were calculated considering a 98% confidence level (Eq. 3-2). Based on the calculated uncertainty levels, the values for the pattern lengths, maximum pattern depths, and minimum pattern depths are respectively expressed by 47 ± 8 mm, 4 ± 1 µT/mm, and 3.1 ± 0.7 µT/mm.
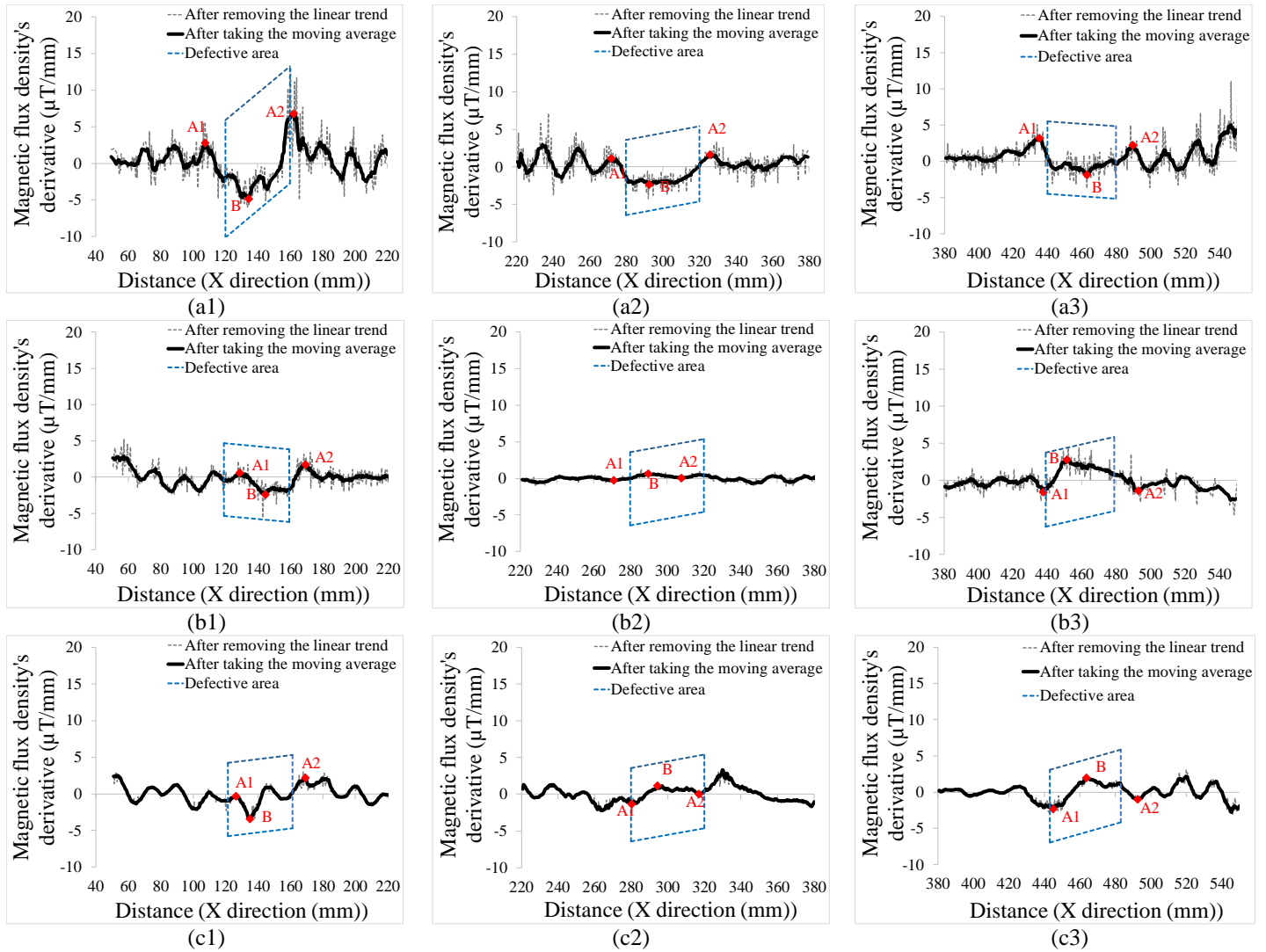
Figure 3.20. Signal processing of the magnetic data using the derivative values: (a1) Section #1 of rebar #1, (a2) Section #2 of rebar #1, (a3) Section #3 of rebar #1, (b1) Section #1 of rebar #2, (b2) Section #2 of rebar #2, (b3) Section #3 of rebar #2, (c1) Section #1 of rebar #3, (c2) Section #2 of rebar #3, (c3) Section #3 of rebar #3.

Table 3-3. Specifications of patterns resulting from magnetic data derivatives representing defective areas.

	Diff between A1 and A2 (mm)	Diff between A1 and B (µT/mm)	Diff between A2 and B(µT/mm)
Section #1 of rebar #1	54.48	7.67	11.63
Section #2 of rebar #1	53.85	3.46	3.95
Section #3 of rebar #1	54.49	5.04	4.1
Section #1 of rebar #2	40.46	3.03	4.16
Section #2 of rebar #2	36.96	0.93	0.6
Section #3 of rebar #2	55.13	4.39	4.19
Section #1 of rebar #3	42.69	3.1	5.59
Section #2 of rebar #3	36.64	2.5	1.17
Section #3 of rebar #3	48.12	4.38	3.05
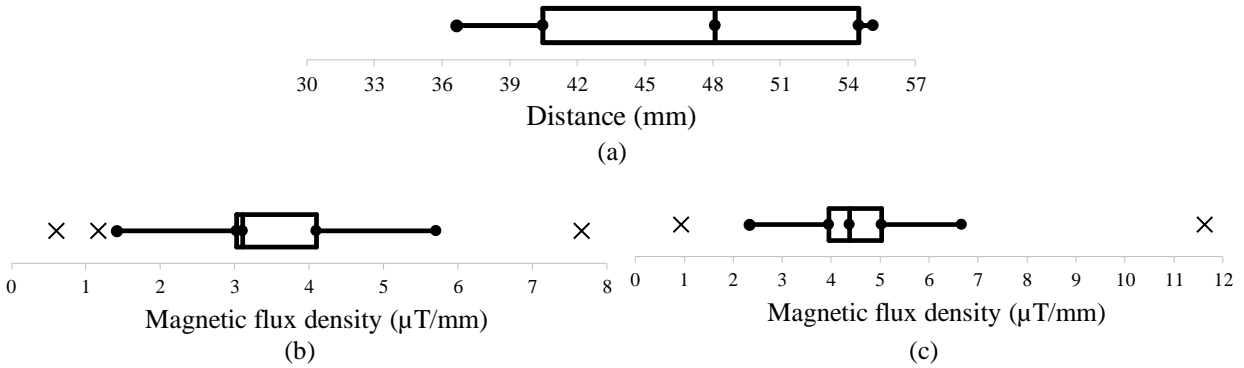
Figure 3.21. Box and whisker plot applied on the values of the pattern parameters: (a) Pattern lengths, (b) Minimum pattern depths, (c) Maximum pattern depths.

3.3.3. Magnetic behaviour at different elevations

Distance from rebar during data recording is an influential parameter that affects magnetic data trends. To investigate such effects and establish a realistic limit of detectability, rebar #1's magnetic flux density values at different elevations from its surface were recorded with the PMI device. It should be noted that the elevations mentioned in this study refer to the distance between rebar and the magnetic sensors implanted in the PMI device's scanner. As shown in Figure 3.22, The magnetic sensors are placed at a vertical distance of 1 cm above the scanner wheel bottom (the point normally in contact with the ground).
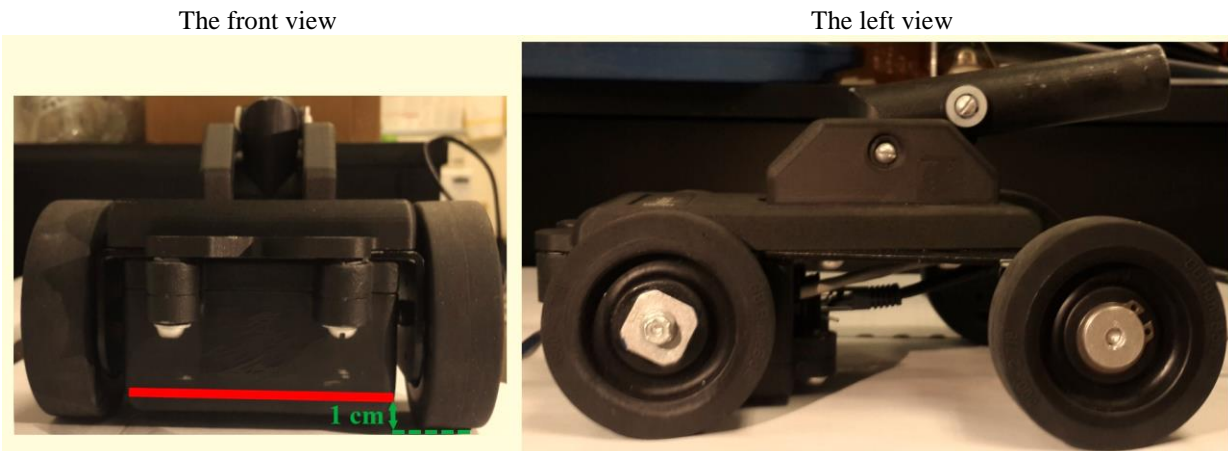
Figure 3.22. Front and left views of the PMI scanner; the red line shows the elevation at which the magnetic sensors are located.

The X component magnetic flux density values were recorded over the rebar's length at ten different elevations (1 cm to 10 cm) from its surface. The rebar was kept in the same position and direction for all the scans; with the defects topmost (Figure 3.23). The scanner's elevation from the surface of the rebar was the only variable parameter. Data recording was conducted five times

under the same conditions along the whole length of the rebar at every elevation. T-tests were done between every two scans, and the scans that were significantly equal to the greatest number of other scans (at a level of 0.002) were chosen for the rest of the investigation.
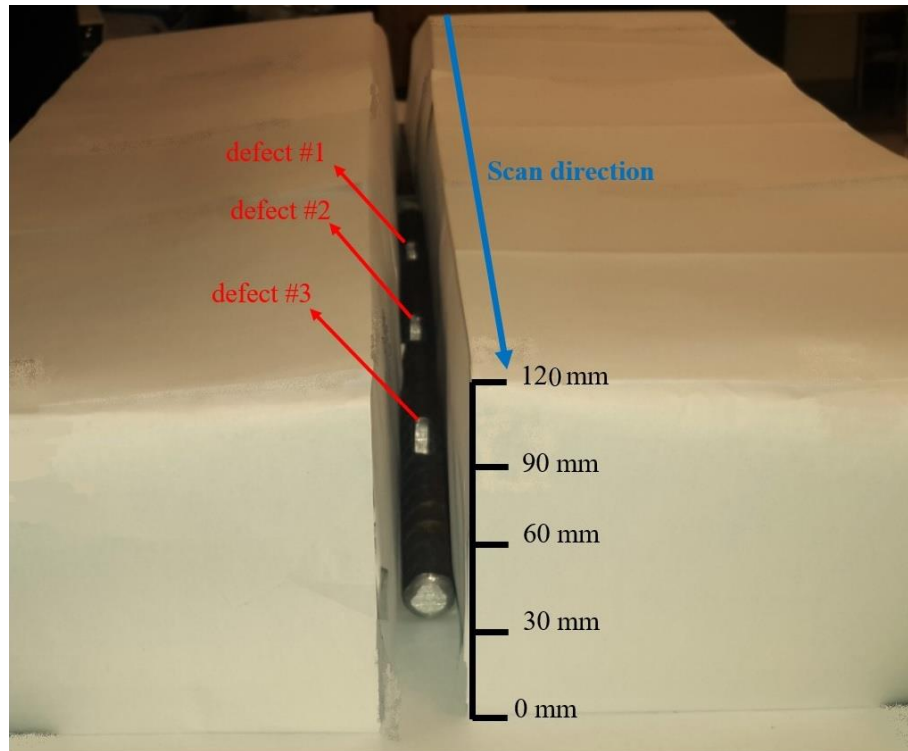
Figure 3.23. Highest elevation for data recording, 10 cm from the surface of the rebar (12 cm from the rebar's bottom).

Figure 3.24a shows the values of X component magnetic flux densities of rebar at different elevations from its surface. Increasing the elevation from the rebar makes the magnetic flux density trend smoother and straighter. The standard deviations of all data recorded at each elevation were calculated (Figure 3.24b). A non-linear reduction of the magnetic flux density variation is observed when the elevation from the surface of the rebar is increased. This finding demonstrates that increasing the vertical distance from the rebar causes the data fluctuations to stay closer to their mean values, thus indicating fewer details of the rebar properties.
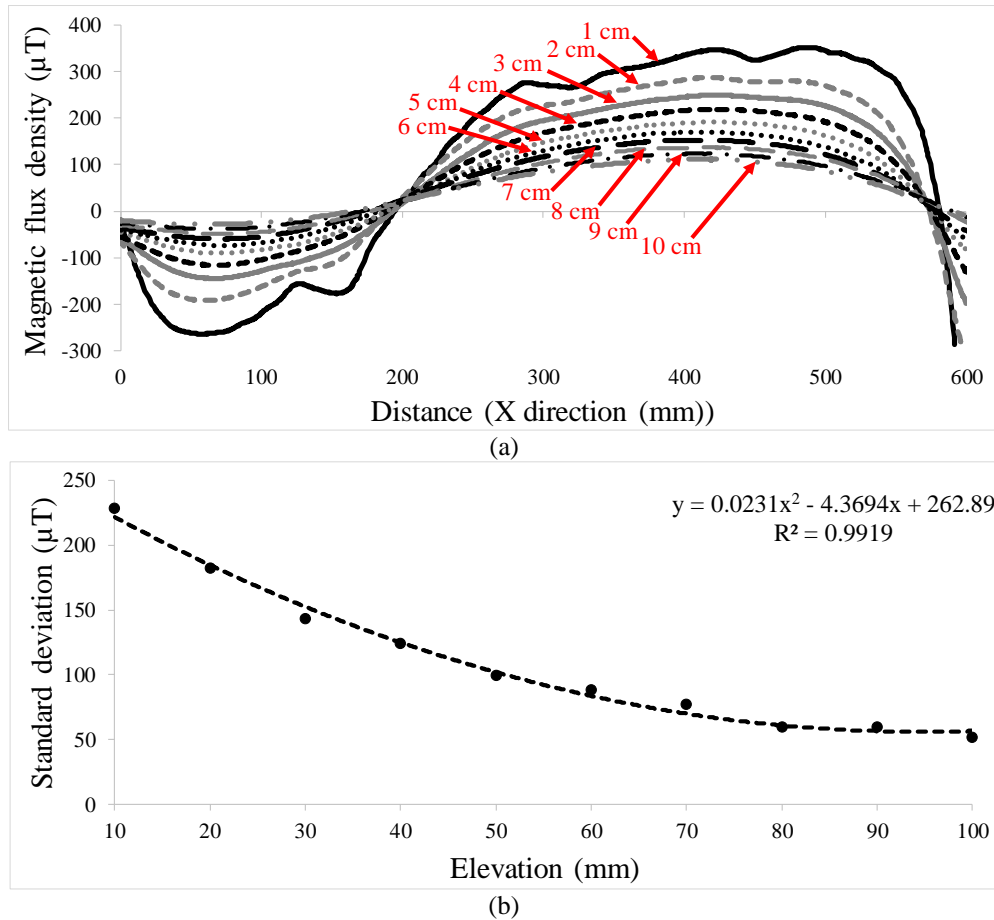
Figure 3.24. Effects of change in the data-recording elevations on the magnetic data: (a) Values of X component magnetic flux densities of rebar #1 at different vertical distances from the surface of the rebar, (b) The standard deviation values for the magnetic data recorded at different vertical distances (red numbers show elevation values).

According to Figure 3.24a, there is a strong overall harmonic trend for the magnetic data at 1 cm elevation. The intensity of this harmonic trend decreases when the elevation is increased. To quantify this behaviour, the single-sided magnitude spectrum of the magnetic data was provided using MATLAB 2018 b for different vertical distances. Figure 3.25a demonstrates that there is a peak at the same frequency ($0.001\ mm^{-1}$) for the magnetic data values of all the elevations, but the magnitude of the peaks decreases when the vertical distance is increased. Enhancing the vertical distance causes the reduction in peak magnitudes to follow a 2nd-order polynomial trend until the elevation of 4 cm, followed by a significant decline between the 4 cm and 5 cm elevations (Figure 3.25b). The reduction in peak magnitudes again shows that a non-linear trend occurs when there is a greater increase in the vertical distance from the rebar's surface (Figure 3.25b). This finding demonstrates an observable difference between the magnetic properties at a vertical distance from 1 cm to 4 cm, and the magnetic properties at a vertical distance greater than 4 cm.

56

(a)

y = 0.0315x² - 3.1302x + 221.3
R² = 0.9945

y = -0.0001x⁴ + 0.0323x³ - 3.636x² + 176.29x - 3009
R² = 0.9941

(b)
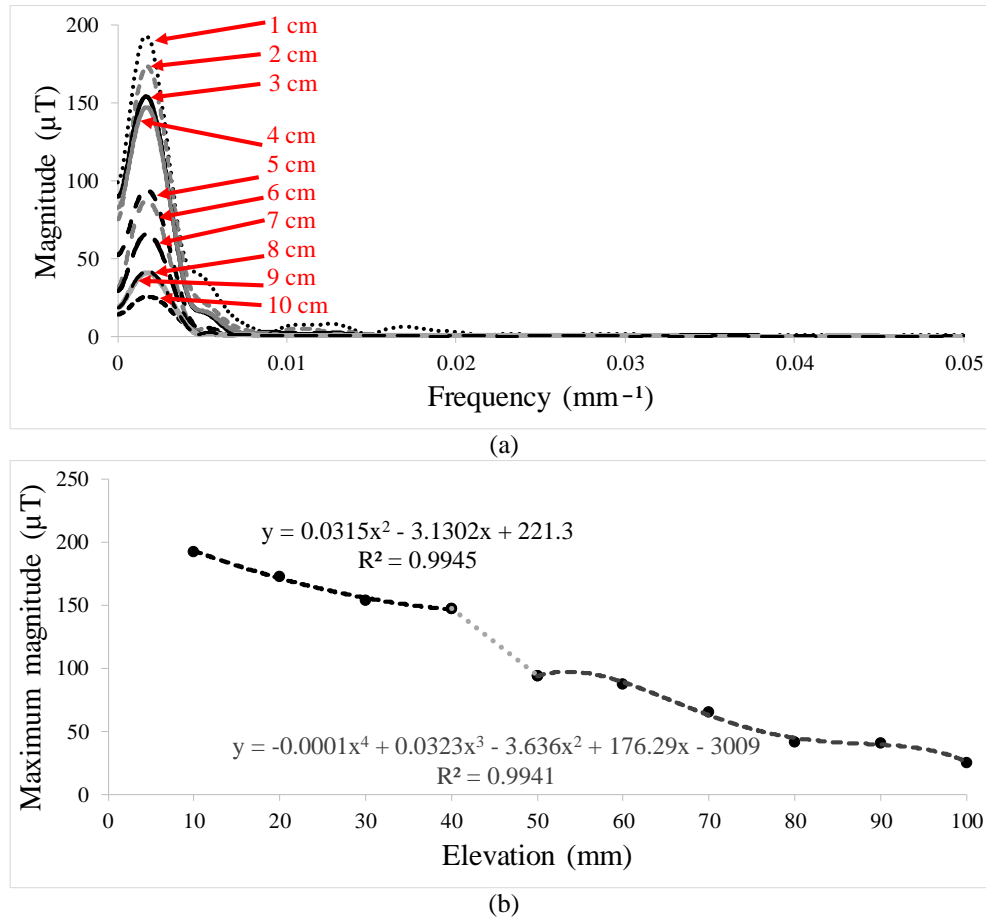
Figure 3.25. Investigation of magnitude spectrums of the magnetic data at different vertical distances: (a) Single-sided magnitude spectrum of the magnetic flux density values (red numbers show elevation values), (b) Behaviour of the maximum magnitude values found at different vertical distances.

To investigate the realistic limit of detectability, the study focused only on the smaller sections of the rebars containing defects. The data related to defects #1 and #2 were considered from 40 mm from either end of the defects, and the data analysis were conducted using approach #4. The derivative values of the magnetic data at different vertical distances were separately computed by MATLAB 2018 b. Next, the linear secular trend was removed from the data, and smoothing was carried out using the moving average technique on every set of data at different vertical distances separately. Figure 3.26 shows that there is a dip, like a defect I pattern (Figure 3.19a), at the defective areas for both defects #1 and #2 at the data-recording vertical distances from 1 cm to 4 cm.

The dips' intensities (pattern depth) are at their highest state at the 1 cm vertical distance (Figures 3.26a1 & 3.26b1). Although the dips' intensities are at their lowest states at the vertical distance of 4 cm, they can still be used to detect the defective areas. However, by increasing the vertical

distance of data recording to more than 4 cm, the data show a random behaviour which can not help in detecting defects (Figure 3.26c1 & 3.26c2). This outcome confirms our understanding, based on the magnitude spectrum graph (Figure 3.25) that the magnetic properties at a vertical distance from 1 cm to 4 cm are noticeably different from those recorded at a vertical distance greater than 4 cm.
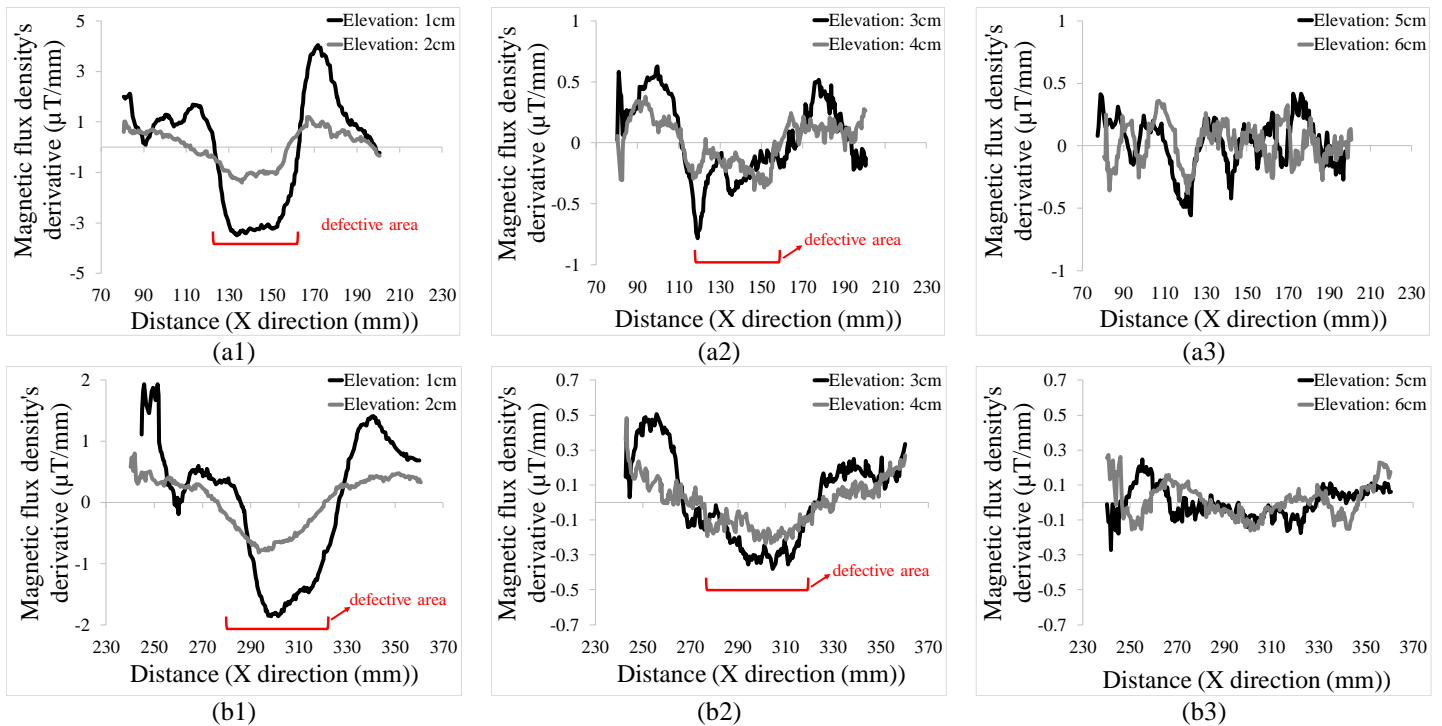
Figure 3.26. Signal processing using the derivative values for recorded data at different vertical distances for defects #1 and #2 of rebar #1: (a1) Defect #1 at vertical distances of 1 cm and 2 cm, (a2) Defect #1 at vertical distances of 3 cm and 4 cm, (a3) Defect #1 at vertical distances of 5 cm and 6 cm; (b1) Defect #2 at vertical distances of 1 cm and 2 cm, (b2) Defect #2 at vertical distances of 3 cm and 4 cm, (b3) Defect #2 at vertical distances of 5 cm and 6 cm.

For better interpretation of the results, the minimum values of the magnetic flux density's derivative (represented in Figure 3.26) were considered for different distances (Figures 3.27a and 3.27b). A logarithmical trend is observed for the minimum values of magnetic properties when the elevation is increased, similar to our outcomes from our previous investigation on a defective rebar's simulation (Mosharafi *et al.*, 2018). Additionally, there is a polynomial trend in magnetic properties until the 4 cm elevation, for both defects #1 and #2. However, the magnetic property values show a constant trend for the vertical distances of more than 4 cm, which again supports our findings on the detectability limitation. To study the consistency of the results obtained from defect #1 and defect #2. The gradients of the data points, represented in Figures 3.27a and 3.27b, from the elevation of 1 cm to 10 cm were calculated (Figure 3.27c). Next the two-sided paired T-

hypothesis test (Montgomery, 2014) was conducted for the two produced data sets for defect #1 and defect #2 in Figure 3.27c (Eq. 3-6). According to the hypothesis test, the mean values of the gradients for both defects are significantly equal with each other, even with a highly significant level such as 0.1. This fact can be considered as representative, demonstrating that magnetic signals show similar behaviours when we increase the data-recording vertical distance for both defects.
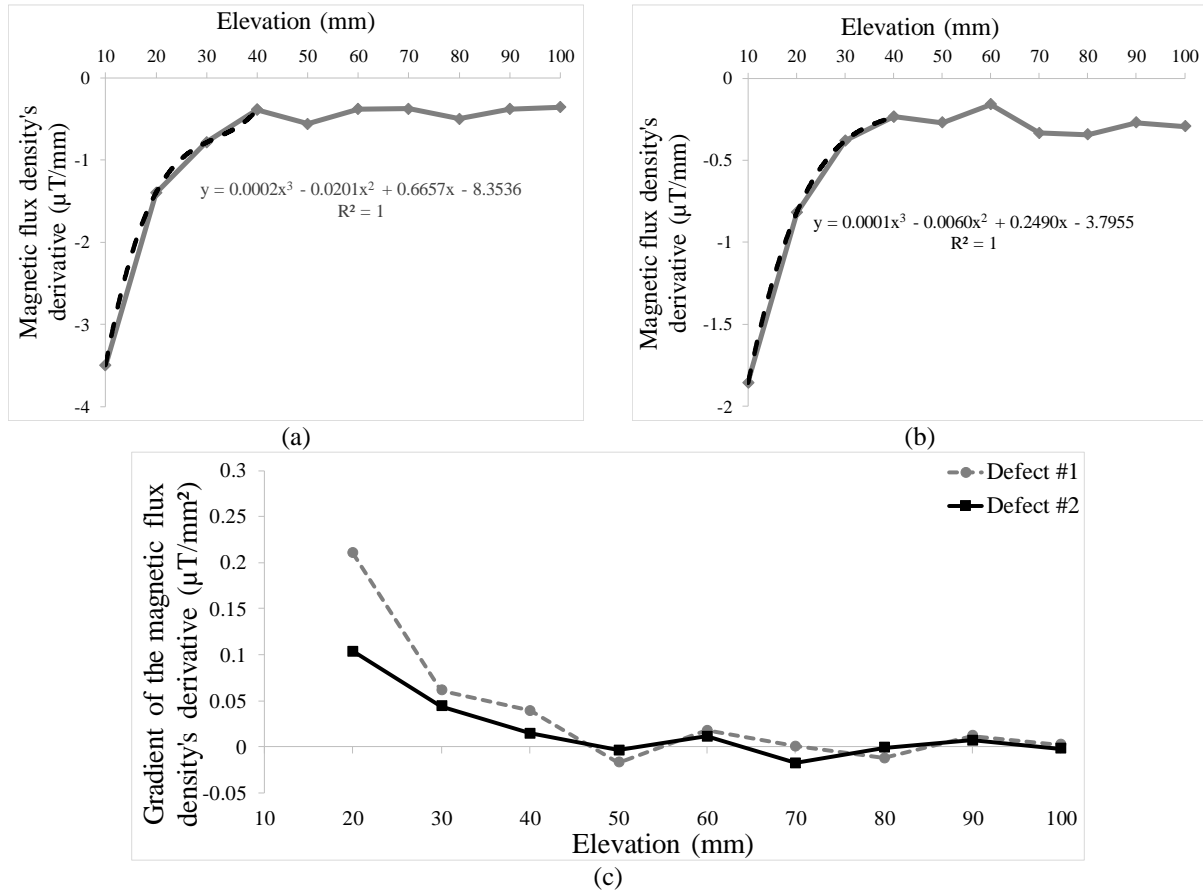
Figure 3.27. The behaviour of the minimum values of X component magnetic flux density's derivative at defective areas, recorded at different vertical distances: (a) Minimum magnetic flux density's derivative values at defect #1's location, (b) Minimum magnetic flux density's derivative values at defect #2's location, (c) Gradient of the minimum values of X component magnetic flux density's derivative.

$$H_0: \mu_D = 0 \tag{3-6}$$

$$H_0: \mu_D \neq 0$$

$$T_{paired} = \frac{\overline{D}}{S_D / \sqrt{n}} \rightarrow T_{paired} = \frac{-0.01754\ \mu T}{0.011904\ \mu T} \rightarrow T_{paired} = -1.354788$$

$$T_{critical} = T_{\frac{\alpha}{2},\ df} \rightarrow T_{critical} = T_{\frac{0.1}{2},\ 8} \rightarrow T_{critical} = 1.86$$

$$\left|T_{paired}\right| < \left|T_{critical}\right| \rightarrow \text{There is insufficient evidence to reject the null hypothesis}$$

$$\rightarrow \mu_D = 0$$

D: Differences between two paired samples

S_D: The sample standard deviation of the differences

n: The sample size

3.3.4. Numerical simulation procedure and results

Numerical simulation was conducted on a 260 mm section of the rebar plotted in Figure 3.4 that contained one longitudinal defect. The selected section of the solid rebar (Figure 3.28) was simulated via COMSOL® software version 5.3a (COMSOL Group, Stockholm, Sweden) with regard to the magnetic field of the Earth. The Earth's magnetic field varies somewhat in time and location. To obtain consistent and realistic results, the PMI scanner was positioned as it would be for the scanning, then left stationary for five minutes before the rebars were put in place. Different components of the local magnetic fields (consisting of the Earth's magnetic field and other external sources of magnetic fields) were recorded according to the inspection path and direction (Figure 3.29). The mean values of the recorded data were used in simulations to achieve more accurate magnetic property values. The mean values of the background's magnetic fields were calculated as 14.64 µT, 2.44 µT, and 54.94 µT for the components X, Y, and Z, respectively. However, the magnetic conditions of ferromagnetic materials are affected by the Earth's magnetic field from the time of their formation, so discrepancies are expected between the outcomes of the simulations and similar experimental outcomes.
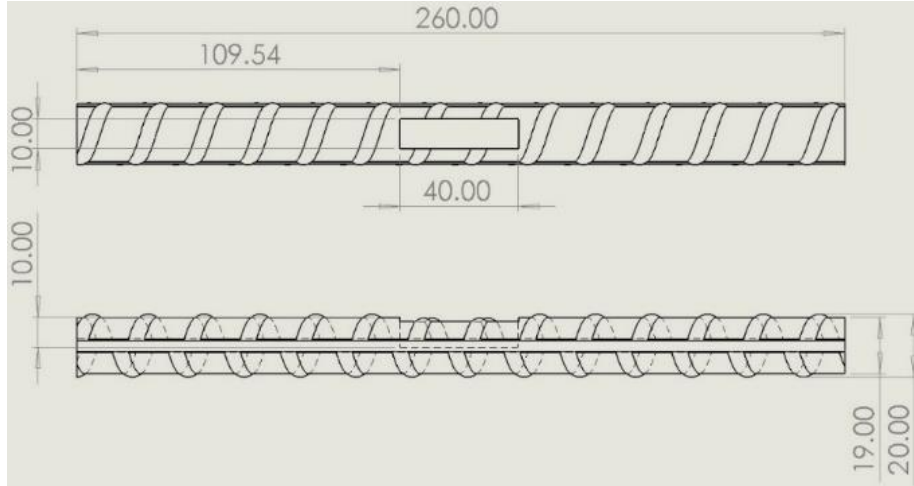
Figure 3.28. The section of the solid rebar used in the numerical simulation.
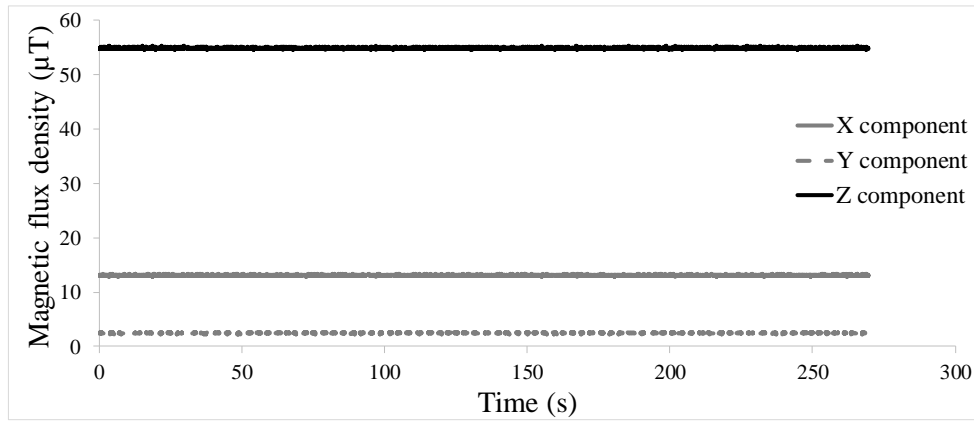
Figure 3.29. Components of local magnetic field recorded to use in numerical simulation.

So that the simulation considered the local magnetic field, the rebar was located in a 280 mm × 40 mm × 40 mm space that included the magnetic field calculated from Figure 3.29. Next, tetrahedral meshes, according to the specifications in Table 3-4, were applied on the rebar and box as a combined system. The simulations started with the initial mesh properties (mesh # 1). To make the outcomes independent of the meshing parameters, some more-accurate element specifications were then implemented in the simulation. The values of the X component magnetic flux density were recorded for the X direction of the rebar (i.e., the path parallel to the rebar's length). This path runs along the middle of the rebar, and 10 mm above its surface of the rebar (to be comparable with the results of approach #1). The path also extends from one side to the other of the solid rebar (Figure 3.30).

Table 3-4. Different mesh specifications used to verify the simulation results.

Rebar mesh #	Maximum element size (mm)	Minimum element size (mm)	Maximum element growth rate	Curvature factor	Resolution of narrow regions	Number of degrees of freedom (in total)
1	22.4	2.8	1.45	0.5	0.6	160623
2	15.4	1.12	1.4	0.4	0.7	384130
3	14.28	0.98	1.39	0.38	0.73	458898
4	13.16	0.84	1.38	0.36	0.76	554067
5	12.04	0.7	1.37	0.34	0.79	681600
6	10.92	0.56	1.36	0.32	0.82	895312
7	9.8	0.42	1.35	0.3	0.85	1299586
8	8.78	0.37	1.34	0.28	0.86	1541328
9	7.7	0.33	1.33	0.27	0.88	1814076
10	6.76	0.29	1.33	0.26	0.9	2122804
11	5.75	0.25	1.32	0.25	0.91	2718323
12	4.74	0.21	1.32	0.24	0.93	2872888
13	3.73	0.17	1.31	0.23	0.95	3251665
14	2.72	0.13	1.31	0.22	0.96	3719555
15	1.71	0.096	1.3	0.21	0.98	5495303
16	1.2	0.09	1.3	0.21	1	9012293
17	1.2	0.085	1.3	0.21	1	9016478
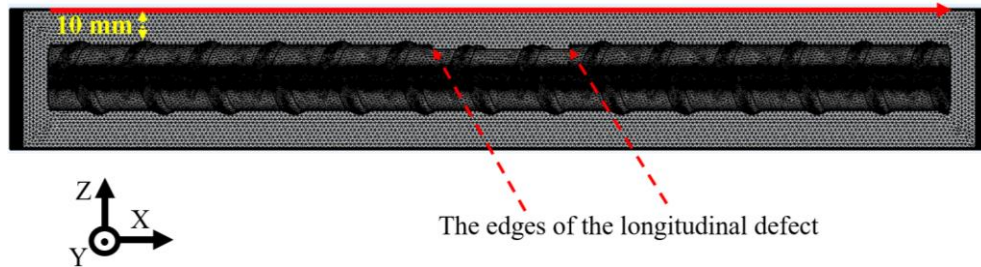
Figure 3.30. Path of data recording (a distance of 10 mm from the surface of the rebar).

To remove the edge effects, the first and last 20 mm of the scans were ignored. Subsequently, the difference between the magnetic values recorded at the two edges of the longitudinal defect (Figure 3.30) were extracted, for each meshing specifications in Table 2-4, as a representative value to verify the convergence of the simulation outcomes. Figure 3.31 shows that the extracted values became stable in mesh #13. However, to ensure the quality of the simulation, the outcomes from the most-accurate element specification (mesh #17) were chosen for the rest of the investigations. Figure 3.32 demonstrates that the magnetic flux density values for mesh #17 have no out-of-range or disorder trend, unlike those for mesh #1. Carrying out simulations with mesh #17 resulted in a graphical representation (Figure 3.33), showing the behaviour of the X component magnetic flux density at the location of the longitudinal defects. According to Figure 3.33, there is a sharp change in magnetic flux density values at the edges of the longitudinal defect. These abrupt changes show themselves in Figure 3.32 in the local maximum and minimum values at the distances of 108.94 mm and 149.62 mm, respectively.
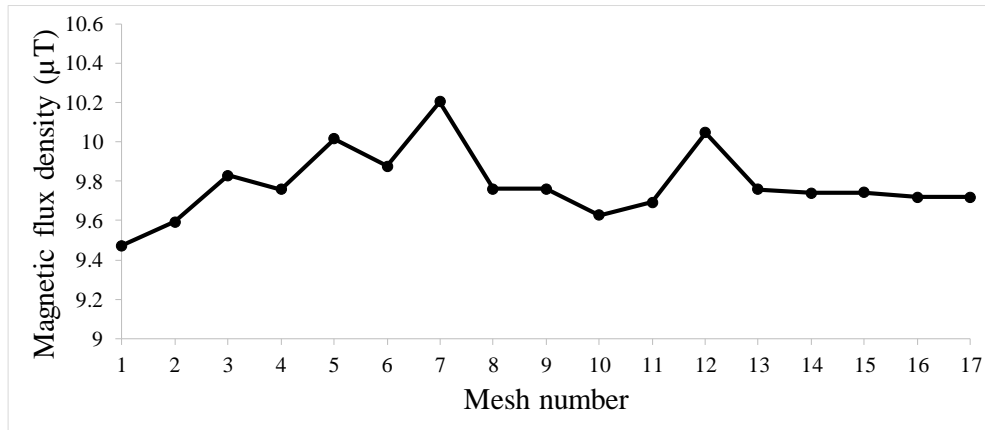
Figure 3.31. Difference between the magnetic values recorded at the two edges of the longitudinal defect, for different mesh specifications.
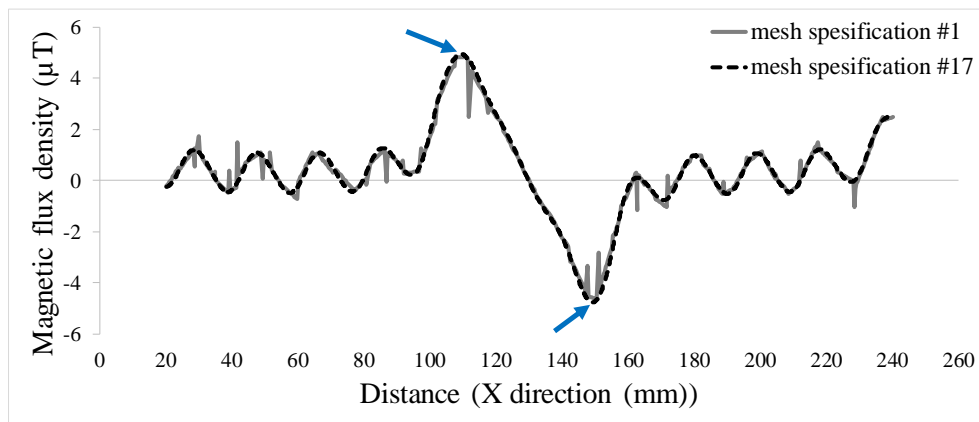
Figure 3.32. Comparing the values of X component magnetic flux density obtained with mesh #1 and those with mesh #17 (blue arrows indicate the magnetic values representing the edges of the longitudinal defect).
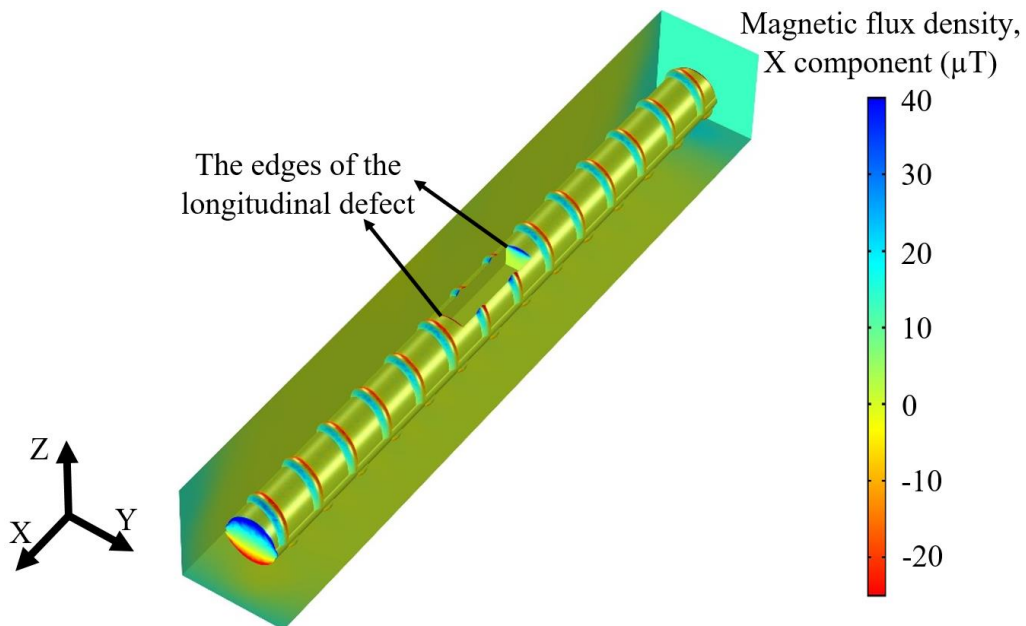
Figure 3.33. Behaviour of the X component magnetic flux density (mesh #17).

3.3.5. Comparison between simulation and experimental results

To better interpret the simulation results, the probability graph method was used for fitting magnetic flux density values (extracted from element specifications, mesh #17) to a probability distribution. This approach was carried out assuming that the magnetic flux densities of different locations on the rebar are independent of one another. The X component magnetic-flux-density data were plotted against various probability distributions (Normal, Log-normal, Weibull, and Gamma); a Normal distribution was chosen based on the method of least-squared error (Figure 3.34a). As observed in Figure 3.34b, a Normal function with a mean of 0.37 µT and a standard deviation of 1.75 µT was used to represent the magnetic data extracted from simulation. Subsequently, the threshold defined for detecting the defects (resulting from the experiments), was applied to the magnetic data resulting from the simulation (red part in Figure 3.34b).

(a)   (b)
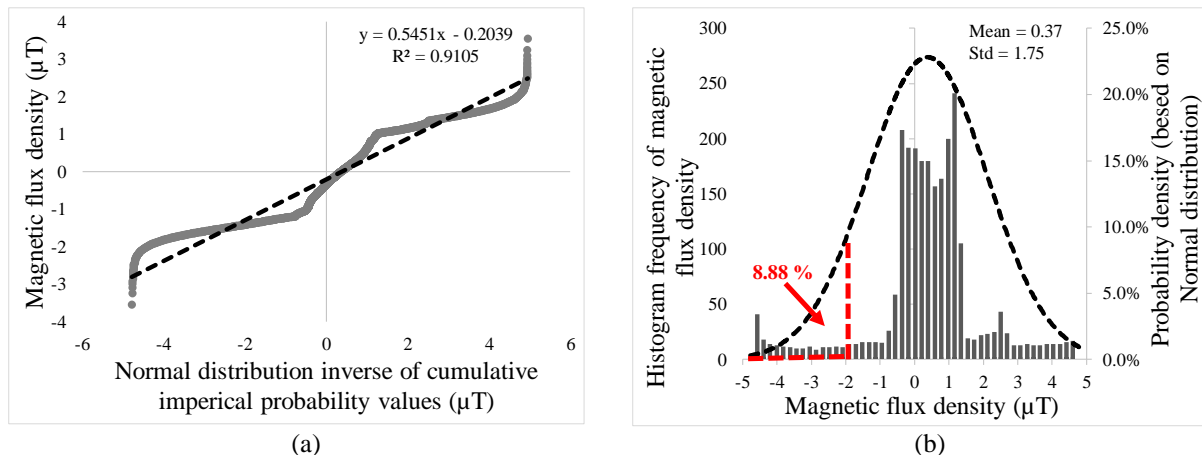
Figure 3.34. Data processing approach conducted on the simulation's data: (a) Normal probability plot for X component magnetic flux density, (b) Lower limit defined on the fitted Normal probability distribution function.

The marked local minimum value (solid red line) found by the applied threshold (the 8.88[th] percentile) in Figure 3.35a1 determines one of the edges of the longitudinal defect, demonstrating that the simulation results correlate well with the experimental outcomes reported in the approach #1 section. Both simulation results (Figure 3.35a1) and experimental outcomes (Figures 3.7a3, 3.8b, and 3.7c3) have a harmonic trend (up and down) because of the corrugated rebar surface. The threshold calculated based on the experimental results of scanning rebars #1, #2, and #3 (in approach #1) can be used for the simulation data to find the defect site. Additionally, like the experimental results of scanning rebars #1 and #2, Figure 3.35a1 shows a local minimum point close to one end of the defect (red solid line). This local minimum point followed by two local maximum points, and the maximum point with the higher value (green solid line) is close to the

other edge of the defect. The inflection point (the point of transiting from concave downwards to the concave upwards) represents a point close to the middle of the defect. The distance between the minimum and the maximum points (red and green solid lines) is equal to 40.68 mm, which is within the confidence interval calculated from the experimental results $(37 \pm 4 \, \mu T)$, and close to the mean value for the defects' lengths calculated by the values in Table 3-1 to be equal to 40.2 mm.

Regarding the outcomes of approaches #1 to #4, the magnetic data is expected to show harmonic behaviour because of the regular corrugated surface of the rebar. Additionally, path defects should lead to more intense non-predictable peaks and troughs that show themselves in two different behaviours (Figure 3.19). These different behaviours in magnetic value lead to distinct behaviours in their divergence values. To mimic such experimental outcomes, the values of the X component magnetic flux density were recorded for the X direction of the rebar along the path shown in Figure 3.30 (Figure 3.35a1) and over a similar path in the opposite direction (Figure 3.35b1). Next, the derivatives of the X magnetic data for both the values over the original direction of the path and the opposite one are respectively shown in Figures 3.35a2 & 3.35b2. The A1, A2, and B parameters then were labeled on the derivative graphs, as done for the experimental outcomes in Figure 3.20. The maximum and minimum values for the pattern's depth were calculated as, respectively, 0.95 µT and 0.85 µT, relatively different from the experimental outcomes. This discrepancy was expected because the inherent magnetic properties of the rebar could not be reflected in the simulation. However, the distance between the features of A1 and A2 in the simulation is equal to 54.95 mm, which is significantly equal to the experimental results (with significance level of 0.02) which was 47±8 mm.
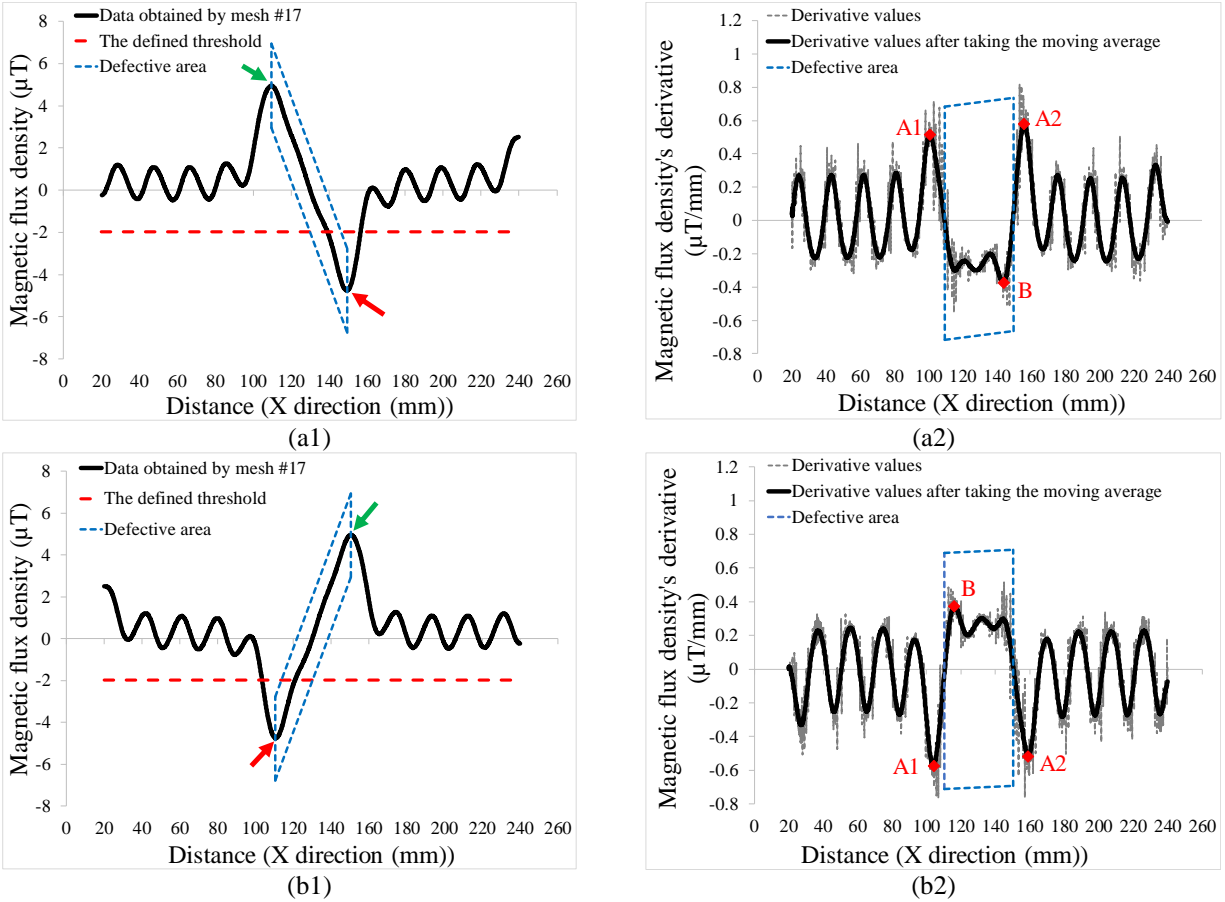
Figure 3.35. Magnetic data values and their derivatives obtained from simulation over the same path, but in two opposite directions: (a1) Magnetic data values recorded over the path shown in Figure 3.30, (a2) Derivative of the magnetic data values in a1, (b1) Magnetic data values recorded along the opposite direction of the path shown in Figure 3.30, (b2) Derivative of the magnetic data values in b1.

For a more detailed comparison between the experimental and simulation results, the experimental results of section #2 of rebar #1 (Figure 3.20a2) was selected, as a representative, to be normalized to the scale of the simulation outcomes with a similar pattern (Figure 3.35a2). The comparison focused on sections of both data sets (from the experiment and the simulation) comprised of the longitudinal defect plus 40 mm on either side of it. Subsequently, Normal probability plots were produced for the experimental magnetic data (Figure 3.36a) and the magnetic data obtained from the simulation (Figure 3.36b). The R-squared coefficient determination of the Normal probability plot for the simulation results was calculated as 90%, a value well below the desired level of normality.

Using the Z-score technique requires the normality behaviour of both data sets. Hence, in the absence of sufficiently normal behaviours for the simulation results, min-max normalization (Eq. 3-7) was used instead of the Z-score technique. Additionally, for ease of comparison, the values

for the distance vector were then started from zero for both data sets (Figure 3.37). A regression model investigated the compatibility of the normalized form of the experimental data and the original values of the simulation's data (Eq. 3-8), resulting in a coefficient of determination $R^2 = 66\%$. This R-squared value can again be considered as reasonable proof of compatibility between the simulation and the experimental outcomes, given the expected discrepancies.

(a)   (b)
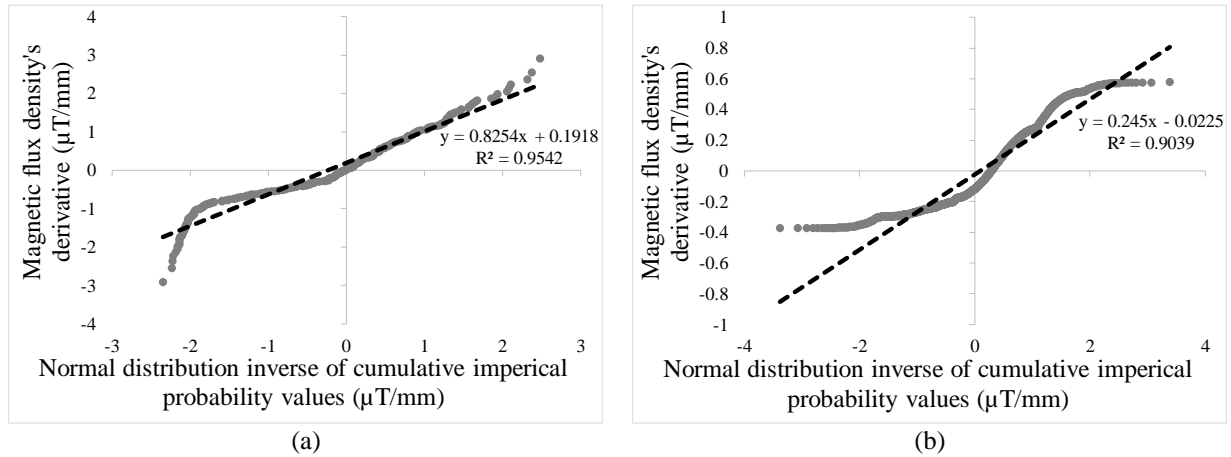
Figure 3.36. Normal probability plot for X component magnetic flux density: (a) Data obtained from the experimental results of section #2 of rebar #1 (Figure 3.20a2), (b) Data obtained from the simulation results (Figure 3.35a2).

$$V' = \frac{V - min_{old}}{max_{old} - min_{old}} (max_{new} - min_{new}) + min_{new}$$

(3-7)

V: old variable

max_{old}: maximum value of the old dataset

min_{old}: minimum value of the old dataset

V': transformed variable

max_{new}: maximum value of the normalized dataset

and min_{new}: minimum value of the normalized dataset
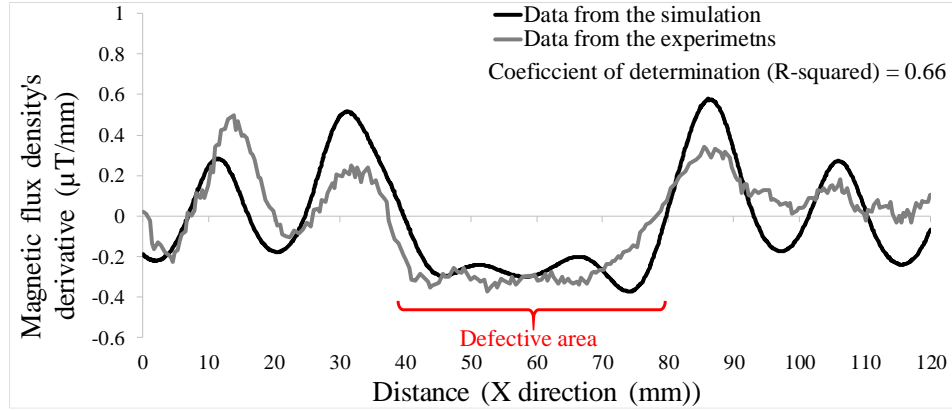
Figure 3.37. Normalized data from the experiment, using the min-max normalizing technique, in conjunction with the simulation results.

$$R^2 = 1 - \frac{\text{Error Sum of Squares}}{\text{Total Sum of Squares}} \rightarrow R^2 = 1 - \frac{6.08 \ \mu T^2}{17.91 \ \mu T^2} = 66\% \qquad (3\text{-}8)$$

3.4. Investigating the rebar with its defects at 9 clock position

3.4.1. Experimental measurements and results

To conduct the study in this section, rebar #1 was turned to one side so that its defects were on the left side of the rebar (Figure 3.38). Next, the magnetic flux density values were recorded over the length of the rebar at an elevation of 1 cm (i.e., the elevation is the distance between the implanted magnetic sensors and the rebar's surface). The PMI scanner contains three magnetic sensors at equal intervals of 25 mm. The rebar was scanned in a way whereby sensors #1, #2, and #3 were respectively recording data at the left side, center, and the right side of the rebar. The path, following the scan direction shown in Figure 3.38, was scanned 5 times. In the previous section (section 3.3) with the defects at 12 clock position, only the magnetic data recorded by sensor #2 (the sensor on the rebar axis) was used for conducting the studies. However, in the current section and the next one, the magnetic data recorded by all three sensors are used. Hence, herein, the T-test was implemented separately for the X component magnetic flux density values recorded by each of the magnetic sensors. Subsequently, the scans that were significantly equal to the greatest number of other scans (at a confidence level of 99.9%) were chosen for the rest of the investigation (Figure 3.39).
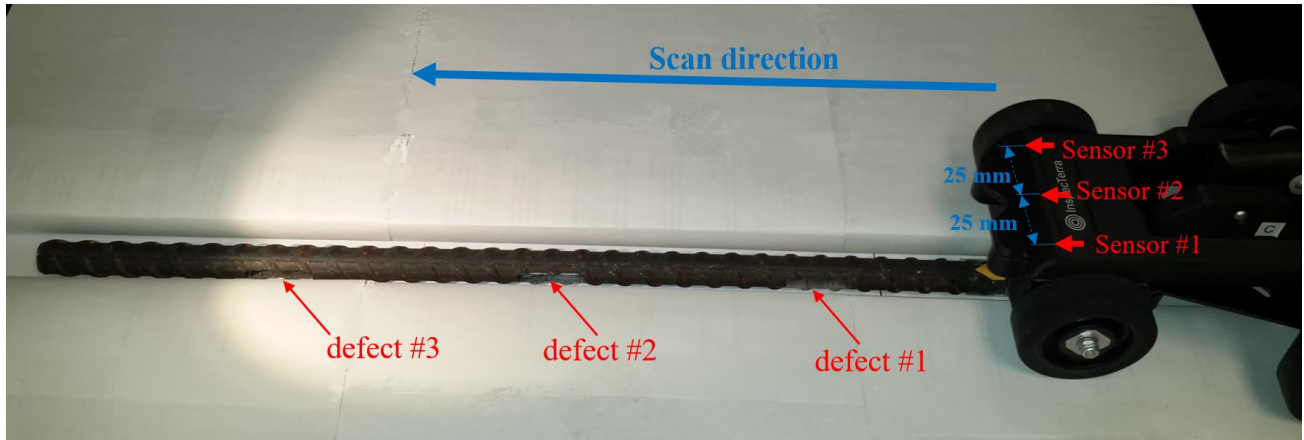
Figure 3.38. Scanning direction over rebar #1 turned so its defects are to the left side (clock position of 9).
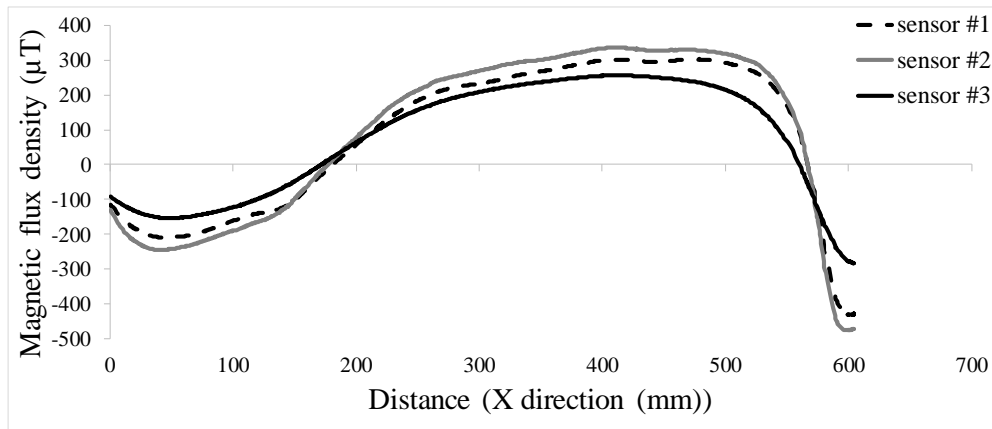
Figure 3.39. Selected X component magnetic flux density values recorded by the PMI scanner's magnetic sensors.

To study how defects on the side of the rebar effect magnetic signals, approach #4 was used. First, to remove the edge effect, the scan's first and last 50 mm were deleted. Subsequently, the data obtained from each sensor were split up into three sections, and the derivative values were separately computed using MATLAB 2018 b for each section. Next, moving average smoothing technique was applied to the data after removing their linear trend (Figure 3.40). Figures 3.40a and 3.40b respectively show that defects #1 and #2 can be detected using the minimum magnetic flux density's derivative values, and also by considering the dips, as in defect I's pattern (Figure 3.19), at the defective areas.

In both Figures 3.40a and 3.40b the pattern does not appear exactly at the defective area but shows up with an offset of about 20 mm. The pattern is clearer in sensor #1's data than in the data recorded by sensors #2 and #3. This finding demonstrates that the

69

data recorded by a sensor at one side of the rebar shows the defects at that side more accurately than that from the other sensors. The magnetic flux density derivative values help in finding the defective areas at the side of the rebar (Figures 3.40a & 3.40b), as it detects the defective areas at the top of the rebar (Figures 3.19a1 & 3.19a2). However, the minimum magnetic flux density values representing defect #1 and defect #2 were respectively changed from -4.87 µT to -1.44 µT and from -2.35 µT to -0.77 µT, by rotating the defective area from rebar's topmost (12 clock) to its left-hand (9 clock) position. This finding respectively shows 70.5% and 67.2% increases in the minimum magnetic flux density values for defect #1 and defect #2 when the defective area is changed from the 9 to the 12 clock position.

Despite the consistent behaviour of magnetic data for the defective areas at sections #1 & #2 (Figures 3.40a & 3.40b), the magnetic data in section #3 (Figures 3.40c) shows an inverse dip, like defect Π's pattern (Figure 3.19), at the defective areas; this pattern is not in accordance with the magnetic pattern at the defective areas resulting from scanning over the rebar when the defects were at 12 clock position (Figure 3.19a3). Additionally, unlike the outcomes resulting from sections #1 & #2 (Figures 3.40a & 3.40b), the magnetic flux density values and the behaviours in section #3 are almost similar for all sensors #1, #2, & #3 at the defective area. The discrepancy between section #3's outcomes and the results of section #1 & #2 might occur due to the slight angular deviation in the locations of the longitudinal defects, or it might happen because of residual stress remaining after the machining that created the defects.
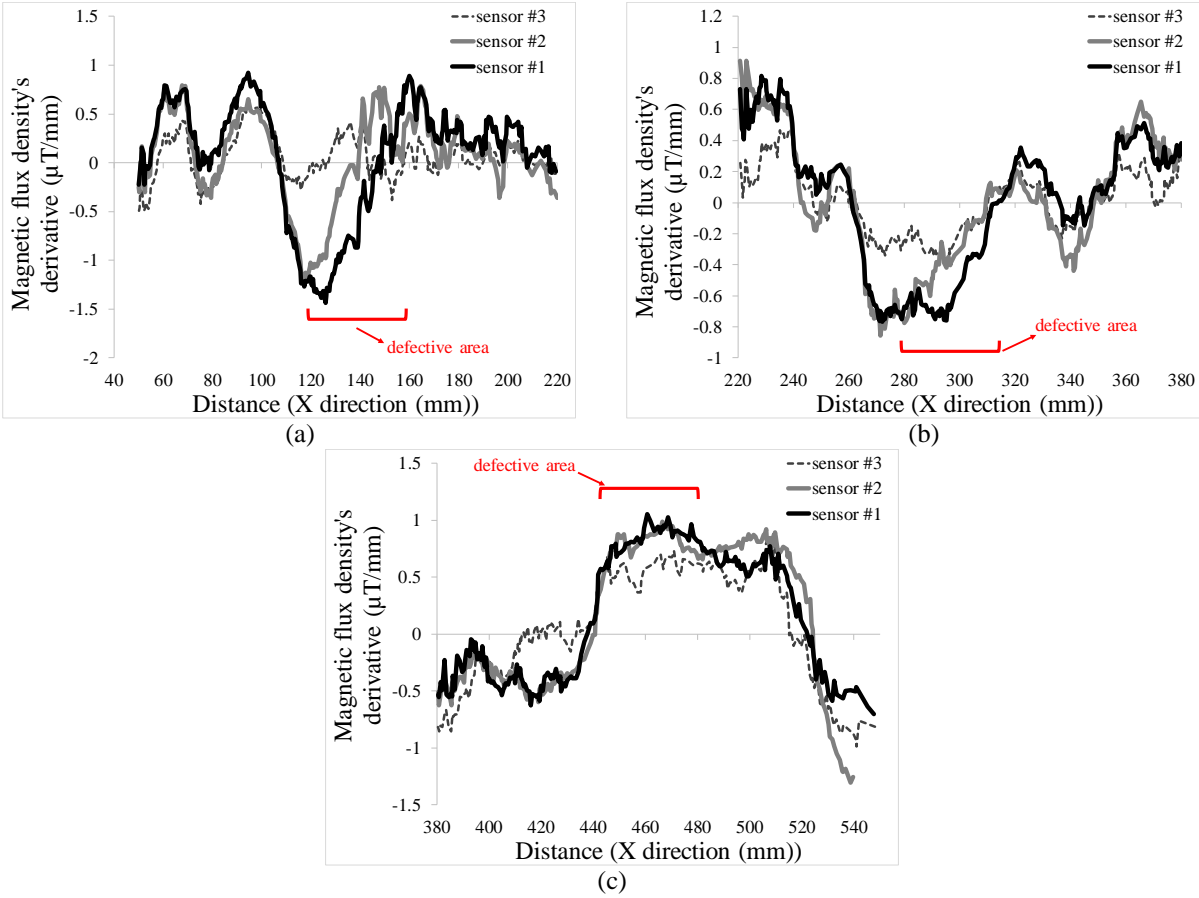
Figure 3.40. Derivative values of the magnetic data recorded over rebar #1, when the defects were along the rebar's left side: (a) Section #1, (b) Section #2, (c) Section #3.

3.4.2. Numerical simulation procedure and results

To investigate the magnetic flux density values over a rebar with a longitudinal defect on its left side, the previously used simulation process (Figure 3.33) was carried out. The solid rebar shown in Figure 3.33 was rotated 90 degrees in the X direction, and the dimensions of the cubic box included the local magnetic field, were changed to 280 mm × 50 mm × 40 mm. The cubic box's Y dimension was increased to enable simulation of the exact paths and directions scanned over the rebar when the magnetic data was recorded using the PMI scanner's magnetic sensors. The most accurate previously used element specification (Mesh #17 in Table 3-4) was implemented in the simulation, and resulted in a graphical representation that showed the behavior of the X-component magnetic flux density at the location of the longitudinal defect.

To show the behaviour of the magnetic flux density's X component at a vertical distance of 1 cm over the surface of the rebar, a planer slice was considered that represented a distinguishable magnetic behaviour over the longitudinal defect. The X component magnetic flux density values

71

were then recorded over paths A, B, & C (shown in Figure 3.41). The trajectories traveled by sensors #1, #2, & #3 (Figure 3.38) are respectively represented by paths A, B, & C. These paths are parallel to the rebar's length, with a vertical distance of 1 cm over the surface of the rebar (i.e., the same vertical distance that was applied in the experimental measurement (Figure 3.38)).
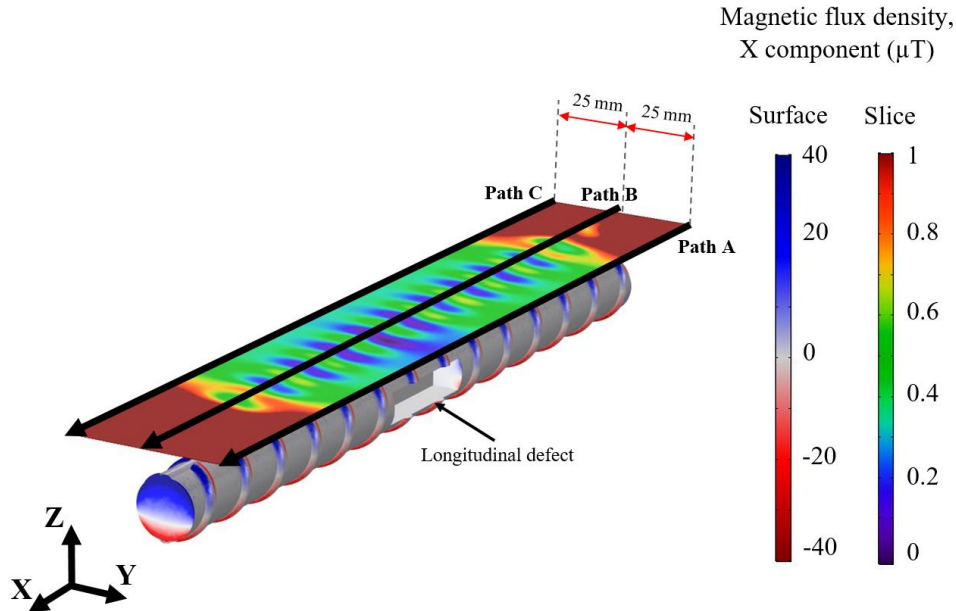
Figure 3.41. The behaviour of X component's magnetic flux density over a rebar with a longitudinal defect at its 9 clock position.

3.4.3. Comparison between simulation and experimental results

The magnetic properties resulted from the simulation (shown in Figure 3.41) at the defective area were investigated by focusing on a smaller section of the data recorded over paths A, B, and C. The data at the longitudinal defect plus 50 mm on either end were analyzed using the magnetic flux density's derivative values. Figure 3.42 shows these values after moving average smoothing. The ranges of the gradient values of the magnetic data recorded over paths A and C (Figure 3.42a) are about ten times smaller than those of data recorded over path B (Figure 3.42b). Path A (i.e., the path beside the longitudinal defect) shows the defective area by the minimum value in the graph. The defect can also be distinguished through the existence of a pattern that is similar to the defect Type I pattern (Figure 3.19), with an offset of about 10 mm. Additionally, the minimum magnetic flux density's derivative value representing the longitudinal defect changes from -0.37 $\frac{\mu T}{mm}$ to -0.015 $\frac{\mu T}{mm}$, when rebar is rotated to move its defect from topmost (12 clock position) to the 9 clock position. This change demonstrates a 95.9% increase in the magnetic flux density's

derivative minimum value. Hence, the magnetic properties recorded over path A are similar to those of experimental outcomes recorded by sensor #1. This similarity can be observed in such a way that in both experimental and simulation data sets, the place of defective areas is detected by the minimum value in the data and a pattern (with an offset) that is similar to the pattern of the Type I defect (Figure 3.19). Additionally, in both experimental and simulation results, the minimum value of the magnetic flux density's derivative increases when the defective area is repositioned from topmost to the side of the rebar.
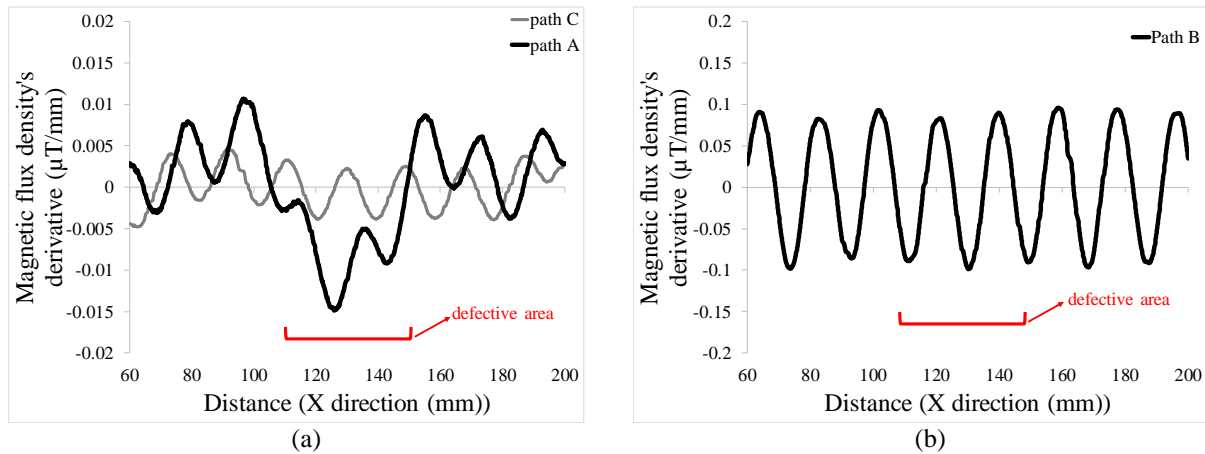
Figure 3.42. The derivative values of the X component magnetic data obtained from the simulation over the paths shown in Figure 3.41: (a) Paths A and C, (b) Path B.

3.5. Investigating the rebar with its defects at 6 clock position

3.5.1. Experimental measurements and results

In this part of the study, rebar #1 was rotated on its axis to reposition the longitudinal defects along the bottom (the inferior) surface. Subsequently, all three of the PMI scanner's magnetic sensors recorded data five times (in five passes of the scanner) over a path 1 cm above the rebar (i.e., the scanner's sensors were 1 cm above the rebar's superior surface). The scans were done while the sensors #1, #2, and #3 were respectively at the left of the centerline, on the centerline, and at the right of the centerline of the rebar. Next, the T-test was applied to the X component magnetic flux density values recorded by each of the magnetic sensors, separately. The scans that were significantly equal to the greatest number of other scans (at a confidence level of 99.8%) were chosen for further studies. Subsequently, the selected scans' first and last 50 mm were eliminated to remove edge effects. The data recorded by each sensor were split into three sections (for a total of nine sections), whose magnetic flux density

derivative values were used for analyzing the data according to approach #4. Figure 3.43 shows that all defects can be detected by the minimum of the magnetic flux density's derivative values. However, the magnetic data at the defective area has a seasonal trend due to the corrugated shape of the rebar, and the magnetic data does not follow defect-Type I or Π's patterns.
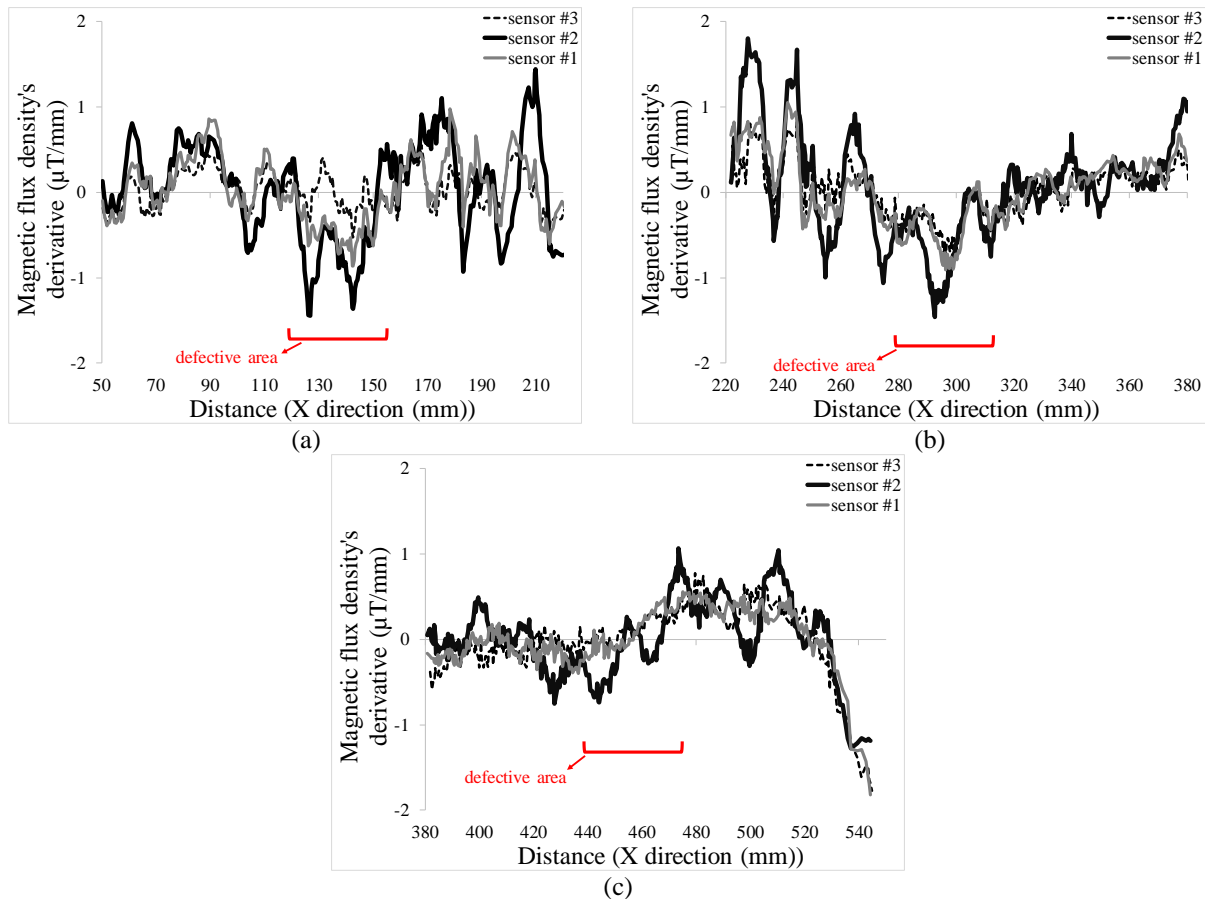
Figure 3.43. Derivative values of the magnetic data recorded over rebar #1, with the defects bottom most: (a) Section #1, (b) Section #2, (c) Section #3.

3.5.2. Numerical simulation procedure and results

To review the experimental results, a numerical simulation was conducted with the previously used process (Figure 3.33) on a solid rebar with a longitudinal defect positioned bottom most. The simulation was implemented using the most accurate element specification shown in Table 3-4 (Mesh #17). According to the graphical representation obtained by simulation (Figure 3.44), magnetic flux density values reflect only the normal rebar corrugation, thus failing to indicate the defective place on the planer slice at a vertical distance of 1 cm above the rebar that mimics the conditions in which the experiments took place.
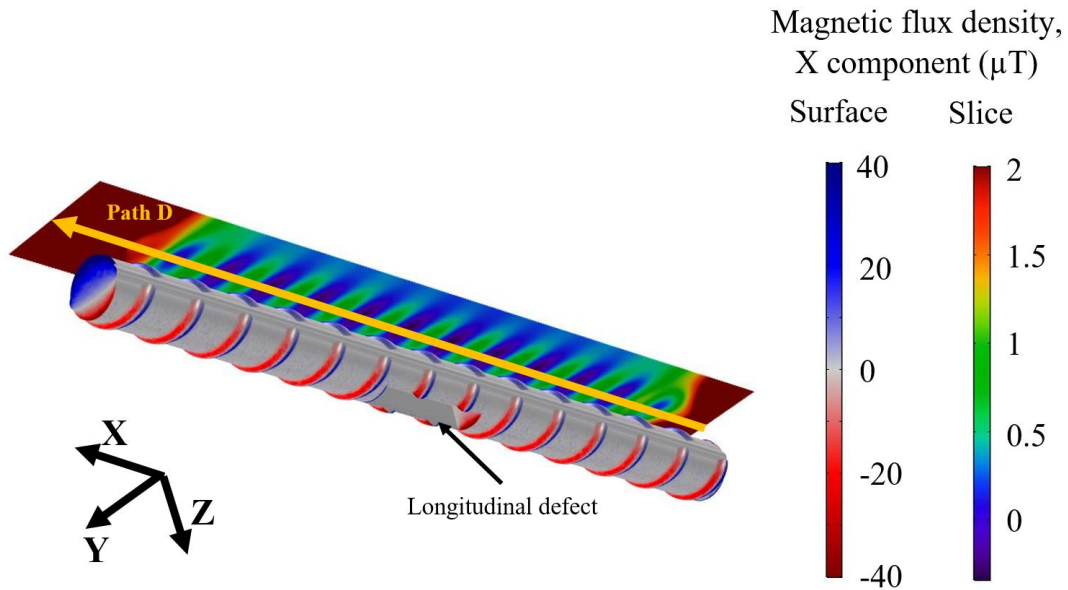
Figure 3.44. X component magnetic flux density behaviour over a rebar with a longitudinal defect at its 6 clock position (magnetic properties on the surface of the rebar and at a planer slice with 1 cm vertical distance from the surface of the rebar)

3.5.3. Comparison between simulation and experimental results

For further review of the simulation (shown in Figure 3.44), the X component magnetic flux density values were taken over path D, which is a representative of the trajectory traveled by sensor #2 in the experiments. These X component values also fail to distinguish the defect (Figure 3.45). Consequently, according to the simulation, the stray magnetic field generated around the rebar is not able to detect a defect on its inferior (bottom) surface. However, the minimum values that represent the defective area in the experimental results might show up, due to the residual stress remaining from the machining process.
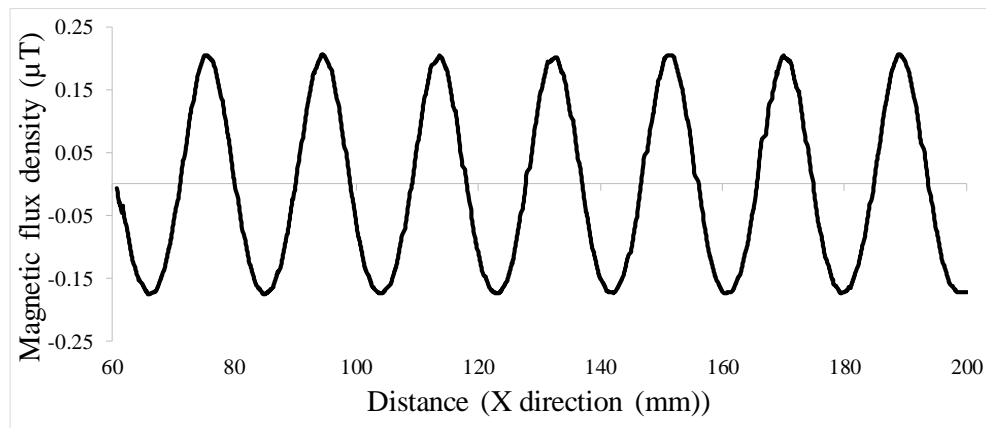
Figure 3.45. X component magnetic flux density values recorded over path D shown in Figure 3.44.

3.6. Conclusion

Quantitatively detecting defects in rebars would significantly mitigate the threats to RC infrastructure's integrity, allowing the assessment of the evolution of defects over time (size, length…). To this end, investigations were conducted on three similar rebars, each with three same-size longitudinal defects with the average sizes (length, width, and height) of 10 mm × 10 mm × 40 mm). The investigations were conducted considering the data recording at different vertical distances, and with defects at different clock positions of rebars. The intent was to study the consistency of the magnetic-value patterns at the defective locations and to establish a reliable threshold for magnetic data to use in detecting defects. The magnetic flux densities recorded over the defective rebars generally showed consistent harmonic trends because of the corrugated shape of the rebars. However, there were specific irregularities in the direction and values of magnetic data at longitudinal defect locations. Additionally, the magnetic behavior of similar ferromagnetic defective rebars was simulated with a finite element-based software while considering the background magnetic field. The results were comparable with the experimental outcomes. In conclusion:

- Magnetic data values recorded in the experiments generally have regular peaks and troughs (harmonic pattern) because of the corrugated rebar surfaces. However, there are more-intense non-repeating peaks and troughs at the locations of the longitudinal defects;

- The intense up-and-down pattern at defective areas in experimentally recorded magnetic data can show up in two ways, and recognizing these patterns allows one to estimate the defect lengths:

  ❖ Magnetic data values slightly increase for a short distance (reaching a local maximum point close to one of the ends of a defect), followed by a sharp decrease for a longer distance (reaching a local minimum point close to the other end of a defect), and again, slightly increasing for a short distance;

  ❖ Magnetic data values slightly decrease for a short distance (reaching a local minimum point close to one of the ends of a defect), followed by a sharp increase for a longer distance (reaching a local maximum point close to the other end of a defect), and again, slightly decreasing for a short distance;

76

- With respect to the experimental results, the locations of the defects can be detected by recognizing these patterns in the magnetic data, and using an 8.88th percentile threshold.

- According to the experiments, unpredictable behaviour occurs in the magnetic data's derivative values at the defective areas. When the distance reaches close to one of the ends of the longitudinal defects, the derivative values noticeably increase (or decrease). The data derivatives continue at relatively constant values until they pass the defective area.

- Similar to the experimental outcomes, simulation results show a pattern at the defective area, with a local minimum point close to one end of the defect, and a local maximum point close to the other end of the defect. The length of the pattern generated at the defective area in simulation results is equal to 40.68 mm, which is statistically equal to that in experimental results, and close to the mean value for the actual defects' lengths (equal to 40.2 mm).

- Applying the threshold (the 8.88th percentile), obtained experimentally, to the magnetic data resulting from the simulation allows identification of the defect location, demonstrating a strong correlation between the simulation and experimental results.

- The pattern of the magnetic data's derivative values at the defective area, generated from the simulation, is also similar to that of the data's derivative values from the experiments. Additionally, the pattern's length in the simulation is (within a significance level of 0. 2) equal to that in the experimental results.

- Normalizing the magnetic data's derivative values obtained experimentally and through simulation into the same scale provided the compatibility, with a coefficient of determination R^2=66%. This R^2 value can again be considered as a proof, showing that the experimental results have been achieved based on accepted physical concepts and not by chance.

- The vertical distance of magnetic sensors from rebars during data recording remarkably affected magnetic data trends. The patterns in the recorded magnetic data showing the defect sites were clearly recognizable at the 1 cm vertical distance. However, Increasing the vertical distance from the rebar resulted in magnetic data sets indicating fewer details of the rebar properties.

- To detect the defects on the side of a rebar, magnetic data sets recorded by the magnetic sensors at the left of the centerline, on the centerline, and at the right of the centerline of the rebar were investigated. Experiments and simulations demonstrated that the data recorded by a sensor at one side of the rebar shows the defects at that side more accurately than that from the other sensors

- According to the experiments and simulation results, the defect site along the bottom (the inferior) surface of a rebar could not be accurately detected by scanning over the 12 clock position of that rebar.

Chapter 4: Transverse-crack size and place detection using PMI technology

Most portions of this chapter are reflective of an original manuscript that has been accepted for publishing in the journal of Measurement.

Mosharafi, M., Mahbaz, S., Dusseault, M.B. 2020. Size and location detection of transverse cracks using a passive magnetic method. Measurement. 154: 107485.

Author Contributions: Conceptualization, M.M., S.M., and M.B.D.; Data curation, M.M.; Formal analysis, M.M.; Funding acquisition, M.B.D.; Investigation, M.M.; Methodology, M.M.; Supervision, M.B.D.; Writing—original draft, M.M.; Writing—review & editing, M.M., S.M., and M.B.D.

4.1. Introduction

RC structure durability can be significantly reduced by the creation of strength-loss anomalies in the steel reinforcement (Alcantara Jr *et al.*, 2016) from causes such as stress conditions (Xin *et al.*, 2012), aggressive environments (Vera *et al.*, 2013), or both (Correia and Salta, 2006). These anomalies can be revealed in different forms such as general corrosion (Perkins, 2000), and local defects such as cracking (Sobieck *et al.*, 2015). Crack initiation is a typical response of structures such as RC bridges that are affected by cyclic loads (Ni, *et al.* 2018) and corrosion. Rebar cracks mostly appear in the transverse direction (Al-Qadi and Elseifi, 2006); their propagation to a condition of sufficient strength loss can result in structure failure (loss-of-function) if detection and repair measures are neglected (Ni *et al.*, 2018).

The previous two chapters investigated magnetic data sets recorded over rebars with holes and longitudinal defects. To continue the technical development of PMI regarding local defects, this chapter focuses on experiments and simulations that investigate steel rebars with different extents of artificial cracks. These cracks are created so as mimic those in defective rebars under actual conditions. The goal is to determine criteria for categorizing detected magnetic anomalies. Investigations are conducted to explore the behaviour of the different components of magnetic flux density where realistic flaws occur.

In this chapter, SMFL data are recorded using a PMI scanner over four defective rebars, each having three same-size cracks. The data are recorded separately for each rebar, post-and pre-

cracking. Investigations are conducted on three components (X, Y, and Z) of magnetic data sets. Thresholds are then defined for the magnetic data for use in identifying locations and sizes of cracks. Next, to verify results, the thresholds are applied to the magnetic data recorded over another rebar with three non-similar cracks. The last experiment is conducted to assess the thresholds' reliability in detecting and categorizing defects based on magnetic properties. Additionally, for further confirmation of the experimental results, the SMFL behavior of solid defective rebars, similar to the rebars used in the experiments, are simulated using a finite-element-based software (COMSOL® software version 5.3a (COMSOL Group, Stockholm, Sweden)).

4.2. Experimental setup and scanning procedure

To investigate the PMI device's ability to detect transverse cracks, five 20 mm diameter steel rebars were cut to approximately the same lengths of 600 mm. Specific paths were then marked on all the rebars. Each rebar was placed in turn in a non-magnetic location and scanned along its whole length using the PMI scanner. The magnetic flux densities of the fixed rebars were measured at three dimensions (X, Y, and Z). Accuracy was ensured by scanning every rebar along the same path and direction five times, with T-tests conducted between every two scans. Subsequently, the scan that was significantly equal to the greatest number of other scans was chosen for use in the rest of the study.

Next, three transverse cuts (thereafter referred to as cracks) per rebar were created, spaced at even distances apart in a line along each rebar (Figure 4.1), using a hand saw with a blade width of 0.96 mm (Figures 4.2 and 4.3; Tables 4-1 and 4-2). Noting that a 10 to 25% reduction in a steel bar cross-section can lead to service failure (O'Flaherty *et al.*, 2008), and also noting that a rebar with more than 25% cross-sectional area reduction should generally be repaired or replaced (Emmons, 1994), crack sizes were chosen to cover various percentages of rebar cross section loss from less than 10 percent to greater than 25 percent.

The specifications of the three cracks were similar to one another in rebars 1, 2, 3, and 4, so that the specifications of cracks in each of those rebars can be observed with a confidence level of 95% in Table 4-3. Additionally, the crack sizes, in order from rebar 1 to 4, went from greatest to smallest. However, rebar 5's cracks were of different sizes: one crack significantly the same as the cracks in rebar 1, one significantly the same as the cracks in rebar 2, and one significantly the same as the cracks in rebar 3 (Table 4-4). For all rebars in this study, the cracks that are significantly the

same as rebar 5's first, second, and third cracks are respectively referred to as small, medium, and large defects (Table 4-4).

The post-crack rebars were placed one by one at the same non-magnetic location and with the same orientation. Once in place, each was scanned along its whole length using the PMI scanner, again over the same specific marked paths (shown by yellow stickers in Figure 4.1). The scanning was repeated five times over the same path, and the scans significantly equal to the greatest number of other scans (based on T-testing) were used in the rest of the study.

Figure 4.1. Prepared rebars with three symmetrically-located transverse cracks.

Figure 4.2. Creating rebar defects using a handsaw.

Left view

Top view
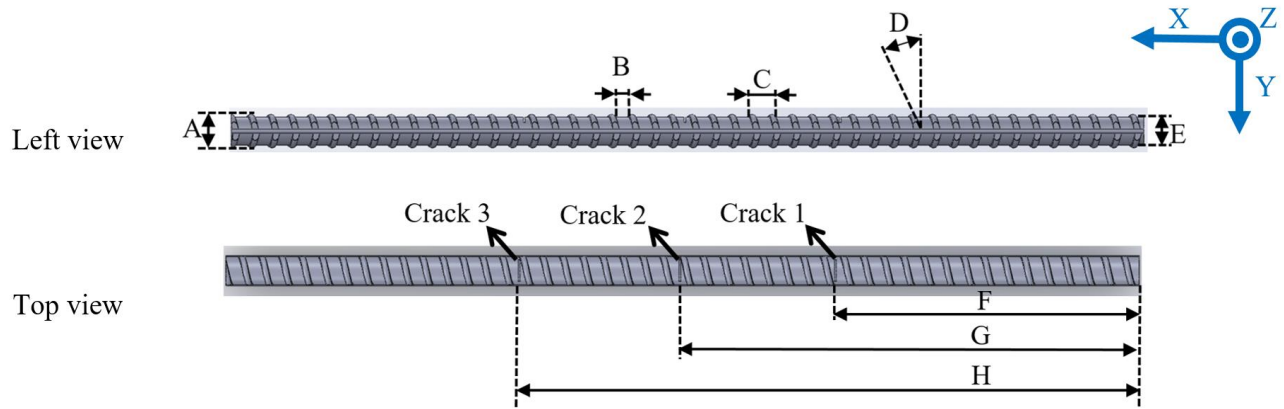
Figure 4.3. Schematic drawing of prepared samples with transverse cracks.

Table 4-1. Values for the parameters shown in Figure 4.3.

Parameter's name	Rebar NO.				
	1	2	3	4	5
A (mm)	22.0 ∓ 0.2	22.0 ∓ 0.2	22.0 ∓ 0.2	22.0 ∓ 0.2	22.0 ∓ 0.2
B (mm)	8.9 ∓ 0.2	8.9 ∓ 0.2	8.9 ∓ 0.2	8.9 ∓ 0.2	8.9 ∓ 0.2
C (mm)	17.5 ∓ 0.2	17.5 ∓ 0.2	17.5 ∓ 0.2	17.5 ∓ 0.2	17.5 ∓ 0.2
D (Deg.)	30	30	30	30	30
E (mm)	18.5 ∓ 0.2	18.5 ∓ 0.2	18.5 ∓ 0.2	18.5 ∓ 0.2	18.5 ∓ 0.2
F (mm)	208.07	203.6	202.03	197.07	205.52
G (mm)	306.84	303.02	300.01	296.08	305.25
H (mm)	406.89	403.39	401.02	395.37	404.66

Table 4-2. Specifications of cracks in rebars shown in Figure 4.3.

	Length (mm)			Depth (mm)			Defective area cross section (mm²)		
	Crack 1	Crack 2	Crack 3	Crack 1	Crack 2	Crack 3	Crack 1	Crack 2	Crack 3
Rebar 1	17.59	17.51	17.55	6.29	6.17	6.23	80.79	78.78	79.78
Rebar 2	14.78	14.57	14.74	3.66	3.52	3.63	37.74	35.76	37.36
Rebar 3	11.67	11.71	11.96	2.06	2.08	2.18	16.42	16.61	17.83
Rebar 4	8.36	8.37	8.37	0.99	0.99	0.99	5.6	5.62	5.62
Rebar 5	17.55	14.74	11.71	6.23	3.63	2.08	79.78	37.34	16.65

Table 4-3. Specifications of cracks in rebars, with a confidence level of 0.95.

	Length (mm)	Depth (mm)	Width (mm)	Defective area cross section (mm²)
Rebar 1	17.55 ± 0.6	6.23 ± 0.09	1.16 ± 0.1	79.8 ± 1.7
Rebar 2	14.7 ± 0.2	3.6 ± 0.1	1.16 ± 0.1	36.9 ± 1.8
Rebar 3	11.78 ± 0.26	2.1 ± 0.1	1.16 ± 0.1	16.9 ± 1.3
Rebar 4	8.36 ± 0.01	0.995 ± 0.002	1.16 ± 0.1	5.61 ± 0.02

Table 4-4. Comparison of the dimensions of cracks in rebar 5 with the cracks in rebars 1, 2, and 3.

		Crack length (mm)	Crack depth (mm)	Defective area (mm²)
Small defect (Cross-sectional loss: 5.8-6.7%)	Crack 1 in rebar 5	11.71	2.08	16.65
	Cracks in rebar 3	11.78 ± 0.26	2.1 ± 0.1	16.9 ± 1.3
	Status	Significantly equal	Significantly equal	Significantly equal
Medium defect (Cross-sectional loss: 13.1-14.4%)	Crack 2 in rebar 5	14.74	3.63	37.34
	Cracks in rebar 2	14.7 ± 0.2	3.6 ± 0.1	36.9 ± 1.8
	Status	Significantly equal	Significantly equal	Significantly equal
Large defect (Cross-sectional loss: 29.1-30.3%)	Crack 3 in rebar 5	17.55	6.23	79.78
	Cracks in rebar 1	17.55 ± 0.6	6.23 ± 0.09	79.8 ± 1.7
	Status	Significantly equal	Significantly equal	Significantly equal

4.3. Reliability of magnetic data for different components

As mentioned in the previous section, specific paths were scanned five times over the rebars, before and after the transverse cracks were created. To reduce the effects of the local magnetic field changes, all the scans were conducted on the same day and within a twenty-four-hour time span. All scanning took place at a vertical distance of 1 cm above the rebar surface (the minimum vertical distance that can be applied with the PMI device). The vertical distances in this study refer to the distance between rebar and the magnetic sensors in the PMI scanner. Next, T hypothesis tests were conducted between every two data sets to select the most-consistent scan. Theses hypothesis tests were carried out separately for all three components of magnetic flux density values recorded at every scan.

As a representative, the magnetic flux density values for rebar 1, after creation of the transverse cracks, are discussed in detail. Figures 4.4a and 4.4b show the X component magnetic flux density values on rebar 1, respectively before and after removing the linear trend. To remove the edge effects, 150 mm of data from either end of the rebar was ignored. Next, the magnetic data set obtained with scan 2 (blue solid line) was found to be equal (with high significance levels) to the greatest number of X component data sets from other scans (Table 4-5). To explore more details, the relation between the magnetic flux density values recorded in scan 2 and other scans were investigated using Pearson correlation. Considering the high correlation coefficients and high significance levels in Table 4-5, the selected X component magnetic values are consistent and reliable.
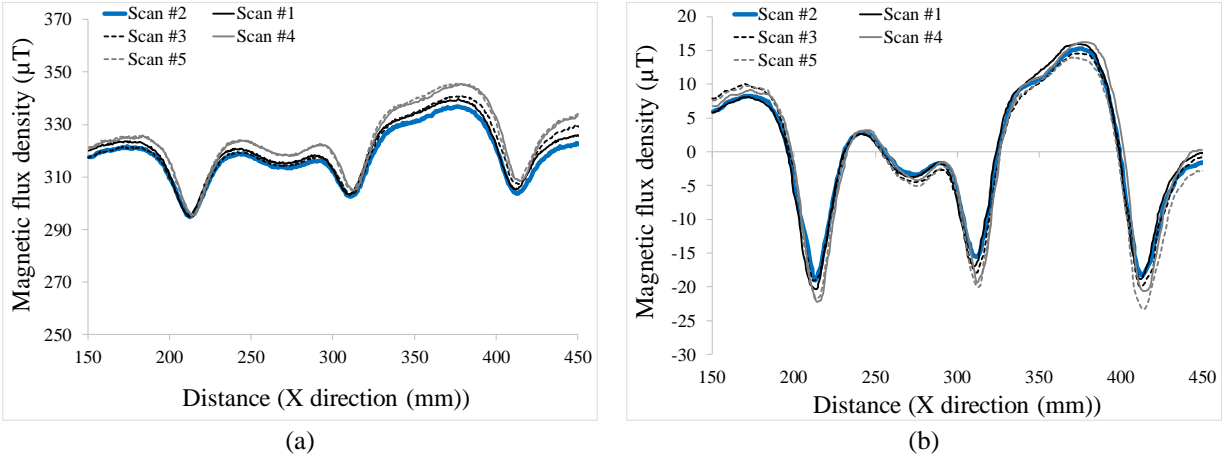
Figure 4.4. X component values of five separate scans recorded by PMI scanner over the path shown in Figure 4.1 on rebar1, post cracking: (a) Before removing the linear trend, (b) After removing the linear trend.

Table 4-5. Comparison of X component values of scan 2 with those of other scans shown in Figure 4.4b.

First data set	Second data set	Status	Correlation coefficient
X component of Scan 2	X component of Scan 1	Equal with a two-tail significance level of **0.3**	**0.89**
X component of Scan 2	X component of Scan 3	Equal with a two-tail significance level of **0.5**	**0.98**
X component of Scan 2	X component of Scan 4	Equal with a two-tail significance level of **0.3**	**0.97**
X component of Scan 2	X component of Scan 5	Equal with a two-tail significance level of **0.5**	**0.94**

T-hypothesis tests were also conducted between every two Z component data sets recorded in the five scans. The Z component magnetic values recorded in scan 2 were found to be significantly equal to the values in the greatest number of Z component data sets for other scans (Figure 4.5). Table 4-6 confirms the high and consistent significance levels of the equality of the Z component magnetic values of scan 2 when compared with those of other scans. Additionally, there is a strong correlation (more than 90%) between the Z component magnetic values of scan 2 and those of other scans (Table 4-6). Next, to find the most significant Y component magnetic values, T-testing was carried out between every two Y component data sets recorded in all scans. The Y component magnetic flux density values in scan 2 were equal to the greatest number of those data sets in other scans (Figure 4.6), but with very low and inconsistent significance levels such as 0.01 (Table 4-7). Furthermore, Table 4-7 shows the weak, and even negative correlations between the Y component magnetic values in scan 2 and those values in other scans. These findings indicate the less-reliable Y component magnetic flux density values compared to the magnetic values recorded in X and Z directions.
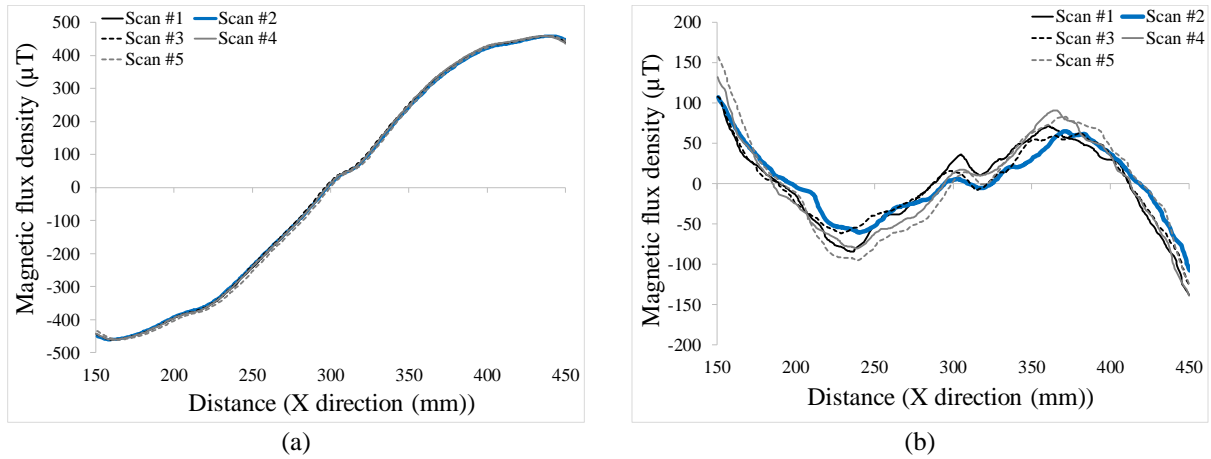
Figure 4.5. Z component values of five separated scans recorded by PMI scanner over the path shown in Figure 4.1 on rebar1, post cracking: (a) Before removing the linear trend, (b) After removing the linear trend.

Table 4-6. Comparison of Z component values of scan 2 with those of other scans shown in Figure 4.5b.

First data set	Second data set	Status	Correlation coefficient
Z component of Scan 2	Z component of Scan 1	Equal with a two-tail significance level of **0.3**	0.91
Z component of Scan 2	Z component of Scan 3	Equal with a two-tail significance level of **0.5**	0.95
Z component of Scan 2	Z component of Scan 4	Equal with a two-tail significance level of **0.5**	0.93
Z component of Scan 2	Z component of Scan 5	Equal with a two-tail significance level of **0.5**	0.96
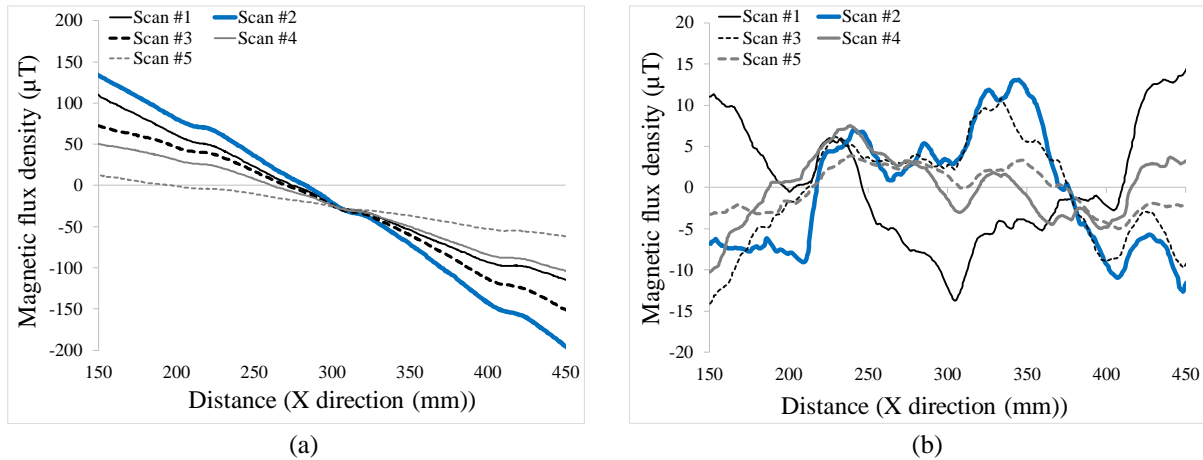
Figure 4.6. Y component values of five separate scans recorded by PMI scanner over the path shown in Figure 4.1 on rebar1, post cracking: (a) Before removing the linear trend, (b) After removing the linear trend.

Table 4-7. Comparison of Y component values of scan 2 with those of other scans shown in Figure 4.6b.

First data set	Second data set	Status	Correlation coefficient
Y component of Scan 2	Y component of Scan 1	Equal with a two-tails significance level of **0.05**	-0.53
Y component of Scan 2	Y component of Scan 3	Equal with a two-tails significance level of **0.01**	0.91
Y component of Scan 2	Y component of Scan 4	Equal with a two-tails significance level of **0.01**	0.32
Y component of Scan 2	Y component of Scan 5	Equal with a two-tails significance level of **0.2**	0.75

4.4. Analysis of X component magnetic flux density values

4.4.1. Rebars, each having three same-size cracks

Investigating the effects of cracks on magnetic data first focused on the X component magnetic flux density values recorded over rebars 1, 2, 3, and 4, before and after cracks were created. The sizes of cracks in each rebar were similar (with slight variation), but the crack sizes differed from rebar to rebar (Table 4-3). Figure 4.7 shows the selected X component values of the scans conducted on rebars 1 to 4, over the paths shown in Figure 4.1. There are two sets of data in every plot: one is the magnetic data recorded pre-cracking, called here the base data; the other is the magnetic data recorded post cracking, called here the test data.

These scans in Figure 4.7 are presented after deleting each rebars' first and last 150 mm of data, and after moving-average smoothing (with a period of about 3 mm). According to Figure 4.7, obvious changes, showing up as dips, appear in the magnetic values at the crack locations in rebars 1, 2, and 3. These changes at defect locations become less intense as the defective area decreases, from rebar 1 to rebar 3. However, no detectable changes are observed in the magnetic data at defect locations in rebar 4, which had the smallest cracks, demonstrating the detection limit of the magnetic sensors.
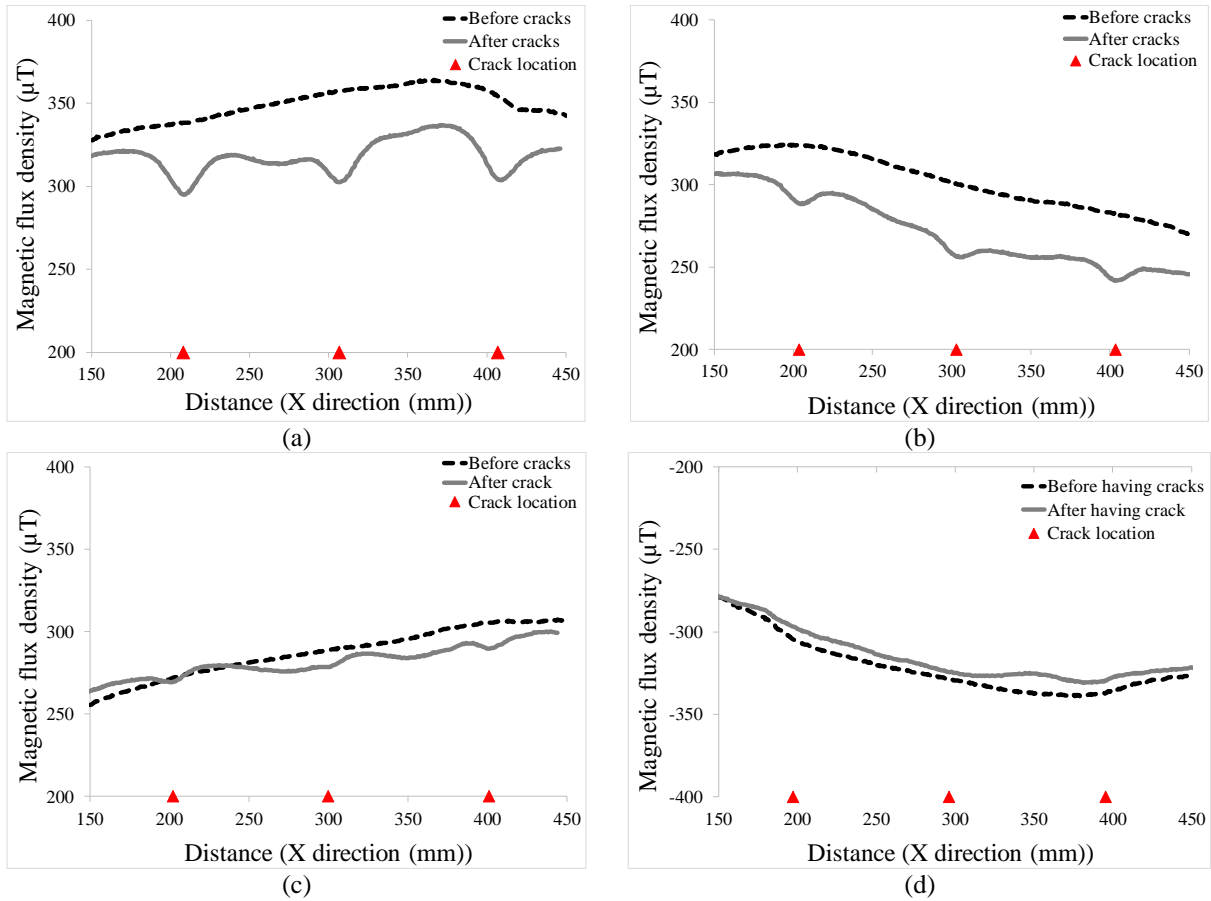
Figure 4.7. X component magnetic flux density values recorded over paths shown in Figure 4.1, post- and pre-cracking: (a) Magnetic data recorded over rebar 1, (b) Magnetic data recorded over rebar 2, (c) Magnetic data recorded over rebar 3, (d) Magnetic data recorded over rebar 4.

To quantify the difference between the magnetic values before and after creation of the transverse cracks, the following steps were applied for every data set separately:

Instead of every magnetic value, a mean value was located. The means were taken from an equal number of data on either side of a central value (with a period of about 3 mm);

The overall linear trend was removed by subtracting the best fitted straight-line from the magnetic data;

The derivative of every set of magnetic data was computed using MATLAB 2018 b;

A mean value was used instead of the individual values (in the graphs of magnetic data's derivatives). The mean values were taken from an equal number of data on either side of a central value (with a period of about 3 mm);

The secular linear trend was removed from the values of the magnetic data's derivatives by subtracting the best fitted straight-line from the values;

Figure 4.8 shows the magnetic data's derivative values for all rebars after the above mentioned steps were carried out. In the magnetic values recorded over rebars 1, 2, and 3, after cracks creation, a pattern become distinguishable. Approaching the defect location, the magnetic derivative's values of test data slightly decrease for a short distance and reach a minimum value (shown with green circles). Next, there is a sharp increase in the magnetic values of the test data's derivatives, followed by an intersection with the derivative values of base data, and reaching to a maximum value (shown with green squares). Subsequently, there is again a slight decrease for a short distance in the values of test-data's derivatives until its values approach those of base data and continue. In the pattern created due to the defects, for all three rebars, the intersection points of the test and base data are very close to the crack locations.
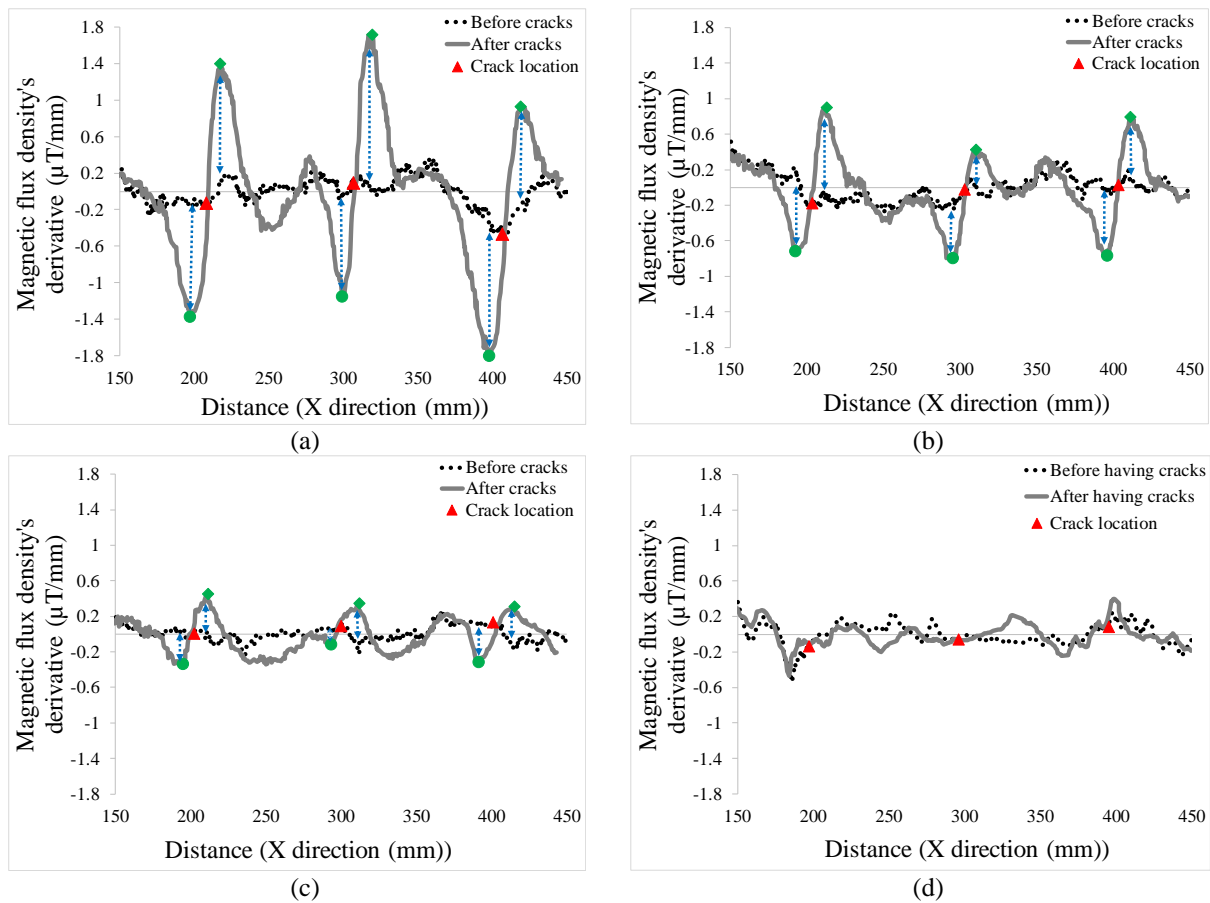
Figure 4.8. Signal processing for X component magnetic data using the derivative values: (a) For magnetic data recorded over rebar 1, (b) For magnetic data recorded over rebar 2, (c) For magnetic data recorded over rebar 3, (d) Magnetic data recorded over rebar 4.

To understand the relation between the pattern's characteristics and the crack sizes, the difference between the magnetic values of test data at extremum points (close to cracks) and their corresponding values resulting from the base data were extracted for rebars 1, 2, and 3 (shown by

dotted blue double arrows in Figure 4.8). Next, box-and-whisker plots were generated separately for the length of dotted blue double arrows, in the magnetic data sets of every rebar to find the outlier behaviour in the patterns. The outliers were ignored; the mean values and the ranges (with a significance level of 0.01) for the lengths of the dotted blue double arrows in Figure 4.8 were calculated for every rebar separately (Figure 4.9). Next, the mean of the defective area was calculated for every rebar (rebars 1, 2, and 3) using the characteristics of their three cracks. Figure 4.10a shows that the mean values of test data's derivative deviation from those of base data (the mean of the lengths of dotted blue double arrows in Figure 4.8 for every rebar) increase when the mean of the defective area increases.

To explore more details about the magnetic data pattern at crack locations, the distance between test magnetic values' extrema at defective locations (distance between the green circle and green square) was calculated for all cracks in rebars 1,2, and 3. Subsequently, the mean values of the distances were calculated separately for rebars 1,2, and 3, keeping in mind the different mean values for their defective areas. According to Figure 4.10b, the mean values of the distances does not noticeably change when the mean of defective area increases. In other words, the distances between the local extrema at crack locations is constant and generally close to 19 mm.

| $1.3 \pm 0.4 \, \mu T/mm$ | $0.7 \pm 0.3 \, \mu T/mm$ | $0.4 \pm 0.1 \, \mu T/mm$ |
| (a) | (b) | (c) |

Figure 4.9. Box-and-whisker plots for the differences between the X component magnetic values of test data at extremum points and their corresponding values resulting from the base data: (a) For magnetic data recorded over rebar 1; (b) for magnetic data recorded over rebar 2, (c) For magnetic data recorded over rebar 3.
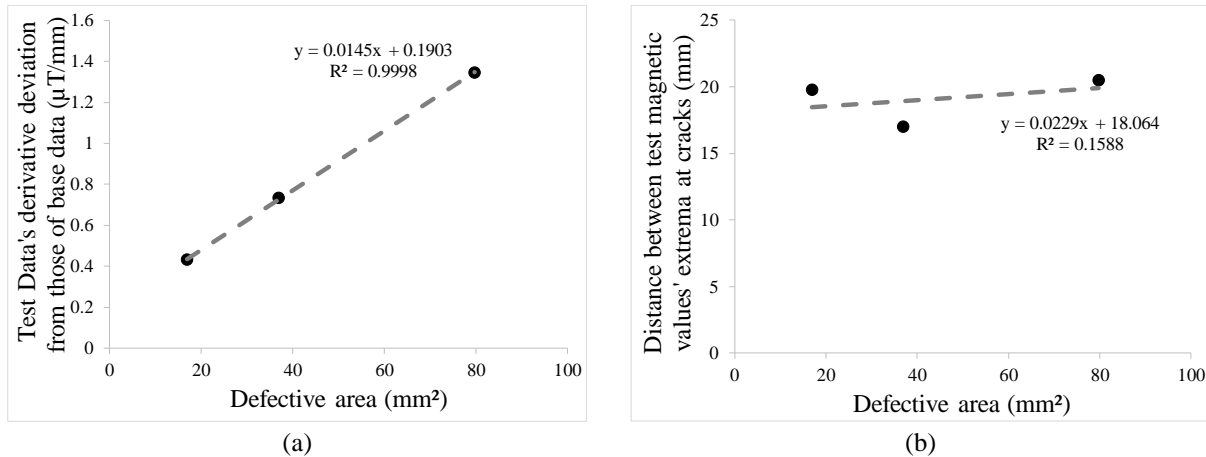
Figure 4.10. Relation between the X component magnetic derivative pattern's characteristics and crack sizes: (a) Test datas' derivative deviation from the derivatives of base data when the defect area increases, (b) Distances between the local maximum and minimum points at defect locations as the defective area increases.

4.4.1.1. Analyzing post-cracking data with absolute gradient values (AG)

In reality, most of the time, defective rebars have to be inspected without knowing their original (pre-cracking) magnetic data values. Hence, specific criteria should be defined to categorize the defects based on the test data (as a representative of the data that can be recorded over defective rebars under actual field conditions). According to the above-mentioned observation, there are obvious patterns in the derivative values of test data at crack locations. To quantify the gradient values of test data based on crack specifications, the same steps for data processing (separately for rebars 1, 2, and 3) were followed as in the previous section. After performing those steps, the absolute values of the processed data were used for further investigations. Therefore, the data analysis procedure applied on every set of test data, in this section, was as follows:

1. The moving average smoothing technique (with a period of about 3 mm) was applied on the test data;
2. The overall secular linear trend was removed from the magnetic data;
3. The derivative of magnetic data was computed using MATLAB 2018 b;
4. The moving average smoothing technique (with a period of about 3 mm) was applied on the derivative values of test data;
5. The overall linear trend was removed from the values of the magnetic data's derivatives;
6. The absolute values of the magnetic flux density's derivative were computed.

Figure 4.11 shows the absolute values of magnetic data's derivative for rebars 1, 2, and 3 with clear extrema (green squares) within 19 mm on either side of the defect location. This distance (19

mm) encompasses the area clearly affected by cracks (Figure 4.10b). To quantify the outcomes, using the extrema magnetic values at the defective locations, the upper and lower defectiveness limits on magnetic data were computed with a 95% confidence level for all three rebars. As seen in Figure 11, the boundaries for defectiveness differ for each rebar in relation to their different crack specifications. This finding can help in categorizing magnetic data based on the physical characteristics of defects in rebars.

Figure 4.11. X component magnetic data subjected to AG analysis approach: (a) For magnetic data recorded over rebar 1, (b) For magnetic data recorded over rebar 2, (c) For magnetic data recorded over rebar 3.

4.4.1.2. Analyzing post-cracking data with the SD of gradient values (SG)

According to Figure 4.8, there are sharp deviations in derivative values of test data at the cracks locations. This feature can help in recognizing the defective area by using magnetic data. To measure and quantify the amount of these dispersions, the following procedure was conducted:

1. The moving average smoothing technique (with a period of about 3 mm) was applied on the test data;

2. The overall secular linear trend was removed from the magnetic data;

3. The derivative of magnetic data was computed using MATLAB 2018 b;

4. The derivative values of test data were subjected to the centered moving average smoothing technique;

5. The obtained data was split into equal sections and the standard deviations of each section's magnetic data were calculated;

6. The SD values were then shown at the places of the average distances included in every section.

To obtain the most reliable results, first the above data analysis steps were conducted on the test data recorded over rebar 2, using different sections length in step 5. As seen in Figures 4.12a, 4.12b, 12c, 12d, 12e, 12f, 12g, and 12h, the maximum SD values happen close to the crack locations. To find the most-appropriate section length, for each of these Figures (4.12a, 4.12b, 4.12c, 4.12d, 4.12e, 4.12f, 4.12g, and 4.12h), the SDs of the highest SD values within 19 mm of the cracks were calculated. According to Figure 4.12i, the most-consistent values for the SDs at crack locations belongs to the results using sections length of 14 mm. More-consistent outcomes may be obtained by increasing the sections length to more than 14 mm. However, increasing the section length definitely reduces the details that can be obtained from the analysis. Hence, the section length of 14 mm was selected to be used in SG analysis approach for the rest of study.
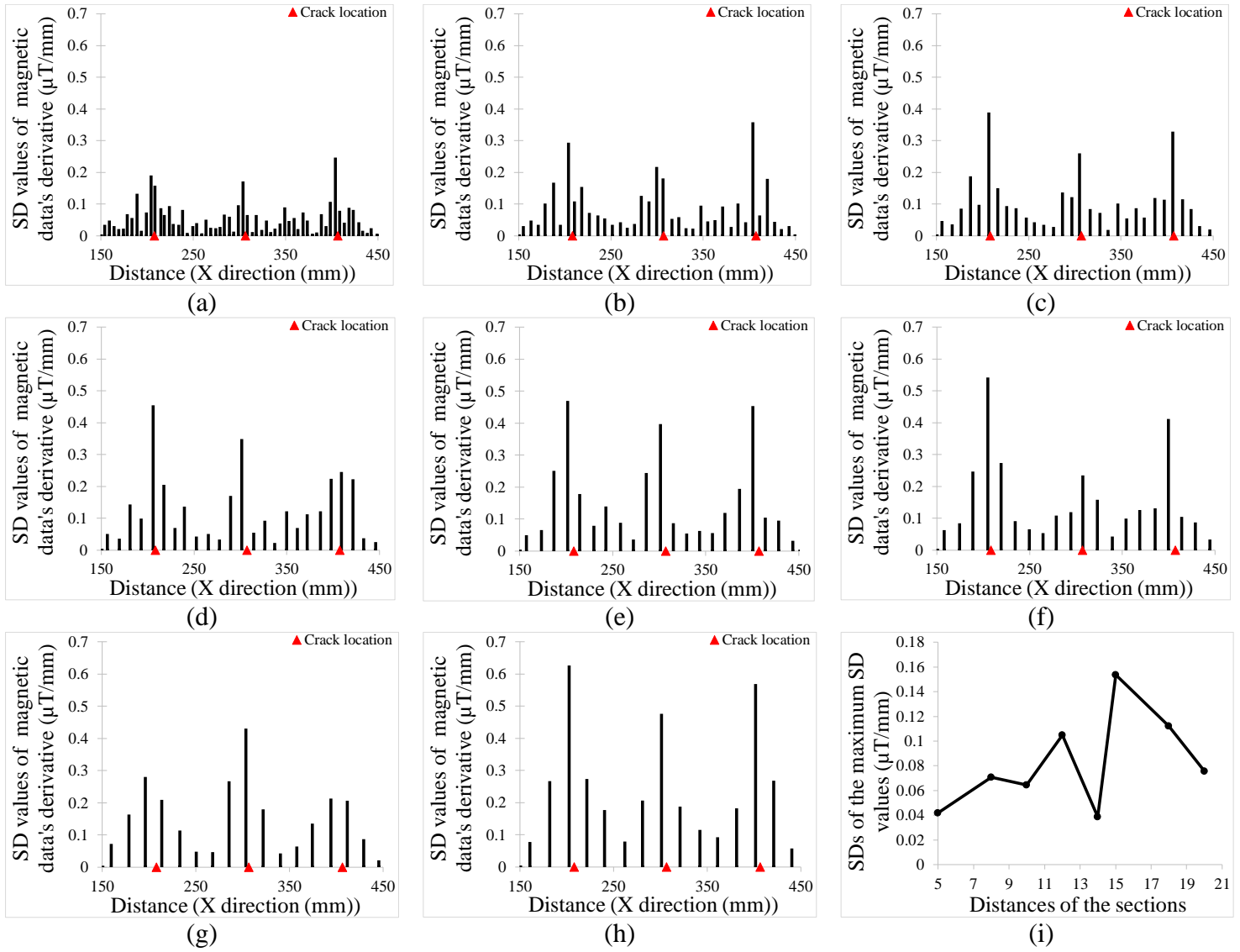
Figure 4.12. The process for finding the appropriate section length for applying SG analysis approach on X component magnetic data recorded over rebar 2: (a) SG analysis result using 5 mm sections length, (b) SG analysis result using 8 mm sections length, (c) SG analysis result using 10 mm sections length, (d) SG analysis result using 12 mm sections length, (e) SG analysis result using 14 mm sections length, (f) SG analysis result using 15 mm sections length, (g) SG analysis result using 18 mm sections length, (h) SG analysis result using 20 mm sections length, (i) the SDs of the highest values within 19 mm of the cracks (in parts a, b, c, d, e, f, g, and h).

Figure 4.13 shows the results of the analysis, using equal sections length of 14 mm, for the selected test data (based on T-hypothesis testing) over the path shown in Figure 4.1 for rebars 1, 2, and 3. As seen, the maximum SD values at crack locations become less as the defective area decreases, from rebar 1 to rebar 3. Using the maximum SD values within 19 mm of the cracks, upper and lower boundaries for defectiveness were calculated with a 95% of confidence on the SDs of magnetic values recorded over all three rebars (Figure 4.13). The upper and lower boundaries on

SD values differ from one rebar to another, due to their different crack sizes. This finding can again help in categorizing the magnetic data based on the rebars' defect intensity.

Figure 4.13. X component magnetic data subjected to SG analysis approach: (a) For magnetic data recorded over rebar 1, (b) For magnetic data recorded over rebar 2; (c) for magnetic data recorded over rebar 3.

4.4.2. Rebar with three non-similar cracks

Continuing the exploration of defect intensity, the limits on magnetic data obtained using the two analysis approaches, were tested against the results for rebar 5. Rebar 5 is a representative of rebars in reality with their different defectiveness conditions, and it has three non-similar cracks with the size specifications (length and depth) shown in Table 4-2. The size specifications of cracks 1, 2, and 3 in rebar 5 (Table 4-2) are respectively in the ranges of the crack specifications of rebars 3, 2, and 1. In other words, the sizes of the three cracks 1, 2, and 3 in rebar 5 are respectively equal (with a significance level of 95%) to the sizes of the cracks in rebars 3, 2, and 1 (Table 4-3).

The investigation on rebar 5, first focused on the magnetic properties, before and after the cracks were created. Figure 4.14a shows the selected X component values (using T-hypothesis testing) of

94

the scans conducted on rebars 5, over the paths shown in Figure 4.1. Two sets of data are observed in Figure 4.14a: one is the base data (magnetic data recorded pre-cracking); the other is the test data (magnetic data recorded post-cracking). The scans in Figure 4.14a are presented after deleting rebar 5's first and last 150 mm of data, and after moving-average smoothing (with a period of about 3 mm). There are recognizable dips in the magnetic values at the crack locations. The dimensions of the dips become bigger from crack 1 to crack 3, corresponding to the crack sizes getting larger.

The same processing procedure for presenting the data in Figure 4.8 was used to quantify the difference between the base and test data for rebar 5 (Figure 4.14b). The processed test data's derivative values for rebar 5 have a pattern at crack locations similar to that observed for rebars 1, 2, and 3 (Figure 4.8). To quantify the relation between the cracks size in rebar 5 and the pattern's characteristics in magnetic data, the difference between the magnetic values of test data at extremum points (green squares and circles) and their corresponding values resulting from the base data were extracted (shown by dotted blue double arrows in Figure 4.14b). Thereafter, these dotted blue double arrows are called "difference at extrema" for convenience.

Table 4-8 shows that the average of two "difference at extrema" within 19 mm on either side of cracks 1, 2, and 3 in rebar 5 are respectively in the range of the "difference at extrema" obtained from rebars 3, 2, and 1. This finding verifies the consistent behaviour in the magnetic data for cracks with different physical dimensions. Hence, the upper and lower defectiveness limits on magnetic data, computed analyzing the test data recorded over rebars 1, 2, and 3, may help in recognizing the locations and the dimensions of cracks in rebar 5.

(a)   (b)

Figure 4.14. X component values and the derivatives of X component values of the magnetic data recorded over rebar 5: (a) Magnetic data recorded over the path shown in Figure 4.1, post- and pre-cracking, (b) Signal processing on magnetic data using the derivative values.

Table 4-8. Comparing the "difference at extrema" for cracks in rebar 5 with those for cracks in rebars 1, 2, and 3.

	Difference at extrema at crack locations
Crack 1 in rebar 5	Avg. (0.31 µT/mm & 0.51 µT/mm) = 0.41 µT/mm
Cracks in rebar 3	0.4 ± 0.1 µT/mm
Status	Significantly equal
Crack 2 in rebar 5	Avg. (0.85 µT/mm & 0.57 µT/mm) = 0.71 µT/mm
Cracks in rebar 2	0.7 ± 0.3 µT/mm
Status	Significantly equal
Crack 3 in rebar 5	Avg. (1.57 µT/mm & 1.47 µT/mm) = 1.52 µT/mm
Cracks in rebar 1	1.3 ± 0.4 µT/mm
Status	Significantly equal

To detect and classify the cracks, AG and SG analysis procedures (as respectively mentioned in sections 3.1.1 and 3.1.2) were conducted on the selected test data (using T-testing) recorded over rebar 5. Additionally, the lower limits calculated using AG and SG analysis, for rebars 1, 2, and 3 were applied to the magnetic data recorded over rebar 5. The lower limits calculated for magnetic data recorded over rebars 1, 2, and 3 respectively corresponded to the threshold of the small, medium, and large defects defined in Table 4-4.

Figures 4.15a and 4.15b respectively show the analysis of rebar 5's test data based on AG and SG analysis approaches. As seen in Figure 4.15a, the places and the dimensions of the cracks are correctly detected using the predefined lower limits shown in Figures 4.11a, 4.11b, and 4.11c. Additionally, the predefined lower limits shown in Figures 4.13a, 4.13b, and 4.13c can appropriately detect the places and the dimensions of the cracks in Figure 4.15b. The lower limits obtained from the investigation of rebars 1, 2, and 3 were then verified by using them to find the

defects in rebar 5. Their effectiveness in that context might be due to the similarity in the magnetic properties of the materials of rebars 1, 2, and 3 and those of rebar5. Changing the magnetic properties of materials, their local magnetic field, or the vertical distance of the magnetic sensors from the rebar can change the scales of magnetic values. Hence, some criteria should be defined that are flexible considering the ranges of the recorded magnetic values, such as specific percentile values of the data.
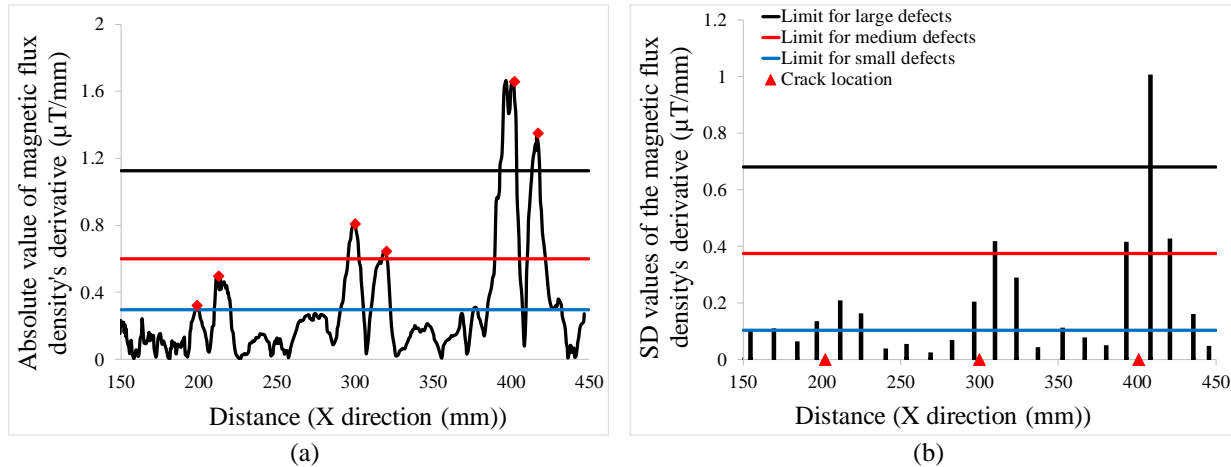
Figure 4.15. Applying analysis approaches on X component magnetic data recorded over rebar 5: (a) Magnetic data subjected to AG analysis, (b) Magnetic data subjected to SG analysis.

The percentile ranks of the limits shown in Figures 4.15a and 4.15b were calculated separately for the values processed based on AG and SG analysis. Table 4-9 demonstrates the thresholds that guide the classification of magnetic data, based on defective conditions, using the percentile values. It should be noted that the threshold values presented in Table 4-9 were calculated with a 95% confidence level (a commonly used confidence level), using the results of the analysis of the magnetic data recorded over rebars 1, 2, and 3. Therefore, alteration in the significance level can change the threshold values.

Using the calculated percentile rank values for small, medium, and large defects, a regression model can be provided for estimating the thresholds to detect the defects which were not investigated experimentally in this study. Considering the regression equation shown in Figure 4.16, interpolations can be conducted on both data sets to find the percentile ranks corresponding to the different percentages of cross-section area lost. However, regarding the regression model, the percentile ranks for a cross-section area loss greater than 30% are not logical (may be greater than one) based on the results of the SG Analysis.

Table 4-9. Thresholds for detecting defects size based on AG and SG analysis approaches.

Defect size	Threshold for the AG processed magnetic data		Threshold for the SG processed magnetic data	
	Value (µT/mm)	Percentile rank	Value (µT/mm)	Percentile rank
Small defect	0.296	0.703	0.104	0.463
Medium defect	0.597	0.87	0.375	0.849
Large defect	1.123	0.95	0.681	0.974
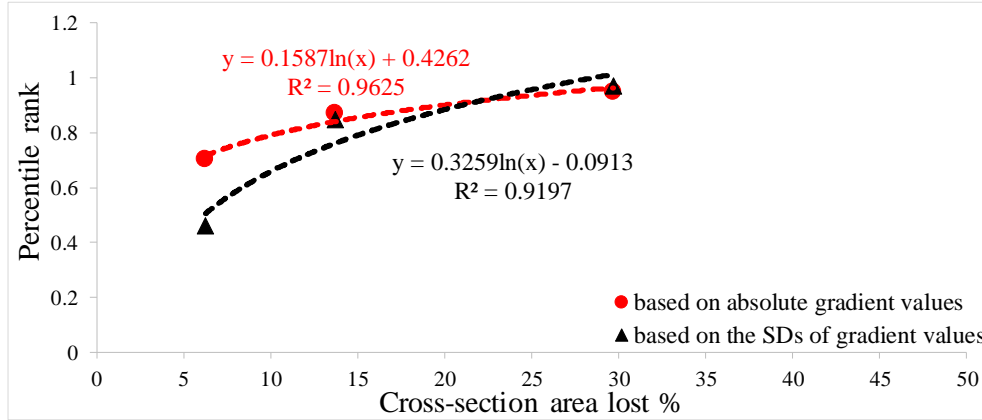
Figure 4.16. Regression model for estimating percentile threshold needed to detect defects of different sizes.

Next, to review the reliability of the percentile rank thresholds mentioned in Table 4-9, magnetic data was recorded at different vertical distances over rebar 5. Additional scans were conducted over the same path on rebar 5 (yellow sticker shown in Figure 4.1) with vertical distances of 2 cm, 3 cm, 4 cm, 5 cm, 6 cm, and 7 cm. The magnetic data for every vertical distance was collected five times, producing scans significantly equal to other scans recorded at the same vertical distances. The most-consistent scans (at each vertical distance) were then used in the rest of the study. For every selected scan, 150 mm from either end of the data was ignored to remove edge effects.

Next, the rest of data were separately subjected to the AG and SG analysis approaches described in sections 4.4.1.1 and 4.4.1.2 (figures shown in Appendix C). Tables 4-10 & 4-11 show the results of analysis on the magnetic data recorded over rebar 5 at the same path and direction, but with different vertical distances. The detection of correct crack sizes and locations, based on magnetic data, with an accuracy of 19 mm (average value of the data points in Figure 4.10b) is considered an accurate result. However, failure to find crack locations, or to correctly classify defects is considered a Type II error, shown in gray in Tables 4-10 & 4-11.

Table 4-10 demonstrates that the locations and the size of all cracks in rebar 5 are accurately recognized using the AG analysis approach for vertical distances of 1 cm and 2 cm. This approach also enables us to detect the place and size of the large crack based on the magnetic data recorded

at a vertical distance up to 5 cm. Additionally, Table 4-11 shows that the locations and the sizes of the cracks in rebar 5 can be distinguished accurately using the SG analysis approach for the data recorded at the vertical distances of 1 cm and 2 cm. The largest crack in rebar 5 can also be identified using SG analysis up to the vertical distance of 5 cm (a result similar to that obtained through AG analysis). However, the high SD values in the data recorded at the elevations of 4 cm and 5 cm occur with distances of 22 mm and 31 mm from the large crack, instead of happening within a 19 mm distance from the crack.

Both AG and SG analyses can help in detecting the sizes and locations of cracks up to specific vertical distances, based on passive magnetic data. However, the analysis outcomes may include false positives (Type I error). To illustrate, Figure 4.17 shows the Type I error percentages in the results of SG analysis, occurring for all three thresholds. As seen, the percentages of Type I errors increase as the data-recording vertical distances increase, so results based on the magnetic data collected at higher vertical distances are less reliable. Given that the magnitude versus distance of an anomaly's influence on the magnetic fields must follow the laws of physics, this is an expected result.

Table 4-10. Results of AG analysis in detecting crack places and sizes (Type II errors are highlighted in gray).

Vertical distance	Crack 1 (small defect)	Crack 2 (medium defect)	Crack 3 (large defect)
1 cm	detected by local peak above the limit for small defects	detected by local peak above the limit for medium defects	detected by local peak above the limit for large defects
2 cm	detected by local peak above the limit for small defects	detected by local peak above the limit for medium defects	detected by local peak above the limit for large defects
3 cm	Not detected	Not detected	detected by local peaks above the limit for large defects
4 cm	detected by local peak above the limit for medium defects	detected by local peak above the limit for small defects	detected by local peaks above the limit for large defects
5 cm	detected by local peak above the limit for small defects	detected by local peak above the limit for small defects	detected by local peaks above the limit for large defects
6 cm	detected by local peak above the limit for small defects	detected by local peak above the limit for small defects	detected by local peak above the limit for medium defects
7 cm	Not detected	detected by local peak above the limit for medium defects	detected by local peak above the limit for medium defects

Table 4-11. Results of SG analysis in detecting crack places and sizes (Type II errors are highlighted in gray).

Vertical distance	Crack 1 (small defect)	Crack 2 (medium defect)	Crack 3 (large defect)
1 cm	detected by high SD value above the limit for small defects	detected by high SD value above the limit for medium defects	detected by high SD value above the limit for large defects
2 cm	detected by high SD value above the limit for small defects	detected by high SD value above the limit for medium defects	detected by high SD value above the limit for large defects
3 cm	detected by high SD value above the limit for small defects	detected by high SD value above the limit for small defects	detected by high SD value above the limit for large defects
4 cm	detected by high SD value above the limit for small defects	detected by high SD value above the limit for medium defects	Not detected within a distance of 19 mm from the crack location, but there is a high SD value above the limit for large defects, within 22 mm of the crack location
5 cm	detected by high SD value above the limit for small defects	detected by high SD value above the limit for small defects	Not detected with in a distance of 19 mm from the crack location, but there is a high SD value above the limit for large defects, within 31 mm of the crack location
6 cm	detected by high SD value above the limit for small defects	detected by high SD value above the limit for medium defects	Not detected
7 cm	detected by high SD value above the limit for small defects	detected by high SD value above the limit for small defects	Not detected
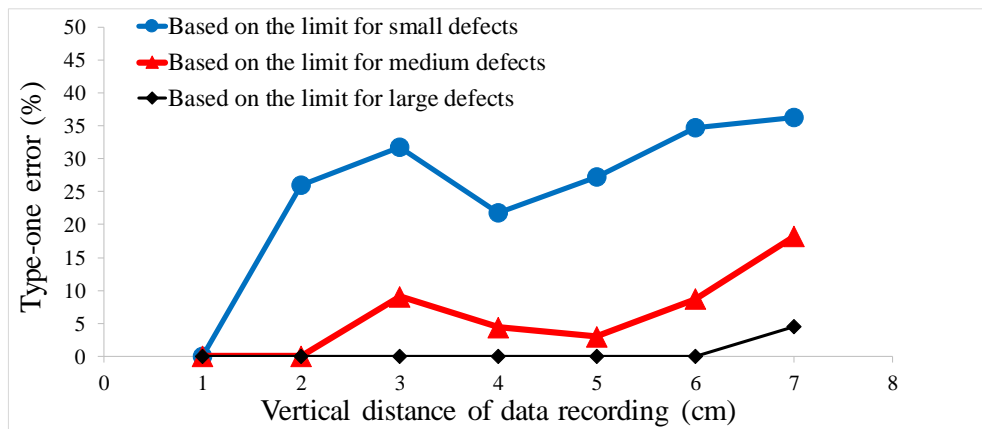
Figure 4.17. Type I error percentages in SG analysis approach for the defined thresholds at different data recording vertical distances.

4.5. Analysis of Y component magnetic flux density values

4.5.1. Rebars, each having three same-size cracks

To consider more information in detecting the defective locations, the Y component magnetic flux density data sets recorded in scans were also investigated. To select the most-consistent magnetic values, T-testing was conducted between every two Y component magnetic data sets, and the scans significantly equal to the greatest number of other scans were chosen for the rest of study. First,

the study focused on the magnetic data of rebars 1,2,3, and 4 recorded over the paths shown in Figure 4.1, pre-cracking and post-cracking. Figure 4.18 shows the selected Y component values of base and test data, after the data had been subjected to moving average smoothing, recorded over rebars 1 to 4. According to Figure 4.18, sudden shifts (a step-like trend) are observed in the magnetic values at the crack locations. These changes at defective locations are obvious in the magnetic data recorded over rebar 1 (a step-like trend shown by the dotted red line in Figure 4.18a). However, the step-like trend is less intense for rebar 2 due to its smaller cracks. Additionally, there is no detectable trend at defective locations for rebars 3 and 4.
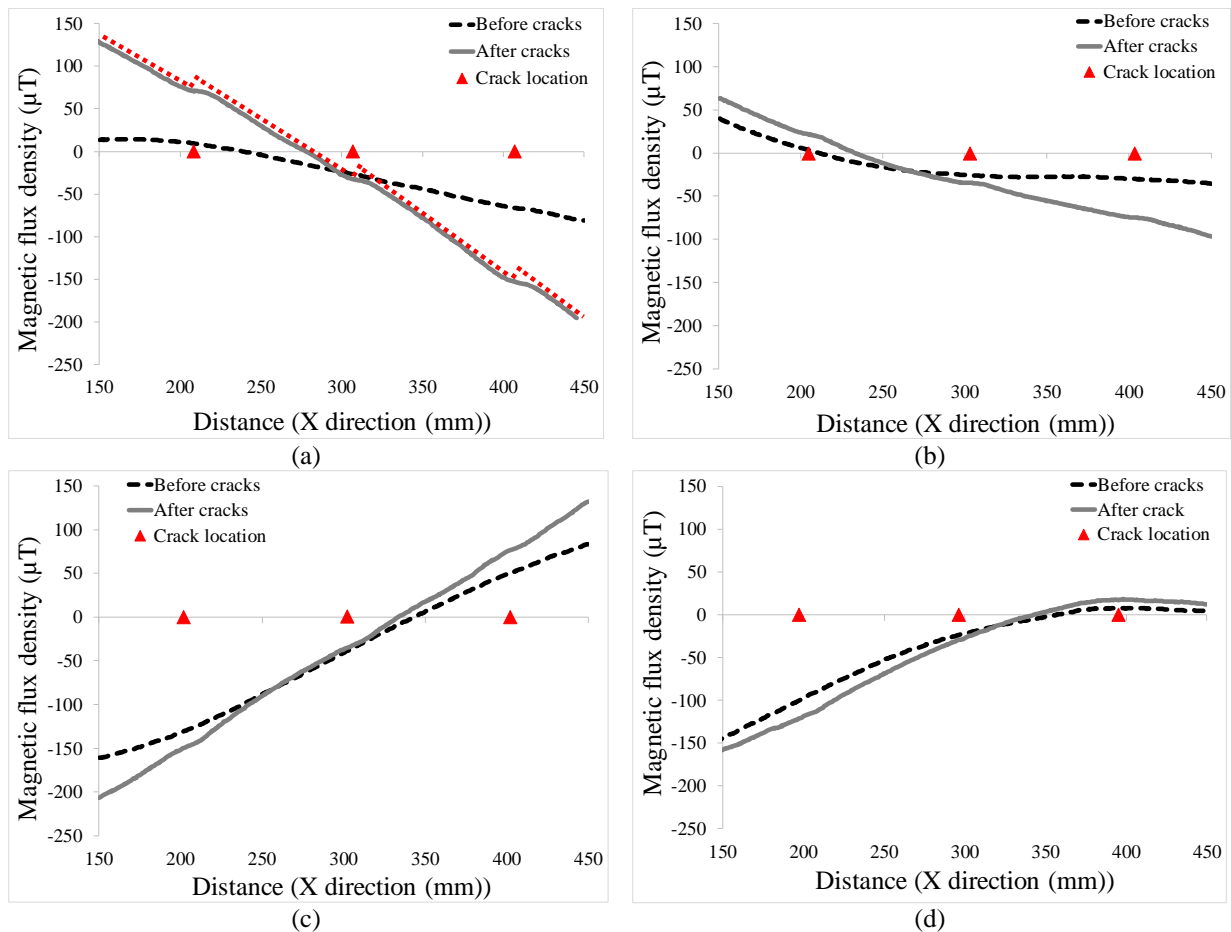
Figure 4.18. Y component magnetic flux density values recorded over paths shown in Figure 4.1, post- and pre-cracking: (a) Magnetic data recorded over rebar 1, (b) Magnetic data recorded over rebar 2, (c) Magnetic data recorded over rebar 3, (d) Magnetic data recorded over rebar 4.

To quantify the difference between the magnetic values before and after crack creation, the derivative of Y component values of base and test data were provided for every data set separately as prepared for the X component values (refer to section 4.4.1). In the prepared magnetic test data's derivative values recorded over rebars 1 and 2, a distinguishable pattern is observed at crack

locations, but no detectable pattern is shown for those values recorded over rebars 3 and 4 (Figure 4.19). In rebars 1 and 2, close to the cracks, the magnetic derivative's values in the test data slightly increase for a short distance and suddenly spike to their maximum (shown with green squares), then dip slightly, before decreasing to hover around base data values and continuing on. In the patterns echoing the defective areas in Figures 4.19a and 4.19b, the maximum points of the test data's derivative happen close to the crack locations.

To explore the relation between the pattern's characteristics and the crack sizes, the difference between the maximum magnetic values of test data and their corresponding values resulting from the base data were calculated for rebars 1 and 2 (shown by dotted blue double arrows in Figures 4.19a and 4.19b). Subsequently, box-and-whisker plots were generated separately for the length of dotted blue double arrows in the magnetic values related to rebars 1 and 2, and show no outlier. The mean values and the ranges (with a significance level of 0.1) for the lengths of the dotted blue double arrows in Figure 4.19 were calculated for rebars 1 and 2, separately (Figure 4.19). A regression line shows that the mean of the lengths of the dotted double blue arrows (the test data's derivative deviation from the base-data values), resulting from the Y-component-values' analysis, decrease as the mean of the defective area decreases. This regression line is strongly parallel to the regression line representing the X component test data's derivative deviation from the derivatives of the base data (Figure 4.21). This finding shows the consistency of the outcomes generated from X and Y component magnetic values recorded over the rebars.
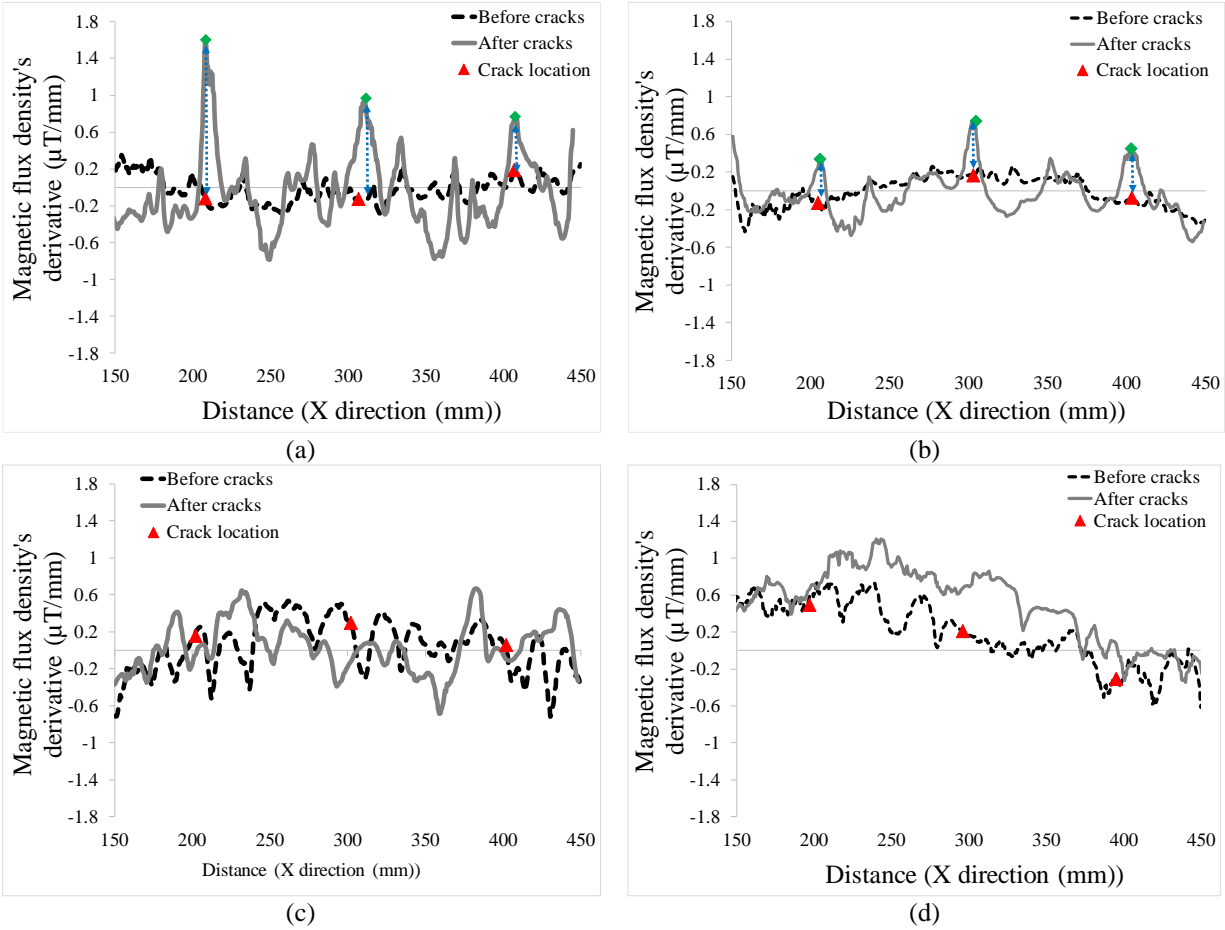
Figure 4.19. Signal processing for Y component magnetic data using the derivative values: (a) For magnetic data recorded over rebar 1, (b) For magnetic data recorded over rebar 2, (c) For magnetic data recorded over rebar 3, (d) Magnetic data recorded over rebar 4.

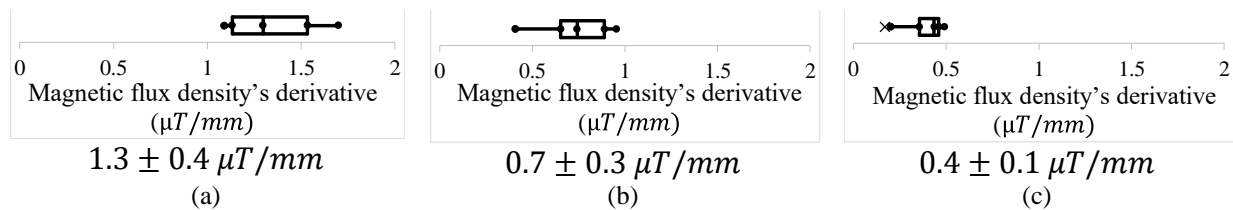$1.13 \pm 0.96 \, \mu T/mm$

(a)

$0.6 \pm 0.1 \, \mu T/mm$

(b)
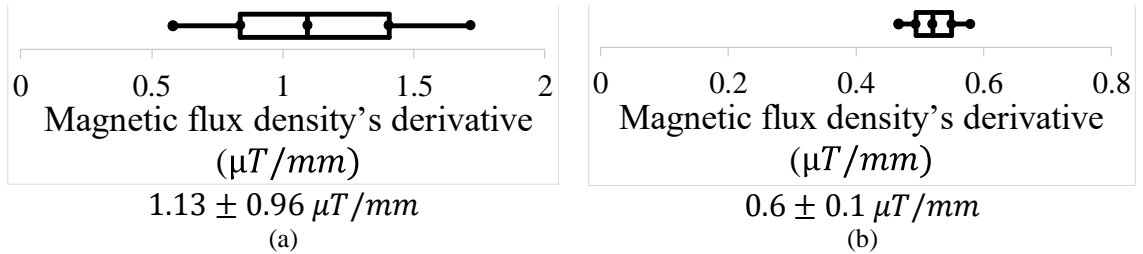
Figure 4.20. Box-and-whisker plots for the differences between the Y component magnetic values of test data at extremum points and their corresponding values resulting from the base data: (a) For magnetic data recorded over rebar 1, (b) For magnetic data recorded over rebar 2.
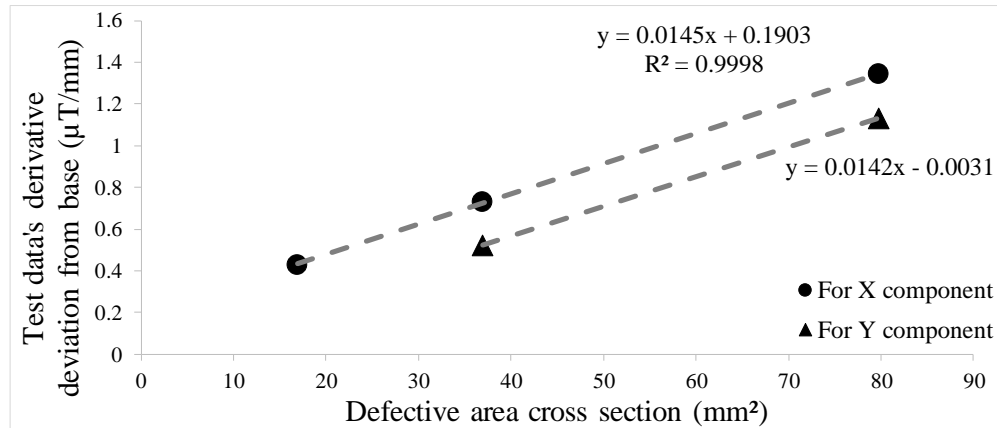
Figure 4.21. Relation between the X and Y components' magnetic derivative pattern's characteristics and crack sizes: X and Y components' test datas' derivative deviations from those of base data as the defective area increases.

4.5.1.1. Analyzing post-cracking data with absolute gradient values (AG)

There are detectable patterns in the Y component derivative values of test data at crack locations. To define specific criteria to categorize the defects based on the test data, the gradient values of test data's Y component were processed as similar to the X component ones (refer to section 4.4.1.1). Figure 4.22 shows the absolute values of Y component magnetic data's derivative for rebars 1 and 2, with clear local maximum points (green squares) close to the defect location. The values of the maximum points close to the defective locations were quantified by computing the upper and lower defect limits on magnetic data, separately for rebars 1 and 2 (Figure 4.22). These limits can guide us in classifying the magnetic properties based on the size of defects in rebars.

The defect limits for processed absolute gradient values of the Y component were calculated with a 95% confidence level, instead of the 90% used for calculating those limits for X component values. The 95% confidence level was used to obtain a narrower confidence band in order to decrease the number of Type I errors. However, some intact parts in rebars 1 and 2 are still indicated as defects (Type I errors) using the lower and upper limits in Figures 4.22a and 4.22b. Hence, Type I errors are more involved in the outcomes generated from the Y component of magnetic data than to those of the X component.
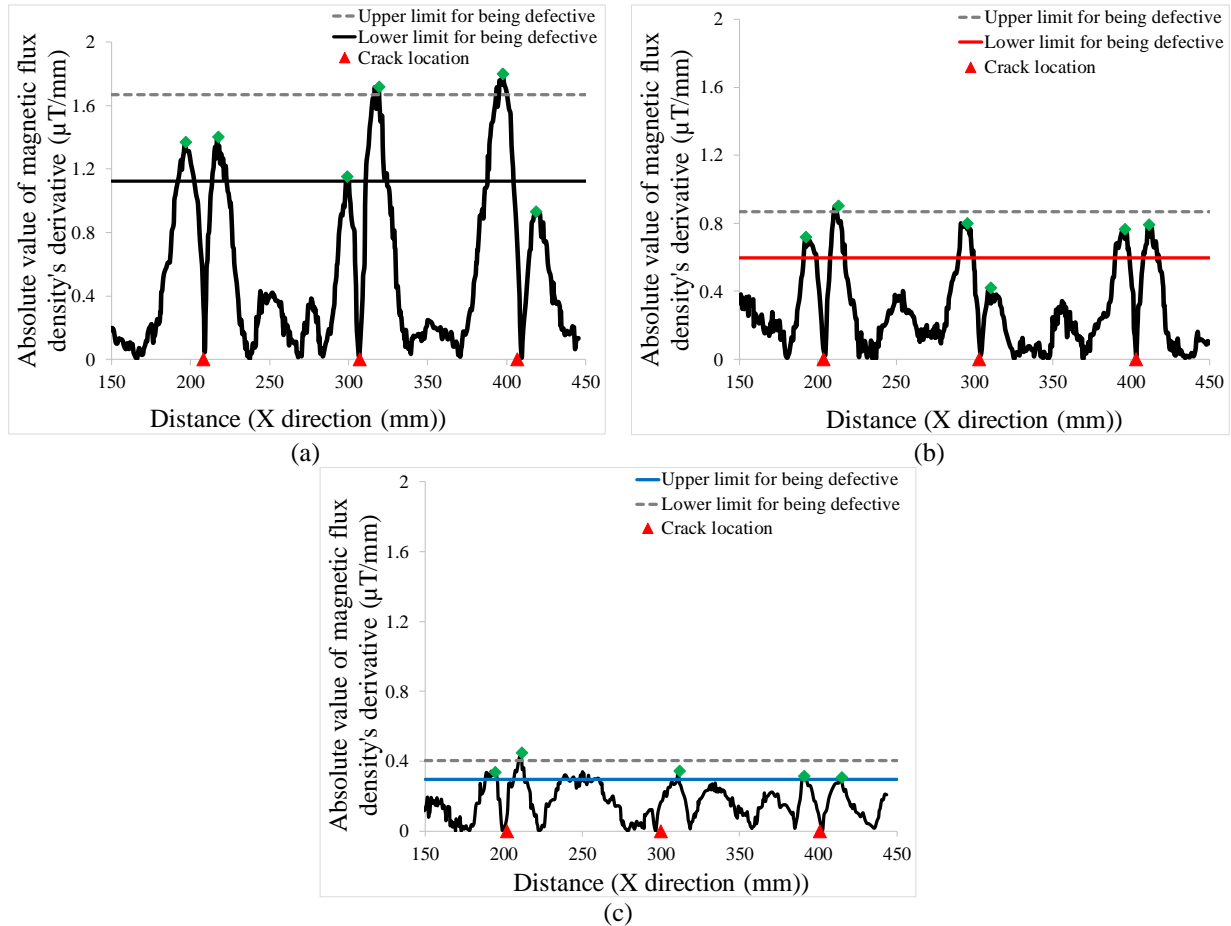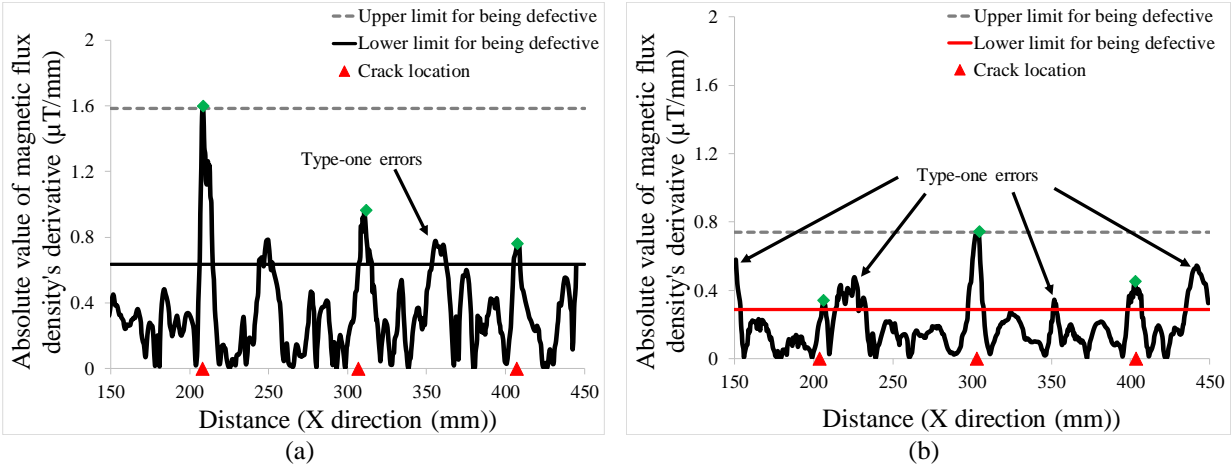
Figure 4.22. Y component magnetic data subjected by AG analysis approach: (a) For magnetic data recorded over rebar 1, (b) For magnetic data recorded over rebar 2.

4.5.1.2. Analyzing post-cracking data with the SD of gradient values (SG)

Figures 4.19a and 4.19b demonstrate sharp deviations in the derivative values of test data's Y component at the cracks in rebars 1 and 2. To detect the cracks' place and severity based on these deviations, the SD values of test data's Y component derivatives at equal intervals were calculated as done for those of the X component (refer to section 4.4.1.2). Figure 4.23 shows that the maximum SD values happen close to the defects. Using the maximum SD values within 19 mm of the defects, the upper and lower limits for defectiveness were calculated with a 90% confidence level.

A period of 19 mm was used, as it had been identified in the analysis of X component test data as the average distance of data affected by cracks. However, a 90% confidence level was applied to the calculations for limits of defectiveness, instead of the 95% confidence level that was used for the similar calculations for X component magnetic values. A lower confidence level was used in the calculations related to Y component magnetic values, to create a narrower confidence band and decrease the Type I errors. Nonetheless, there are high SD values, actually corresponding to intact sections of rebar, within the limits of defects (Figures 4.23a and 4.23b). These errors show the lower reliability of results based on the Y component of test data compared to those of the X component, which involved no Type I or Type II errors under similar data gathering and analysis procedures (refer to section 4.4.1.2).
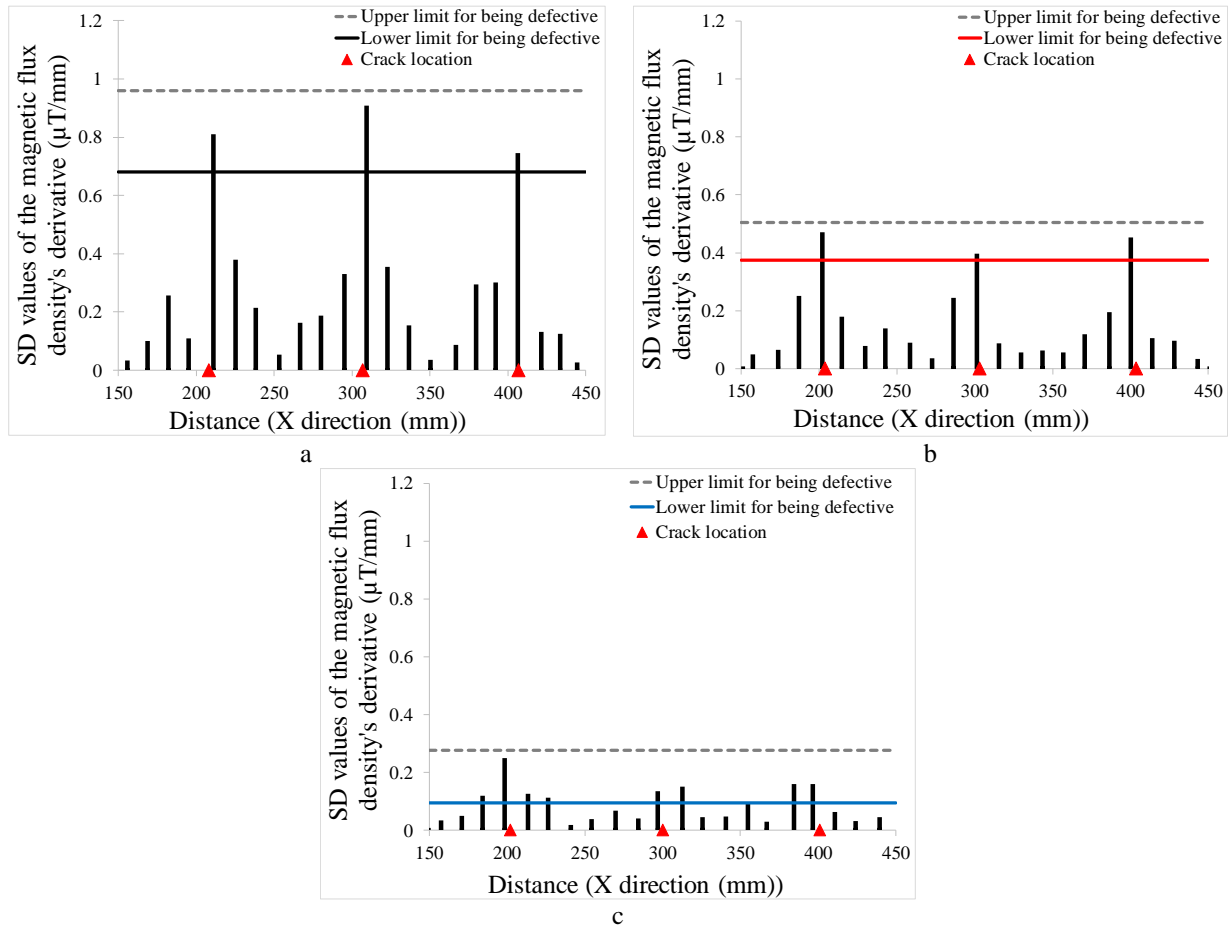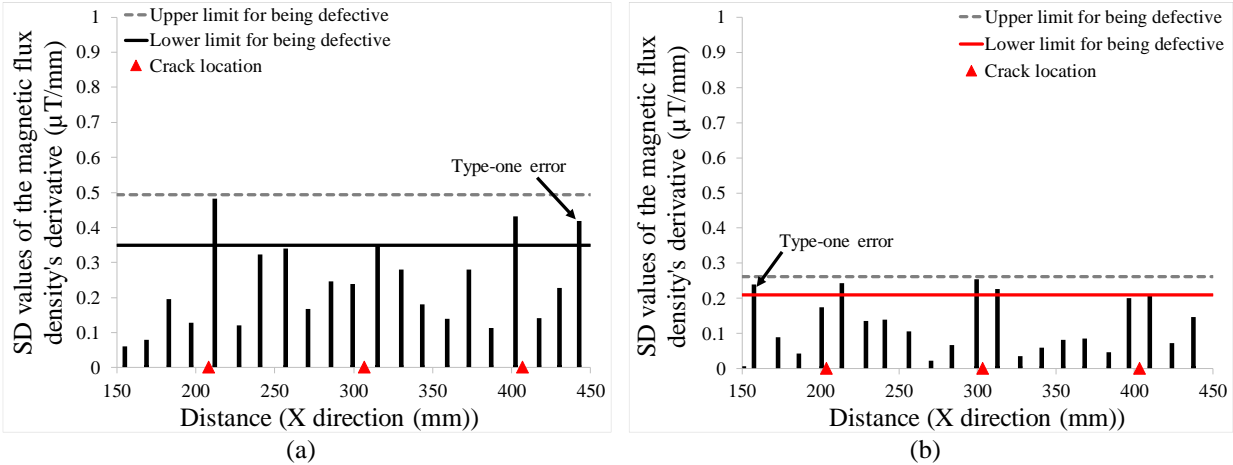
Figure 4.23. Y component magnetic data subjected by SG analysis approach: (a) For magnetic data recorded over rebar 1, (b) For magnetic data recorded over rebar 2.

4.5.2. Rebar with three non-similar cracks

The upper and lower limits of defectiveness on magnetic data defined based on AG and SG analyses are reviewed focusing on rebar 5's magnetic data. This test rebar represents actual rebars in concrete that have different non-similar cracks (Table 4-2). Section 4.2 discussed the specifications of rebar 5's cracks and their similarity with the cracks in the other rebars. Figure 4.24a shows the selected (using T-hypothesis testing) pre- and post-cracking Y component data sets of the scans conducted over rebar 5 along the path shown in Figure 4.1. The scans in Figure 4.24a are presented after deleting the first and last 150 mm of data, and subjection to moving average smoothing. In contrast to the results from magnetic data recorded over rebars 1 and 2, there is no recognizable difference between the post- and pre-cracking magnetic values, recorded over rebar 5.

For further review, the same preparation procedure used on the data in Figure 4.8 was separately applied on the Y component of the base and test data sets recorded over rebar 5. However, there was no recognizable pattern at defective location in the Y component test data's derivative values (Figure 4.24b). Additionally, AG and SG analyses were done on the test data recorded over rebar 5 at a vertical distance of 1 cm. Subsequently, the lower limits calculated based on magnetic data recorded over rebars 1 and 2, representing the threshold for medium and large defects (Table 4-9), were applied to the processed magnetic data recorded over rebar 5 (Figure 4.25). However, neither approaches detected the place nor the severity of the cracks in rebar 5.

Although the locations of medium and large defects (Table 4-9) were appropriately identified through the analysis of Y component magnetic values recorded over rebars 1 and 2, such defects were not detected using the same component of magnetic data recorded over rebar 5. This inconsistency was expected, based on the very low reliability of Y component magnetic flux density values, discussed in section 4.3.
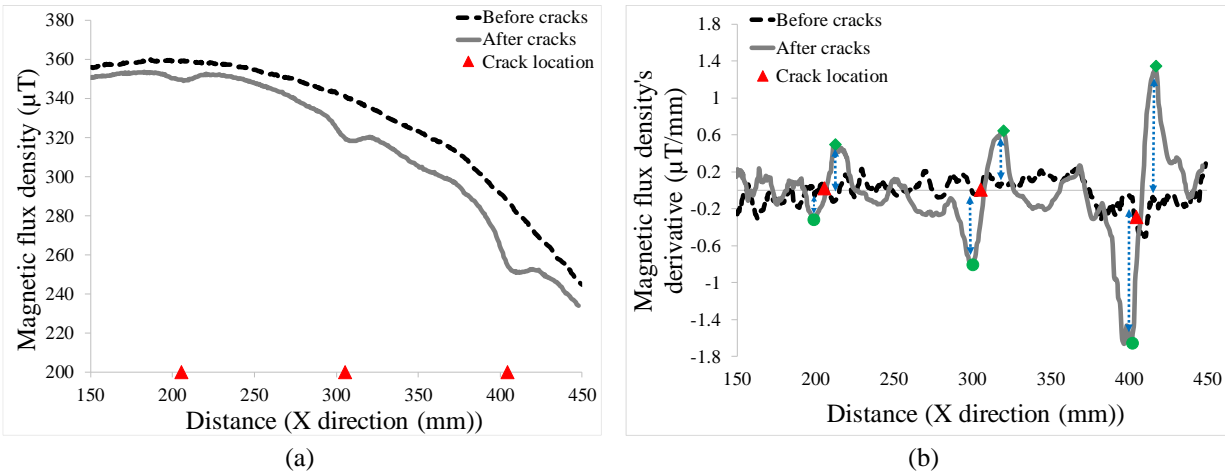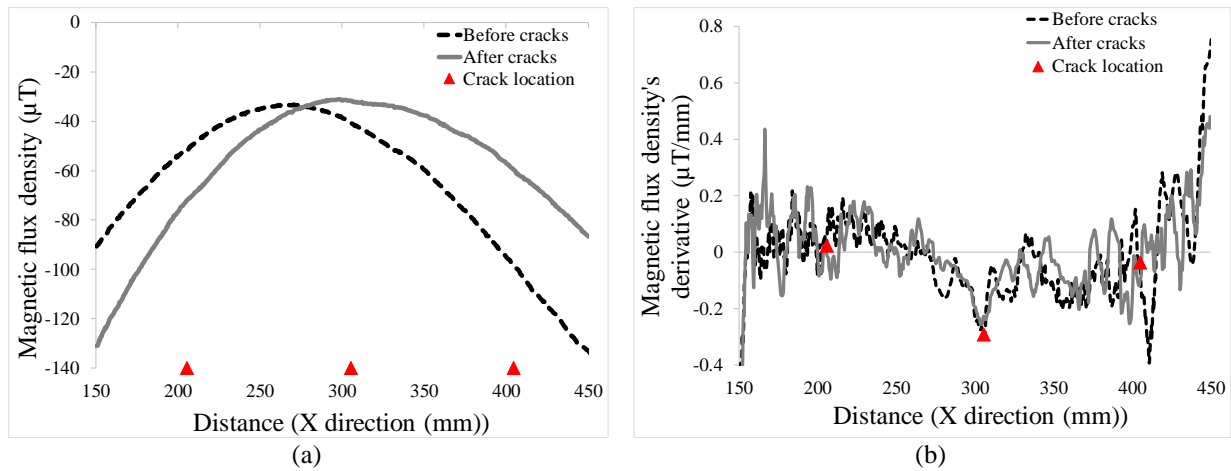

Figure 4.24. Y component values and the derivatives of Y component values of the magnetic data recorded over rebar 5: (a) Magnetic data recorded over the path shown in Figure 4.1, post- and pre-cracking, (b) Signal processing on magnetic data using the derivative values.
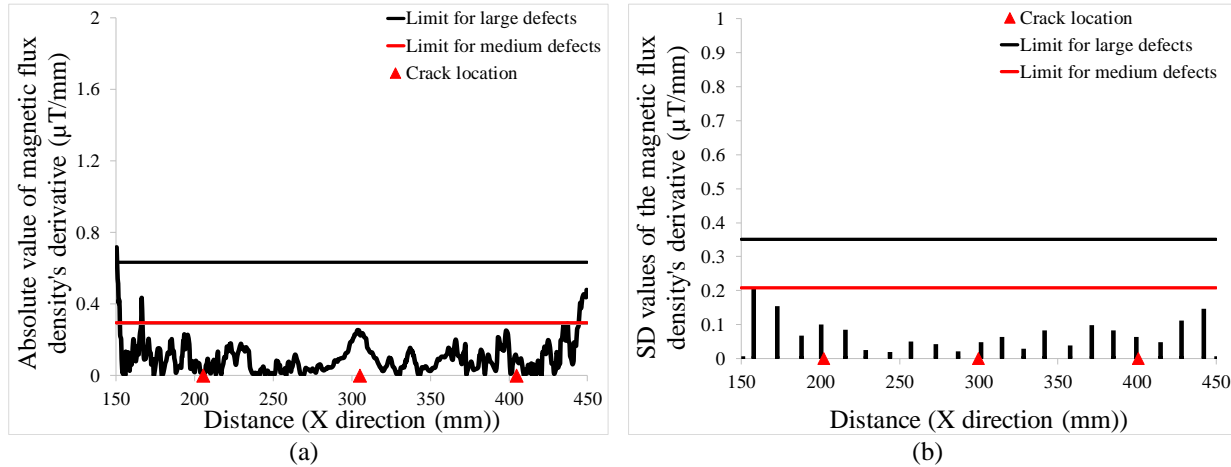
Figure 4.25. Applying analysis approaches on Y component magnetic data recorded over rebar 5: (a) Magnetic data subjected to AG analysis approaches, (b) Magnetic data subjected to SG analysis approaches.

4.6. Analysis of Z component magnetic flux density values

4.6.1. Rebars, each having three same-size cracks

In this section, the behaviors of Z component magnetic flux densities recorded over the rebars are reviewed. T-testing was conducted between every two Z component magnetic data sets, and the scans significantly equal to the greatest number of other scans were chosen as having the most

consistent magnetic values. Figure 4.26 shows the selected Z component values of base and test data recorded over rebars 1 to 4, after being subjected to moving average smoothing. There are slight irregularities in the magnetic values at the first and second cracks in rebar 1, and at the second crack in rebar 2 (dotted red lines rectangles in Figures 4.26a and 4.26b). However, there is no distinguishable behavior for the other cracks of rebar 1 and 2. There is also no detectable trend at defect locations in the magnetic data recorded over rebars 3 and 4.

To quantify the difference between the post- and pre-cracking magnetic values, the derivatives of the Z component values of base and test data were prepared for every data set separately (Figure 4.27), as was done for the X and Y component values (refer to sections 4.4.1 and 4.5.1). In the prepared test data's derivative values recorded over rebar 1, a pattern was observed at cracks 1 and 2 (Figure 4.27a). A similar pattern was also observed at the second crack in the test data's derivative values recorded over rebar 2 (Figure 4.27b). Approaching the mentioned cracks, the magnetic derivative's values in the test data slightly decrease for a short distance and reach a minimum point (shown with green squares). Next, there is a slight increase in the values of the test data's derivatives until they fluctuate closer to those of the base data and continue. Additionally, in the patterns related to defects, the minimum points of the test data's derivatives happen close to crack locations (Figures 4.27a and 4.27b).

To explore the relation between the pattern's characteristics and the cracks sizes, the difference between the minimum magnetic values of test data and their corresponding values resulting from the base data were calculated for rebars 1, and 2 (shown by dotted blue double arrows in Figures 4.27a and 4.27b). Since two and one values were obtained respectively for rebars 1 and 2, constructing box-and-whisker plots separately for each rebar so as to find the outliers was not logical. Hence, all the values for the lengths of dotted blue double arrows in Figures 4.27a and 4.27b were taken into consideration.

The mean values for the lengths of the dotted blue double arrows in Figures 4.27a were calculated for rebar 1. According to Figure 4.27b, there was only one value for rebar 2, and no need to take the average. A regression line shows that the mean of the lengths of the dotted blue double arrows (the test data's derivative deviation from the values of base data), resulting from Z component value analysis, decreases with a decrease in the mean of the defective area. However, the slope of this regression line is quite different from the slopes of the regression lines representing the X and

Y component test data's derivative deviation from the values of their base data (Figure 4.28). This finding shows the inconsistency between the outcomes generated from Z component magnetic values and those generated from X and Y components.
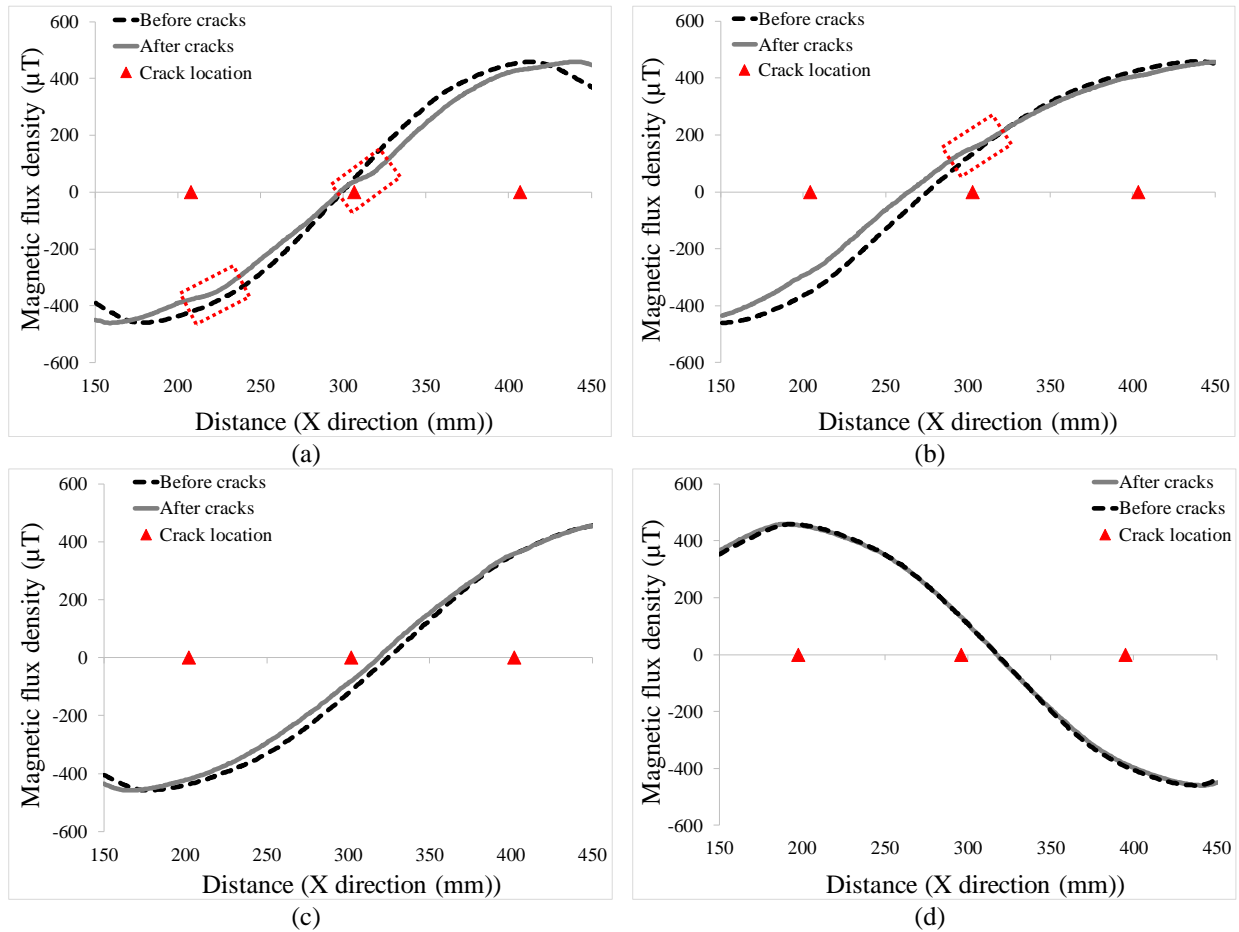
Figure 4.26. Z component magnetic flux density values recorded over paths shown in Figure 4.1, post- and pre-cracking: (a) Magnetic data recorded over rebar 1, (b) Magnetic data recorded over rebar 2, (c) Magnetic data recorded over rebar 3, (d) Magnetic data recorded over rebar 4.
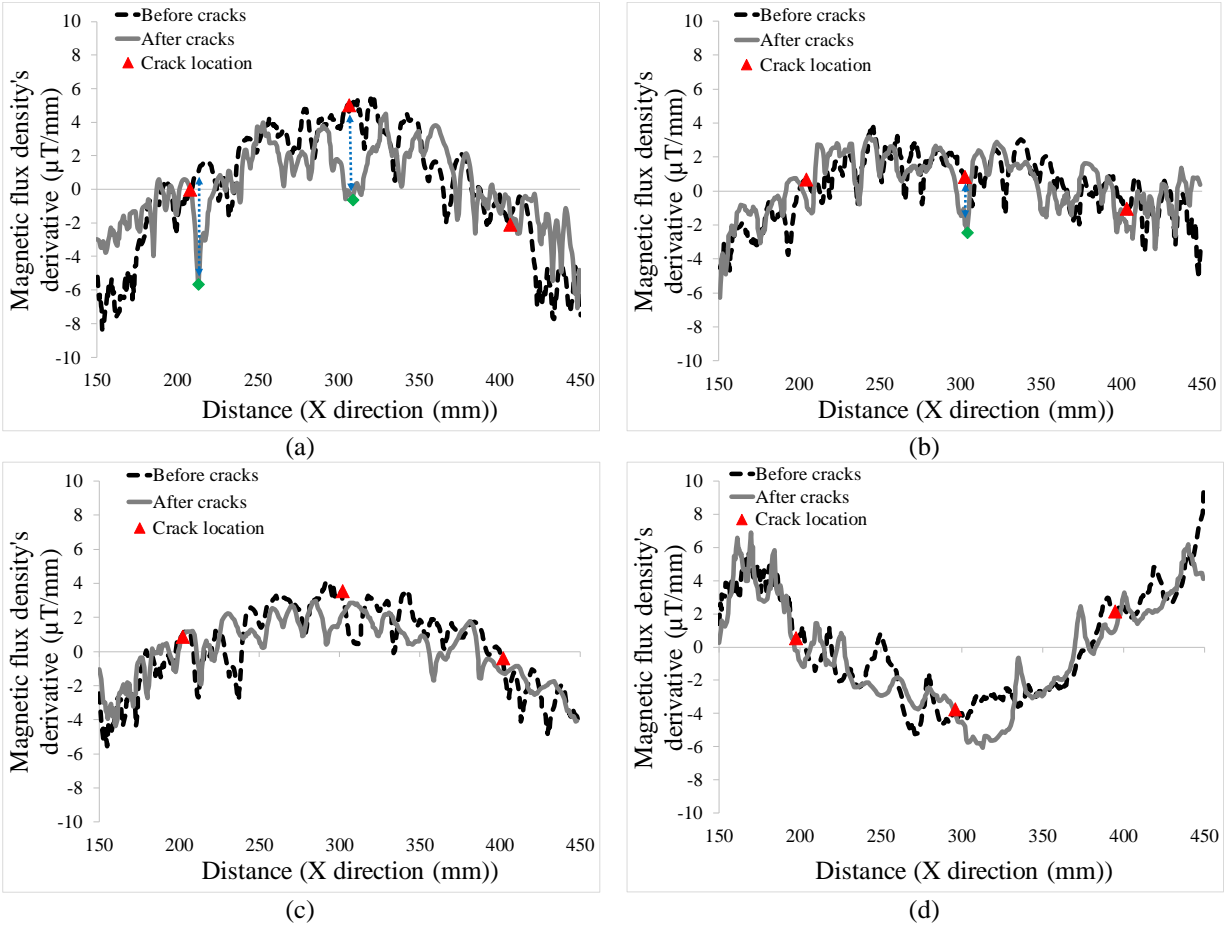
Figure 4.27. Signal processing for Z component magnetic data using the derivative values: (a) For magnetic data recorded over rebar 1, (b) For magnetic data recorded over rebar 2, (c) For magnetic data recorded over rebar 3, (d) Magnetic data recorded over rebar 4.
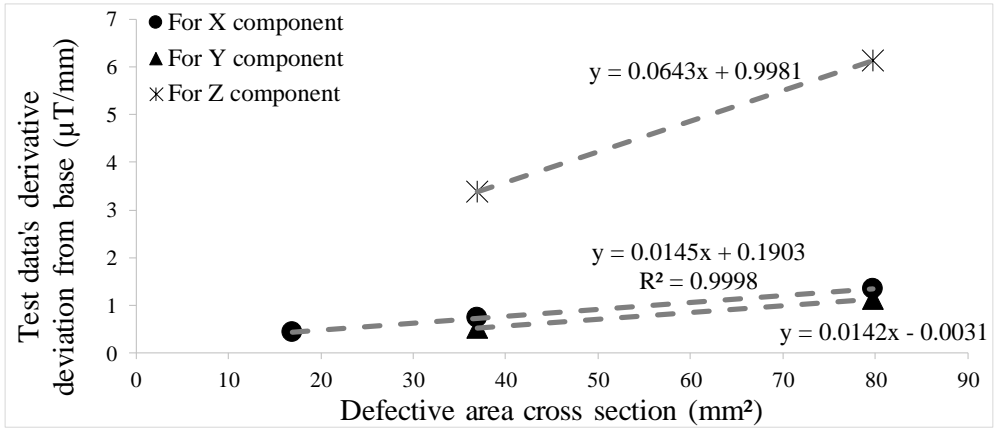
Figure 4.28. Relation between the X, Y, and Z components' magnetic derivative pattern characteristics and cracks sizes: X, Y, and Z components' test data's derivative deviations from those of base data as the defective area increases.

4.6.1.1. Analyzing post-cracking data with absolute gradient values (AG)

Patterns in the Z component derivative values of test data are detectable at the locations of only three cracks among the total cracks in rebars 1 and 2. To define specific criteria for categorizing defects based on the test data, the gradient values of test data's Z component were processed as done for those of X and Y components (as in sections 4.4.1.1 and 4.5.1.1). Figure 4.29 shows the absolute values of Z component magnetic data's derivatives for rebars 1 and 2. Clear local maximum points (green squares) do not occur close to all the three cracks identified in Figures 4.27a and 4.27b. According to Figure 4.29a, the magnetic values of the maximum points close to the identified defective locations (green square points) differ markedly from one another. Hence, computing the upper and lower defectiveness limits on magnetic data is not logical for rebars 1 and 2.

The difference between the magnetic values of the maximum points close to the identified cracks (cracks 1 and 2) in rebar 1, can be moderated through splitting the magnetic data in Figures 4.26a into smaller sections and removing the linear trend at every section. Another method for showing up the defect pattern is to remove the non-linear trend from the data in Figures 4.29a and 4.29b. However, these approaches are affected by certain parameters that must be changed based on the conditions of every dataset, and so they cannot be used uniformly under all conditions. Hence, conducting these approaches are in contrast with the effort in this study which is pursuing the consistency within all the analysis methods used on every dataset.

(a)   (b)
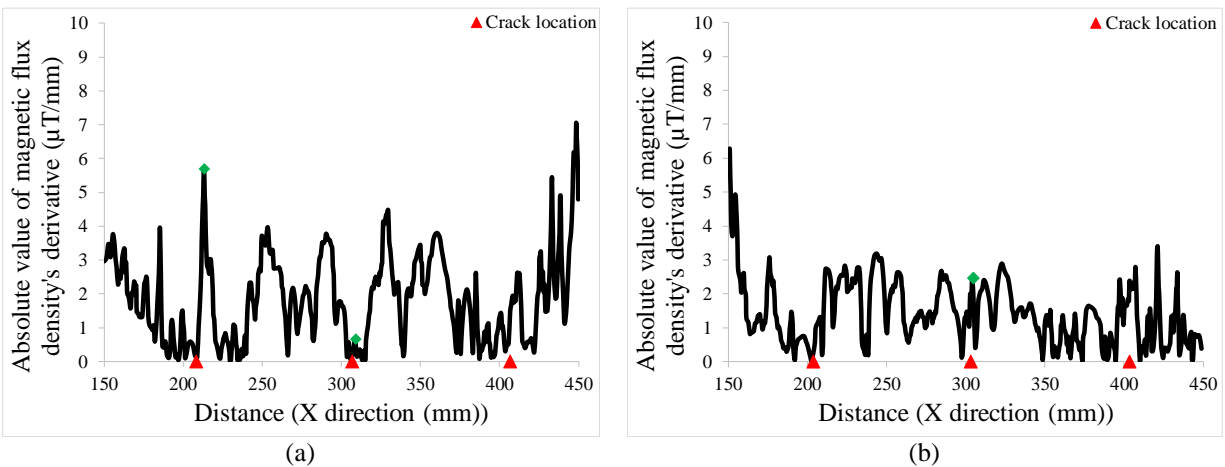
Figure 4.29. Z component magnetic data subjected by AG analysis approach: (a) For magnetic data recorded over rebar 1; (b) For magnetic data recorded over rebar 2.

4.6.1.2. Analyzing post-cracking data with the SD of gradient values (SG)

Figures 4.27a and 4.27b demonstrated sharp irregularities in the Z component derivative values of test data at the locations of only three cracks of the total cracks in rebars 1 and 2 (cracks 1 and 2 in rebar 1; crack 2 in rebar 2). To detect crack locations and severity based on these deviations, the SD values of the test data's Z component derivatives at equal sections were calculated as was done for those of X and Y components (refer to sections 4.4.1.2 and 4.5.1.2). However, according to Figures 4.30a and 4.30b, the highest SD values do not always occur close to defects, and different SD values are randomly located at different distances. Therefore, no specific arrangement is observed in the magnetic data that could help in detecting defects and their severity.
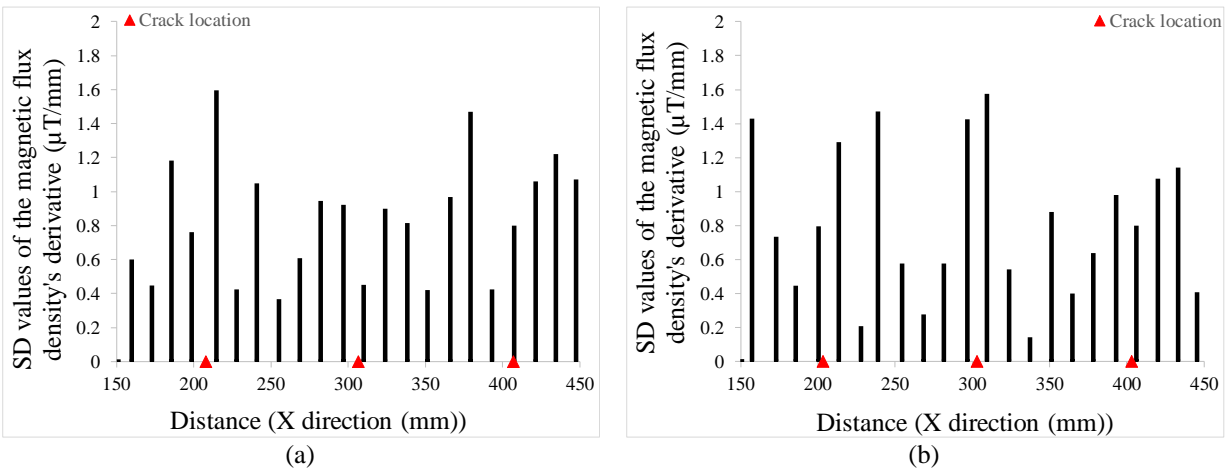
Figure 4.30. Z component magnetic data subjected to SG analysis approach: (a) For magnetic data recorded over rebar 1, (b) For magnetic data recorded over rebar 2.

4.6.2. Rebar with three non-similar cracks

To confirm the results obtained from the analysis of Z component magnetic flux density values recorded over rebars 1 and 2, the results relating to rebar 5 (shown in Figure 4.1) are next discussed. The selected (using T-hypothesis testing), pre- and post-cracking Z component values of the scans conducted over rebar 5 are shown in Figure 4.31a. These values are presented after deleting the first and last 150 mm of data, and subjecting them to moving average smoothing. As seen in Figure 4.31a there is no recognizable difference between post- and pre-cracking magnetic values recorded over rebar 5. For further review, the same preparation procedure used in presenting the data in Figure 4.8 was separately applied on the base and test Z component datasets for rebar 5. However, no recognizable pattern occurred over the defect locations in the Z component test data's derivative values for rebar 5 (Figure 4.31b). AG and SG analyses were then conducted on the test data

recorded over rebar 5, but no specific behaviour was observed to help in distinguishing the defect specifications (Figure 4.32). Consequently, according to the results obtained from the data recorded over all rebars, taking the Z component magnetic flux density values into consideration for finding crack specifications is unreliable.

(a)   (b)
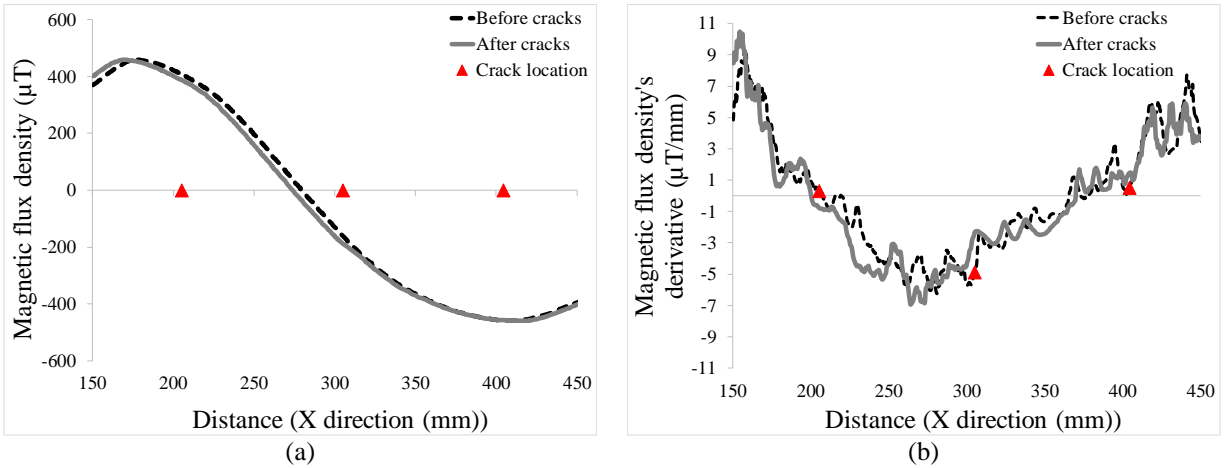
Figure 4.31. Z component values and the derivatives of Z component values of the magnetic data recorded over rebar 5: (a) Magnetic data recorded over the path shown in Figure 4.1, post- and pre-cracking, (b) Signal processing on magnetic data using the derivative values.

(a)   (b)
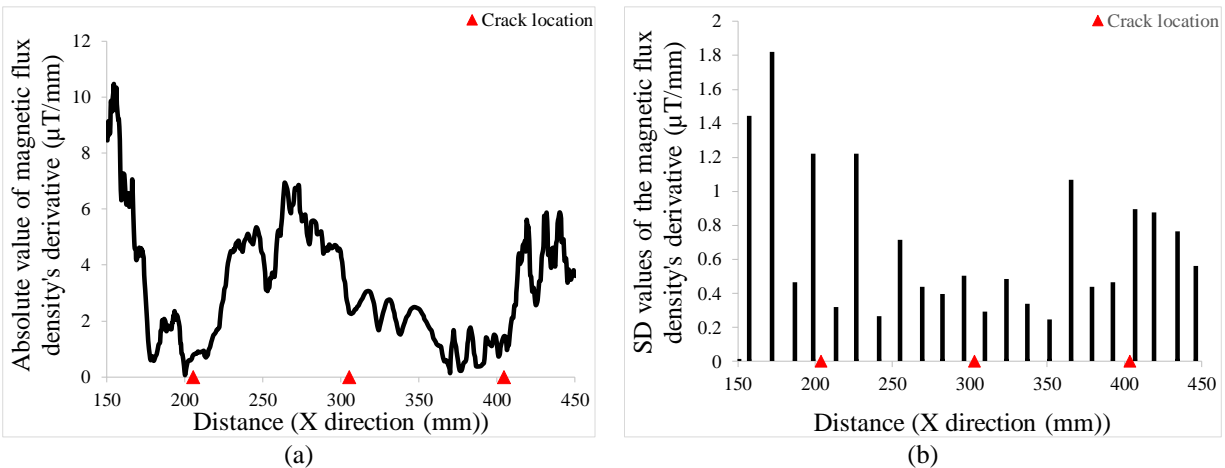
Figure 4.32. Applying analysis approaches on Z component magnetic data recorded over rebar 5: (a) Magnetic data subjected to AG analysis approaches, (b) Magnetic data subjected to SG analysis approaches.

4.7. Numerical simulation

Numerical simulation was conducted separately on four equal 120 mm sections of rebar with the specifications plotted in Figure 4.3. Section 1 had no transverse crack; section 2 had a transverse crack the same as crack 1 in rebar 5 (the small defect in Table 4-4); section 3 had a transverse crack the same as crack 2 in rebar 5 (the medium defect in Table 4-4); section 4 had a transverse crack the same as crack 3 in rebar 5 (the large defect in Table 4-4). The solid rebar sections were

113

separately simulated via COMSOL® software version 5.3a (COMSOL Group, Stockholm, Sweden) with regard to the Earth's magnetic field.

The Earth's magnetic field varies somewhat over time and location. To obtain consistent and realistic results, the PMI scanner was positioned as it would be for the scanning (at the same location that experiments were conducted), then left stationary for 400 seconds before the rebars were put in place. Different components of the local magnetic fields (consisting of the Earth's magnetic field and other external sources of magnetic fields) were recorded in keeping with the inspection path and direction used in the experiments. The mean values of the recorded data were used in the simulations to achieve more-accurate magnetic property values. The mean values of the background's magnetic fields were calculated as 15.508 µT, -24.469 µT, and 33.471 µT for the components X, Y, and Z, respectively (Figure 4.33). However, the magnetic conditions of ferromagnetic materials are affected by the Earth's magnetic field from the time of their formation, so discrepancies are expected between the outcomes of the simulations and similar experimental results.
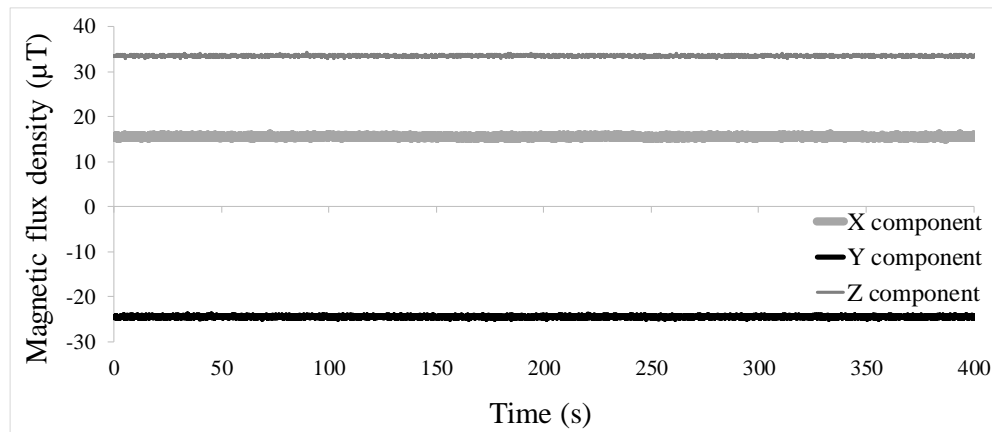
Figure 4.33. Components of local magnetic field recorded to use in numerical simulation.

So that the simulation considered the local magnetic field, the rebar sections were separately (one by one) located in a 140 mm × 45 mm × 45 mm cubic space that included the magnetic field calculated from Figure 4.33. Next, very fine tetrahedral constant meshing specifications (Table 4-12) were applied on the rebar and box as a combined system, separately, for the simulations of each section. As a representative, the final meshing configuration of the system including rebar section 4 is presented in Figure 4.34. It should be mentioned that to increase the number of nodes (obtain more data) at defect locations, the edges of the cracks were rounded to a radius of 0.5 mm. Carrying out simulations with these specifications led to graphical representations of each section

114

(Figure 4.34), showing the irregular behavior of the X component magnetic flux density at the location of cracks in Figures 4.35b, 4.35c, and 4.35d.

Table 4-12. Mesh specifications used in the simulations.

Maximum element size	1 mm
Minimum element size	0.4 mm
Maximum element growth rate	1.45
Curvature factor	0.35
Resolution of narrow regions	0.82
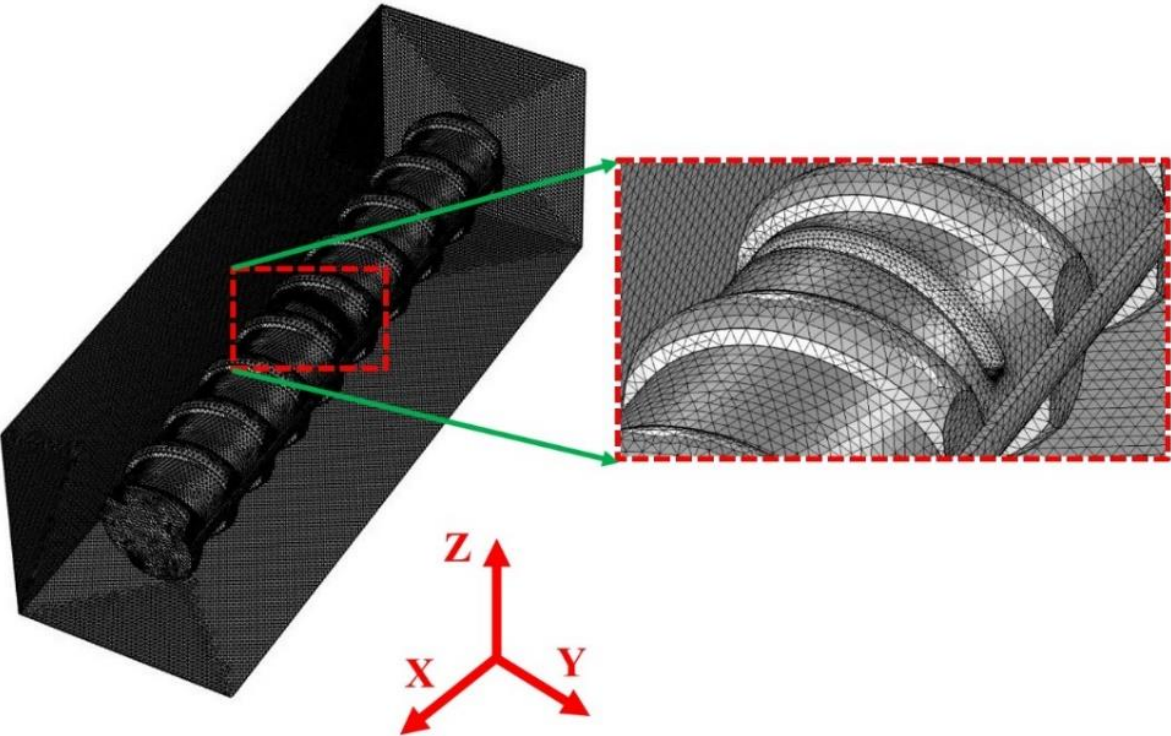
Figure 4.34. Defective rebar placed in box including Earth's magnetic field (combined system after meshing).
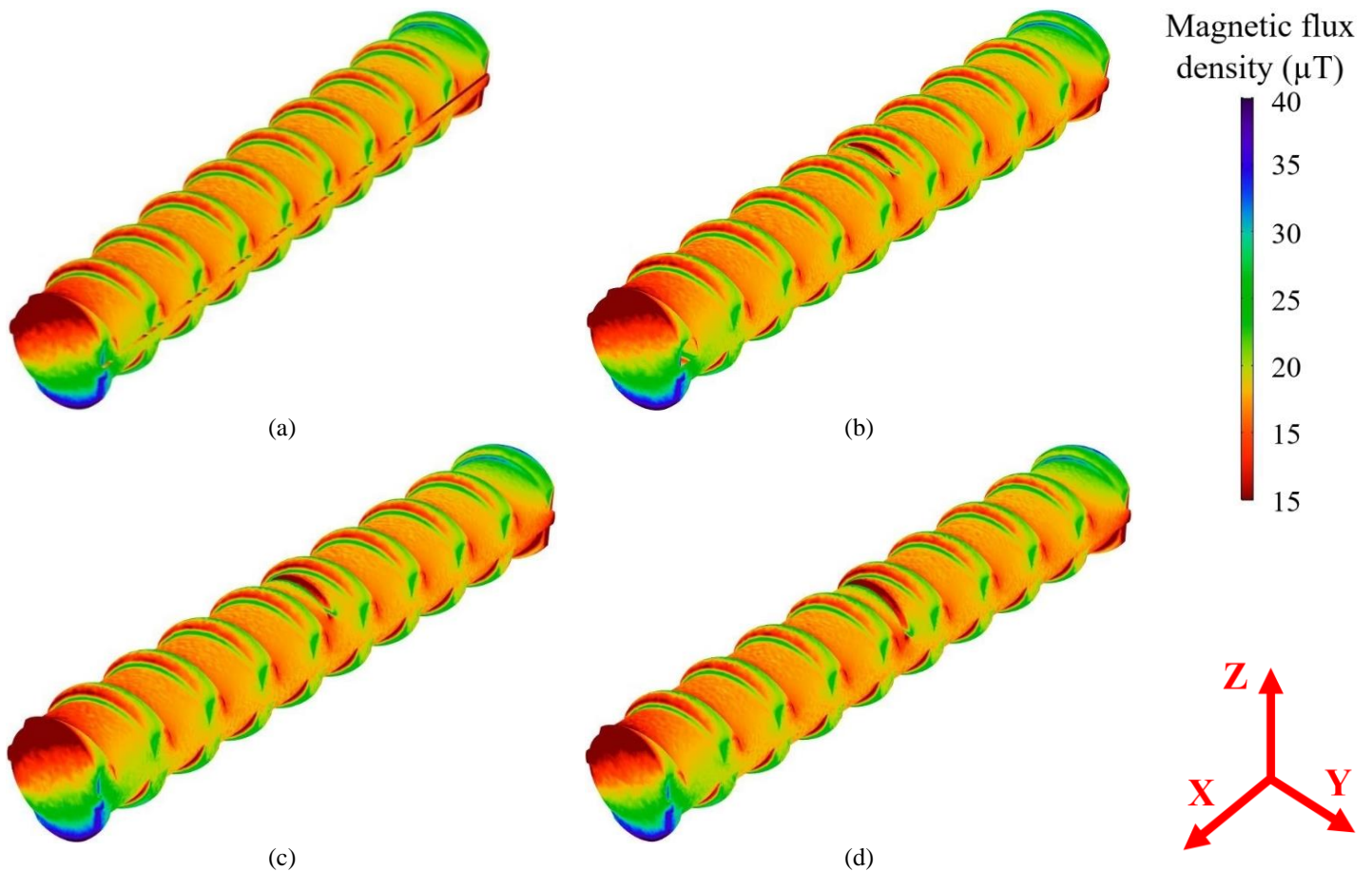
Figure 4.35. Behaviour of X component magnetic flux density on the surfaces of rebars: (a) With no crack, (b) With a small crack, (c) With a medium crack, (d) With a large crack.

4.8. Comparison between simulation and experimental results

As seen in Figure 4.35, the extents of the irregularities increase when the crack sizes increases. The irregularities show up as lower magnetic flux density values (red color) than neighboring ones, in accordance with the experimental results. For a more-detailed comparison of the simulation results of all rebar sections with the outcomes generated from experiments, magnetic data were separately recorded over the rebar sections shown in Figure 4.35. The values of the X component magnetic flux density were recorded for the X direction of the rebar sections (i.e., a path similar to those shown in Figure 4.1), to facilitate comparison of the simulation results and the experimental ones. Figure 4.36 shows the magnetic data recorded over all sections shown in Figure 4.35, for the distance of 35 mm on either side of cracks in the solid rebars. The magnetic values recorded over the different sections are almost equal to each other in the initial distances. However, approaching the cracks, the magnetic values recorded over different rebar sections start to deviate from each other. Additionally, the local minimums of the data sets, close to the cracks (the section

116

shown by dotted green line circle), have lower values for solid rebars that have larger defects. In other words, a more-intense dip is observed close to cracks, from rebar section 1 to rebar section 4, as the defective area increases. Observing more-intense dips, as defective area increases, is in agreement with the results obtained experimentally.
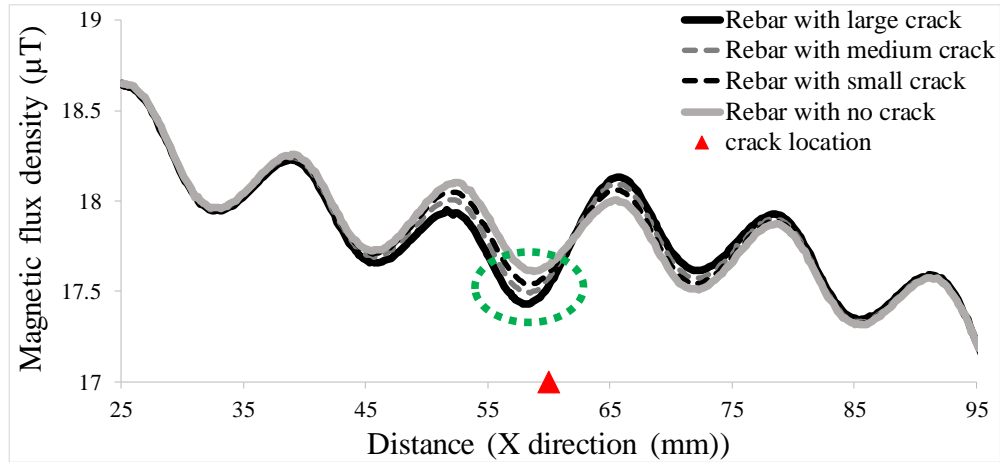
Figure 4.36. X component values of four separate scans recorded over the sections shown in Figure 4.34.

To explore the simulation results in more detail, AG analysis approach was applied on each data set separately. Figure 4.37 shows the absolute values of the magnetic data's derivative for solid rebar sections 1, 2, 3, and 4 with clear extrema (green squares) close to the defective locations. The maximum absolute values of magnetic-data derivatives increase as the crack sizes increase, which is in agreement with the experimental results. The difference between the magnetic data recorded over different rebar sections were quantified by calculating the deviation of the test data sets' derivative maximum values (green squares) from that of the base data (blue circle). Figure 4.38 shows that as the defective area increases, the test data's derivative maximum values deviations from that of base data increases. This finding is in accordance with the related experimental outcomes. However, the slope of the regression line in Figure 4.37 is remarkably less than that of the regression line found based on experimentally (Figure 4.10a). This higher slope in the results generated from experiments was expected due to the residual stress remaining from the time of crack creation using a hand saw.
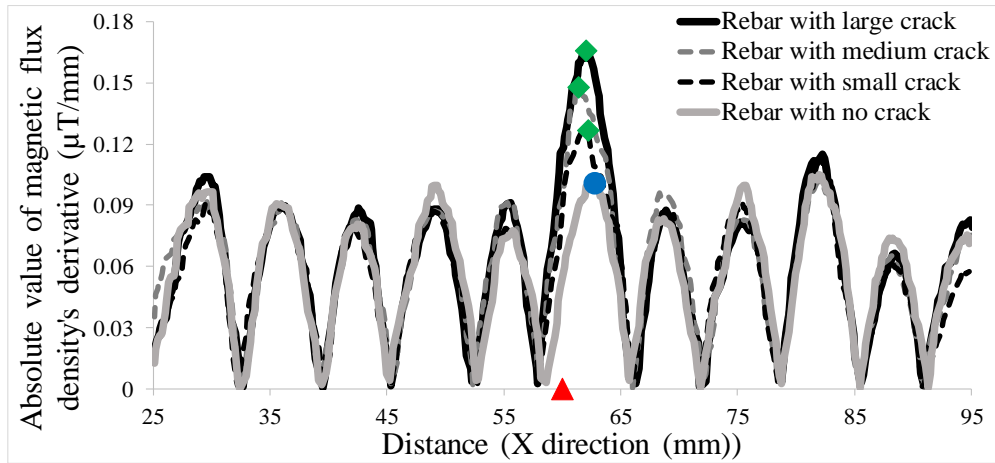
Figure 4.37. Magnetic data set, shown in Figure 4.35, subjected to AG analysis.
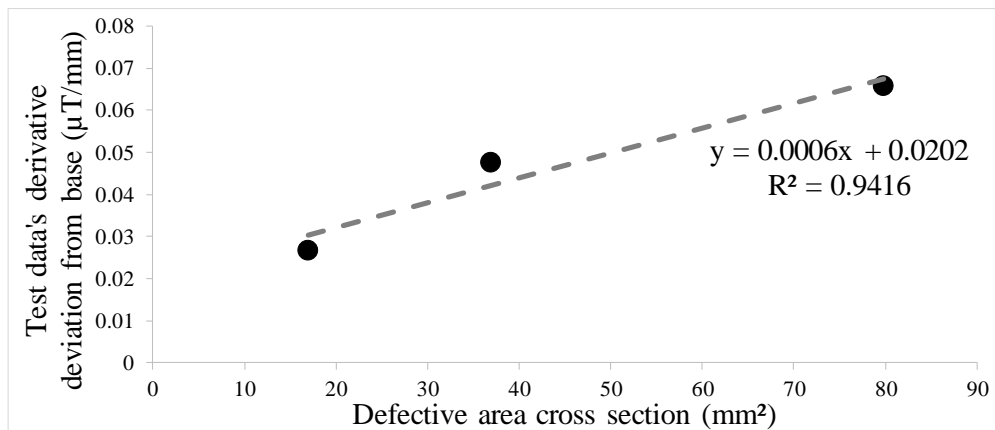
Figure 4.38. Simulation results showing X component test data's derivative deviations from those of base data with increase in the defective area.

4.9. Conclusion

Detecting and categorizing defects in rebars helps in providing an accurate schedule for maintenance activities, thus mitigating the risk of future infrastructure failures or unexpected deterioration of serviceability. To this end, investigations were conducted on five 20 mm diameter steel rebars of the same lengths of 600 mm, each having three transverse cracks. The specifications of the three cracks were similar to one another in rebars 1, 2, 3, and 4. Additionally, the crack sizes, in order from rebar 1 to 4, went from greatest to smallest. However, rebar 5's cracks were of different sizes: one crack significantly the same as the cracks in rebar 1 (referred to as large defects), one significantly the same as the cracks in rebar 2 (referred to as medium defects), and one significantly the same as the cracks in rebar 3 (referred to as small defects).

The rebars were placed one by one with the same orientation and at the same non-magnetic location, post- and pre-cracking. Once in place, each was scanned along its whole length using the

PMI scanner, over the same specific paths. For convenience, the magnetic data recorded pre-cracking was called the base data, and the magnetic data recorded post-cracking was called the test data. The intent was to study the consistency of the magnetic-value patterns at the crack locations and to establish a reliable threshold for magnetic data to use in detecting and categorizing the defects based on their physical size. There were substantial differences between the behaviours of magnetic values recorded over the rebars post- and pre-cracking. Specific irregularities were observed in the direction and values of magnetic data at crack locations. The magnetic behaviors of similar ferromagnetic defective rebars were also simulated with a finite element-based software, considering the background Earth's magnetic field. The results were in accordance with the experimental outcomes.

Investigations were carried out on three components of the magnetic flux density values. According to the experimental results, taking the Z component magnetic flux density values into consideration for finding crack specifications was unreliable. Additionally, findings indicated the lower reliability of results based on the Y component of magnetic data compared to those of the X component. Considering the most reliable results, generated from the investigations on the X component magnetic flux density values, the following findings were concluded:

- Magnetic data values recorded in the experiments represent obvious irregularities, showing up as dips, at the crack locations. These dips at crack locations become less intense as the defective area decreases;
- According to the experiments, a specific pattern occurs in the magnetic data's derivative values at the crack locations. The pattern shape and its characteristics are as follows:
  - Approaching a crack location, the magnetic data's derivative values slightly decrease for a short distance and reach a minimum value. Next, there is a sharp increase in the test data's derivative values, followed by an intersection with the base data's derivative values, before they reach a maximum value. Subsequently, there is again a slight decrease for a short distance in the test-data's derivative values until they approach those of the base data and continue. In the created pattern, the intersection points of the test and base data's derivative values are very close to the crack locations;
  - Test data's derivative values' deviation from those of base data at extremum points (close to cracks) increases when the defective area increases;

119

- The distances between the test data's derivative maximum and minimum values at crack locations do not noticeably change when the cracks' sizes increase. The distances between the local extrema at crack locations are constant and generally close to 19 mm;

- With respect to the experimental results, magnetic data analysed by SG and AG approaches showed clear extrema within 19 mm either side of the defect locations. Additionally, the cracks' places and sizes can be detected on the AG and SG processed test data by applying specific percentile rank values as thresholds:
  - In the SG processed test data set: the 0.46, 0.85, and 0.97 percentile ranks are the thresholds confirmed to indicate the small, medium, and large defects;
  - In AG processed test data set: the 0.7, 0.87, and 0.95 percentile ranks are the thresholds confirmed to indicate the small, medium, and large defects;

- Similar to the experimental outcomes, simulation results show a pattern at the defective area, with a dip in the magnetic values close to the cracks. In other words, magnetic flux density values at the location of cracks were lower than neighboring ones. Additionally, a more-intense dip was observed close to cracks as the defective area increased;

- The behaviour of magnetic data subjected to AG analysis at the defective area, generated from the simulation, was also similar to that of the magnetic data from the experiments. The processed magnetic data in the simulation showed local maximum values close to the defective locations. The maximum absolute values increased as the crack sizes increased.

Chapter 5: Self-magnetic behaviors of a non-corroded and a corroded reinforcement element

The contents of this chapter are reflective of an original manuscript published in the journal of NDT & E International.

Author Contributions: Conceptualization, M.M., S.M., and M.B.D.; Data curation, M.M.; Formal analysis, M.M.; Funding acquisition, M.B.D.; Investigation, M.M.; Methodology, M.M., and S.M.; Supervision, M.B.D.; Writing—original draft, M.M.; Writing—review & editing, M.M., S.M., M.B.D., and Ph.V.

5.1. Introduction

Rebar corrosion in concrete is an electrochemical process; corrosion outcomes can be grouped into two categories based on the mechanical changes of the rebar and concrete: local corrosion (pitting) and general corrosion (Perkins, 2000). Both pitting and general corrosion are considered threats to the serviceability of RC structures; their adverse consequences can be predicted based on parameters such as cover depth, moisture content, salt content, stray currents, and microbial activity (Mackechnie and Alexander, 2001). Local corrosion reduces the rebar cross-sectional area at pitting locations, but with no significant (visible) internal strain on the structure. However, general corrosion results in corrosion-product formation, which leads to expansion and tensile stress in the concrete, causing cracking and spalling (Zhao *et al.*, 2011). Additionally, cracks and corrosion-product formation cause deterioration of the rebar/concrete bond, which reduces the load capacity of the structure (Zhao *et al.*, 2011).

The previous three chapters investigated the self-magnetic properties of rebars with local defects. To continue the technical development of PMI with respect to general corrosion, the current chapter studies the experiments and simulations conducted on two ferromagnetic rebars, one intact and one with general corrosion (with a metal loss of 14.3%). First, the rebars are scanned by a 3D laser scanner. The point cloud data thus obtained are used to simulate their geometry using a finite-element-based software (COMSOL® software version 5.3a - COMSOL Group, Stockholm, Sweden). Simulations are also carried out under the effects of Earth's magnetic field, similar to those conducted by Mosharafi *et al.* (2018). Magnetic data for the two rebars are extracted through

the COMSOL® outputs and compared. Next, (Self-Magnetic Flux Leakage) SMFL data are recorded through the experiment, using PMI, and the test results are compared with the simulations results (Figure 5.1). In other words, a forward simulation is compared with actual laboratory measurements.
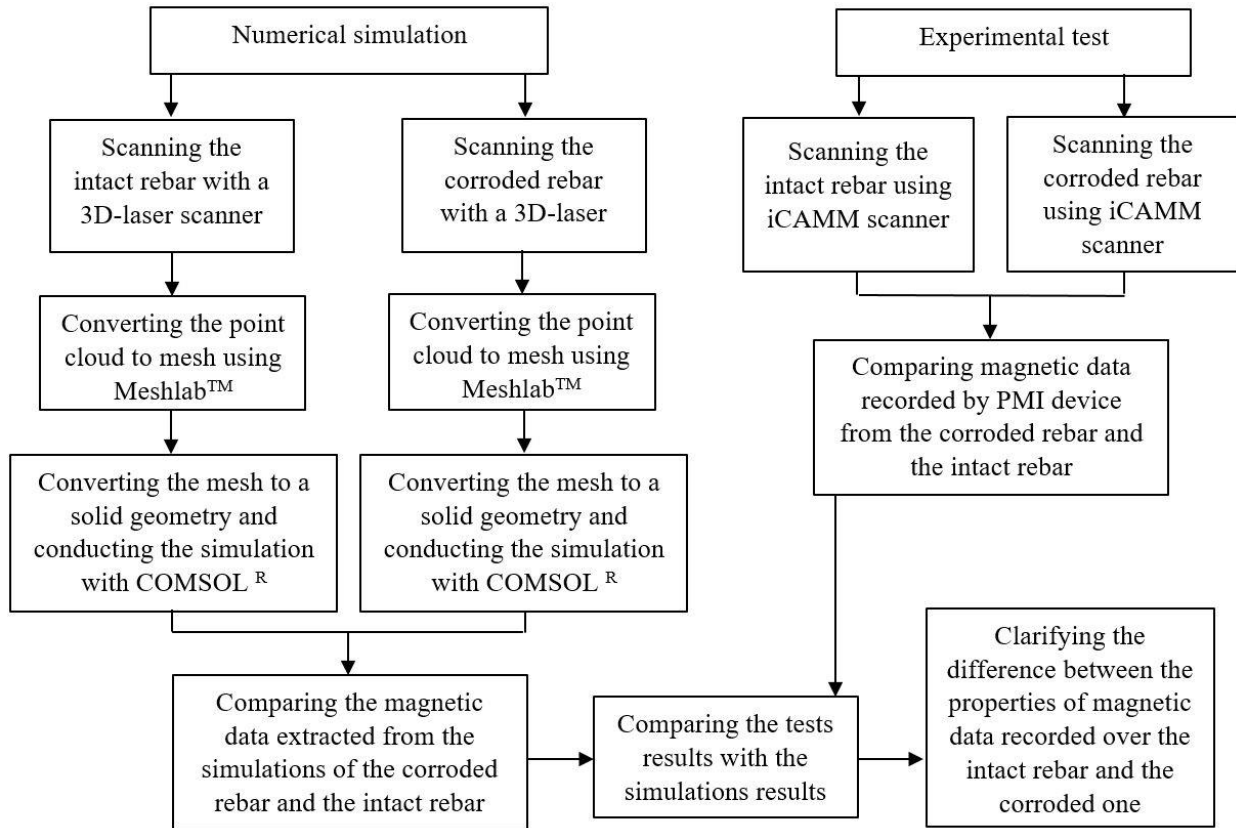
Figure 5.1. Methodology flowchart, showing the sequence of the experimental and numerical processes.

5.2. Simulations

The surfaces of two low-carbon steel rebars (Figure 5.2) with 8 mm radius – one intact (with a length of 553 mm) and the other, corroded (with a length of 532 mm) – were scanned using a high-resolution 3D laser scanner (FARO LS 840 HE) (Nahangi and Haas, 2014). The scanned results as a point cloud were then converted to a numerical mesh by MeshLab V1.3.2 ("Meshlab," 2017). The resulting mesh was imported to COMSOL® software version 5.3a (COMSOL Group, Stockholm, Sweden) and converted to a surface and solid, respectively (Figure 5.3a & Figure 5.3b). Then, 365.77 mm of intact and 365.48 mm of corroded rebars were simulated via COMSOL® software under the influence of the Earth's magnetic field ("Natural Resources Canada," 2017). A relative magnetic permeability of 75 was used for the rebars' simulations, based

on previously reported values for the relative magnetic permeability of low-carbon steels (Rose *et al.*, 1995; Ribichini, 2011).
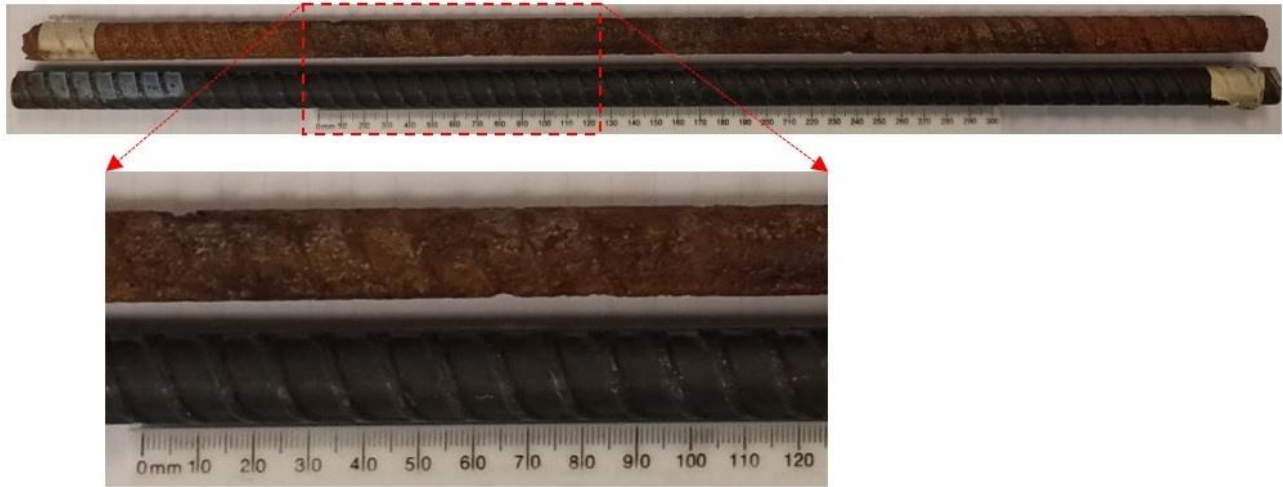
Figure 5.2. Low-carbon steel corroded and intact rebars.
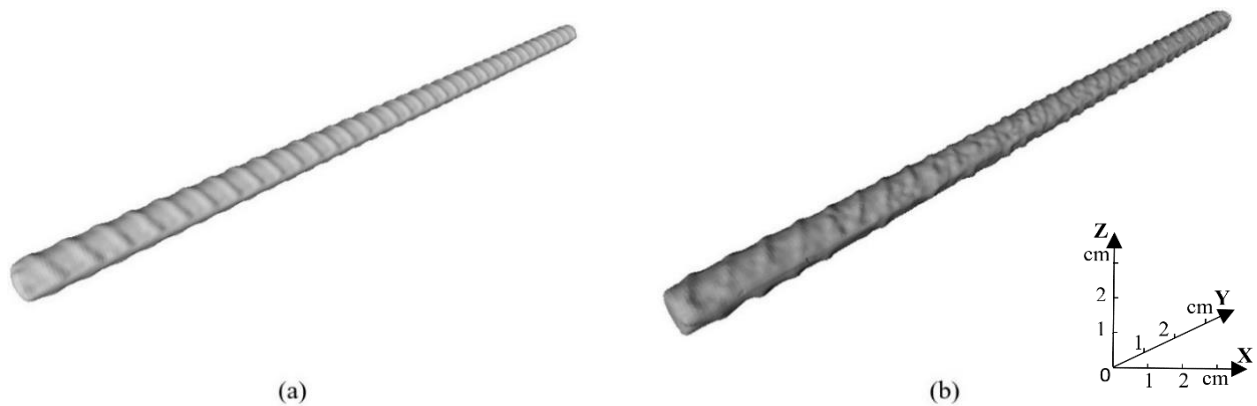
Figure 5.3. Solid illustration of rebars: (a) Intact rebar, (b) Corroded rebar.

Because Earth's magnetic field varies with time and location, the annual averages for the various components at the specific location of the experiments (Waterloo region, Ontario, Canada) were considered in the simulations ("Natural Resources Canada," 2017). The averages of the Earth's magnetic fields (from August of 2016 to August of 2017) were estimated as 14.64 (A/m), -2.49 (A/m), and 40.26 (A/m) for the X, Y, and Z components, respectively. However, magnetic conditions of ferromagnetic materials are affected by Earth's magnetic field from the time of their formation. The magnetic behavior of such materials is also affected by other external magnetic sources (Li *et al.*, 2017). Thus, discrepancies are expected between the outcomes of the simulations and geometrically similar experimental outcomes.

The magnetic-behavior simulation of rebars was begun by placing them in a cubic space (a virtual box) (Mosharafi *et al.*, 2018) with dimensions of $100 \times 140 \times 410$ mm, using the appropriate Earth's magnetic field values to reflect real conditions. Additionally, for appropriate control of simulation parameters, the box and rebar were meshed separately through tetrahedral meshes and applied finally in the simulation process, in what the software terms a union form (a combined one). The simulations for both the corroded and the intact rebars started with the initial mesh properties (rebar mesh #1 and box mesh #1 in Table 5-1 & Table 5-2). Then, more accurate element specifications (Table 5-1 & Table 5-2) were implemented to make the outcomes independent of the meshing parameters.

Table 5-1. Mesh specifications of rebar, with the fixed mesh specifications of box mesh #1, and mesh specifications of the box, with the fixed mesh specifications of rebar mesh #11 (for the intact rebar).

Rebar mesh #	Maximum element size (mm)	Minimum element size (mm)	Number of degrees of freedom	Box Mesh #	Maximum element size (mm)	Minimum element size (mm)	Number of degrees of freedom
1	2.5	1.4	433506	1	8	4.1	11621899
2	2.3	1.2	478369	2	7.9	3.8	11849679
3	2	1	578678	3	7.8	3.6	12140071
4	1.5	0.8	950776	4	7.71	3.2	12373031
5	1.34	0.67	1201120	5	7.3	2.8	12501870
6	1	0.5	2368787	6	6.82	2.3	12659466
7	0.89	0.44	3172992	7	6.5	1.9	12924371
8	0.6	0.3	9115613	8	6.1	1.6	13113933
9	0.57	0.28	10515947	9	5.81	1.4	13460773
10	0.56	0.278	11053065	10	5.1	1.3	14434104
11	0.55	0.27	11621899	11	4.11	1.1	15681794
12	0.53	0.24	12898612	12	2.84	0.85	20482253
13	0.5	0.2	15192730	13	2.51	0.84	23299639
14	0.46	0.16	19249760	14	2.25	0.82	26326445
15	0.41	0.1	26763917	15	2.21	0.815	27422793

Table 5-2. Mesh specifications of rebar, with the fixed mesh specifications of box mesh #1, and mesh specifications of the box, with the fixed mesh specifications of rebar mesh #10 (for the corroded rebar).

Rebar mesh #	Maximum element size (mm)	Minimum element size (mm)	Number of degrees of freedom	Box Mesh #	Maximum element size (mm)	Minimum element size (mm)	Number of degrees of freedom
1	2.5	1.4	419950	1	8	4.1	9585920
2	2.3	1.2	461838	2	7.9	3.8	9790481
3	2	1	554134	3	7.8	3.6	10052437
4	1.5	0.8	895844	4	7.71	3.2	10264693
5	1.4	0.75	1026195	5	7.3	2.8	10383543
6	1.34	0.67	1123125	6	6.82	2.23	10526231
7	1	0.5	2188615	7	6.5	1.9	10772781
8	0.89	0.44	2922169	8	6.1	1.6	10962113
9	0.6	0.3	8317283	9	5.81	1.4	11274447
10	0.57	0.28	9585920	10	5.1	1.3	12178630
11	0.56	0.278	10063717	11	4.11	1.1	13390187
12	0.55	0.27	10586562	12	2.84	0.85	18063568
13	0.54	0.26	11140628	13	2.21	0.815	24927363
				14	2.19	0.81	25746972
				15	2.185	0.805	26461257

The values of the Y magnetic flux density were recorded for the Y direction of the rebar (i.e., the path parallel to the rebar's length). This path runs one millimeter above the surface of the rebar (i.e., 9 mm from its center) and extends from one end (Line A) to the other end (Line D) of the box (Figure 5.4). Subsequently, the minimum values of the Y component magnetic flux density (as a representative value) from 9.8 mm to 355.8 mm of the intact rebar, and from 10.74 mm to 355.69 mm of the corroded rebar, were extracted to verify the convergence of the simulations' outcomes (the edge effects and background magnetic data were ignored).
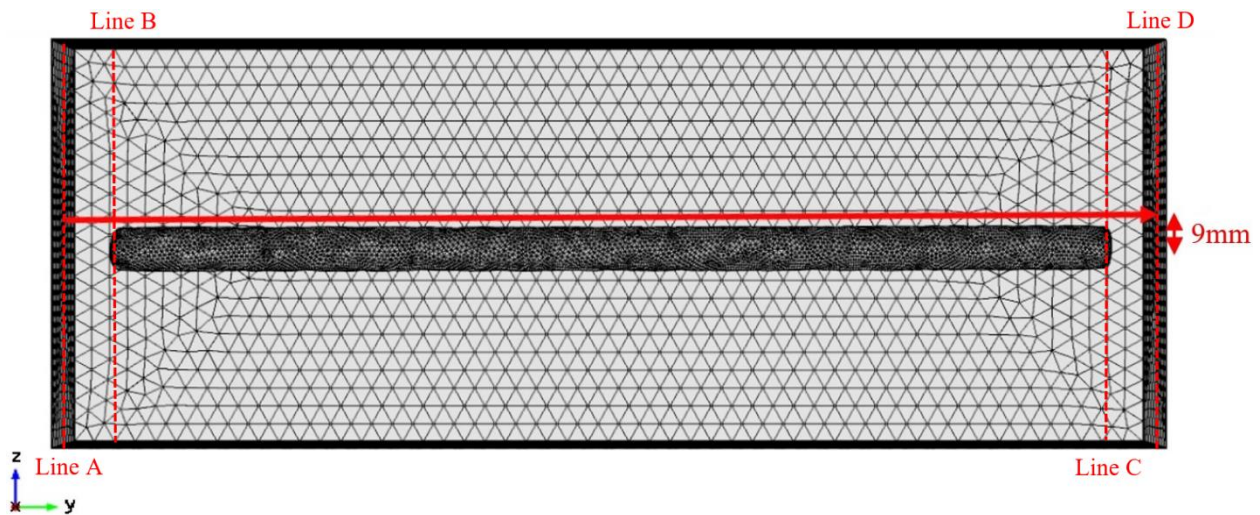
Figure 5.4. Path of data recording (with a vertical distance of 9 mm from the center of rebar).

Outcome convergence was done for the intact and corroded rebar simulations in two steps: for the mesh specifications of the rebar, and for the mesh specifications of the box. Values of minimum magnetic flux densities became stable at rebar meshes #11 and #10 for the intact and corroded rebars, respectively (Figure 5.5a & Figure 5.6a). Hence, the results obtained with these mesh numbers were used to continue the convergence process for the boxes. Next, considering the fixed mesh specifications of the rebar that were used, more accurate mesh specifications were applied to the box. It was found that the minimum magnetic flux density in the Y component stabilized at box meshes #9 and #11 for the intact and corroded rebar simulations, respectively (Figure 5.5b & Figure 5.6b).

(a)

(b)
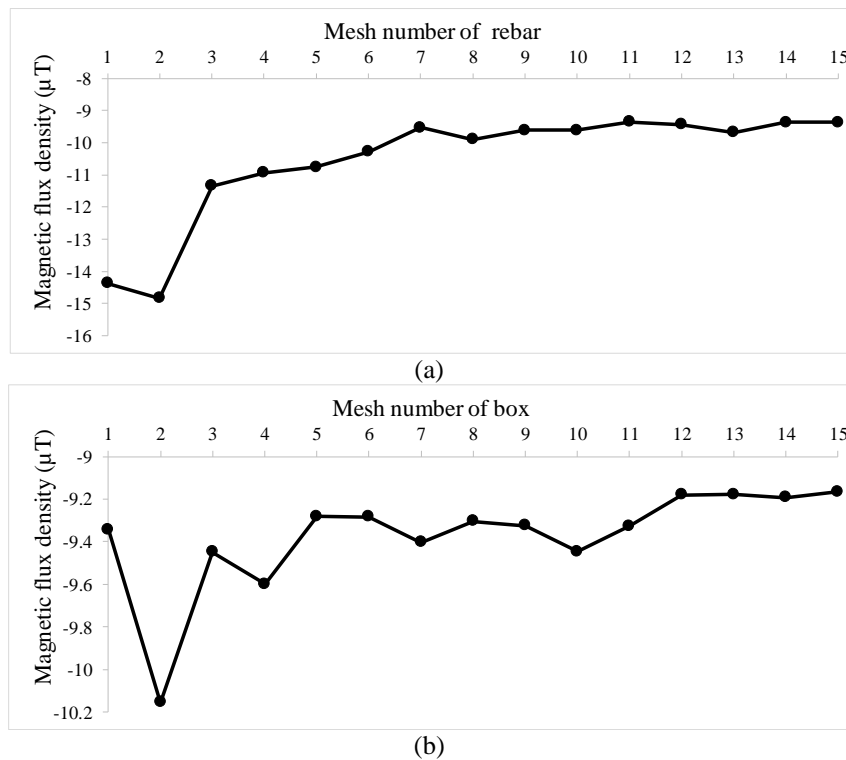
Figure 5.5. Minimum values of Y component magnetic flux density of intact rebar, from Line B to Line C: (a) Different meshing specifications of rebar with fixed box mesh #1, (b) Different meshing specifications of the box with fixed rebar mesh #11.
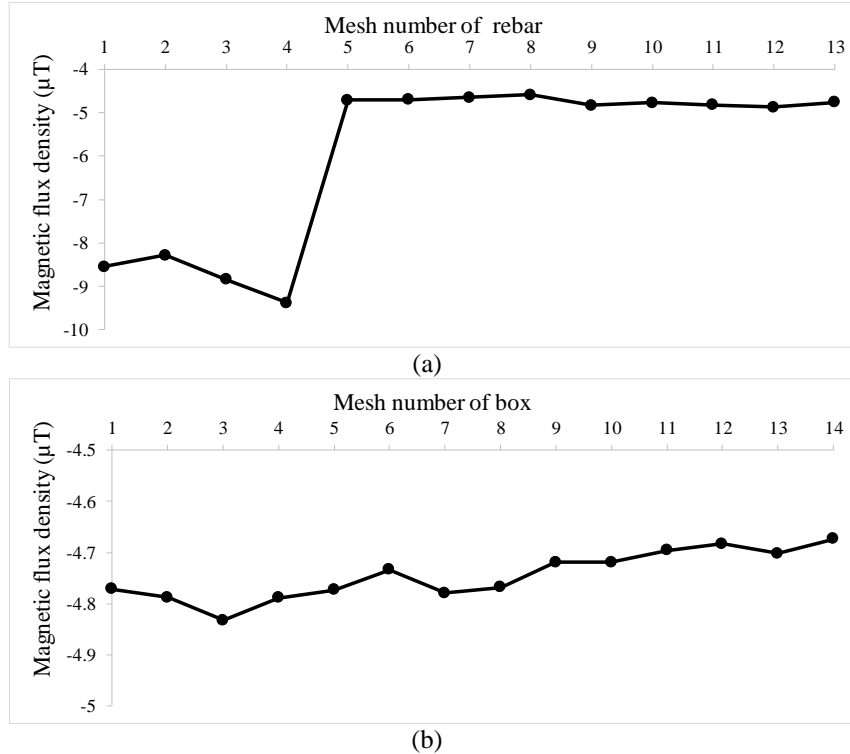
Figure 5.6. Minimum values of Y component magnetic flux density of corroded rebar, from Line B to Line C: (a) Different meshing specifications of rebar with fixed box mesh #1, (b) Different meshing specifications of the box with fixed rebar mesh #10.

Convergence of the intact and the corroded rebars' simulations was also confirmed through examining their standard deviations (SDs) (Figures 5.7 & 5.8). SD values of the Y component magnetic flux densities on the path shown in Figure 5.4 (without considering the edge effect and background magnetic field) were calculated for different mesh specifications (Table 5-1 & Table 2). SD values were calculated for the simulation result from the first rebar mesh specifications to the optimum rebar mesh specifications (rebar meshes #11 and #10, for intact and corroded rebar, respectively), using the constant specifications of the box mesh (box mesh #1). Confirmation of convergence was then achieved by calculating the SD values for the simulation results with more accurate mesh specifications of the box, but with the fixed optimum rebar mesh specifications. It was observed that the SD values of the corroded and intact rebars' magnetic data became linearly stable when the meshing accuracy of the rebar and the box was increased.
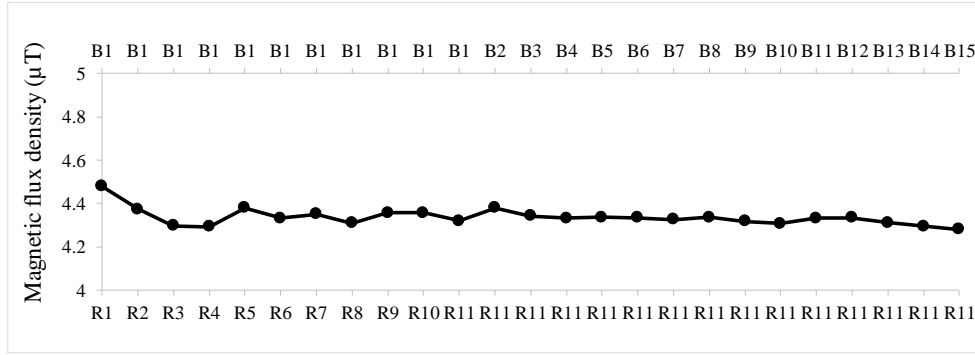
Figure 5.7. SD values of Y component magnetic flux density of intact rebar, from Line B to Line C (on the horizontal axis. R refers to the different meshing specifications number of rebar; B refers to the different meshing specifications number of the box).
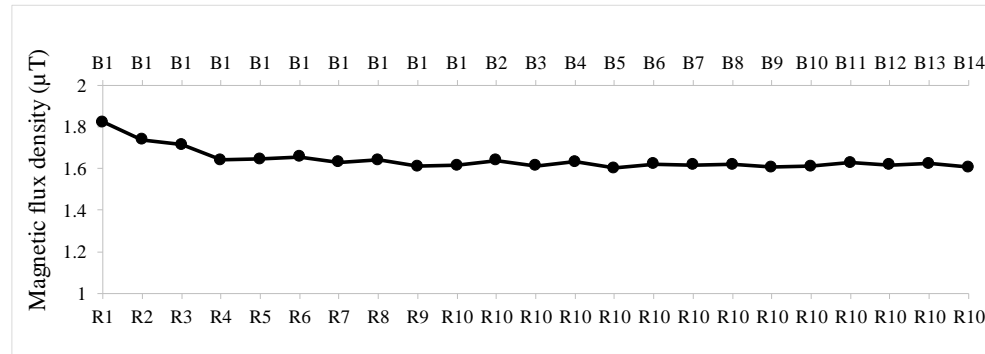
Figure 5.8. SD values of Y component magnetic flux density of corroded rebar, from Line B to Line C (on the horizontal axis. R refers to the different meshing specifications number of rebar; B refers to the different meshing specifications number of the box).

Figures 5.9 and 5.10 represent the Y component magnetic flux density of the intact and corroded rebars with initial and final mesh specifications. The magnetic densities extracted from the simulation with the final mesh have no outliers and a disordered trend, unlike the results of the simulation with the initial mesh specification. The Y component values of magnetic flux density for both corroded and intact rebar are initially equal to the Y component value of background magnetic flux (the magnetic field of the Earth). However, when the distance (in the Y direction) reaches about 22 mm (the edge of the rebar), the flux intensity values change based on the magnetic properties of the ferromagnetic rebars. The magnetic intensity of intact rebar has a harmonic trend (up and down) because of the corrugated shape on the rebar surface, but there is no detectable regular trend for the corroded one. When the distance in the Y direction reaches the end of the rebar (at about 388 mm), the magnetic density values return to the magnitudes of their background magnetic field.

128
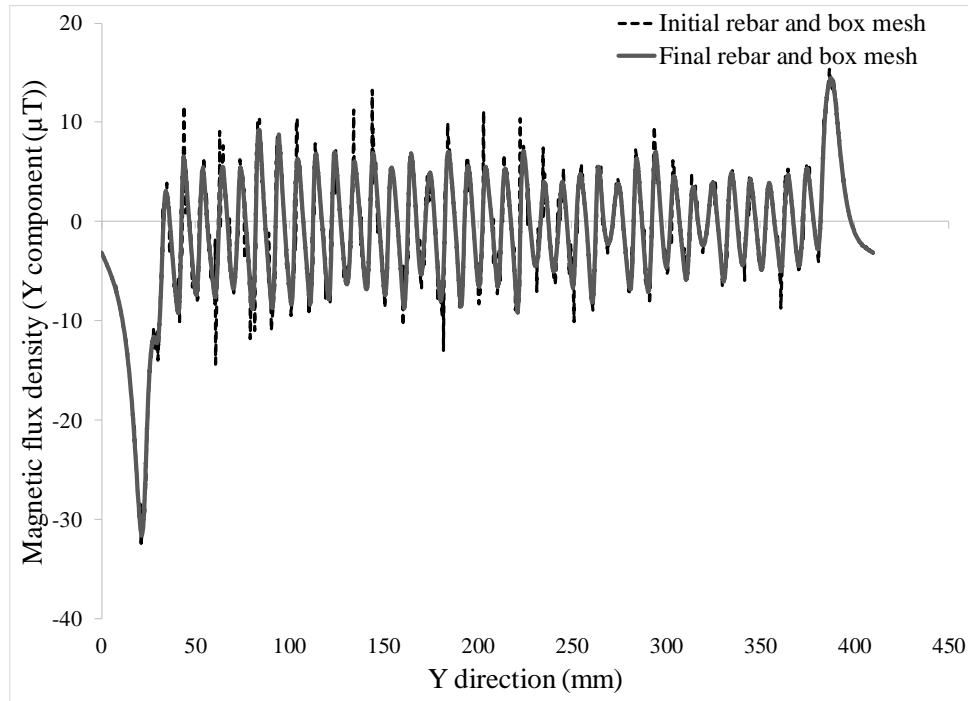
Figure 5.9. Comparing the values of Y component magnetic flux density of the intact rebar simulation for initial mesh and final mesh (from the Line A to the Line D).
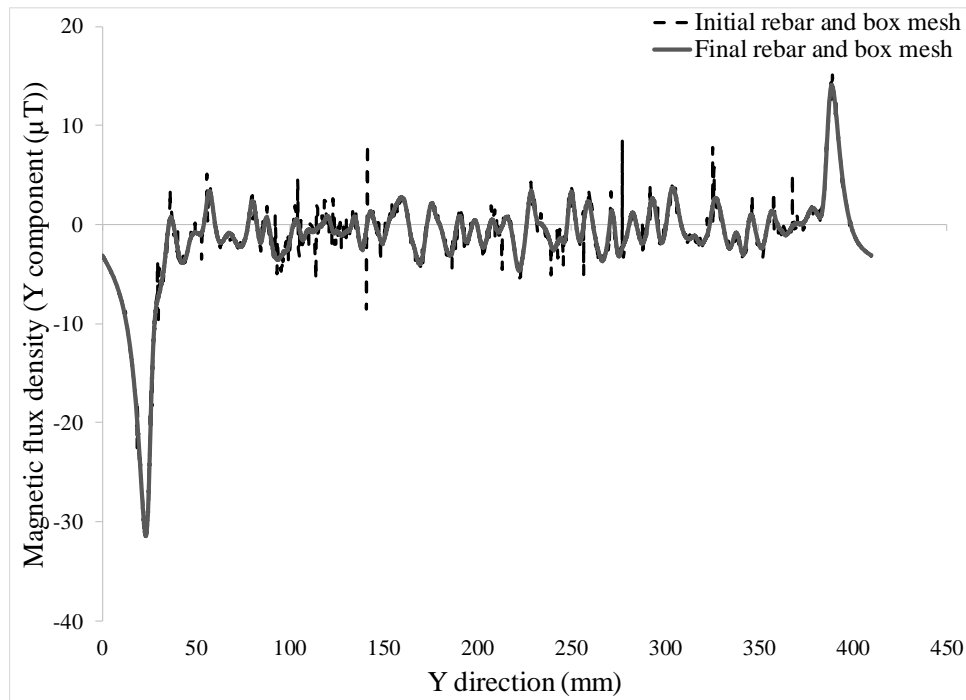
Figure 5.10. Comparing the values of Y component magnetic flux density of the corroded rebar simulation for initial mesh and final mesh (from the Line A to the Line D).

5.3. Experiment

To validate the simulation results, the magnetic flux densities of the intact and corroded rebars were separately recorded along their whole length using an existing PMI device (Mahbaz, 2016).

129

Scanning was conducted on fixed rebars in non-magnetic locations, at the vertical distance of 10 mm (the minimum vertical distance that can be applied with the PMI device), in order to record accurate magnetic data (Figure 5.11a & Figure 5.11b)

<div align="center">(a)   (b)</div>
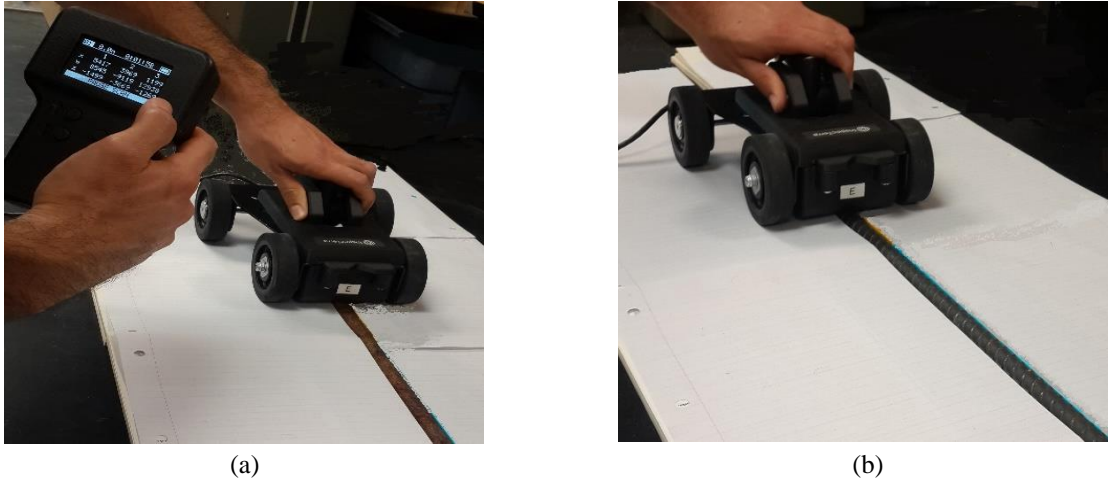
Figure 5.11. Experimental data recording process: (a) For the corroded rebar, (b) For the intact rebar.

Figure 5.12 shows the Y component of the magnetic flux density (parallel to the rebar direction) of the two rebars, with clearly distinguishable differences. These differences are related to the inherent magnetic properties of the materials and are difficult to replicate in simulations. For quantifying the differences between the magnetic data of the two rebars, the single-sided magnitude spectrum of the magnetic data was provided using MATLAB 2018 b (Figure 5.13). The magnitude spectrum was generated through appending 99000 zeros to the distance domain magnetic data and using a Hanning window function. In Figure 5.13, the overall magnetic-flux-density curves of both intact and corroded rebars show a dominant low frequency of about $0.0025\ mm^{-1}$. However, the amplitude of the dominant low frequency of the intact rebar is 2.51 times greater than that value for the corroded rebar.
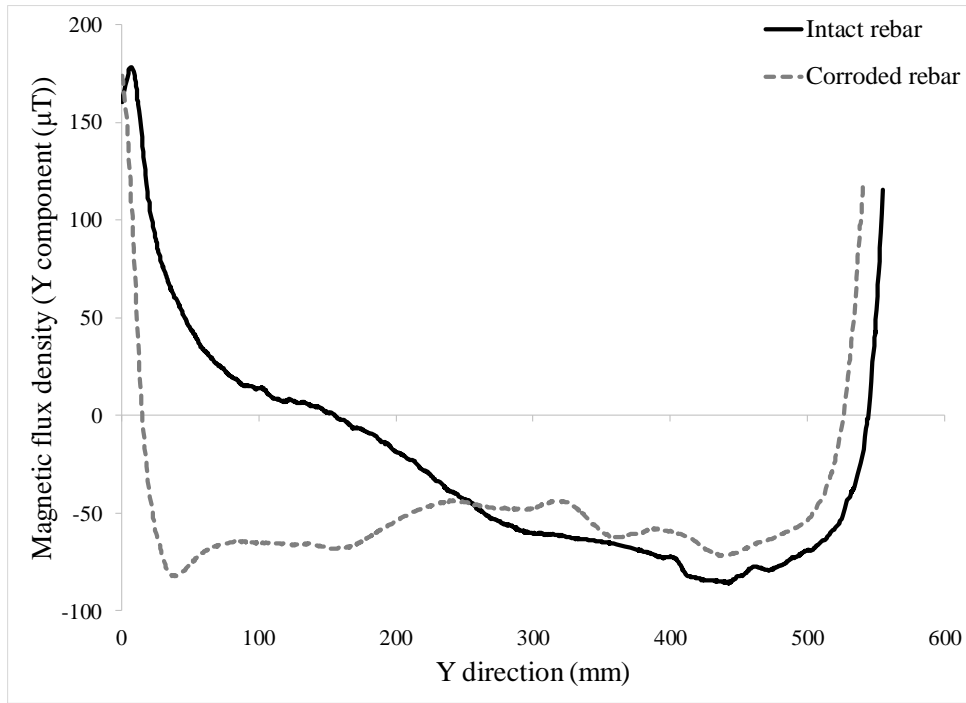
Figure 5.12. Experimental magnetic flux density values for both rebars.
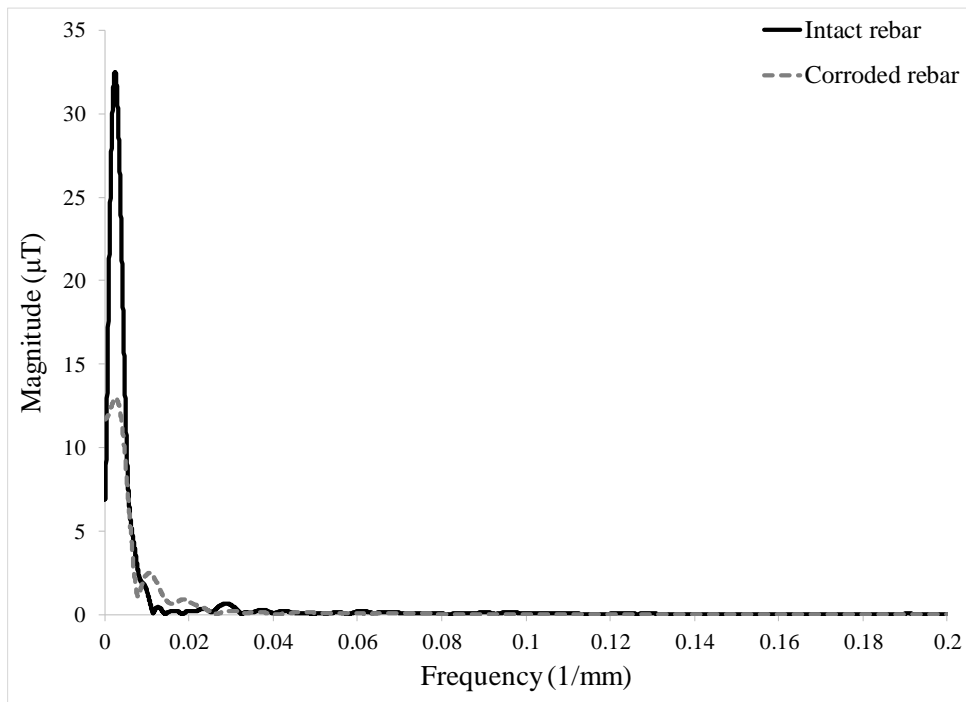
Figure 5.13. Experimental single-sided magnitude spectrum of the Y component magnetic flux density.

5.4. Comparison of experimental and simulations outcomes

According to the simulation results, the intact rebar's magnetic-flux-density values follow a regular up-and-down pattern that matches the corrugated rebar surface. However, no predictable behavior is found for the Y-component magnetic flux densities on the surface of the corroded rebar

because of its extensive general corrosion and flattened bumps. To find the intact rebar's harmonic behavior, the final converged data for the Y-component magnetic flux density (in the Y direction) was fitted to a sine function with an R-square value of $R^2 = 0.86$ (Eq. 5-1) (Figure 5.14). The frequency of the sine function was estimated to be 0.099 ($\frac{1}{mm}$). The periodic parameter of the estimated sine function ($\frac{1}{0.099} \approx 10mm$) is exactly equal to the center-to-center distances of the bumps on the surface of the intact rebar (Figure 5.2).

$$R^2 = 1 - \frac{\text{Error Sum of Squares}}{Total\ sum\ of\ squares} \rightarrow R^2 = 1 - \frac{52269.92\ \mu T^2}{381282.6\ \mu T^2} = 86\%$$ (5-1)
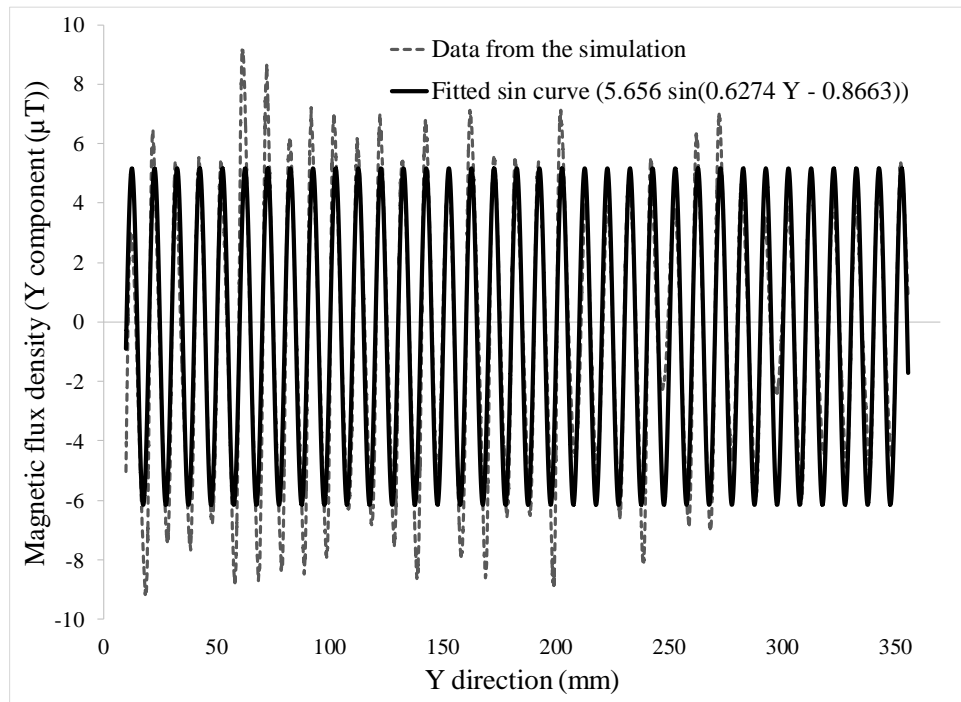
Figure 5.14. Y component magnetic flux density, obtained from the simulation, at the surface of the intact rebar, fitted with a sine curve (from 9.9 mm (Line B) to 355.8 mm (Line C) of the rebar length).

To check the harmonic trend of the obtained values from the simulation, the single-sided magnitude spectrum of the magnetic data recorded over corroded and intact rebars were plotted using MATLAB 2018 b (Figure 5.15). In the magnitude spectrum generated from the values recorded over the intact rebar, a considerable peak happens at the frequency of 0.1 ($\frac{1}{mm}$) with an amplitude of 5.18 µT, verifying the frequency value resulting from the fitted sine function. This detected frequency (0.1 ($\frac{1}{mm}$)) again indicates that the period parameter of the magnetic data is equal to the distance between the ribs on the surface of the intact rebar. However, in the magnitude

132

spectrum associated with the corroded rebar a suppressed extremum is observed close to the frequency of 0.1 ($\frac{1}{mm}$). Additionally, no considerable peak happens in the magnitude spectrum plot, showing a considerable dominate frequency affecting the data.
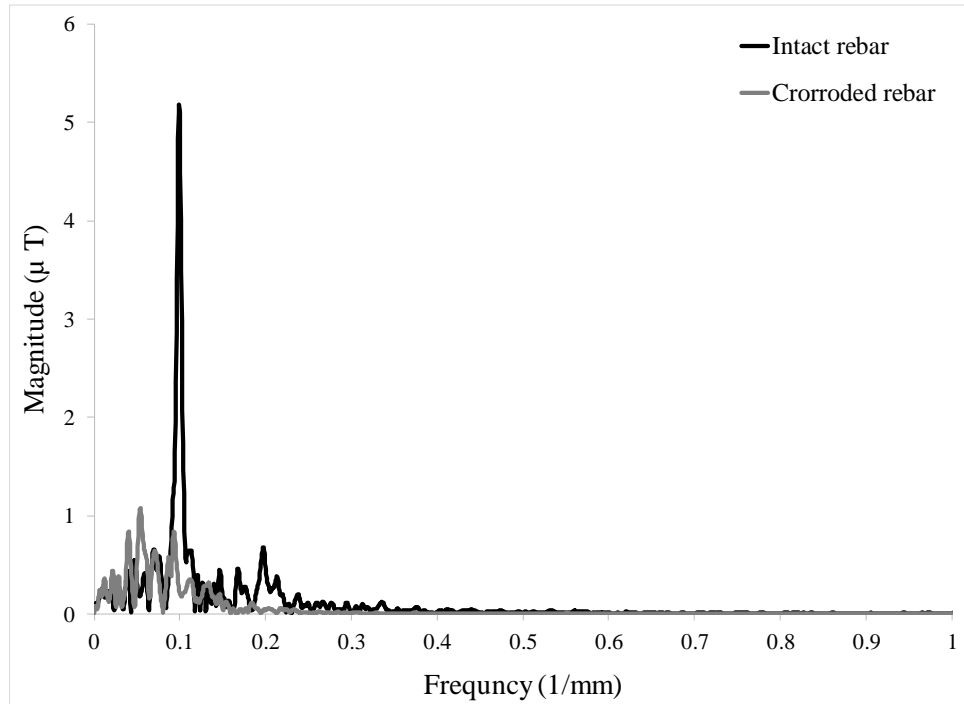
Figure 5.15. Single-sided magnitude spectrum of the Y component magnetic flux density, obtained from the simulation, at the surface of the intact and corroded rebars (from 9.9 mm (Line B) to 355.8 mm (Line C) of the rebars length).

Assuming that the magnetic flux densities at different locations on the rebars are independent, the probability plot method was implemented to fit Y component magnetic flux densities into a probability distribution. The magnetic-flux-density data of both intact and corroded rebars were plotted against various probability distributions (normal, log-normal, Weibull, and gamma). Next, Weibull (with $R^2 = 0.98$) and Gamma ($R^2 = 0.99$) distributions were chosen to represent the intact and corroded rebars, respectively (Figure 5.16a & Figure 5.16b). Both Weibull and Gamma distributions are extensions of the exponential distribution involving the gamma function (Navidi, 2010).
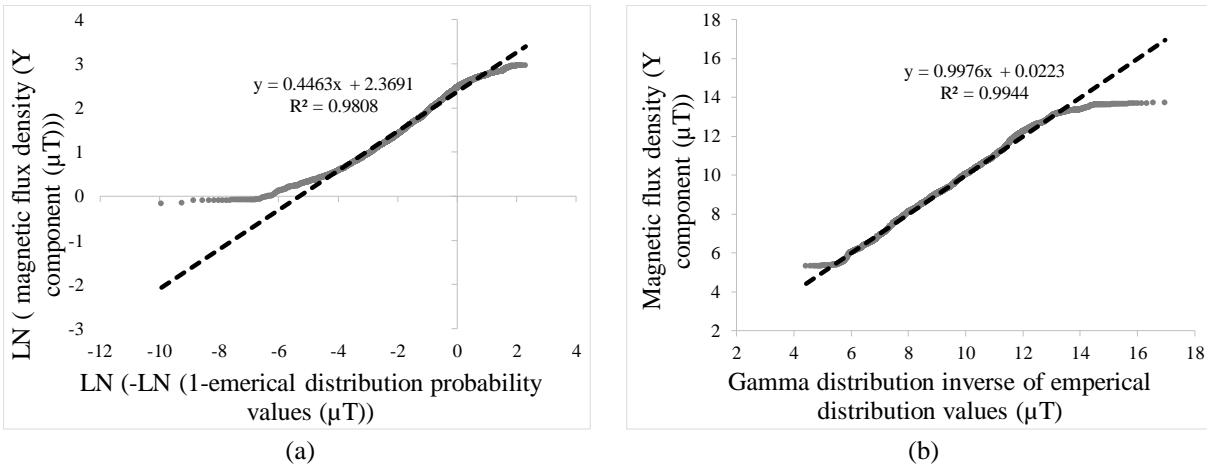
Figure 5.16. Finding appropriate probability distribution functions: (a) Probability plot for investigating the correlation of intact rebar data, obtained from simulation, with a Weibull distribution, (b) Probability plot for investigating the correlation of corroded rebar data, obtained from simulation, with a Gamma distribution.

It should be noted that a constant value of 10 µT was added to the magnetic data to eliminate negative values for Weibull and Gamma distribution plots. After conducting the probability plot, the values were returned to their original state. Figures 5.17 & 5.18 show good correlations between the histogram frequency of data and the chosen cumulative distributions. The parameters of the Weibull cumulative distribution were calculated based on the mean and SD of the intact rebar magnetic data, -0.52 micro-tesla and 4.28 micro-tesla, respectively. In addition, the features of the Gamma cumulative distribution were estimated through the mean and SD of the corroded rebar's magnetic data: -0.57 micro-tesla and 1.6 micro-tesla, respectively.

The mean value of the Y component magnetic flux densities for corroded and intact rebars are very close, indicating that the magnetic data for both rebars fluctuates at approximately the same value. However, the SD of the intact rebar's magnetic data is 2.6 times greater than the SD value of the corroded rebar's magnetic data. In other words, magnetic data for the corroded rebar tend to fluctuate more closely around the mean value, but the magnetic data of the intact rebar is distributed relatively uniformly over a wider range, probably because the intact rebar has higher bumps than the corroded rebar.

134
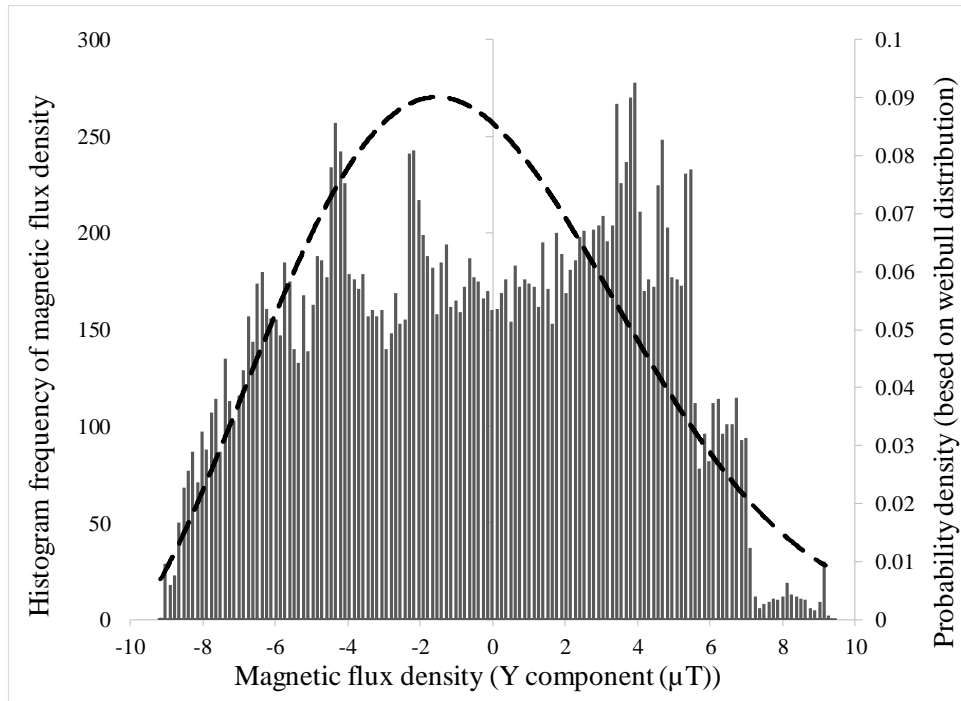
Figure 5.17. Histogram frequency of intact rebar data, obtained from simulation, in conjunction with probability density of the Weibull distribution.
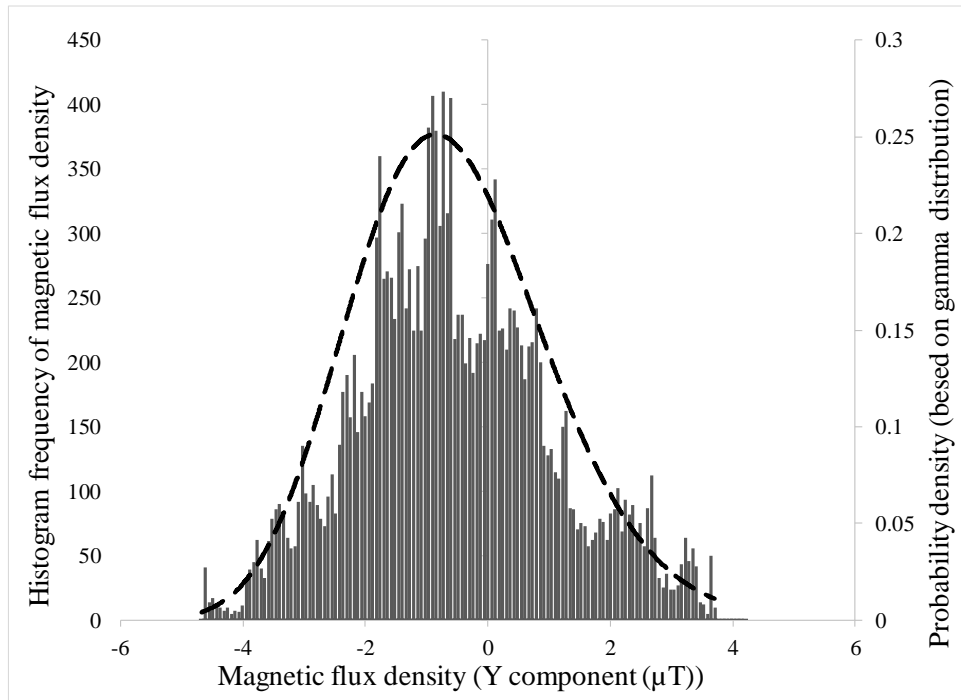
Figure 5.18. Histogram frequency of corroded rebar data, obtained from simulation, in conjunction with probability density of the Gamma distribution.

For better interpretation of the experimental results, the focus is now directed to smaller sections of the rebars to study them at expanded scales. Figure 5.19 shows that in the selected section of the intact rebar's magnetic data, the moving average smoothing technique (with a period of about

1 mm) was used to smooth out short-scale fluctuations and highlight longer-scale trends. The overall linear trend was then removed by subtracting the best fitted straight-line from the magnetic data. Subsequently, the overall non-linear trend was removed by subtracting the best-fitted seven-degree polynomial function to create a straight baseline (Figure 5.19). Next, a multiple sine curve was fitted to the graph with $R^2 = 0.9$ to visually represent the sinusoidal behavior of the magnetic data. For better interpretation of the sinusoidal parameters, the single-sided magnitude spectrum of the magnetic data (after removal of the linear and non-linear trends) was calculated (Figure 5.21). According to the magnitude spectrum, the highest peak occurs at a low frequency of about $0.03 \frac{1}{mm}$, and the second highest peak is found at a frequency of $0.1 \frac{1}{mm}$, which is the same as the frequency of the intact rebar's sine curve obtained from the simulation.
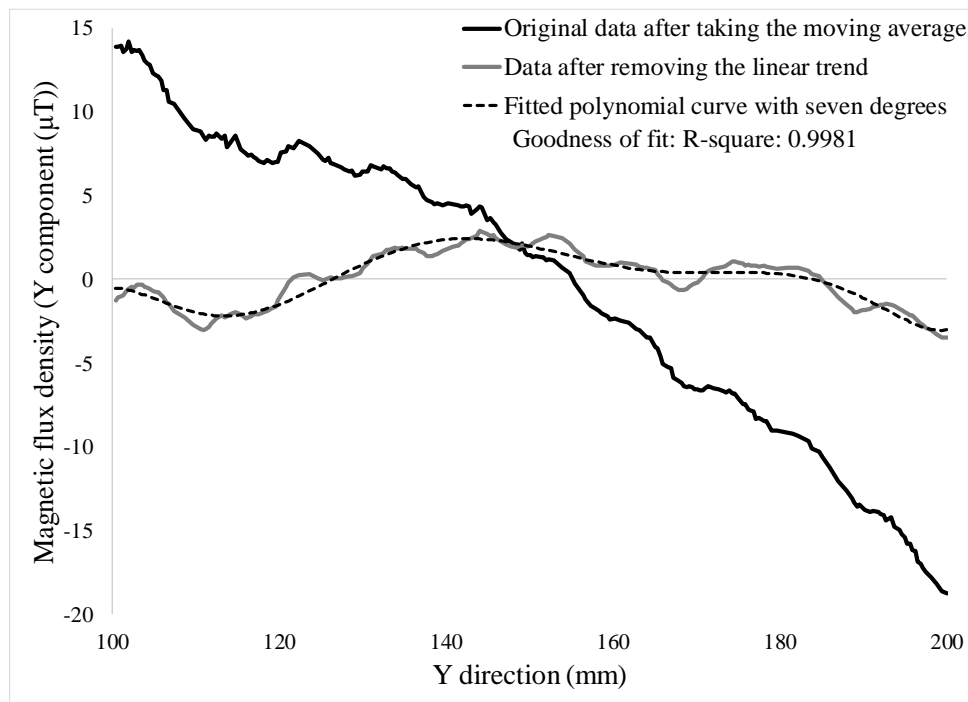
Figure 5.19. Magnetic flux density values, taken from experiments, at the surface of a small section of the intact rebar.
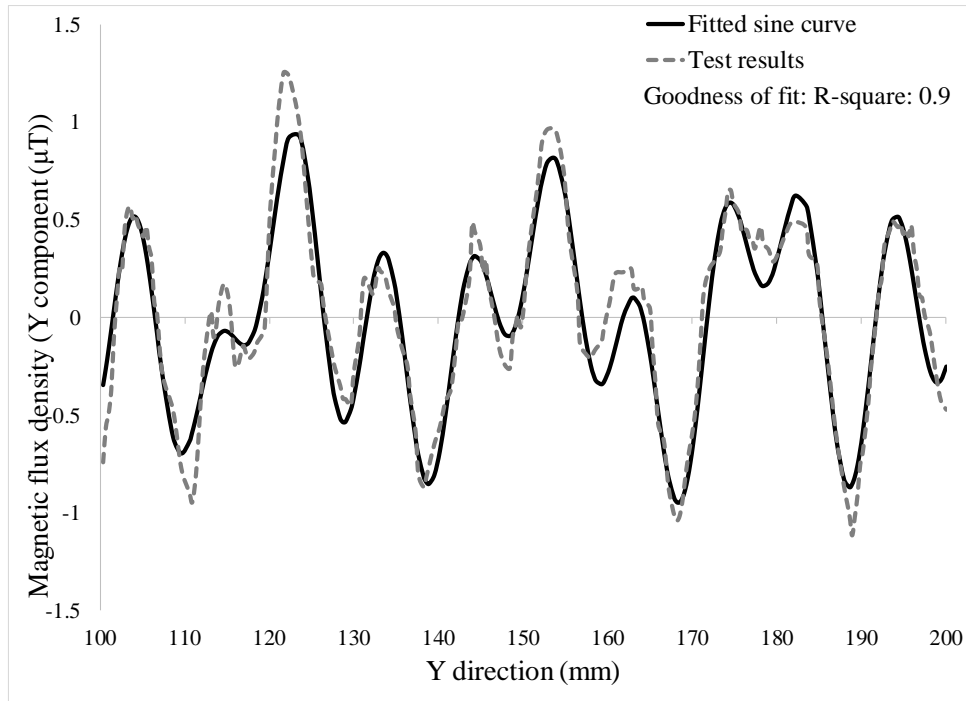
Figure 5.20. Magnetic flux density values, taken from experiments, at the surface of a small section of the intact rebar, fitted with a sine function.
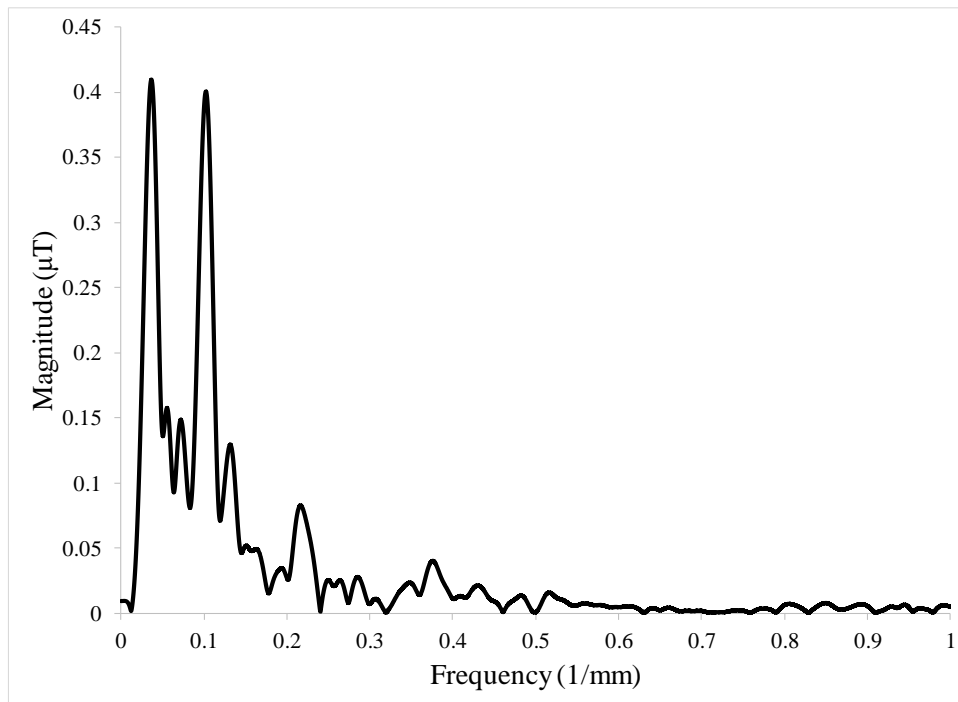
Figure 5.21. Single-sided magnitude spectrum of the magnetic flux density values, taken from experiments, at the surface of a small section of the intact rebar.

Figure 5.22 shows a smaller section of the corroded rebar at a larger scale after the moving average smoothing technique has been applied. The corroded rebar's magnetic curve has an overall polynomial trend, as does the magnetic data of the intact rebar (Figure 5.22). However, no multiple

sine curve can be fitted with strong correlation to the data after removal of the non-linear trend. The magnetic flux density values of the corroded rebar are clustered more closely to the fitted polynomial curve than the magnetic flux density values of the intact rebar, which fluctuate over a larger range around its fitted non-linear curve. This behavior is in accordance with the statistical studies of the simulations, which showed that the magnetic flux density values of the corroded rebar are concentrated around the mean value, and the magnetic flux density values of the intact rebar have a greater SD.

For a more detailed study on the standard deviation of the magnetic values, the experimental data for both corroded and intact rebars were separately split into equal sections of 15 mm (i.e., the distance for the sections was chosen in a way guaranteed to include the rebars' bumps). Next, the linear trends were separately removed from data at every section, and each section's standard deviation was calculated. Figure 5.23 shows the standard deviation for all sections of the corroded and intact rebars' magnetic data, with the SDs shown at the places of the average distances included in every section. Using Figure 5.23, the average for the SDs calculated for the intact rebar is 2.4 times greater than that for the corroded rebar. This ratio confirms the simulation results, which showed that the SD of the intact rebar's magnetic data was 2.6 times greater than that of corroded rebar's.
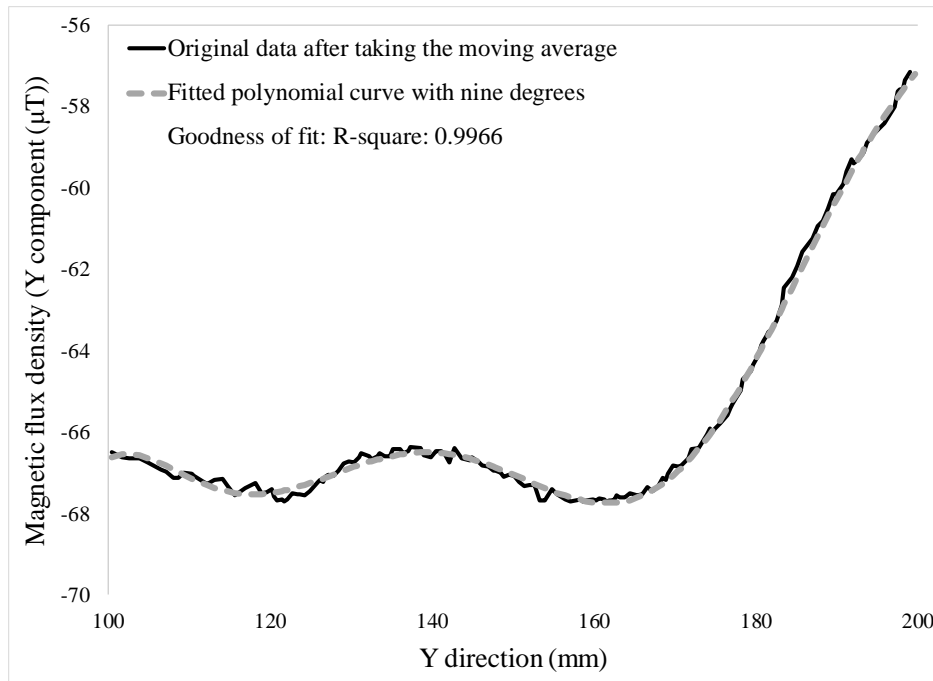
Figure 5.22. Experimental magnetic flux density values at the surface of a small section of the corroded rebar (along with its local baseline value).

138
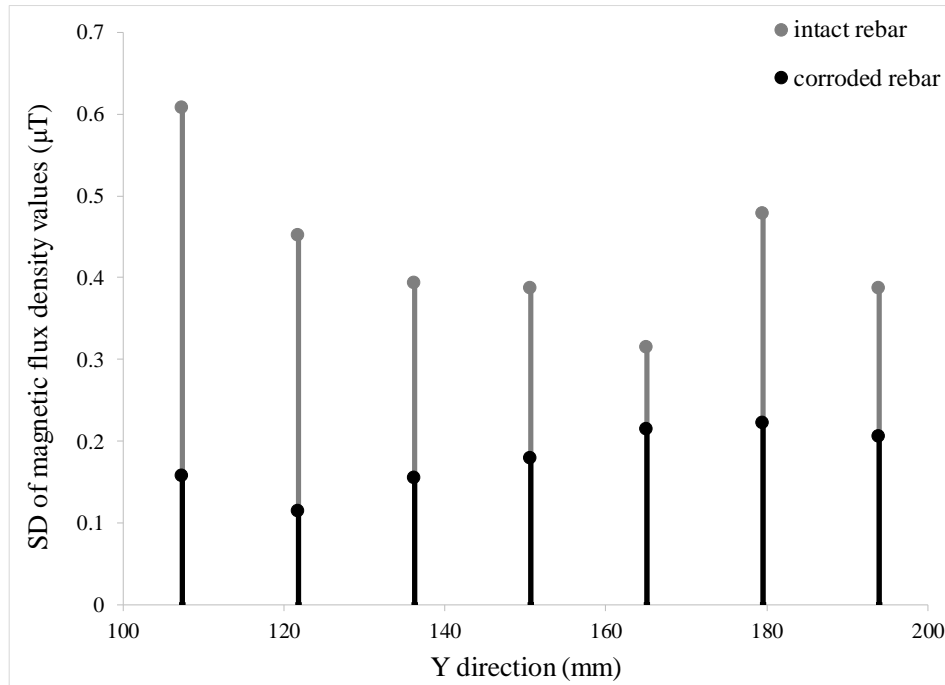
Figure 5.23. Standard deviations of equal sections of magnetic data (after removing their linear trends), resulting from experiments, for both corroded and intact rebars.

5.5. Conclusion

The magnetic behavior of an intact and a corroded rebar in a background magnetic field were simulated with a finite-element-based software. Distinguishable differences were observed between the trends of the magnetic data for the two rebars. Regarding the simulation results, the general corrosion of concrete-embedded rebars can be detected accurately by comparing the recorded magnetic data trend, mean, and SD to those of an intact rebar sample with known geometrical properties and magnetic specifications. Subsequently, the magnetic behavior of the intact and the corroded rebars were measured using a PMI device. The test results, assessed from different points of view, correlated well when compared with the simulation results. In conclusion:

- Simulation and experiments showed that the magnetic flux density values of the corroded rebar were more concentrated around its baseline, compared to the magnetic values of the intact rebar (i.e., according to the simulation results, the SD of the intact rebar's magnetic data was about three times greater than the SD of the corroded rebar's magnetic data).

- Experiments showed that the corroded and the intact rebar can be differentiated by their magnitude values resulting from a magnitude spectrum plot, considering the low-frequency peak that results from their inherent magnetic properties.

- Simulation and experiments showed that the intact rebar could be identified by a peak at a frequency value that demonstrates a periodic value equal to the rebar rib distance.
- Simulation and experiments demonstrated a sinusoidal trend (about a specific frequency) for the magnetic data of the intact rebar and no predictable trend for the corroded rebar's magnetic data.

Chapter 6: Comparison of magnetic data recorded over reinforcement steel with different degrees of corrosion

The contents of this chapter are reflective of an original manuscript submitted by the Ph.D. candidate (Milad Mosharafi) to the journal of Construction and Building Materials in November 2019.

6.1. Introduction

Corrosion in reinforcement may take two forms: local or general (Perkins, 2000). Local corrosion reduces reinforcements' cross-sectional area, and general corrosion forms corrosion products that create internal tensile stress in concrete, with resultant cracking and spalling (Zhao *et al.*, 2011). The previous chapter described the distinguishable differences between the magnetic properties recorded over an intact rebar and over a rebar with general corrosion. The studies are explored to achieve more-accurate and better-calibrated results based on improved data acquisition approaches, superior signal processing and statistical analysis methods, and in a wider range of conditions. To advance improvements in PMI technology with respect to general corrosion, the current chapter focuses on experiments that investigate ferromagnetic steel rebars with different mass loss percentages. Such investigations are required to achieve a reliable relation between the magnetic properties and the corrosion degrees of steel reinforcements under concrete cover.

In the research described in this chapter, first, self-magnetic flux leakage (SMFL) data are recorded using the PMI scanner along the axis of a rebar with 0% mass loss. The scanner is run nine times over a pre-determined path to statistically help in estimating the required number of replicates for subsequent experiments. Next, SMFL data are collected by running the PMI scanner over six rebars, each having different degrees of general corrosion. Two different paths, with the same direction, are identified along the lengths of each rebar. Magnetic properties are then recorded over each path, considering the required replicants estimated from the previous step. The consistency of the data recorded on each rebar is investigated using three different statistical approaches to ensure the reliability of the outcomes. Finally, to determine the relation between the magnetic properties and the degree of corrosion, the recorded data are subjected to three distinct data-processing approaches (Figure 6.1):

- Data-processing approach #1: Calculating the power of the magnetic flux density's derivative signal;

- Data-processing approach #2: Calculating the dominant frequencies affecting the magnetic data and their corresponding magnitudes
- Data-processing approach #3: Calculating the standard deviation of the magnetic data
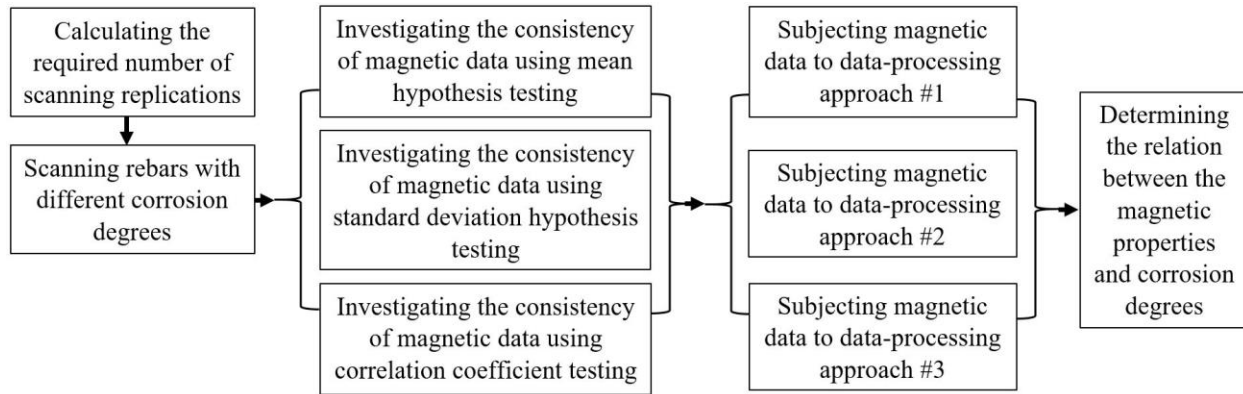
Figure 6.1. Methodology flowchart, showing the sequence of the experiments and analyses.

6.2. Sample creation procedure

To explore the relation between the magnetic properties and the degree of general corrosion, investigations were done on six 16 mm-diameter rebars made of grade 400 steel. The rebars were of various lengths, from 423 mm to 699 mm, and had different degrees of general corrosion (mass loss percentages), from 0% to 14.3% (Figure 6.2). The general corrosion on rebars was obtained by placing them in a corrosive environment (salted concrete) and subjecting them to a constant current (Al-Hammoud *et al.*, 2011). Next, the corrosion degrees were identified using the procedure explained in ASTM G1-03 (2003) standard.
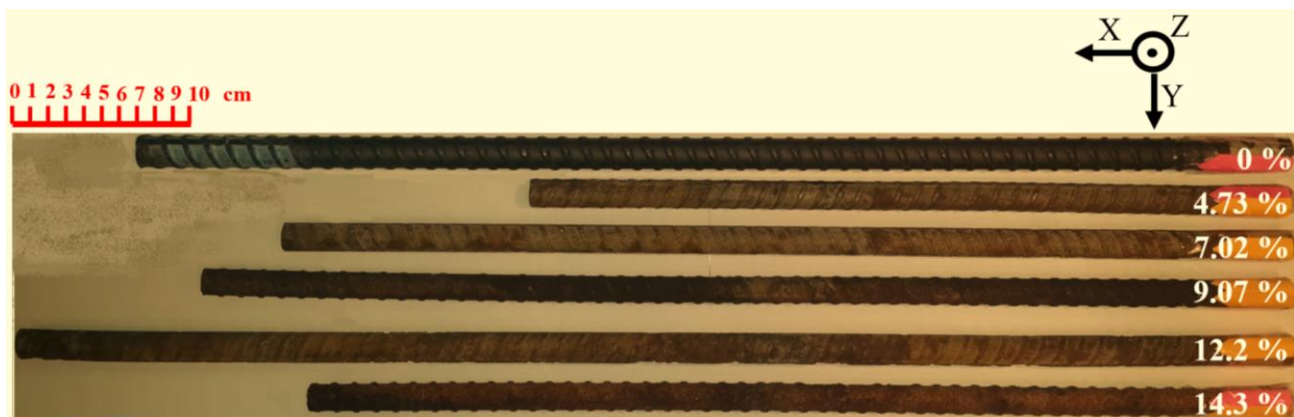
Figure 6.2. Rebars with different mass loss percentages.

142

6.3. Required scanning replications

To investigate the required scanning replications, a 200 mm pre-determined path along the axis of the intact rebar (i.e. the rebar with 0% mass loss - Figure 6.2) was scanned nine times at a vertical distance of 1 cm (Figure 6.3). The scans were conducted with a continuous movement of the PMI scanner over the rebar, referred to as scanning approach #1, to emulate a "normal" scanning approach that might be used for PMI inspection of infrastructure elements. Based on the nine scans (considering each as a sample), the limits for the mean of the population were estimated for each scan, using the T distribution and a significance level of 5% (Eq. 6-1 and Figure 6.4). The upper and lower boundaries for the standard deviation (SD) of the population's magnetic values were also calculated, considering the same significance level and using a Chi-squared distribution (Eq. 6-2 and Figure 6.5).
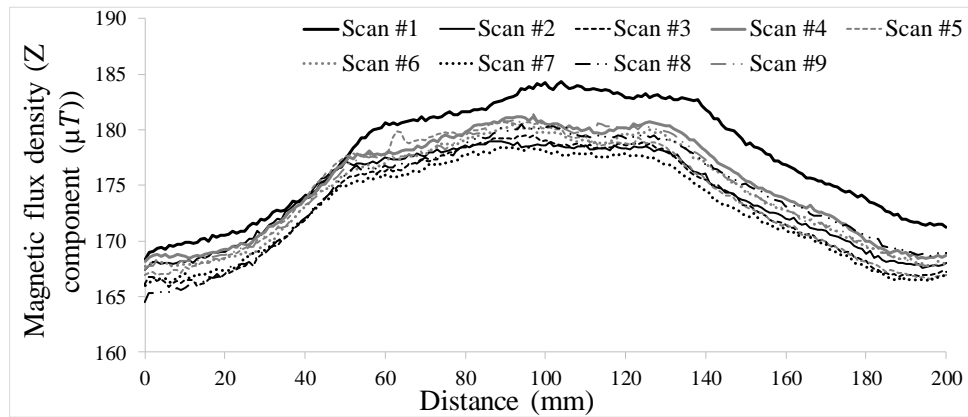
Figure 6.3. Nine separate scans recorded by the continuous movement of a PMI scanner (scanning approach #1) over a certain path and direction of the intact rebar.

$$\mu_k = \bar{X}_k \mp T_{\frac{\alpha}{2}} \frac{s_k}{\sqrt{n}} \tag{6-1}$$

$k: 0, 1, \dots, 200 \qquad (integer\ numbers\ showing\ the\ distance\ (in\ mm) over\ rebars)$

$\mu_k: population's\ mean\ at\ every\ k$

$\bar{X}: sample\ mean\ (mean\ of\ magnetic\ values\ recorded\ by\ diffrent\ scans\ at\ k)$

$\alpha: significance\ level$
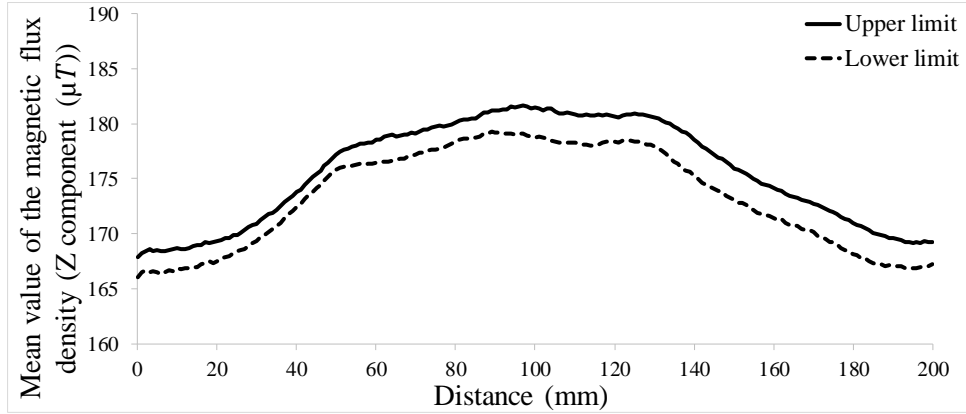
Figure 6.4. Lower and upper limits of the mean value of the magnetic data with 95% confidence, based on nine separate scans recorded by scanning approach #1.

$$\sigma_k = \sqrt{\frac{(n-1)s_k^2}{\chi^2_{\frac{\alpha}{2}, \ right \ (or \ left)}}}$$

(6-2)

$k: 0, 1, \dots, 200$ $(integer \ numbers \ showing \ the \ distance \ (in \ mm) \ over \ rebars)$

$\alpha: significance \ level$

$s: sample \ SD$ $(SD \ of \ magnetic \ values \ recorded \ by \ different \ scans \ at \ k)$

$\sigma_k: population's \ mean \ at \ every \ k$

$n: data \ number$ $(number \ of \ scans)$
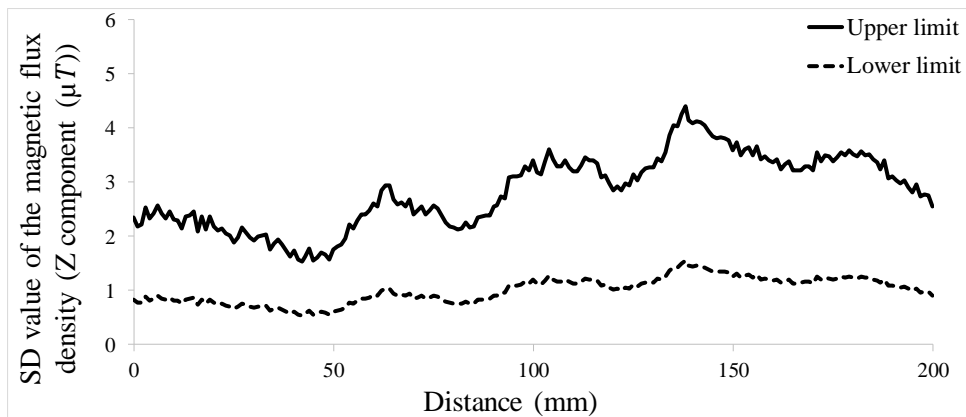
Figure 6.5. Lower and upper limits of the SD value of the magnetic data with 95% confidence, based on nine separate scans recorded by scanning approach #1.

According to Figure 6.4, the minimum and maximum differences between the limits of the mean values are respectively 1.23 μT and 3.58 µT, a relatively wide range. The limits for the mean values and SDs are affected by the values of magnetic data recorded in the scans. The scans were

144

consecutively conducted for the same location, path, and direction, so they are expected to be consistent and reasonably similar to each other. To investigate this issue, multiple comparisons were conducted between all possible pairs of the nine scans based on simple T-testing, considering the model shown in Eq. 6-3. To conduct the multiple comparisons, an ANOVA Eq was organized (Table 6-1). Additionally, to check the underlying assumption of the model, the normal probability plot of its residuals was reviewed, showing a coefficient of determination of $R^2 = 0.9005$ (Figure 6.6). According to the ANOVA table, $F_{Observed}$ is greater than $F_{Critical}$ (with 95% confidence), so the null hypothesis is rejected. This result shows that at least for one of the scans, $\tau_t \neq 0$. In other words, at least one of the scans differs significantly from the others.

$$Model: y_{ti} = \mu + \tau_t + \varepsilon_{ti} \tag{6-3}$$

$t = 1, 2, 3, ..., 9$ *(number of scans)*

$i = 1, 2, ..., 201$ *(number of data at every scan)*

$\mu = Overall\ mean$

$\tau_t = \mu_t - \mu$ *(deviation of every scan's mean from the overall mean)*

$\varepsilon_{ti} = error\ for\ i^{th}\ data\ of\ the\ t^{th}\ treatment,\ assuming\ that\ the\ error\ is\ normally$ *distributed.*

$H_0: \tau_1 = \tau_2 = \cdots = \tau_9 = 0$

$H_1: \tau_t \neq 0$ *(at least for one of the scans)*

Table 6-1. ANOVA table based on the magnetic data values recorded for the nine scans.

Source	Degrees of freedom (DF)	Sum of squares (SS)	Mean squared (MS)	$F_{Observed}$	$F_{Critical}$
Between scans	8	2924.496	365.562	16.980132	$F_{8,\ 1800,\ 0.05}$ =1.94
Within scans	1800	38751.86	21.52881		
Total	1808	41676.35			
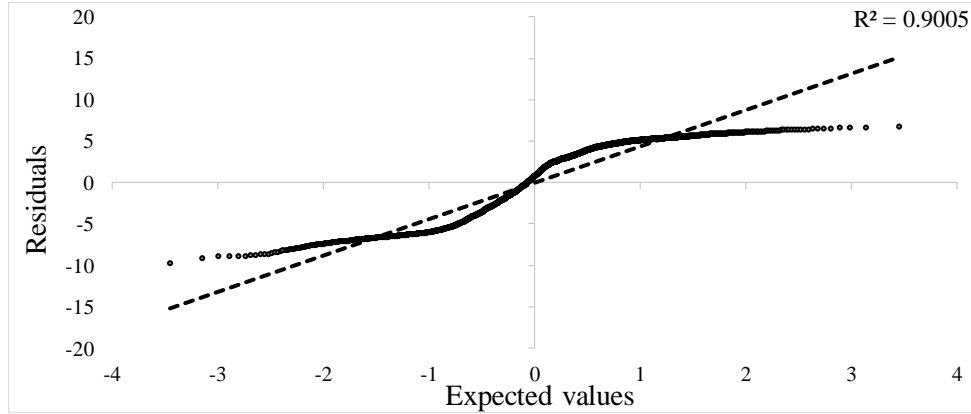
Figure 6.6. Normal probability for the residuals based on Eq. 6-3

For a more comprehensive assessment, multiple comparisons based on the Least Significant Difference (LSD) were conducted between every two scans. Assuming an overall significance level of 0.1 (b) and the 36 possible pair comparisons after the nine scans (c), the individual significance level of 0.003 ($\frac{b}{c}$) was used for every individual comparison. Subsequently, the LSD value was calculated using the mean squared value within scans (from Table 6-1) based on Eq. 6-4 and Eq. 6-5, to be compared with the absolute difference between every two scans. Consequently, according to Table 6-2, despite the alterations in the magnetic data between the nine scans (in Figure 6.5), the scans are mostly one-to-one equal to each other (with the overall significance level of 0.1). This result confirms the reliability of the measurements by the PMI device. However, scan #1 is not significantly equal to the other eight scans, and removing it from the calculations produces more-accurate outcomes.

$$Standard\ error\ (Se) \approx \sqrt{\frac{2 \times MS_{With\ in\ scans}}{Avg.\ numbers\ of\ data\ at\ every\ scan}} \to Se = \sqrt{\frac{2 \times 21.52881}{201}} \to \tag{6-4}$$

$Se = 0.4628$

$$LSD = T_{Critical} \times Se \to LSD = T_{\frac{0.003}{2},\ 1800} \times 0.4628 \to LSD = 1.3754 \tag{6-5}$$

Table 6- 2. Multiple comparisons based on LSD method (a difference between a specific pair of means is significant if it exceeds the LSD ($\times$); a difference between a specific pair of means is insignificant if it is less than the LSD ($\checkmark$)).

Difference between means	Status	Difference between means	Status	Difference between means	Status
$\bar{y}_1 - \bar{y}_2 = 3.4932$	$\times$	$\bar{y}_2 - \bar{y}_7 = 1.2358$	$\checkmark$	$\bar{y}_4 - \bar{y}_8 = 1.0171$	$\checkmark$
$\bar{y}_1 - \bar{y}_3 = 4.261$	$\times$	$\bar{y}_2 - \bar{y}_8 = -0.1406$	$\checkmark$	$\bar{y}_4 - \bar{y}_9 = 0.5224$	$\checkmark$
$\bar{y}_1 - \bar{y}_4 = 2.3354$	$\times$	$\bar{y}_2 - \bar{y}_9 = -0.6353$	$\checkmark$	$\bar{y}_5 - \bar{y}_6 = -0.2075$	$\checkmark$
$\bar{y}_1 - \bar{y}_5 = 3.3843$	$\times$	$\bar{y}_3 - \bar{y}_4 = -1.9255$	$\times$	$\bar{y}_5 - \bar{y}_7 = 1.3447$	$\checkmark$
$\bar{y}_1 - \bar{y}_6 = 3.1767$	$\times$	$\bar{y}_3 - \bar{y}_5 = -0.8767$	$\checkmark$	$\bar{y}_5 - \bar{y}_8 = -0.0317$	$\checkmark$
$\bar{y}_1 - \bar{y}_7 = 4.7291$	$\times$	$\bar{y}_3 - \bar{y}_6 = -1.0842$	$\checkmark$	$\bar{y}_5 - \bar{y}_9 = -0.5264$	$\checkmark$
$\bar{y}_1 - \bar{y}_8 = 3.3526$	$\times$	$\bar{y}_3 - \bar{y}_7 = 0.468$	$\checkmark$	$\bar{y}_6 - \bar{y}_7 = 1.5523$	$\checkmark$
$\bar{y}_1 - \bar{y}_9 = 2.8579$	$\times$	$\bar{y}_3 - \bar{y}_8 = -0.9084$	$\checkmark$	$\bar{y}_6 - \bar{y}_8 = 0.1758$	$\checkmark$
$\bar{y}_2 - \bar{y}_3 = 0.7677$	$\checkmark$	$\bar{y}_3 - \bar{y}_9 = -1.4031$	$\checkmark$	$\bar{y}_6 - \bar{y}_9 = -0.3188$	$\checkmark$
$\bar{y}_2 - \bar{y}_4 = -1.1577$	$\checkmark$	$\bar{y}_4 - \bar{y}_5 = 1.0488$	$\checkmark$	$\bar{y}_7 - \bar{y}_8 = -1.3764$	$\checkmark$
$\bar{y}_2 - \bar{y}_5 = -0.1089$	$\checkmark$	$\bar{y}_4 - \bar{y}_6 = 0.8412$	$\checkmark$	$\bar{y}_7 - \bar{y}_8 = -1.8711$	$\checkmark$
$\bar{y}_2 - \bar{y}_6 = -0.3164$	$\checkmark$	$\bar{y}_4 - \bar{y}_7 = 2.3936$	$\times$	$\bar{y}_8 - \bar{y}_9 = -0.4947$	$\checkmark$

Scanning approach #1 was conducted with a continuous movement of the PMI scanner over the rebar. Scanning approaches #2 and #3 are introduced to help in distinguishing between the sources of variations in the recorded magnetic data. To reduce the effects of local magnetic field changes, the scans by all scanning approaches were conducted on the same day and within a two-hour time span. In scanning approach #2, the rebar was scanned over the same path for the same distance and direction as the scans in scanning approach #1, but the scanner was halted approximately every one centimeter for 30 seconds to record magnetic data (i.e., about 600 data samples were recorded on each 30-second halt) (Figure 6.7a). Next, the standard deviations of the magnetic data of the rebar were calculated at every centimeter during one scan with 95% confidence (Figure 6.7b). Scanning approach #3 repeated scanning approach #2 in the same direction and at the same location, but with no rebar in place (Figure 6.8a); thus, the standard deviations of the environmental magnetic properties were calculated at approximately one-centimeter intervals (Figure 6.8b).
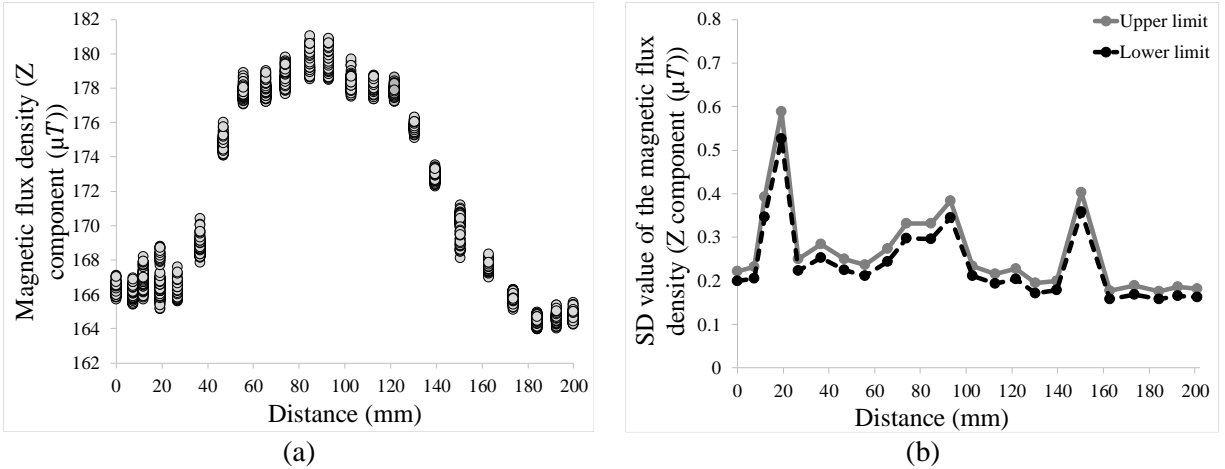
Figure 6.7. Investigation of the magnetic data recorded by scanning approach #2: (a) Magnetic flux density values recorded at approximately one-centimeter intervals in the presence of the rebar, (b) Limits of the standard deviation for the magnetic data shown in part a (with 95% confidence).
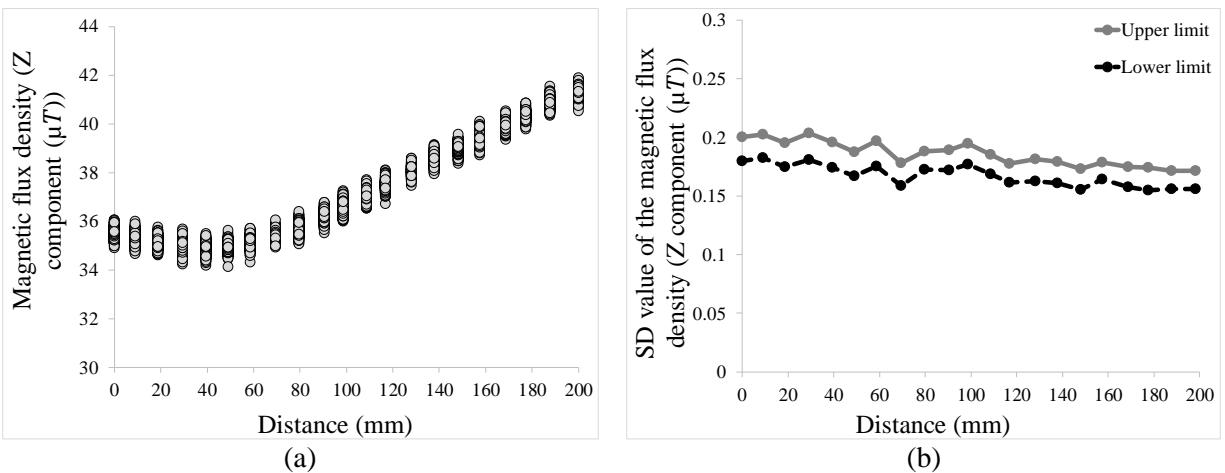
Figure 6.8. Investigation of the magnetic data recorded by scanning approach #3: (a) Magnetic flux density values recorded at approximately one-centimeter intervals with no rebar in place, (b) Limits of the standard deviation for the magnetic data shown in part b (with 95% confidence).

To assess data variation sources, the upper standard deviation boundaries obtained with scanning approach #1 (considering all nine scans), #2, and #3 were compared (Figure 6.9). Calculating the areas under the upper boundaries showed that 2% and 8% of the total variations were respectively covered by lines C (variation due to changes in environmental magnetic properties and inherent sensor errors) and B (variation covered by line C plus the variation due to inherent changes at one point of the rebar's magnetic properties during the scanning time). Hence, the remaining portion of the total variance (about 92% (the gray section in Figure 6.9)) is related to operator errors such as small deviations from the set path during scanning. The other type of operator error arises with a slight inaccuracy in stipulating the scan's starting point.

148
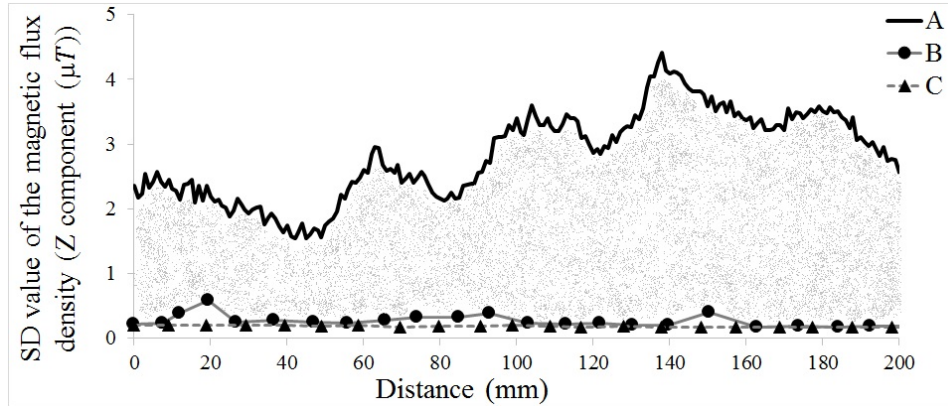
Figure 6.9. Upper boundaries of the SDs of magnetic data based on all three scanning approaches. The gray section shows variations due to operator error (A: upper boundary based on scanning approach #1; B: upper boundary based on scanning approach #2; C: upper boundary based on scanning approach #3).

To determine the number of scans required for confirming the accuracy of PMI measurements, all nine scans obtained by scanning approach #1 (Figure 6.3) were used. Although it was confirmed that scan #1 is not significantly equal to any of the other eight scans (due to operator error), its values are included in the current calculations so as to consider the probable operator errors that can happen in actual inspections. First, the total SD of the scans based on Cook's distances relation (Eq. 6-6) was calculated, which was equal to 1.53 µT. This SD value in conjunction with a chosen true difference of 0.1 μT was used to determine the minimum required numbers of replications using a table from Cochran and Gertrude (1957); thus, the maximum number of replications needed can be selected from Table 6-3, considering the desired significance level and power.

$$\sigma^2 = \frac{\sum\sum d_i^{j\,2}}{(i-1)(j-1)}$$

(6-6)

$i = Number\ of\ readings\ in\ every\ scan$

$j = Number\ of\ scans$

$d = The\ difference\ from\ the\ mean\ value$

Table 6-3. Number of replications for a given probability of significance level and power.

Number of replications	Significance level (%)	Power (%)
3	5	80
4	5	90
7	1	95

149

6.4. Scanning results for rebars with different degrees of corrosion

All six rebars (shown in Figure 6.2) were visually investigated, and two different paths were identified along their lengths. Both paths on each rebar had the same direction and were selected so as to pass over the most-corroded parts of the rebars. Next, the magnetic properties of the rebars were recorded by passing the PMI scanner over each path (in the X direction) at a vertical distance of 1 cm. The two paths on each rebar were used to review the consistency of the data recorded on each rebar. Consistency between the magnetic properties over path 1 and path 2 of every rebar (shown in Figure 6.2) can logically ensure the purpose behind this study, which is the classification of the magnetic properties based on the rebars' general corrosion.

To ensure the accuracy of data recording, each path on every rebar was scanned five times. The number of scans was chosen based on Table 6-3, representing a significance level of less than 5% and a power of greater than 90%. Subsequently, T-tests (Montgomery, 2014) were conducted between the X component of every two scans separately for all five scans recorded along the same path (a total of ten tests for every path). The scans that were significantly equal to the greatest number of other scans (with a confidence level of greater than 95%) was then chosen for use in the rest of the study (shown in Figures 6.10a and 6.10b).
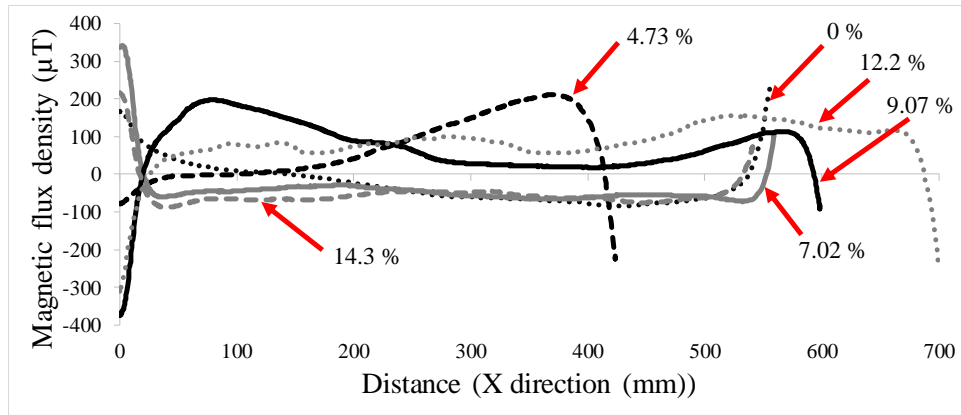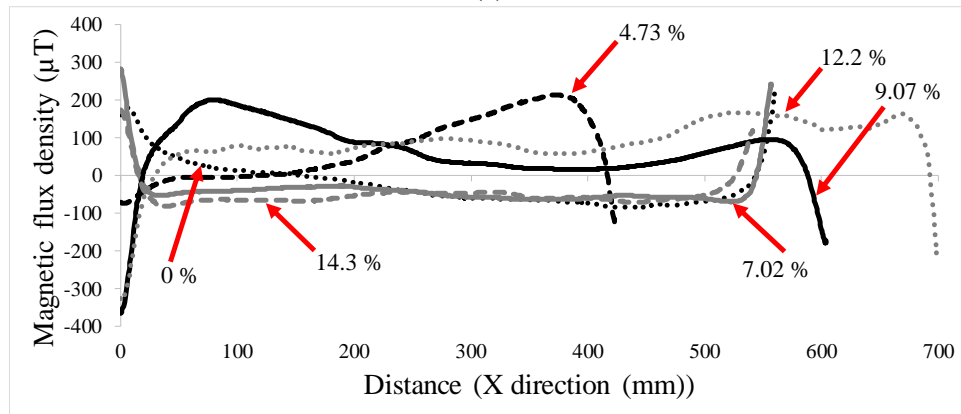
Figure 6.10. Whole values of the selected X component magnetic flux density recorded over the paths on rebars with different percentages of mass loss: (a) Over path 1, (b) Over path 2.

6.5. Investigating the consistency of magnetic data recorded over different paths of the same rebars

6.5.1. Correlation coefficient testing

The selected scans (shown in Figure 6.10) were subjected to centered moving average smoothing technique (Eq. 6-7) with a period of about 1.5 mm. Subsequently, 70 mm of data from both ends of every scan were deleted so as to remove the edge effects. The consistency of magnetic properties recorded over a rebar was assessed by comparing the data obtained for paths 1 and 2 of every rebar (Figure 6.11). To quantify the comparison, the correlations between the two paths' magnetic data were investigated using Pearson correlation (Eq. 6-8). Correlation expresses the strength and direction of the relationship between two data sets, and Pearson is the method most commonly used for evaluating a monotonic association (Schober and Schwarte, 2018). Table 6-4 shows a strong positive correlation between paths 1 and 2 for almost all the rebars (with correlation

coefficients of greater than 0.96). The exception is the rebar with 12.2% mass loss, which has a correlation coefficient of 0.77, a value that still confirms a good mutual association between the rebar's two data sets.

$$magnetic\ \widehat{value}_t = \frac{\left(\sum_{i=1}^{\frac{n-1}{2}} magnetic\ value_{t-i}\right) + magnetic\ value_t + \left(\sum_{i=1}^{\frac{n-1}{2}} magnetic\ value_{t+i}\right)}{n} \tag{6-7}$$
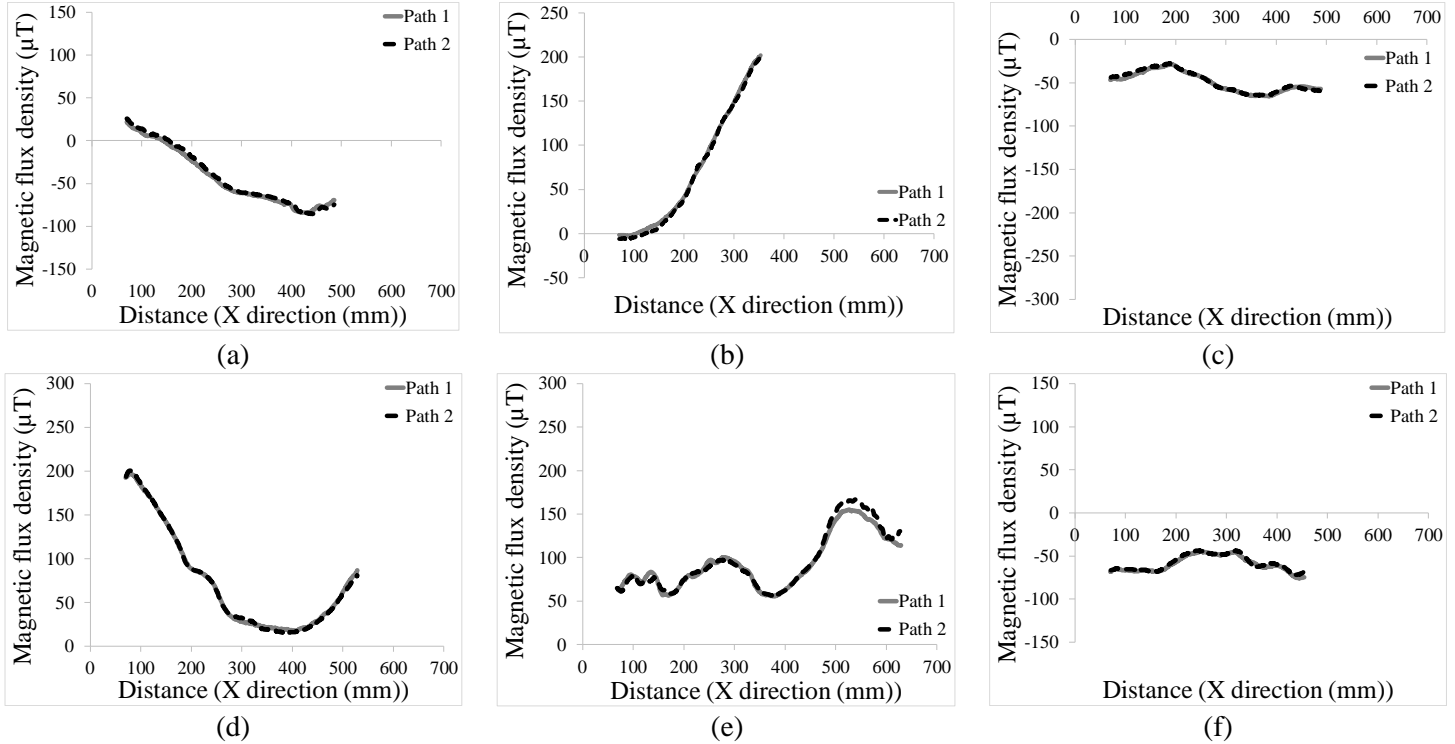
Figure 6.11. X component magnetic flux density values for path 1 and path 2 for each rebar with different percentages of mass loss: (a) For the rebar with 0% mass loss, (b) For the rebar with 4.73% mass loss, (c) For the rebar with 7.02% mass loss, (d) For the rebar with 9.07% mass loss, (e) For the rebar with 12.2% mass loss, (f) For the rebar with 14.3% mass loss.

$$\rho_{path1,\ path2} = \frac{\sum_{i=1}^{n}(path1_i - \overline{path1})(path2_i - \overline{path2})}{\sqrt{\sum_{i=1}^{n}(path1_i - \overline{path1})}\ \sqrt{\sum_{i=1}^{n}(path2_i - \overline{path2})}} \tag{6-8}$$

$path1_i$: ith data in path 1

$path2_i$: ith data in path 2

$\overline{path1}$: mean value for path 1 data set

$\overline{path2}$: mean value for path 2 data set

Table 6-4. The correlation coefficient between the magnetic data recorded over paths 1 and 2 for rebars with different percentages of mass loss.

Mass loss (%)	Correlation coefficient between the magnetic data recorded over paths 1 and 2 ($\rho_{path1,\ path2}$)
0	0.998
4.73	0.998
7.02	0.979
9.07	0.994
12.2	0.772
14.3	0.961

6.5.2. Mean hypothesis testing

For a more detailed investigation of the consistency of magnetic data recorded over two paths along the same rebar, T hypothesis tests were conducted between the two data sets using Eq. 6-9. Hypothesis tests were conducted assuming that every magnetic value recorded over any path is independent from the others, every data set recorded over a path is a sample, all the data sets that can be collected over any rebar are considered one population. Using Table 6-5, the difference between the values of the magnetic data recorded over two different paths of a rebar can be reviewed using the p-values, and considering the comparison of T_{probe} and $T_{critical}$. If we consider different significance levels, the comparison between T_{probe} and $T_{critical}$ shows that the mean values of the magnetic flux densities recorded over two paths for any rebar are significantly equal to each other. Additionally, regarding the P-values, there is very weak evidence for rejecting the null hypothesis (H_o) mentioned in Eq. 6-9, except for the rebars with mass loss percentages of 4.73 and 14.3. For these two rebars, although the P-values show strong evidence for rejecting the H_o, the mean values of data recorded over two different paths of the each of the two rebars are considered equal using the comparison between the T_{probe} and $T_{critical}$, with the low significance levels of 0.001 and 0.02. Consequently, using the results of the T-tests, the populations' mean values for every two data sets recorded over two different paths of the same rebar are significantly equal to each other.

$$T_{probe} = \frac{(\bar{X}_{path\,1} - \bar{X}_{path\,2})}{S_P \sqrt{\dfrac{1}{n_{path\,1}} + \dfrac{1}{n_{path\,2}}}}$$

<div align="right">(6-9)</div>

$$S_P = \sqrt{\frac{(n_{path\,1} - 1)S^2_{path\,1} + (n_{path\,2} - 1)S^2_{path\,2}}{n_{path\,1} + n_{path\,2} - 2}}$$

S: $Standard\ deviation$

n: $total\ number\ of\ data$

$Null\ hypothesis$: H_o: $\mu_{path\,1} = \mu_{path\,2}$

$Alternative\ hypothesis$: H_1: $\mu_{path\,1} \neq \mu_{path\,2}$

Table 6-5. Comparisons of the mean values of the magnetic data recorded over paths 1 and 2 for all rebars.

Two data sets subjected to T-testing	$T_{critical} = T_{df,\frac{\alpha}{2}}$	T_{probe}	P-value	Conclusion
Data recorded over paths 1 and 2 of the rebar with 0% mass loss	$T_{560,\frac{0.2}{2}} = 1.282$	-1.080	0.282	$\|T_{probe}\| < \|T_{critical}\|$ $\rightarrow H_o\ is\ true$
Data recorded over paths 1 and 2 of the rebar with 4.73% mass loss	$T_{662,\frac{0.02}{2}} = 2.326$	2.136	0.032	$\|T_{probe}\| < \|T_{critical}\|$ $\rightarrow H_o\ is\ true$
Data recorded over paths 1 and 2 of the rebar with 7.02% mass loss	$T_{787,\frac{0.02}{2}} = 1.645$	-1.375	0.169	$\|T_{probe}\| < \|T_{critical}\|$ $\rightarrow H_o\ is\ true$
Data recorded over paths 1 and 2 of the rebar with 9.07% mass loss	$T_{769,\frac{0.5}{2}} = 0.674$	-0.455	0.648	$\|T_{probe}\| < \|T_{critical}\|$ $\rightarrow H_o\ is\ true$
Data recorded over paths 1 and 2 of the rebar with 12.2% mass loss	$T_{698,\frac{0.05}{2}} = 1.960$	1.864	0.062	$\|T_{probe}\| < \|T_{critical}\|$ $\rightarrow H_o\ is\ true$
Data recorded over paths 1 and 2 of the rebar with 14.3% mass loss	$T_{641,\frac{0.001}{2}} = 1.960$	-3.219	0.001	$\|T_{probe}\| < \|T_{critical}\|$ $\rightarrow H_o\ is\ true$

6.5.3. Standard deviation hypothesis testing

For the final step of reviewing the consistency of magnetic data recorded over two different paths of the same rebar, F-testing was implemented (using Eq. 6-10). These F-tests were done using the same assumptions considered for the T-tests, and examined whether the variances of the two data sets' populations are equal. The difference between the variances of every two samples is revealed by comparing $F_{critical}$ and F_{ratio}, and also by examining the P-values. Table 6-6 shows that the p-values are very weak for rejecting the null hypothesis, demonstrating that H_o is true and that the populations' SDs of the data sets recorded over two different paths for any rebar are significantly

equal to each other. Additionally, the absolute values for the F_{ratio} are less than corresponding absolute $F_{critical}$ values in the F-tests. The $F_{critical}$ and F_{ratio} values were compared considering a significance level of 0.1 to test between the data recorded over two different paths for all the rebars, except for the rebar with 4.73% mass loss, which involved a significance level of 0.05. These results extracted from the comparison of the $F_{critical}$ and F_{ratio} values again confirm the understandings, based on the P-values, that the variances of the populations of the two data sets, recorded over two different paths for the same rebar, are significantly equal to each other.

$$F_{ratio} = \frac{S^2_{path\ 1}}{S^2_{path\ 2}}$$

(6-10)

$S: Standard\ deviation$

$Null\ hypothesis: H_o: \sigma^2_{path\ 1} = \sigma^2_{path\ 2}$

$Alternative\ hypothesis: H_1: \sigma^2_{path\ 1} > \sigma^2_{path\ 2}$

Table 6-6. Comparisons of the SD values of the magnetic data recorded over paths 1 and 2 for all rebars.

Two data sets subjected to F-testing	$F_{critical} = F_{df\ in\ numerator,\ df\ in\ denominator\ ,\ \alpha}$	F_{ratio}	P-value	Conclusion
Data recorded over paths 1 and 2 of the rebar with 0% mass loss	$F_{560,\ 560,\ 0.1} = 1.114$	0.9243	0.824	$\|F_{ratio}\| < \|F_{critical}\|$ → H_o is true
Data recorded over paths 1 and 2 of the rebar with 4.73% mass loss	$F_{662,\ 662,\ 0.05} = 1.136$	1.1068	0.096	$\|F_{ratio}\| < \|F_{critical}\|$ → H_o is true
Data recorded over paths 1 and 2 of the rebar with 7.02% mass loss	$F_{787,\ 787,\ 0.1} = 1.095$	0.9935	0.536	$\|F_{ratio}\| < \|F_{critical}\|$ → H_o is true
Data recorded over paths 1 and 2 of the rebar with 9.07% mass loss	$F_{769,\ 769,\ 0.1} = 1.096$	1.0913	0.112	$\|F_{ratio}\| < \|F_{critical}\|$ → H_o is true
Data recorded over paths 1 and 2 of the rebar with 12.2% mass loss	$F_{698,\ 698,\ 0.1} = 1.101$	0.9596	0.706	$\|F_{ratio}\| < \|F_{critical}\|$ → H_o is true
Data recorded over paths 1 and 2 of the rebar with 14.3% mass loss	$F_{641,\ 641,\ 0.1} = 1.106$	0.9993	0.503	$\|F_{ratio}\| < \|F_{critical}\|$ → H_o is true

6.6. Data processing and discussion on the scanning results

Investigations using correlation coefficients calculations, T-tests, and F-tests showed strong consistencies between the magnetic data recorded over paths 1 and 2 for all the rebars. Hence, the magnetic data recorded over one of those paths (path 2) for all the rebars were selected for the rest

of the study. Next, three different data-processing approaches were used to compare the magnetic data recorded over different rebars.

6.6.1. Data-processing approach #1: calculating the power of magnetic data's derivative signal

Data-processing approach #1 was conducted for the selected scans over each of the six rebars shown in Figure 6.2. First, 70 mm of the either end of the scans was deleted to remove edge effects. The derivative values were then computed by MATLAB 2018 b for every data set separately. Subsequently, for every rebar, the best fitted straight-line was subtracted from the data to remove the secular linear trend. Next, centered moving average smoothing technique (Eq. 6-7), with a period of about 3 mm, was applied to the data post removal of the linear trend.

Figure 6.12 shows the magnetic data's derivative values for all six rebars after removal of their linear trends and subjecting them to moving average smoothing. The derivative values of different rebars' data varied from one rebar to the other. For instance, the range of the values for the rebars with 9.07 and 12.2 mass loss percentages is noticeably greater than for the other rebars. These remarkable differences were probably generated by the approach used to produce the corroded rebars. For creating different degrees of corrosion, multiple rebars were embedded in different concrete slabs and subjected to a constant current (Al-Hammoud *et al.*, 2011). Hence, based on the Biot-Savart law, the magnetic properties of the rebars might be affected by the current intensity and the distance from the current injection point.
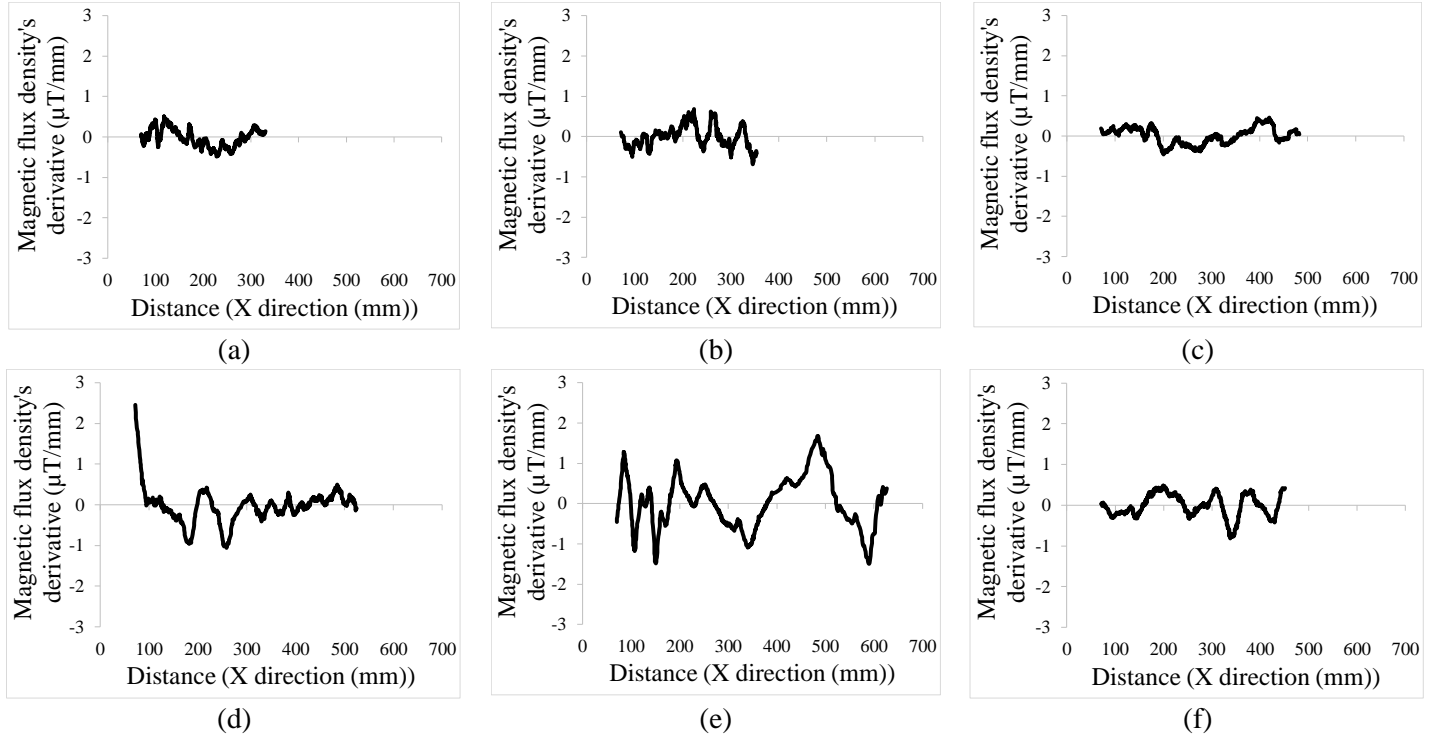
Figure 6.12. Magnetic flux density's derivative values, after removing linear trends and taking the centered moving averages: (a) For the rebar with 0% mass loss, (b) For the rebar with 4.73% mass loss, (c) For the rebar with 7.02% mass loss, (d) For the rebar with 9.07% mass loss, (e) For the rebar with 12.2% mass loss, (f) For the rebar with 14.3% mass loss.

Considering the magnetic flux density's derivative values as a discrete-distance domain signal, the energy (size) of the data can be used to quantify the outcomes produced in this section. Eq. 6-11 shows the signal's energy formula for a finite interval, from data number $-N$ to N. The energies of the data sets shown in Figure 6.12 are affected by the lengths of the rebars (i.e., the total number of data recorded over the length of the rebars). To remove the effect of the rebars' lengths, the average power of the signals (Eq. 6-12) can be considered by normalizing the energy values. Assuming that the data sets of the magnetic flux density's derivative values are power signals and are periodic with fundamental periods equal to the lengths of rebars, the Eq. 6-12 is simplified to Eq. 6-13 (Proakis and Manolakis, 1996) that was used in this study.

$$E_N \equiv \sum_{n=-N}^{N} |magnetic\ data\ (n)|^2 \tag{6-11}$$

$$P \equiv lim_{n \to \infty} \frac{1}{2N+1} E_N \tag{6-12}$$

$$P = \frac{1}{N} \sum_{n=0}^{N-1} |x(n)|^2 \qquad (6\text{-}13)$$

Figure 6.13a shows an ascending trend in signal power with the increase in rebar corrosion. The ascending trend was estimated by linear regression with a small correlation coefficient of $R^2 = 0.2137$. To increase the reliability of the linear regression, the box and whisker plot of the powers' values was plotted, and the value related to the rebar with a 12.2% mass loss was recognized as an outlier (Figure 6.13b). Subsequently, the linear regression was conducted on data again, but without considering the outlier value (Figure 6.13c). Removing the value related to the rebar with a 12.2% mass loss remarkably decreased the slope of the ascending trend; it also reduced the goodness of fit (R^2) of the regression. However, this regression line (Figure 6.13c) is the most accurate one that can be calculated using the current data and the approach of calculating the power of the magnetic flux density's derivative signal.

| (a) | (b) | (c) |
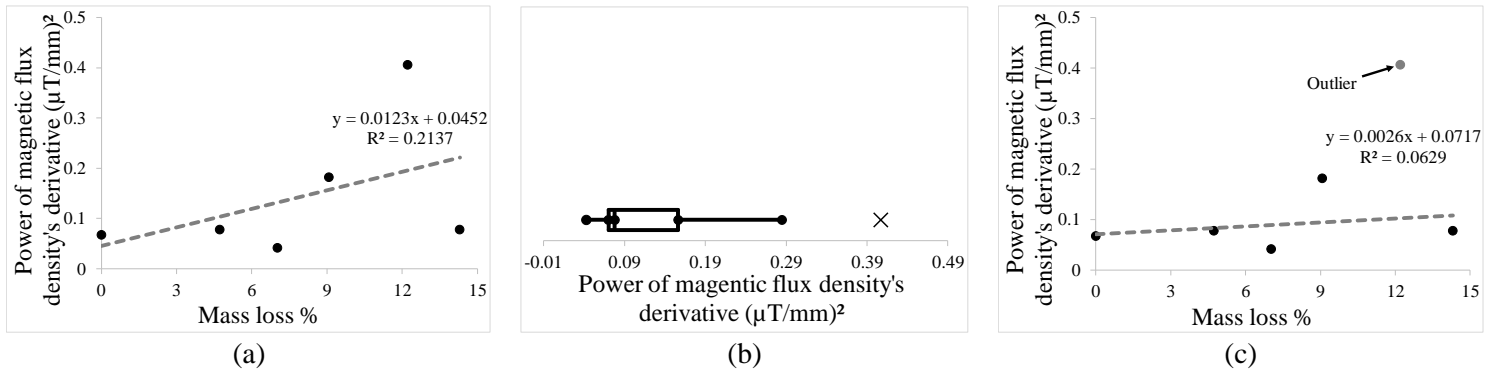
Figure 6.13. Power of the magnetic flux density's derivative values for all the rebars: (a) Linear regression for all the power values, (b) Box and whisker plot applied to power values, (c) Linear regression for the power values with no outliers.

6.6.2. Data-processing approach #2: calculating the dominant frequencies affecting magnetic data and their corresponding magnitudes

Figure 6.10 shows that the overall behavior of magnetic flux density values for different rebars are clearly different from each other. These differences might be related to the inherent magnetic properties resulting from the corrosion products, seen by the different colors covering the surfaces of the rebars. To quantify the differences between the magnetic data of different rebars, the single-sided magnitude spectrum of the magnetic data was provided using MATLAB 2018 b (Data-processing approach #2). The magnitude spectrums were produced for all the selected magnetic data (based on T-hypothesis testing) recorded over path 2 of the rebars (Figure 6.14a). At first, to remove the sharp changes due to edge effects, 70 mm of the first and the last of the scans were

ignored. Subsequently, a centered moving average data smoothing technique (Eq. 6-7) with a period of about 3 mm was carried out on the remaining data. Next, 99000 zeros were appended to the distance domain magnetic data, and the magnitude spectrum was generated using a Hanning window function.

In Figure 6.14a the magnetic-flux-density curves for all the rebars show a dominant low frequency. Using a box and whisker plot helped in finding the outliers for the values of dominant low frequencies (Figure 6.14b). Using the remaining values, Figures 6.14c and 6.14d show that increasing the rebars' corrosion exponentially increases the dominant low frequency values and decreases their corresponding magnitude values. However, the goodness of fit (R^2) for the exponential regression for the magnitude values is much higher than that for their corresponding frequency values, showing the better reliability of the results found by the magnitude values.
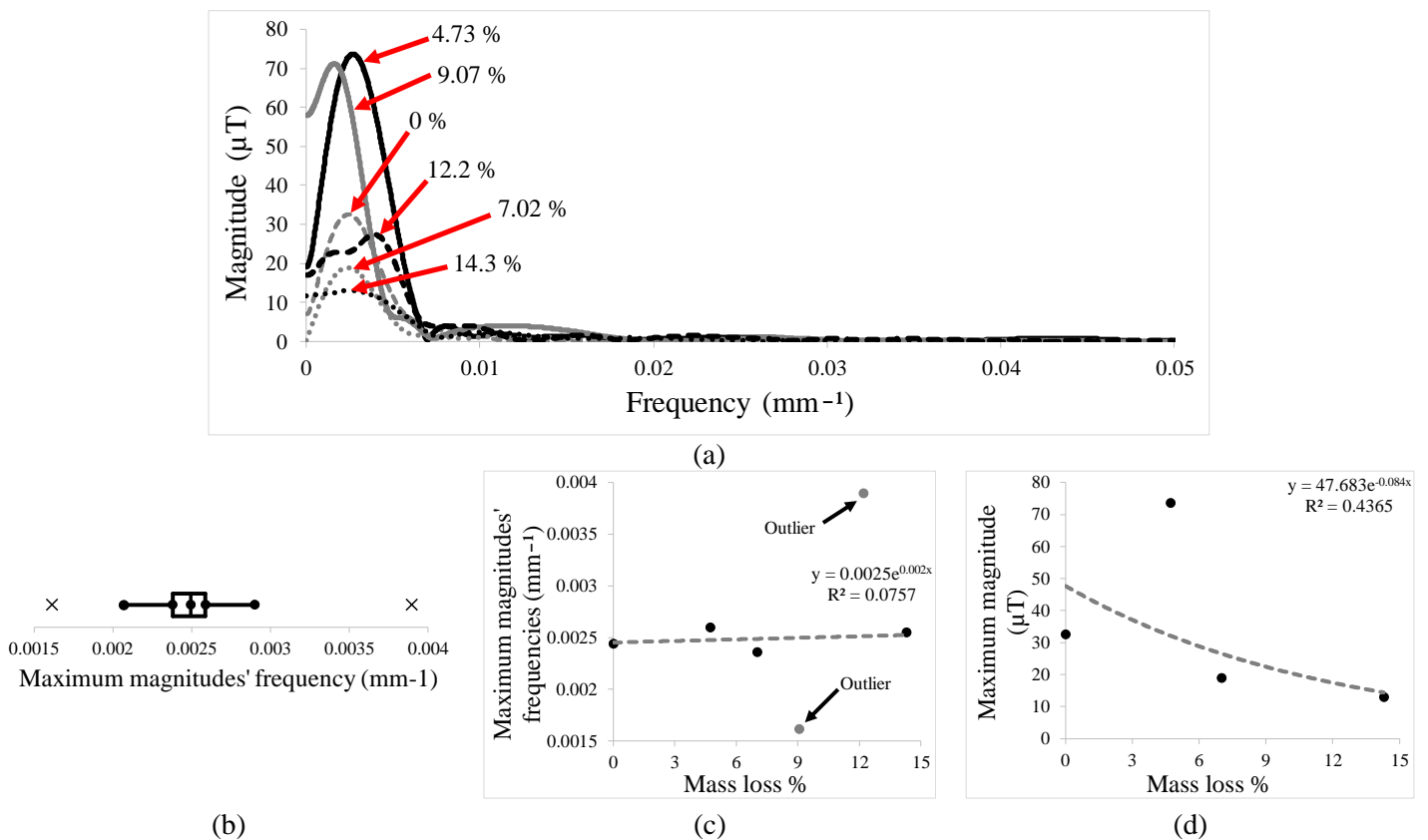
Figure 6.14. Investigation of the magnitude spectrums of the magnetic data recorded over rebars with different mass loss percentages: (a) Single-sided magnitude spectrum of the magnetic flux density values (red arrows show the percentages of mass loss), (b) Box and whisker plot applied on dominant-low frequency values, (c) Exponential regression for the dominant-low frequency values (without considering the outliers), (d) Exponential regression for the magnitude values corresponding to the frequency values used for the regression in part c.

6.6.3. Data-processing approach #3: calculating the standard deviation of magnetic data

For the final analysis, data-processing approach #3 was carried out for the selected scans (based on T-hypothesis testing) over path 2 for all six rebars (Figure 6.10b). Initially, 70 mm of data from both ends of every scan were deleted to remove the edge effects. The rest of the data was then subjected to the centered moving average smoothing technique (Eq. 6-7). The data recorded over all the rebars were separately split into equal sections of 15 mm. A 15 mm length was decided for the sections in a way guaranteed to include the rebars' ribs. Next, the linear trends were separately removed by subtracting the best-fit straight-line from the magnetic data at every section. Subsequently, the standard deviations of each section's magnetic data were calculated. The SD values were then shown at the places of the average distances included in every section (Figure 6.15). Separately for each rebar, the mean values of the standard deviations of all the sections were calculated to quantify the results.

The magnetic data recorded over the surface of the intact rebar is expected to have a clear regular up and down trend due to the rebar's corrugated shape (Mosharafi *et al.*, 2018). General corrosion flattens the rebar's surface bumps, so the magnetic data recorded over the corroded rebar tend to fluctuate closer to their mean value compared to those of an intact rebar. The degree of general corrosion based on the mass loss criterion does not mean a consistent and uniform lowering of the manufactured ribs, so considering the average conditions of rebars is more helpful than point-to-point checking. Therefore, it is expected that the mean values of all the standard deviations calculated for each corroded rebar would be less than that for the intact rebar. However, the mean values of the standard deviations calculated for the rebars with mass loss percentages of 9.07 and 12.2 are greater than that for the rebar with a 0% mass loss.

The unexpected high values for the standard deviations are not related to the surface shape of the rebars and might have been generated by the procedure used in creating the required corroded samples. One of these high standard deviation values (related to the rebar with 12.2% mass loss) was identified as an outlier (Figure 6.16a), but there was not enough evidence for ignoring other high values (related to the rebar with 9.07% mass loss). The regression for determining the best-fitted line in Figure 6.16b was conducted without considering the outlier (a value related to the rebar with 12.2% mass loss). Based on the regression, an exponential descending trend is observed for the mean values of standard deviations of the magnetic data by increasing the percentages of

the mass loss. The goodness of fit of the fitted line is equal to 0.5334, which demonstrates the greater reliability of the results of data-processing approach #3 compared to the outcomes extracted from data-processing approaches #1 and #2.

(a)

(b)

(c)

(d)

(e)

(f)
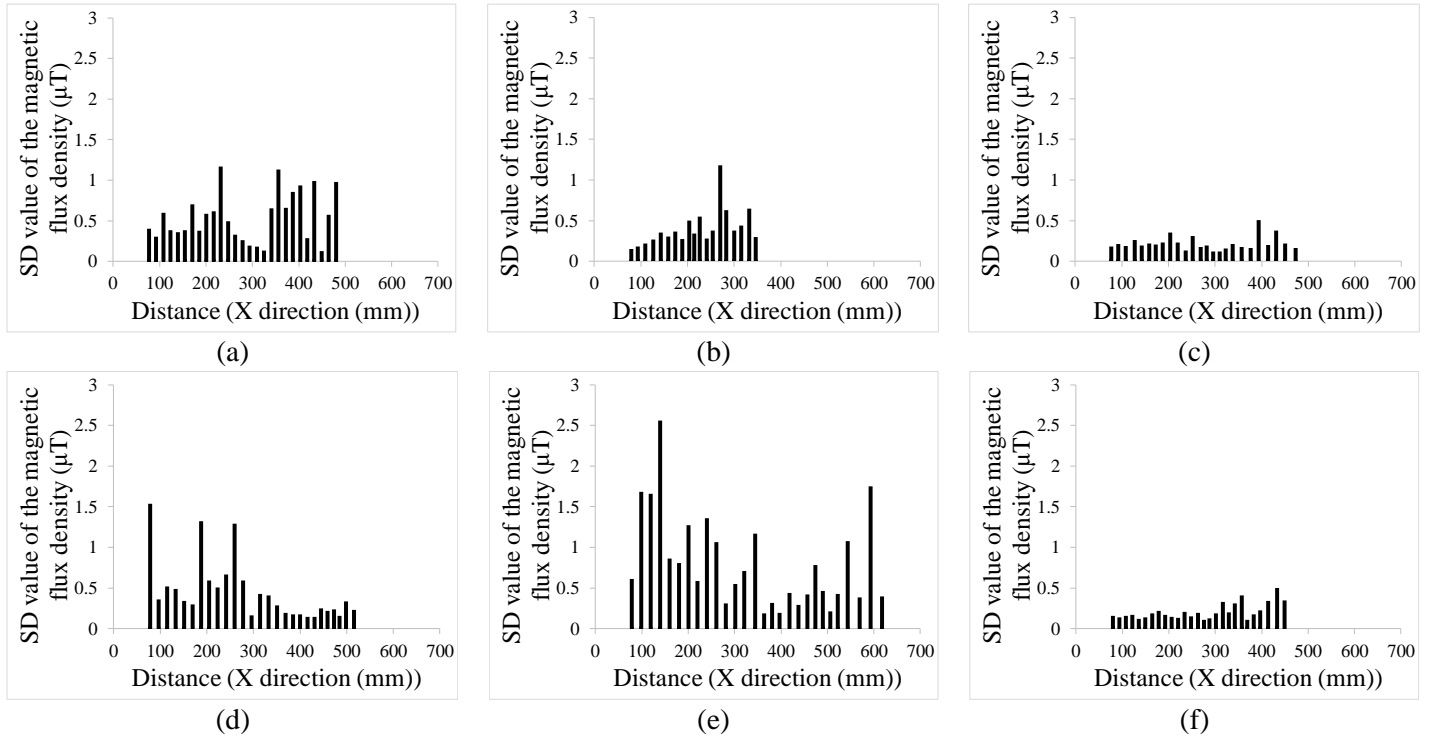
Figure 6.15. Standard deviations of equal sections of magnetic data, after removing their linear trends: (a) For the rebar with 0% mass loss, (b) For the rebar with 4.73% mass loss, (c) For the rebar with 7.02% mass loss, (d) For the rebar with 9.07% mass loss, (e) For the rebar with 12.2% mass loss, (f) For the rebar with 14.3% mass loss.

(a)

(b)
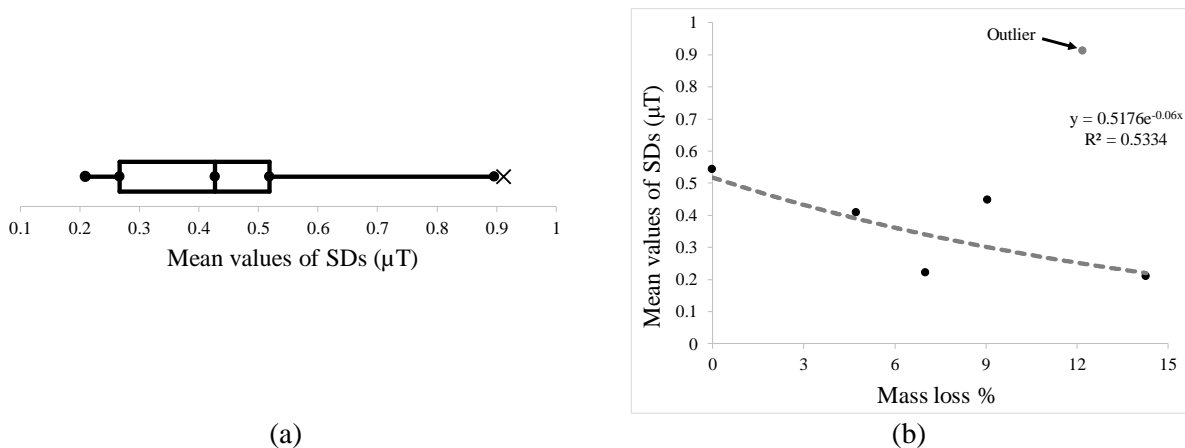
Figure 6.16. Investigating standard deviations in magnetic data recorded over rebars with different mass loss percentages: (a) Box and whisker plot applied on the mean values of all standard deviations calculated for each rebar, (b) Exponential regression for the values in part a (without considering the outlier) in relation to mass loss percentages.

6.7. Conclusion

Categorizing the reinforcement steel embedded in concrete based on corrosion provides an appropriate schedule for maintenance activities, thus mitigating the risk of unexpected infrastructure loss-of-service or structural failures. To this end, investigations were conducted on six rebars with different corrosion degrees, from zero to 14.3 percentage of mass loss. First, the required number of replications were statistically determined so as to obtain necessary significance and power levels, using the magnetic data sets recorded over an intact rebar. The statistical analysis also assisted in detecting the sources affecting the variations between scans, conducted over the same path, by the same PMI scanner. Next, one by one, rebars with different percentages of mass loss were placed along the same orientation and at the same non-magnetic location. Once in place, each was scanned (considering required replications) along its whole length using the PMI scanner, over two specific paths. Subsequently, the consistency between the magnetic data sets recorded over the two paths on each rebar was confirmed through three different statistical approaches. After ensuring this consistency, the magnetic data sets, recorded over the six rebars, were subjected to three data-processing approaches to help in determining the relation between the magnetic properties and the rebars' corrosion degrees. In conclusion:

- According to the statistical analysis of magnetic data sets recorded over the same path on the intact rebar, the variations between the scans are generated for the following reasons:
  - 8% of the total variation is due to changes in the local magnetic field and inherent sensor errors plus the changes at one point of the rebar's magnetic values at the scanning time;
  - 92% of the total variation is due to operator errors during scanning, such as deviations from the set path, or inaccuracy in the scan's starting point;
- With respect to the statistical investigations' outcomes, scans can be repeated over the same path, to satisfy different significance levels and powers. For instance, the same path on every rebar should be scanned five times to obtain a significance level of less than 5% and a power of greater than 90%;
- Regarding the investigations on rebars with different corrosion degrees, the magnetic data sets recorded over two different paths for the same rebar correlated well. Those magnetic data sets also had significantly equal mean and standard deviation values. This finding confirms the reliability of the magnetic values collected by the PMI scanner;

162

- Subjecting the magnetic data recorded over the rebars with different mass loss percentages to the three data-processing approaches, led to the following outcomes:
  - Data-processing approach #1: the power of the magnetic datas' derivative signal decreases as the corrosion degree increases;
  - Data-processing approach #2: the magnitude of the dominant frequencies affecting magnetic data decreases as the corrosion degree increases;
  - Data-processing approach #3: the mean value of all standard deviations, calculated at equal sections of a magnetic data set, decreases as the corrosion increases;
- The relations between the different parameters generated from magnetic data and the mass loss percentages in the data-processing approaches' outcomes were obtained using regression analyses. The R-squared values for the regression models associated with data-processing approaches #1, #2, and #3 were respectively equal to 0.06, 0.44, and 0.53. Thus, the results of data-processing approach #3 showed greater reliability than the outcomes generated with data-processing approaches #1 and #2.
- A statistical and reliability context has been generated in the laboratory for corroded rebars, and because the self-magnetic field is unaffected by non-ferromagnetic substances or environmental conditions, extrapolation of these findings to field condition scanning is appropriate.

Chapter 7: Assessing a bridge structure using PMI technology

7.1. Introduction

PMI technology's physical concept and theoretical background have been presented in the first chapter. Subsequently, Chapters 2 to 6 described experiments and simulations conducted to investigate PMI's potential for detecting anomalies in steel reinforcements. Through the findings from the previous chapters, to verify the reliability of PMI technology under actual field conditions, this chapter reports the field investigation of a culvert (small bridge) structure (C072). The results from the PMI inspection are then compared with the results of a visual inspection and previous assessments.

For conducting this study, historical information related to culvert C072 is evaluated. The information was generated from visual inspection and from measuring the half-cell potential, the concrete's compressive strength and air content, and the chloride content at some parts of the culvert's deck. Next, the reinforcement orientation and concrete cover thicknesses of selected sections of the culvert's deck are detected. Subsequently, the SMFL values are recorded over the detected reinforcements using the PMI technology. The recorded magnetic datasets are subjected to two data processing approaches, and the outcomes are compared with the historical information. Using the results of PMI technology assessment, concrete cover thicknesses values, and the historical information, the culvert's condition is represented quantitatively as a map of condition. Recommendations are then made for improving the culvert's condition (Figure 7.1).
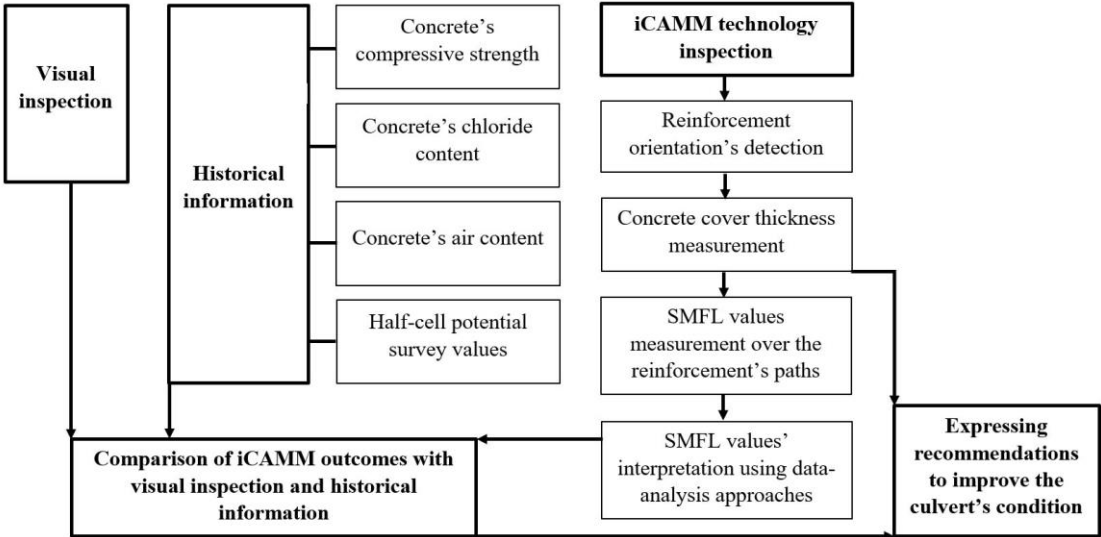
Figure 7.1. Methodology flowchart, showing the sequence of the assessments.

7.2. Culvert specifications

Culvert C072 is located in the north end of the City of Markham (Ontario, Canada), at 19th Avenue – 150m west of McCowan Road (Figure 7.2). The culvert structure, built in 1982, carries two lanes of traffic over a Little Rouge Creek tributary (Figure 7.3); its specifications are shown in Table 7-1 and Figure 7.4.
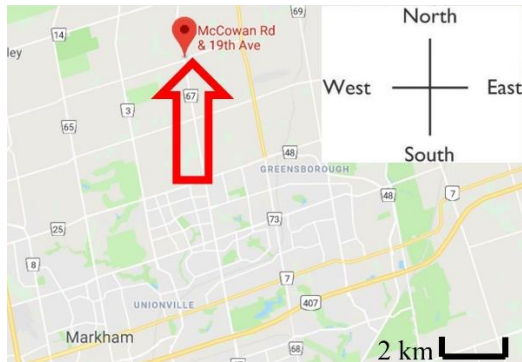
Figure 7.2. Culvert C072 location.

Figure 7.3. Culvert C072, with walls' names (North wall is on the other side of the road and cannot be seen in this picture).

Table 7-1. Specifications of culvert C072.

Total deck length	6.74 m
Overall deck width	13.4 m
Roadway width	7.43 m
Total deck area	90.3 m^2
Span lengths	6.06 m
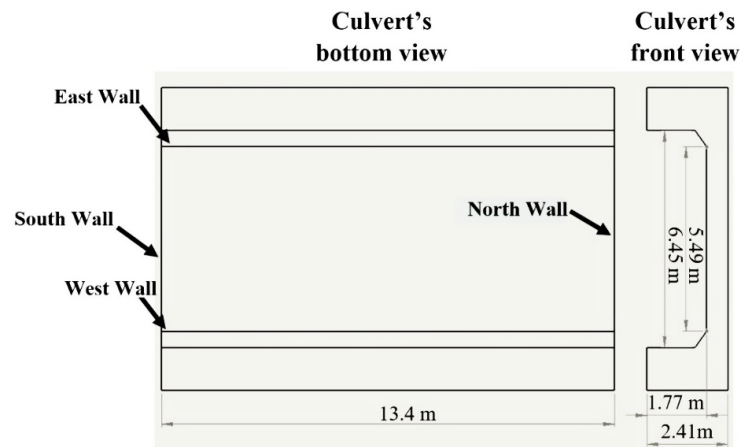
Figure 7.4. The bottom and front view of the culvert structure.

7.3. Historical assessment results

Detailed visual inspection of the culvert was done in October 2017, and the general concrete condition of the culvert structure was investigated in the spring of 2019. In the visual inspection,

certain conditions on the undersurface of the culvert deck (the top slab soffit) indicated probable reinforcement corrosion (Figure 7.5). The signs included discoloration, delamination, scaling, bugholes, and cracks. These signs could be observed throughout the structure, but were more intense closer to the south and north ends of the deck undersurface where, at the time of inspection using PMI technology, concrete spalling spots had become obvious.

The condition of the culvert's deck was further investigated by extracting powder and core samples and subjecting them to different experiments. Figure 7.5 shows the measurement values of the air content, compressive strength, and chloride ion content extracted from the samples. The air content was measured from one of the samples (in accordance with ASTM C457); the value was marginal and did not indicate any specific corrosion condition. Four cores were tested to determine the concrete's compressive strength (in accordance with CSA A23.2-09-14C (CSA group, 2014)). The lowest strength value was measured on a sample extracted close to the culvert's south end. Reduction in the concrete's strength indicates a higher permeability, and thus greater likelihood of steel reinforcement corrosion (Rashid *et al.*, 2010).

The chloride ion levels were measured at different points in the core samples; the average values are reported in Figure 7.5. The protective passive film on steel rebars can be damaged by chloride ions. The probability of corrosion also increases as the chloride content increases (Verma *et al.*, 2013). Regarding the experiments conducted on concrete samples (in accordance with MTO LS-417 (Ministry of Transportation of Ontario, 1996)), the lowest chloride ion content was in the sample located in the middle of the north and south ends, but this amount still demonstrates heavily chloride-contaminated concrete. Additionally, the first and second highest chloride ion contents were respectively in samples extracted close to the south and north ends.

Half-cell survey corrosion mapping was also conducted on the undersurface of the culvert deck, as an additional method to estimate the corrosion extent. However, the measured potential values can vary significantly due to the effects of different parameters, such as moisture level and chloride concentration (Zaki *et al.*, 2015). As seen in Figure 7.6, the measured potential values are more negative at the soffit south and north ends, indicating a high probability of active corrosion. A moderate probability of active corrosion is also demonstrated in the middle of the north and south ends, with a potential value of -0.340 V.

East wall

A-C	Air content		Delaminations
C-S	Compressive strength		Light scaling
Ch-I-C	Chloride ion content		Medium concrete cracks
			Sample location
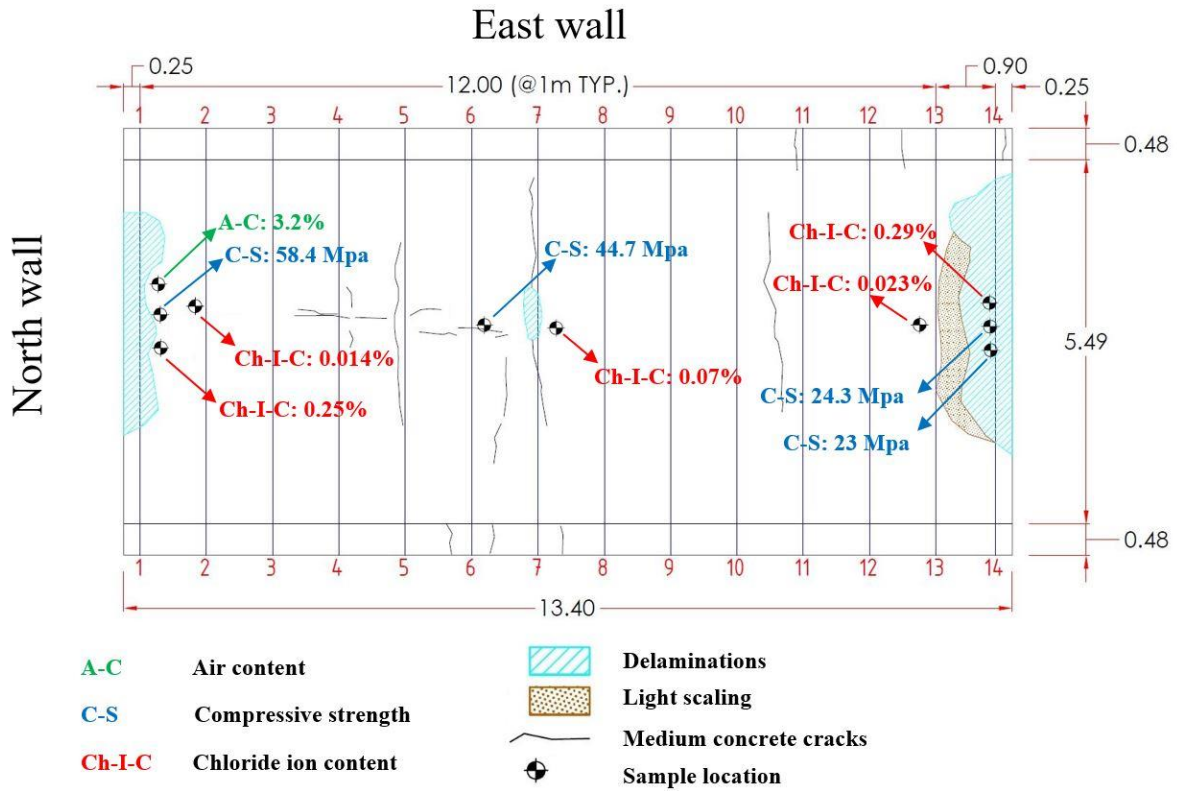
Figure 7.5. Surface deterioration of the top slab soffit and information extracted from the concrete samples.

East wall

C1	Core sample location		0.000 to -0.199 volts
PS1	Powder sample location		-0.200 to -0.299 volts
	Copper-copper sulphate half cell potential (negative volts $\times 10^{-3}$)		-0.300 to -0.349 volts
			-0.350 to -0.449 volts
			More negative than -0.450 volts
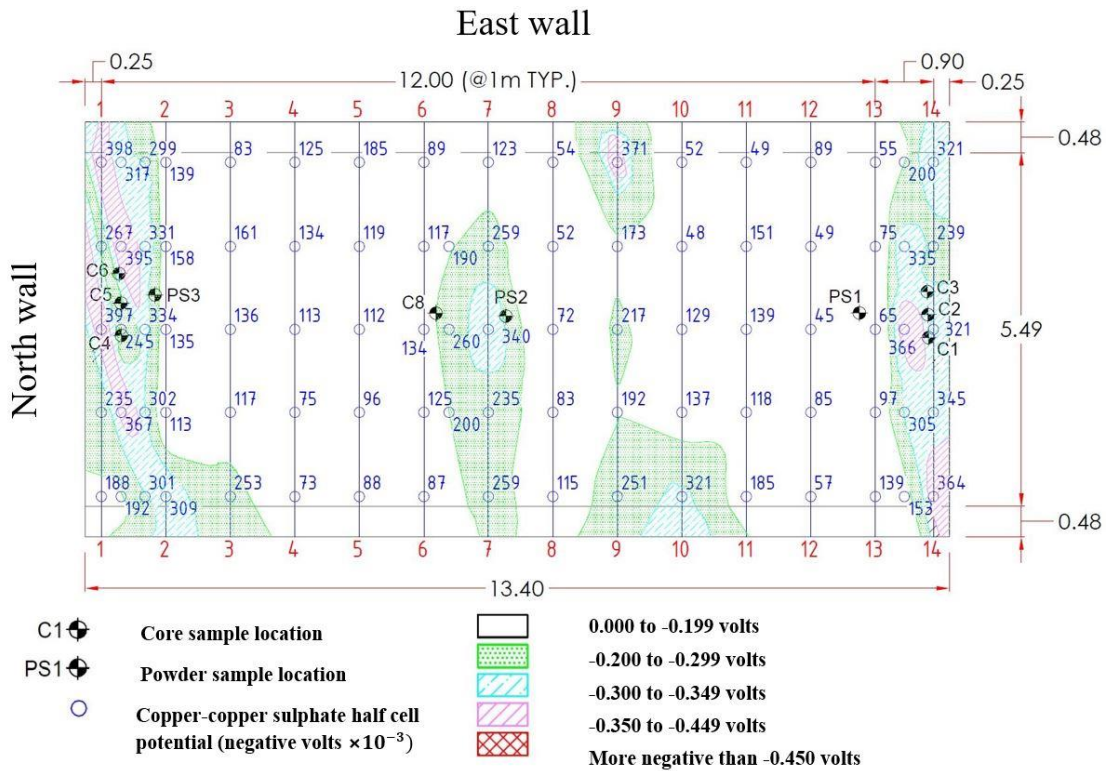
Figure 7.6. Half-cell survey potential values of the top slab soffit.

167

7.4. PMI data gathering procedure

For a general overview of the reinforcement condition of the culvert, PMI inspection focused on three sections:

- Section #1, close to the north end (where significant corrosion signs were observed on the surface of the concrete);

- Section #2, in the middle of the north and south ends (where no significant corrosion signs were observed); and,

- Section #3, close to the south end (where significant corrosion signs were observed as well).

To start the inspection, the locations, concrete covers, and paths of rebars oriented in the west to the east direction in the sections defined above were determined using an industrial rebar detector – the Bosch D-Tect 150 (Figure 7.7a). Next, the identified paths were marked on the concrete surface using a permanent marker (Figure 7.7b). To represent the corrosion conditions in each section, three, four, and two rebar paths were detected and marked respectively in sections #1, #2, and #3 (Figure 7.8). These paths were at the surface of the concrete and extended from 17.5 cm after the West wall to 3 cm before the East wall.

| (a) | (b) |

Figure 7.7. Pre-inspection activities before recording the magnetic data: (a) Locating rebars using a rebar detector; (b) Marking rebar paths using a permanent marker.
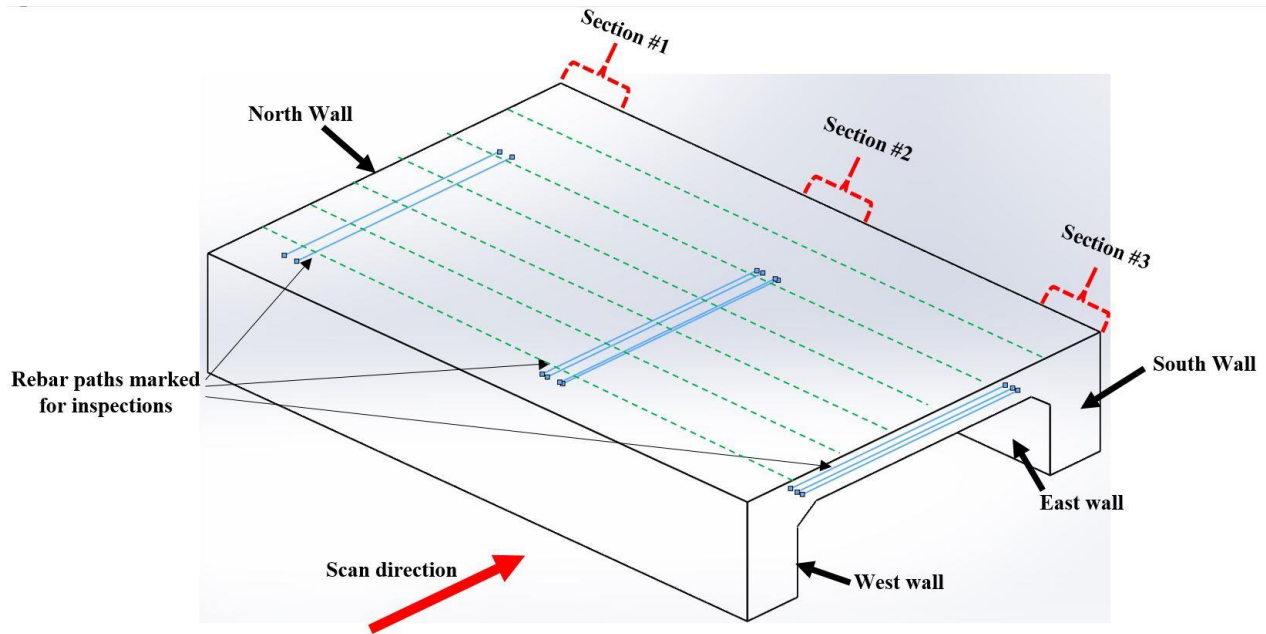
Figure 7.8. An overall view of the culvert deck (blue solid lines show the rebar paths marked for inspections; green dashed lines represent crossed reinforcement paths in the culvert structure).

For the next step, the raw magnetic data were recorded by moving the PMI scanner (Figure 7.9) separately over each path shown in Figure 7.8. Nine separate scans were conducted to cover all the paths in sections #1, #2, and #3. Additionally, so the same scanning paths could easily be found again for re-inspections or for future maintenance activities, the scans' specifications were accurately determined and documented (Figure 7.10).

Figure 7.9. Recording the rebar's magnetic data from the surface of concrete using PMI scanner (blue line shows the rebar's orientation).

169
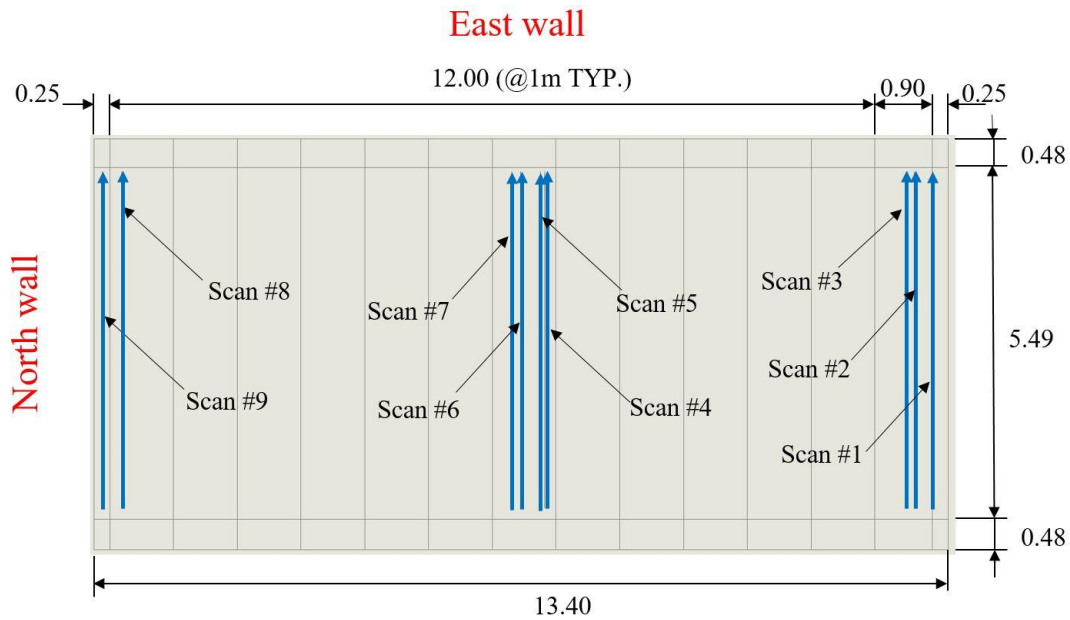
Figure 7.10. Deck map showing the paths, direction, and the names of scans (Culverts' top view; dimension values are in meters).

7.5. Cover thickness measurement and PMI inspection results

Concrete cover integrity over reinforcing steel is one of the significant parameters that affect structural corrosion conditions. Reduction in concrete cover or breaching the seal can increase the corrosion rate and structural failure probability (Vu and Stewart, 2000). For a better understanding of rebar conditions in the culvert deck, the concrete cover thickness values were measured at the start, middle, and the end of each scan (in Figure 7.10) using the rebar detector shown in Figure 7.7a. As seen in Figure 7.11, the thickness of concrete at the places closer to the East and West walls is generally greater than that at locations in the middle of the two walls. The least value for the concrete cover thickness was measured in the middle of scan #5, at approximately the center of the culvert deck (equal to 4.4 cm). These findings may indicate the site of culvert sagging (between the East and West walls) due to ongoing pressure from external loads, such as structural loads or passing vehicles. Additionally, the deck map (Figure 7.11) shows that the overall concrete cover thickness values close to the North wall (for the paths of scans #8 and #9) are less than those for the other scans.
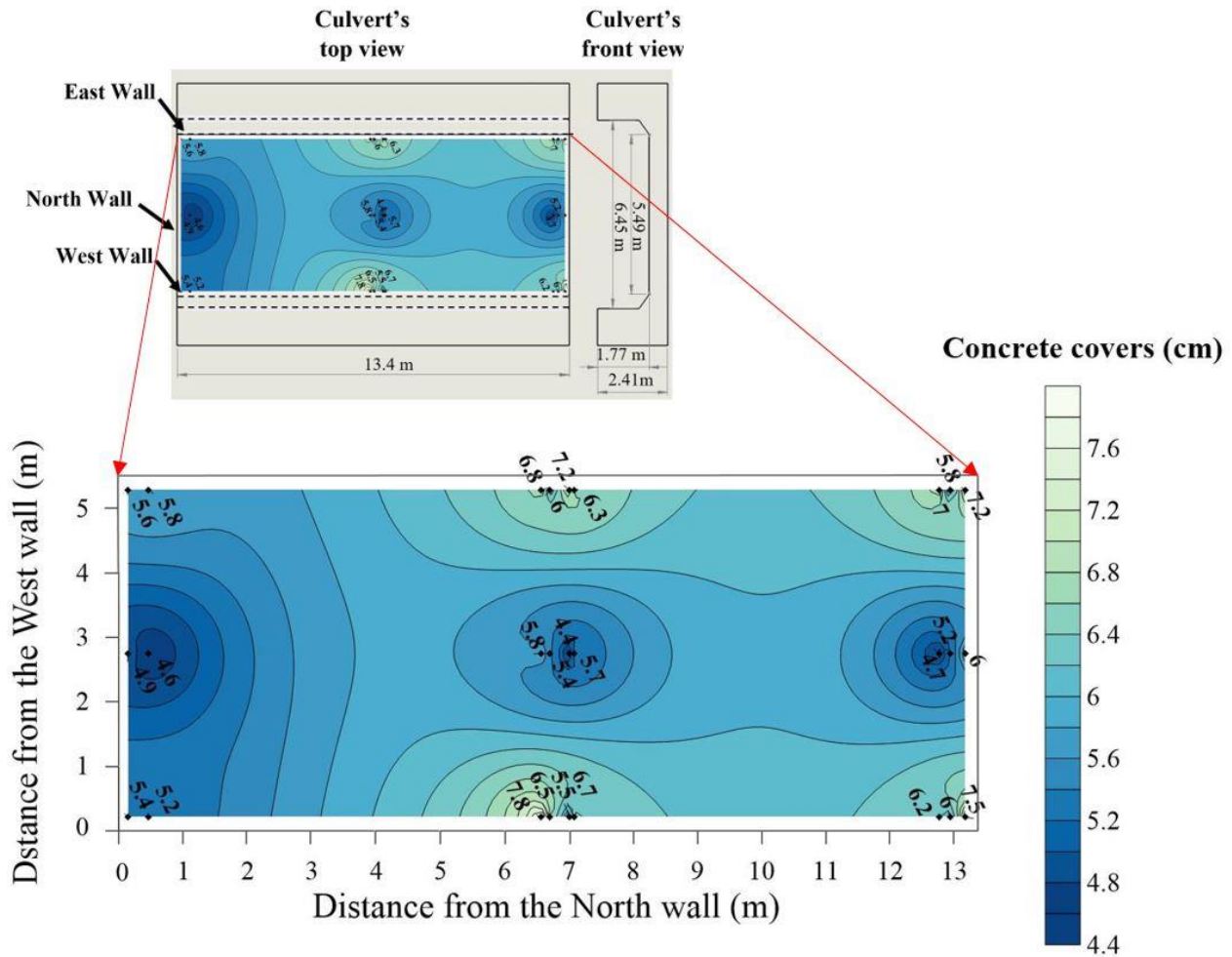
Figure 7.11. Deck map demonstrating the concrete cover thickness (black numbers in the map show the cover thickness in cm).

Magnetic data sets recorded in the scans (shown in Figures 7.8 and 7.10) and the derivative of each data set are shown in Figures a and b of all scans in the Appendix D. Some sharp irregularities can be observed in the magnetic derivative values (marked by red dotted-line squares in Figures D-1b, D-3b, D-7b, D-8b, D-9b), representing the possibility of changes in the physical conditions of the reinforcement steel. To quantify the magnetic data so as to detect the locations of defects in the reinforcement, two analysis approaches were used: analysis of data based on absolute gradient values (AG), and analysis of data based on the standard deviation of the gradient values (SG).

In the AG analysis approach, the derivative of the processed magnetic data set is computed, and the derivative absolute values are presented after removing the overall secular linear trend. However, in the SG analysis approach, the derivative of the processed magnetic data set is split into equal sections, and the standard deviation (SD) of each section is calculated. The SD values are then shown at the places of the average distances included in every section. Figures b and c of

171

all scans in the Appendix D show that the results generated from approaches AG and SG are in accordance with each other in each scan. The maximum values generated by both approaches mostly occur close to each other. However, the outcomes calculated by AG and SG analyses differ from one scan to another, as different rebar sections evidence different corrosion states.

To appropriately quantify the analyses outcomes, the results were calibrated based on evidence representing the actual physical conditions of the reinforcement steel. With respect to Figures b and c in all scans in the Appendix D, the highest values generated by the AG and SG analysis approaches happen in scan #1 at a distance of 236.2 cm to 246.9 cm from the West wall. The location coincides with the most-severe visible concrete spalling marring the undersurface of the culvert deck (Figure 7.12). Concrete spalling can happen due to swelling associated with corrosion products (ACI Committee 201 and American Concrete Institute, 2008), so this finding confirms the reliability of the results from the AG and SG analyses. The severity of corrosion associated with the concrete spalling can also be used in calibrating the analysis results, quantifying them based on the current physical conditions of the reinforcement.
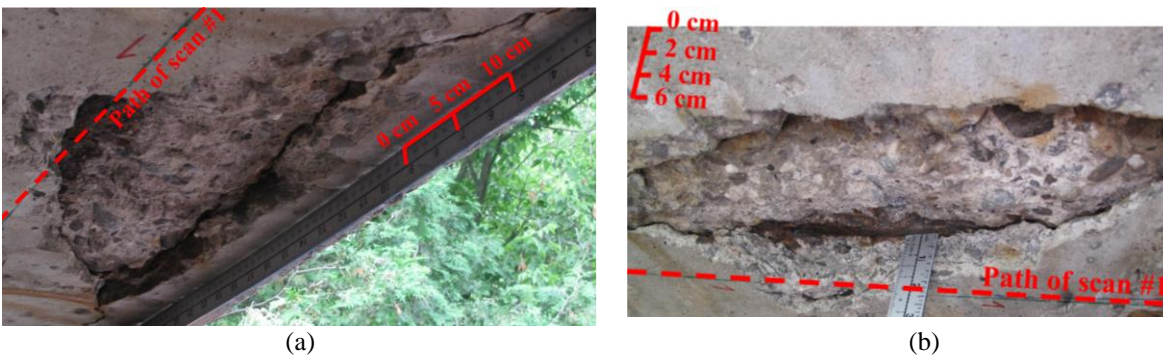
(a)   (b)
Figure 7.12. Most-severe concrete spalling in the undersurface of culvert deck (at approximately 240 cm to 300 cm from West wall, in scan #1): (a) Spalling extension, (b) Spalling depth.

Visual investigation and measurement of metal loss from the exposed rebar (Figure 7.12) indicated a roughly 20% loss in cross-section area, which corresponded to the highest extrema generated by AG and SG analysis approaches (in scan #1). This finding was then used to determine the metal loss percentages corresponding to other extrema in all scans by means of a proportionality concept, and separately for the two analysis approaches. To illustrate, Figure 7.13 shows the loss in cross-section area, based on the SG analysis approach, in reinforcement embedded in the culvert deck.

According to the deck survey map shown in Figure 7.13, the most severe corrosion is close to the South and North walls. Additionally, the plot shows noticeable metal loss in the middle of the

172

West and East walls, at about 700 cm from the South wall. There is also significant continuous corrosion about 120 cm from the West wall, starting from the South wall and extending about 700 cm. It should be mentioned that the corrosion conditions in Figure 7.13 are based on the interpolation of the nine scans conducted on the three sections (shown in Figure 7.8). The accuracy of the plot could be significantly increased by conducting more scans and using the extended results in the analysis.

In a magnetic based inspection method, defects are referred to as any change in the magnetic-domain properties of ferromagnetic reinforcement (Wang *et al.*, 2012). Magnetic domains' structures in ferromagnetic materials can change for various reasons, such as cracking, fatigue, stress concentration, and corrosion (oxidation and sulphate reactions). Thus, the defective locations identified in this chapter may reflect one or a combination of reasons for changes in the rebars' magnetic domains' structures. However, based on the calibration point (shown in Figure 7.8), assuming all other defects are of the same type, the reinforcement conditions were categorized. To categorize the defects for future maintenance plans, three limits were defined for the two analysis approaches:

- A limit for small defects, with the defects causing approximately a 4-7% loss in cross-sectional area;
- A limit for medium defects, with the defects causing approximately a 7-10% loss in a cross-sectional area;
- A limit for large defects, with those defects causing greater than 10% loss in cross-sectional area.

The local extrema identified by both analysis approaches indicating defects with greater than 4% loss in cross-sectional area are shown in the deck survey map (Figure 7.13) and recorded in the tables shown in the Appendix. Each table in the Appendix includes the number of defects, defect distances from the West wall, and the loss in cross-sectional area at extrema locations (resulting from SG and AG analysis approaches). The average loss in the cross-sectional area, determined using the AG and SG analysis approaches, is also shown in Tables A-1 to A-9. These average values are the most reliable outcomes and are represented in three colors representing the cross-sectional area loss categories: defects causing 4% to 7% loss are blue; defects causing 7% to 10% loss are red; and defects causing greater than 10% loss are black. It should be noted that the defects'

lengths were extracted based on AG analysis values, showing greater than 4% loss in the cross-sectional area, on either side of the extremum points. Considering the difference between the actual length of scans and the distances measured by the PMI scanner, an average of 5 cm error is expected in reported defect locations.
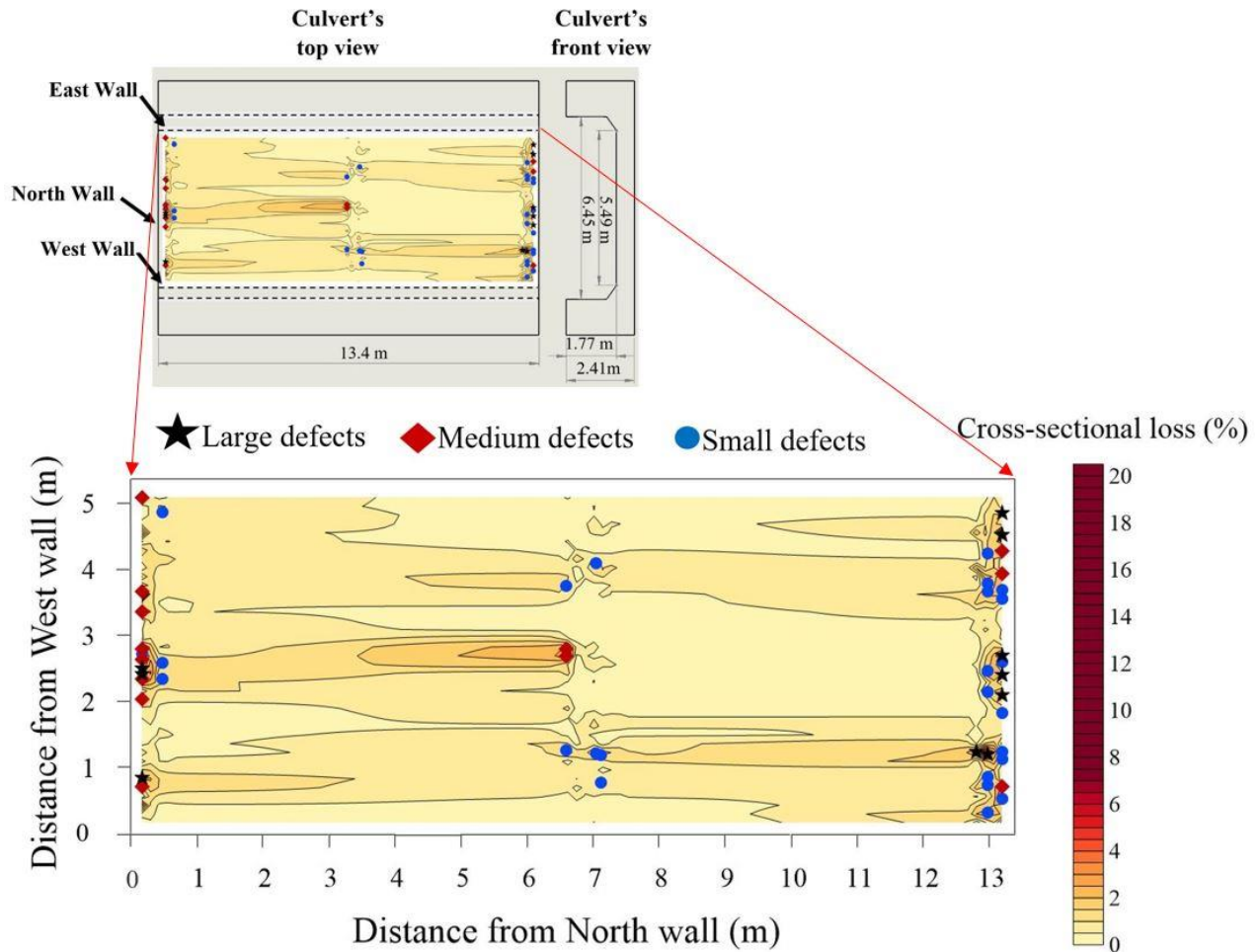
Figure 7.13. Deck survey map for reinforcement cross-sectional loss based on the SG analysis (large, medium, and small defects are represented regarding the average cross-section loss based on SG and AG approaches in the Tables shown in the Appendix D).

7.6. Discussion and recommendations

According to the results of compressive strength measurements, the sample extracted from the culvert's south end (representing section 3 in Figure 7.8), showed the most severe probability of corrosion. Chloride ion content measurements also demonstrated that the first, second, and third most-severe corrosion probabilities are related to sections #3, #2, and #1 (shown in Figure 7.8). Furthermore, the outcomes of half-cell survey corrosion mapping show probable active corrosion in the culvert deck's south and north ends, and in its center (Figure 7.6). All the above-mentioned

results from the measurements of compressive strength, chloride content, and half-cell potential survey agree with the PMI inspection's outcomes. Additionally, the deck survey maps resulting from visual inspection (Figure 7.5) and the half-cell potential survey (Figure 7.6) are strongly correlated with the map provided by the PMI technology (Figure 7.13). The following section presents the main outcomes of the PMI inspection in conjunction with other assessment outcomes, and the resulting practical recommendations.

Scan #1 shows the greatest number of defects with more than 4% loss in cross-sectional area. Scan #1's most severe section is from defect #6 to defect #9 (the slightly spalled concrete shown in Figure 7.12). This section includes three severe defects near one another, which can be repaired together. Additionally, two other defects in scan #1 (between 400 cm to 500 cm) show greater than 10% loss in cross-sectional area. This section includes concrete scaling, disintegration, and cracking (Figure 7.14). This part of the culvert has the greatest number of reinforcement defects with more than 4% loss in cross-sectional area, the highest concrete chloride content, and the lowest concrete compressive strength. It must therefore be considered the first priority in the repair schedule.

Figure 7.14. Concrete conditions from 400 cm to 500 cm (from the West wall) in the path of scan #1.

In both scans #2 and #3, a defect exists between 100 cm to 200 cm from the West wall, representing greater than 10% loss in cross-sectional area. At this location, concrete disintegration, discoloration, cracking, and a medium popout (Guide for conducting a visual inspection of concrete in service, 2008) are observed (Figure 7.15).

Figure 7.15. Concrete conditions from 100 cm to 200 cm (from the West wall) in the path of scans #2 and #3.

Based on the AG and SG analyses results, no significant loss in the cross-section area was identified in section #2. The only concern is at the distance of 250 cm to 300 cm in scan #7, where two defects, representing 7.1% and 8.5% loss in cross-sectional area, occur. There is also a sudden change in the sign and values of the magnetic flux density's derivative at this part of scan #7. This intense irregularity in magnetic properties happens at the place shown by a red vector in Figure 7.16. The concrete appears different at this location than in the surrounding areas, with a concrete patch as evidence of previous repairs or coring. Additionally, the reinforcement defects in the center of the deck are in an aggressive environment identified by the half-cell potential survey map. Hence, a relatively high corrosion rate is an issue in this section. This section also includes the least value of concrete cover thickness (Figure 7.11) and several transverse cracks on its concrete surface (Figure 7.5), indicating the site of culvert's sagging due to external loads. Thus, future re-inspections are necessary in this section to avoid unexpected loss of service.
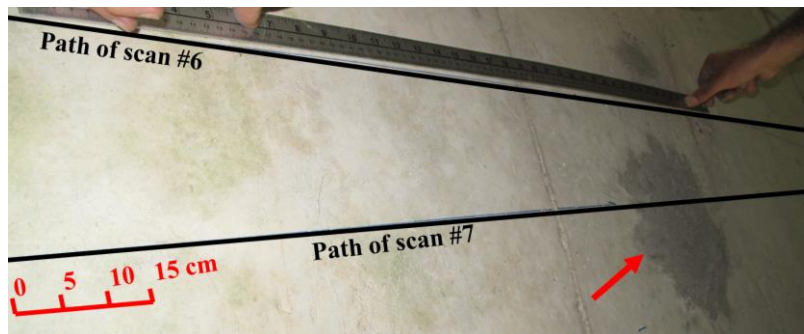
Figure 7.16. Concrete conditions from 200 cm to 300 cm (from the West wall) in the path of scans #7.

Scan #9 has the second greatest number of defects with greater than 4% loss in cross-sectional area. According to the results of SG and AG analyses, the most severe deterioration in scan #9 appears between 230 cm and 280 cm, where spalling, cracking, discoloration, and disintegration are obvious in the concrete (Figure 7.17). Although the measurements showed that this section has

176

only the second-highest chloride ion content (0.25%), it is still considered heavily contaminated. Additionally, Figure 7.11 shows that the overall concrete cover thickness value at this section is less than that for the other sections of the culvert. To increase the lifetime of structures in heavily chloride-contaminated environments, increasing the concrete cover is even more effective than using corrosion-resistant reinforcements (Verma *et al.*, 2013). Hence, if repairing this section is not economically possible, its concrete cover must be thickened to retard chloride-ion attack and corrosion acceleration.

(a)

(b)   (c)
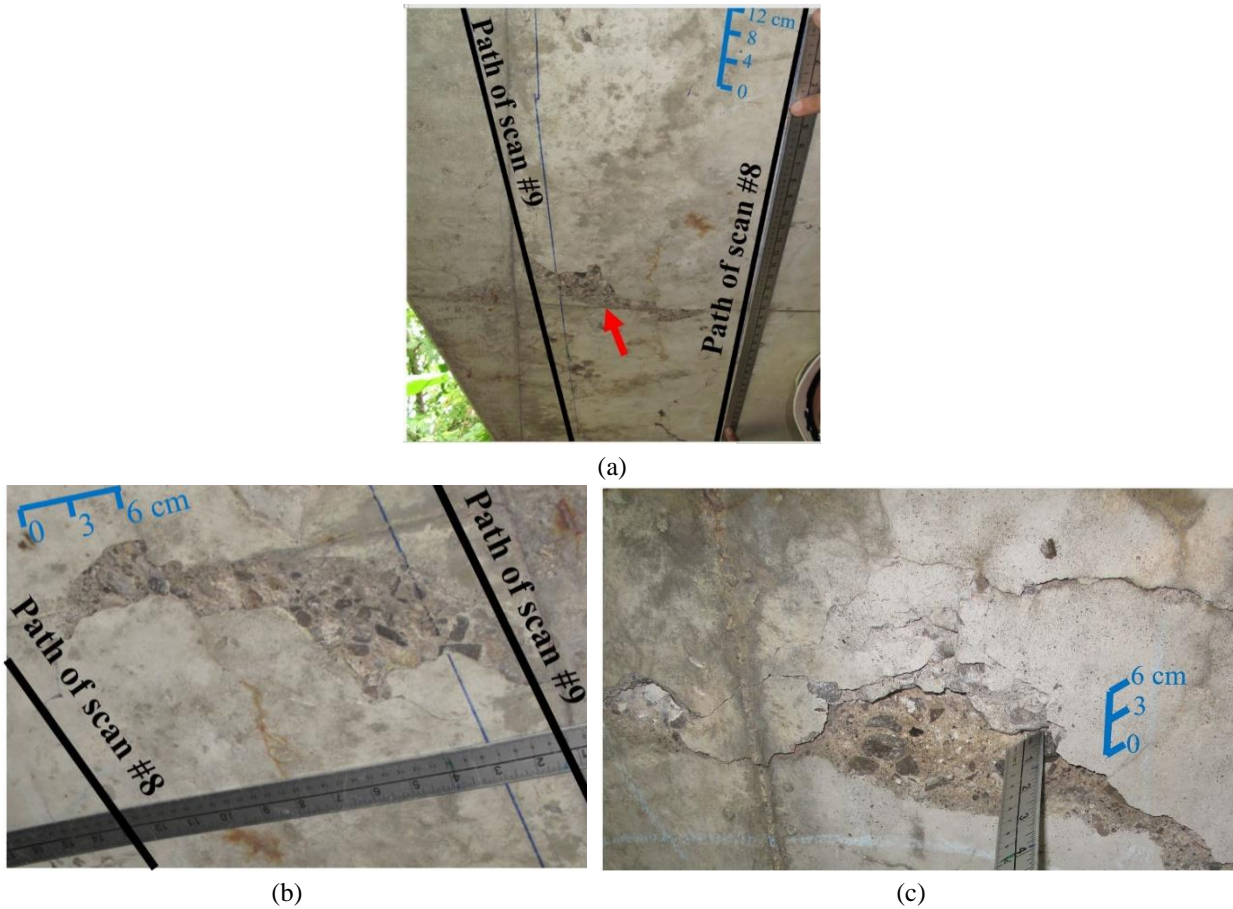
Figure 7.17. Concrete conditions from 200 cm to 300 cm (from West wall) in the path of scans #9: (a) indicating the place of concrete spalling; (b) closer view of the concrete spalling, representing its extension scale; (c) closer view of the concrete spalling, representing its depth scale.

In addition to these findings and recommendations, regarding the visual inspection, in some parts of both sections #1 and #3 (culvert's north and south ends), the reinforcement is visible due to concrete spalling. Yield strength values and resistance to cyclic loading of reinforcement steel logarithmically decreases as its corrosion percentage increases (Fernandez *et al.*, 2015). Corrosion also results in bond loss between reinforcement and concrete, reducing the structural load

177

capability (Zhao *et al.*, 2011). In a worse state, spalling totally removes the bond between the rebar and the concrete and facilitates conditions for further corrosion (Kearsley and Joyce, 2014). According to the Canadian Highway Bridge Design Code, reinforcement's corrosion-related deterioration shall be repaired before taking any other strengthening measures (CSA Group, 2006). Therefore, the reinforcement corrosion in these sections must be repaired, and the concrete should be renovated.

7.7. Conclusion

Quantitatively detecting reinforcement defects in RC infrastructure would significantly mitigate risks, allow better planning for repair and replacement, and reduce unexpected service loss events. To this end, investigations were conducted on culvert C072's reinforced concrete (RC) bridge structure, located in the north of the City of Markham, Ontario, Canada). The condition of the structure was examined under the supervision of the Corporation of the City of Markham, using a novel passive magnetic-based NDT method: PMI technology. This investigation was carried out in order to:

- Obtain a general overview of the culvert's steel reinforcement conditions;
- Quantitatively detect anomalies (defects) in the steel reinforcement under concrete cover;
- Categorize the anomalies in the culvert's steel reinforcements;
- Determine the approximate loss in the reinforcements' steel cross-sectional area.

To obtain a thorough overview of the bridge's corrosion conditions, inspections were undertaken on three sections. Two were determined in such a way as to cover either end of the bridge (the north and south ends); the other section was midway between the bridge's north and south ends. The results generated from the magnetic data, collected using the PMI scanner, were in very good agreement with the visual investigation's outcomes and the historical information obtaining from prior evaluations (e.g., the concrete's chloride content and compressive strength values, and results of a half-cell potential survey). PMI technology detected internal corrosion in the concrete, with roughly maximum respective losses of 20% and 14% in the reinforcement's cross-sectional area close to the culvert's south and north ends. Therefore, reinforcing steel and concrete repair should be carried out expeditiously at several sites near the north and south ends of the culvert. Also, additional inspection of the centre of the structure, where there is clear indication of corrosion

based on the PMI method, should be conducted in more detail with appropriate technologies. The quantification of the level of the corrosion provided by PMI technology can provide guidance for the rehabilitation actions.

The major conclusions are:

1. There were visibly corroded reinforcement sections arising from the large area of concrete spalling close to the culvert's south and north ends. The corroded reinforcements were corroborated by PMI measurements, and they must be repaired and the concrete renovated.

2. PMI measurements detected medium reinforcement defects in the middle of the culvert's North and South walls, where a relatively high corrosion rate was determined by half-cell potential survey. This section also includes the lowest value for the concrete cover thickness and displayed several transverse cracks on its concrete surface. Future regular re-inspections of concrete strength (e.g., by ultrasonic guided wave and Schmidt hammer) are deemed necessary for this section.

3. The overall concrete cover thickness value close to the culvert's north end is less than that for the other sections of the culvert. The PMI technology detected several medium and large defects in this section. Considering the heavily chloride-contaminated environment, if repairing the reinforcement at this section is not economically possible, at least its concrete cover must be thickened to retard chloride-ion attack and avoid corrosion acceleration.

4. Visual inspection detected several longitudinal and transverse concrete cracks in the middle of the West and East walls, where the highest structural stress values are expected. These cracks may join together over time because of ongoing cyclic external loads, potentially resulting in the total failure of the concrete. Hence, re-inspection of concrete strength (e.g., by ultrasonic guided wave and Schmidt hammer) is deemed necessary for this section.

Chapter 8: Conclusion and recommendations

Reinforced concrete is one of the most-commonly used construction materials worldwide. This versatile composite material is being exploited in urban and industrial structures such as buildings, floating structures, hydro-power tunnels, highways, and bridges. Quantifying the condition of the reinforcing steel can help manage the human and financial risks arising from unexpected reinforced concrete structure functional impairment or failure. Also, a quantitative time history of reinforcing steel condition can be used to make decisions on rehabilitation, decommissioning, or replacement. Reinforcement condition can be assessed using a novel, time- and cost-efficient NDT method based on the self-magnetic behaviour of ferromagnetic materials.

Passive Magnetic Inspection (PMI) technology, an NDT method for reinforced concrete assessment, was developed through simulation and experiments (Dusseault and Mahbaz, 2020; Mahbaz, 2016). Its physical concept and theoretical background have been presented, and its potential for detecting anomalies in steel reinforcement is under investigation (Mahbaz *et al.*, 2017; Mosharafi *et al.*, 2018). To achieve more-accurate and better-calibrated outcomes, additional studies were conducted to improve the analysis and interpretation approaches conducted on the magnetic data.

This thesis first focused on experiments and simulations that investigated ferromagnetic steel rebars with different sizes and types of artificial defects. Next, investigations were conducted to distinguish between the self-magnetic flux density values generated from an intact rebar and one with general corrosion. Subsequently, the magnetic responses of rebars with different degrees of general corrosion were assessed and compared. These investigations were needed to develop reliable and robust relationships between the NDT magnetic properties and the physical defect conditions in steel reinforcement. More specifically, for anomaly detection, state quantification (e.g., cross-sectional area loss, corroded length, etc.) and risk assessment thresholding approaches to data were developed for comparative and absolute RC infrastructure condition assessment.

This research project makes many contributions, and the most important one being establishing a novel procedure for recording magnetic data under actual conditions (using PMI technology), and introducing creative methods for data analysis, signal processing, and interpretation of the results. These innovations were implemented in a field test inspecting embedded reinforcement conditions

in a bridging structure. The validity of PMI inspection outcomes was confirmed by the Corporation of the City of Markham. The main contributions of this research project are as follows:

1. Novel data-gathering, data-analysis, and interpretation procedures were introduced and implemented in the first field test inspecting reinforcement conditions of the C072 bridging structure, located north of the City of Markham;

2. Novel data processing approaches were established and confirmed as being capable of analysing raw magnetic data and processing them so as to detect the locations and sizes of defects in reinforcement;

3. The patterns of magnetic data and data derivative values were extracted, with appropriate confidence levels, for different types of local defects. This contribution presents information for conducting signal feature recognition for detecting the types of local defects in reinforcement;

4. A novel statistical approach was developed to estimate the probability of defectiveness for a rebar using its magnetic properties. Investigations of the probability distribution fitted on the magnetic data also resulted in the ability to predict subsequent magnetic data over the rebar with an appropriate confidence level;

5. Effects of defects' clock position on the stray magnetic field were investigated using all three sensors embedded in the PMI scanner. Subsequently, the experimental results were confirmed using a simulated rebar with similar conditions. This innovative investigation provides guidance for finding defects at different clock positions within a rebar;

6. The sinusoidal behaviour of magnetic data sets was investigated for distinguishing between the data recorded over an intact rebar and a corroded one. This contribution was confirmed by Fourier analysis showing the power and magnitude spectral density of the data sets;

7. Different novel processing approaches were used on the magnetic data recorded over rebars with different corrosion degrees. Investigations derived practical equations between magnetic flux density values and the mass loss percentages of steel rebars;

8. The values of different components (X, Y, and Z) of magnetic data were investigated using different signal processing approaches and statistical analysis. These investigations helped in understanding the reliability of different components of the magnetic data and recognizing their behaviour at the location of different types of defects;

9. The reliability and consistency of the magnetic data recorded by the PMI scanner were investigated for the first time using different statistical methods. Additionally, the main sources of errors were recognized; based on desirable probabilities of type-one and type-two errors, repetition times for each scan have been determined;

10. The detectability limit of the magnetic sensors was investigated by recording and analysing data at different vertical distances. This investigation was conducted in experiments and simulations using different novel procedures over various rebars with different types of defects;

11. Defective and corroded rebars were simulated with their real geometry obtained by a three-dimensional (3D) laser scanner under a realistic local magnetic field. This approach resulted in accurate outcomes, in good accordance with reality, confirming the physical principles behind the PMI technology.

8.1. Conclusions

The following sub-sections summarize the conclusions resulting from the various chapters of this thesis.

8.1.1. Investigations of the self-magnetic behaviour of rebars with local defects

Studies on the magnetic flux density values recorded over rebars with installed holes and longitudinal defects demonstrated the feasibility of identifying defects in covered reinforcing steel in RC infrastructure. For each case, a threshold value from data analysis was determined to serve as a defect identification process. The site of defects can then be re-assessed with a reasonable degree of accuracy, permitting year-to-year condition evaluation of reinforced concrete structures in a quantitative manner. The detectability of cracks in a ferromagnetic rebar was thence explored with view to developing a method of condition assessment over time. Results indicated that it is feasible to reliably detect cracks of sufficient size, but at a limited distance from the magnetometer sensors. These results can guide the development of threshold detection criteria for infrastructure assessment using the method. The main outcomes resulting from the simulation and experiments conducted on rebars with different types and sizes of local defects are as follows:

- Specific patterns in the magnetic data sets and their derivative values indicate different types of local defects;

- The places and sizes of defects in reinforcement can be detected by applying certain thresholds to a magnetic data set after it has been processed by appropriate methods;

- Increasing the stand-off distances of magnetic sensors (embedded in the PMI scanner) from the surface of a defective rebar changes the trend and values of the magnetic data in line with physical principles. At greater stand-off distances, fewer details of the rebar properties are shown, and anomalies may become undetectable;

- In detecting defects on a specific side of a rebar, the magnetic data recorded by the sensor at that side of the rebar provides greater accuracy than the other sensors (the clock position effect).

8.1.2. Investigations of the self-magnetic behaviour of rebars with general corrosion

Assessments indicated distinguishable differences between the self-magnetic behaviour of a rebar with general corrosion and an intact one. For instance, a sinusoidal trend (about a specific frequency) was demonstrated for the magnetic data of the intact rebar, yet no sinusoidal trend matched well with the corroded rebar's magnetic data. Furthermore, regression analyses were implemented to obtain relations between parameters generated from magnetic data and the mass loss percentages of rebars. Such findings can be applied to the quantification of the corrosion state of concrete-embedded reinforcing steel bars to identify various levels of damage, and the quantitative condition of reinforced concrete structures undergoing corrosion over time can therefore be tracked. According to the experiments and simulations conducted on an intact rebar and rebars with various degrees of general corrosion, the most important achievements are as follows:

- The magnetic data recorded over intact rebar shows a sinusoidal pattern due to the regular corrugated shape of the rebar. The period parameter of the sinusoidal function fitted to magnetic data is precisely equal to the rib-to-rib distances for the rebar;

- No predictable sinusoidal pattern can be identified for the magnetic data recorded over a rebar with extensive corrosion, the lack of a regular pattern is indicative of general corrosion of the outside of the rebar;

- General corrosion flattens the bumps of the rebar, so the SD of the magnetic values recorded over the corroded rebar would be lower than that calculated for the magnetic values recorded over an intact rebar;

- Investigating the standard deviation of the magnetic data is the most accurate procedure for estimating the degree of general corrosion.

8.1.3. Field test conduction

Using the findings from the investigations on rebars with local defects and general corrosion, culvert C072's RC bridging structure was inspected by PMI technology under the supervision of the Corporation of the City of Markham. This RC structure had been previously assessed using conventional methods. PMI technology not only complemented and confirmed conventional assessment methods, it quantitatively identified reinforcement deterioration and categorized defects to allow planning for required maintenance, repair or replacement activities. With this approach, owners of infrastructure can look forward to far-more-quantitative condition statements over time, and thereby track the condition evolution of infrastructure elements. Doing so will permit active and quantitative risk management, and should lead to reduced costs through better decisions about repair and replacement. This innovation can also lead to reduced insurance costs for owners, once the insurance industry realizes the power of the technology. For the field test outcomes, the main conclusions are as follows:

- The accuracy of analysis approaches described in different sections of the thesis has been verified by the success of the field test.
- The PMI technology has been confirmed as a reliable method for assessing the condition of rebars embedded in a reinforced concrete structure under actual conditions.

8.2. Future work

PMI technology was developed at the University of Waterloo (Dusseault and Mahbaz, 2020; Mahbaz, 2016). Since then, the device has been modified, and as described in this thesis, technical improvements were conducted in the technology's data gathering and data analysis techniques. Innovative approaches were used for interpreting the results, detecting the defects, and categorizing the magnetic anomalies based on the defectiveness condition of steel reinforcements. These achievements were implemented in the inspection of a RC bridging structure, and the outcomes were successfully in accordance with the historical information from different conventional assessment techniques. The report of the case study, mentioned in Chapter 7 of this thesis, was successfully approved by the external client (Corporation of the City of Markham).

Experiments and simulations, along with the case study presented in this thesis confirmed the PMI technology's abilities from both the scientific and industrial points of views. However, additional developments on the technology and further studies on the magnetic behavior of ferromagnetic materials could achieve more accurate and better calibrated outcomes for engineering applications. Possible future work is listed as follows:

8.2.1. Investigations on welding joints

Welding rebars is a common practice needed in reinforced structures, and is useful for overcoming the length limitations of rebars and keeping thier continuity (Apostolopoulos *et al.*, 2011). However, welding changes the metallurgical and microstructural properties of rebar. This alteration can reduce the yield strength and ductility of rebars (Ahmed, 2015). In addition, deficiencies in rebars can be found in welding joints (Ahmed, 2015). To continue the technical development of PMI, future studies can focus on the magnetic behaviour of rebars at the sites of welds, and its difference to the behaviour at the sites of local defects such as cracks.

8.2.2. Improvements of the PMI device

Every data-gathering session reported in this thesis was conducted by moving the PMI's scanner on a path defined along the length of a rebar. For confirming the quality of experiments, every scanning was conducted several times. Such replication gave an accurate evaluation of the quality of measurement of rebars' magnetic flux density values. Additionally, the statistical analysis of magnetic data sets recorded over the same path (in Chapter 6) showed that 92% of the total variation between the scans is due to operator errors during scanning. Such errors can happen due to deviations from the set path, or inaccuracy in the scan's starting point. To reduce the errors caused by procedural factors, investigations should be conducted on the concept of automating the scanner's movements over the rebar.

8.2.3. Investigations on the relations between stress condition and magnetic behavior of rebars

Another useful improvement relevant to PMI method would be to clarify the relation between the stress conditions (mechanical load) and magnetic behaviour of steel reinforcements. This practical subject can help in evaluating the safety level of RC structures. To achieve this, in future studies, the connection between the stress behaviour and magnetic properties of rebar can be investigated through application of static and dynamic loads. The different components of the SMFL data of

the subject rebars under the various tests can be recorded by the PMI device. Such experiments can be conducted on different types of rebars (intact, defective, and with varying degrees of general corrosion percentages). The stress conditions of a rebar can be simulated for comparison with its magnetic behaviour, and an appropriate relation between the two under different loading conditions can be sought.

8.2.4. Further field tests

Field tests are conducted in the real-world, with no tampering of the variables of natural conditions. Additionally, real case studies reveal some details that are not considered in lab work and simulations. Every field study has the potential to reveal a new set of challenges, thereby opening up new lines of thinking. Confronting such challenges may necessitate upgrading the device, as well as upgrading the data gathering, data processing and interpretation approaches. Consequently, the more field tests conducted, the more knowledge will be obtained about the PMI method's capabilities and requirements as an engineering tool. This will lead to a better understanding of the PMI method, delineating its advantages and limitations, and helping to suggest further improvements.

Bibliography

Abouhamad, M., Dawood, T., Jabri, A., Alsharqawi, and M., Zayed, T. 2017. Corrosiveness mapping of bridge decks using image-based analysis of GPR data. Automation in Construction, 80:104-117.

ACI Committee 201, and American Concrete Institute. 2008. Guide for conducting a visual inspection of concrete in service, Farmington Hills, MI: American Concrete Institute.

Ahmad, M.I.M., Arifin, A., Abdullah, S., Jusoh, W.Z.W., Singh, S.S.K. 2015. Fatigue crack effect on magnetic flux leakage for A283 grade C steel. Steel and Composite Structures, 19(6): 1549-1560.

Ahmed, Gh.H. 2015. Mechanical properties of welded deformed reinforcing steel bars. The Scientific Journal of Koya University, 3(1): 27-39.

Ahrens, T.J. 1995. Global Earth physics: A handbook of physical constants. American Geophysical Union, Washington.

Alcantara, Jr.N.P.d., Silva, F.M.d., Guimarães, M.T., Pereira, M.D. 2016. Corrosion assessment of steel bars used in reinforced concrete structures by means of eddy current testing. Sensors, 16(1):15.

Al-Hammoud, R., Soudki, Kh., Topper, T.H. 2011. Fatigue flexural behavior of corroded reinforced concrete beams repaired with CFRP sheets. Journal of Composites for Construction, 15(1): 42-51.

Al-Qadi, I.L., Elseifi, M.A. 2006. Mechanism and modeling of transverse cracking development in continuously reinforced concrete pavement. International Journal of Pavement Engineering, 7(4): 341-349.

Apostolopoulos, Ch. Alk., Savvopoulos, P.Th., Dimitrov, L. 2011. Design problems in lap welded joints of reinforcing steel bars. Scientific proceedings VIII international congress "Machines, Technologies, Materials", 18th-21st September, Varna, Bulgaria.

ASTM International. 2002. A1020/A1020M-01 standard specification for steel tubes, carbon and carbon manganese, fusion welded, for boiler, superheater, heat exchanger and condenser applications, West Conshohocken, PA.

ASTM International. 2003. G1-03 standard practice for preparing, cleaning, and evaluating corrosion test specimens, West Conshohocken, PA.

ASTM International. 2006. C457-06 Standard test method for microscopical determination of parameters of the air-void system in hardened concrete, West Conshohocken, PA.

Babaei, M., Tavassolian, H. 2015. Optimal design of intermediate reinforced concrete moment resisting frames with shear walls for different arrangements of columns. International Journal of Engineering and Technology, 7(5): 1743-1753.

Bezděk, A., Sebera, J., Klokočník, J. 2017. Validation of swarm accelerometer data by modelled nongravitational forces. Advances in Space Research, 59(10): 2512-2521.

Boyle, H.C., Karbhari, V.M. 1995. Bond and behavior of composite reinforcing bars in concrete. Polymer-Plastics Technology and Engineering, 34(5): 697-720.

Bulte, D.P., Langman, R.A. 2002. Origins of the magnetomechanical effect. Journal of Magnetism and Magnetic Materials, 251(2): 229-243.

Canadian Standards Association. 2006. Canadian highway bridge design code, CAN/CSA-S6-06, Ont.

Canadian Standards Association. 2014. Compressive strength of cylindrical concrete specimens, CAN/CSA-A23.2-9C-14, Ont.

Clifton, J.R., Carino, N.J. 1982. Nondestructive evaluation methods for quality acceptance of installed building materials. Journal of Research of the National Bureau of Standards (United States), 87(5): 407-438.

Cochran, W.G., Gertrude, M.C. 1957. Experimental design. John Wiley and Sons, New York, P. 20.

Concu, G., Nicolo, B.D., Pani, L. 2011. Non-destructive testing as a tool in reinforced concrete buildings refurbishments. Structural Survey, 29(2): 147-161.

Correia, M.J., Salta, M.M. 2006. Stress corrosion cracking of austenitic stainless steel alloys for reinforced concrete. Materials Science Forum, 514-516(PART 2): 1511-1515.

Daniel, J., Abudhahir, A., Paulin, J. 2017. Magnetic flux leakage (MFL) based defect characterization of steam generator tubes using artificial neural networks. Journal of Magnetics, 22(1): 34–42.

Davies, C., Constable, C. 2017. Geomagnetic spikes on the core-mantle boundary. Nature Communications, 8:15593.

Da-wei, Y., Bin-shi, X., Shi-yun, D., Shang-lin, Y., Li-hong, D. 2005. Characteristics of magnetic memory signals for medium carbon steel under static tensile conditions. Journal of Central South University of Technology, 12(2): 107-111.

Dubov, A.A. 1997. A study of metal properties using the method of magnetic memory. Metal Science and Heat Treatment, 39(9-10):401-405.

Dubov, A.A. 2012. Development of a metal magnetic memory method. Chemical and Petroleum Engineering, 47(11-12): 837-839.

Dubov, A., Kawka, A., Jurashek, J. 2010. Application of the Metal Magnetic Memory Method for Investigation and Analysis of Stressed States of Hoisting Mine Structure Bearing Rods. 10th European Conference on Non-Destructive Testing, 7-11 June 2010, Moscow, Russia.

Dubov, A., Kolokolnikov, S. 2008. New standards ISO 24497 on the metal magnetic memory method. The program of personal training and certification, 17th world conference on nondestructive testing, 25-28 October 2008, Shanghai, China, pp. 1-5.

Dubov, A., Kolokolnikov, S. 2012. Assessment of the material state of oil and gas pipelines based on the metal magnetic memory method. 56(3–4): 11-19.

Dusseault M.B., Mahbaz, S.B. 2020. System and method for detecting irregularities in rebar in reinforced concrete. United States Patent Application publication. Pub. No: US 10,533,970 B2.

Dubov, A., Vlasov, V. 2007. About the new classification of NDT methods based on positions of risks and equipment life assessment. 5th International conference on certification and standardization in NDT, Sept 2007, Berlin, Germany.

Emmons, P. 1994. Concrete repair and maintenance illustrated. 1st ed. Kingston, Massachusetts: R. S. Means Company, Inc. pp. 150.

Fernandez, I., Bairán, J.M., Marí, A.R. 2015. Corrosion effects on the mechanical properties of reinforcing steel bars. Fatigue and σ-ε behavior. Construction and Building Materials, 101: 772-783.

Gholizadeh, S. 2016. A review of non-destructive testing methods of composite materials. Procedia Structural Integrity, 1(2016): 50-57.

Gontarz, S., Mączak, J., Szulim, P. 2015. Online monitoring of steel constructions using passive methods. Engineering Asset Management - Systems, Professional Practices and Certification, Lecture Notes in Mechanical Engineering, Springer, Cham, pp. 625-635.

Guiñón, J.L., Ortega, E., García-Antón, J., Pérez-Herranz, V. 2007. Moving average and Savitzki-Golay smoothing filters using Mathcad. In Proceedings of the International Conference on Engineering Education-ICEE, 3–7 September 2007, Coimbra, Portugal.

Guo, L., Shu, D., Yin, L., Chen, J., Qi, X. 2016. The effect of temperature on the average volume of Barkhausen jump on Q235 carbon steel. Journal of Magnetism and Magnetic Materials, 407: 262-265.

Gupta, B., Szielasko, K. 2016. Magnetic sensor principle for susceptibility imaging of para- and diamagnetic materials. Journal of Nondestructive Evaluation, 35: 41.

Hadi, M.N. 2008. Bond of high strength concrete with high strength reinforcing steel. The Open Civil Engineering Journal, 2: 143-147.

Hameed, R., Sellier, A., Turatsinze, A., Duprat, F. 2017. Simplified approach to model steel rebar-concrete interface in reinforced concrete. KSCE Journal of Civil Engineering, 21(4): 1291-1298.

Hu, K., Ma, Y., Xu, J. 2017. Stable finite element methods preserving $\nabla \cdot B = 0$ exactly for MHD models. Numerische Mathematik, 135: 371-396.

Huang, H., Qian, Z., Yang, C., Han, G., Liu, Z. 2017. Magnetic memory signals of ferromagnetic weldment induced by dynamic bending load. Nondestructive Testing and Evaluation, 32(2): 166-184.

Hubert, A., Schafer, R. 1998. Magnetic domains: the analysis of magnetic microstructures. Springer-Verlag Berlin Heidelberg, Germany, ISBN978-3-540-64108-7.

Hughes, D.W., Cattaneo, F. 2016. Strong-field dynamo action in rapidly rotating convection with no inertia. Physical Review E, 53(1): 6200108.

Hussain, A., Akhtar, S. 2017. Review of non-destructive tests for evaluation of historic masonry and concrete structures. Arabian Journal for Science and Engineering, 42(3): 925-940.

Jarram, P. 2016. Remote measurement of stress in carbon steel pipelines - Developments in remote magnetic monitoring. NACE International Corrosion Conference, 6-10 March 2016, British Columbia, Canada, pp. 663-671.

Jiang, J.-y., Liu, Y., Chu, H.-y., Wang, D., Ma, H., Sun, W. 2017. Pitting corrosion behaviour of new corrosion-resistant reinforcement bars in chloride-containing concrete pore solution. Materials, 10(8):903.

Jiles, D.C. 1995. Theory of the magnetomechanical effect. Journal of Physics D: Applied Physics. 28(8): 1537-1546.

Kaur, N. 2014. Testing of hypothesis parametric test (T, Z, F) Chi-Square. Scholarly Research Journal for Humanity Sciences & English Language, I(V): 730-739.

Kearsley, E.P., Joyce, A. 2014. Effect of corrosion products on bond strength and flexural behaviour of reinforced concrete slabs. Journal of the South African Institution of Civil Engineering, 56(2): 21-29.

Kittel, C., Galt, J.K. 1956. Ferromagnetic domain theory, Solid State Physics - Advances in Research and Applications, 3(C): 437-564.

Kopas, P., Jakubovičová, L., Vaško, M., Handrik, M. 2016. Fatigue resistance of reinforcing steel bars. Procedia Engineering, 136: 193-197.

Kronmuller, H. 1987, Theory of nucleation fields in inhomogeneous ferromagnets. Physica Status Solidi (b), 144(1): 385-396.

Lam, R. B., Wieboldt, R. C., Isenhour, T. L. 1981. Practical computation with fourier hunsforms for data analysis. Analytical Chemistry, 53 (7): 889-899.

Leng, J., Xu, M., Li, J., Zhang, J. 2010. Characterization of the elastic-plastic region based on magnetic memory effect. Chinese Journal of Mechanical Engineering (English Edition). 23(4): 532-536.

Li, J., Xu, M. 2012. Influence of uniaxial plastic deformation on surface magnetic field in steel. Meccanica, 47(1): 135-139.

Li, F., Ye, W. 2017. A Parameter Sensitivity Analysis of the Effect of Rebar Corrosion on the Stress Field in the Surrounding Concrete. Advances in Materials Science and Engineering, 2017: 9858506.

Luming, L., Songling, H., Xiaofeng, W., Keren, S., Su, W. 2003. Magnetic field abnormality caused by welding residual stress. Journal of Magnetism and Magnetic Materials, 261(3): 385-391.

Ma, Y., Wang, Q., Guo, Z., Wang, G., Wang, L., Zhang, J. 2017. Static and fatigue behavior investigation of artificial notched steel reinforcement. Materials, 10(5): 532.

Mahbaz, S.B. 2016. Non-Destructive Passive Magnetic and Ultrasonic Inspection Methods for Condition Assessment of Reinforced Concrete. Ph.D. Thesis, Department of Civil and Environmental Engineering, University of Waterloo, Waterloo, ON, Canada.

Mahbaz, S.B., Dusseault, M.B., Cascante, G., Vanheeghe, Ph. 2017. Detecting defects in steel reinforcement using the passive magnetic inspection method. Journal of Environmental and Engineering Geophysics, 22(2): 153-166.

Mackechnie, J.R., Alexander, M.G. 2001. Repair principles for corrosion-damaged reinforced concrete structures. Research Monograph NO. 5, Department of Civil Engineering, University of Cape Town, pp. 5-36.

Makar, J., Desnoyers, R. 2001. Magnetic field techniques for the inspection of steel under concrete cover. NDT and E International, 34(7): 445-456.

Matsagar, V. 2015. Advances in Structural Engineering: Materials, Volume Three. Springer: New Delhi, India, pp. 1896. ISBN 8132221877, 9788132221876.

Meshlab. 2017. Retrieved from http://www.meshlab.net/

Ministry of transportation of Ontario (Ontario laboratory testing manual). 1996. Method of test for determination of total chloride ion in concrete - (acid soluble), MTO LS-417, Ont.

Mironov, S., Devizorova, Z., Clergerie, A., Buzdin, A. 2016. Magnetic mapping of defects in type-II superconductors. Applied Physics Letters, 108(21): 212602.

Miya, K. 2002. Recent advancement of electromagnetic nondestructive inspection technology in Japan. IEEE Transactions on Magnetics. 38(2): 321-326.

Montemor, M.F., Simões, A.M.P., Ferreira, M.G.S. 2003. Chloride-induced corrosion on reinforcing steel: from the fundamentals to the monitoring techniques. Cement and Concrete Composites. 25(4-5): 491- 502.

Malo, N., Hanley, J.A., Cerquozzi, S., Pelletier, J., Nadon, R. 2006. Statistical practice in high-throughput screening data analysis. Nature Biotechnology, 24(2): 167-175.

Montgomery. D.C. 2014. Design and analysis of experiments. Eighth edition. John Wiley & sons, Inc.

Mosharafi, M., Mahbaz, S., Dusseault, M.B. 2018. Simulation of real defect geometry and its detection using passive magnetic inspection (PMI) method. Applied Sciences (Switzerland), 8(7): 1147.

Mosharafi, M., Mahbaz, S., Dusseault, M.B. 2020. Size and location detection of transverse cracks using a passive magnetic method. Measurement, 154: 107485.

Mosharafi, M., Mahbaz, S., Dusseault, M.B., and Ph. Vanheeghe. 2020. Magnetic detection of corroded steel rebar: reality and simulations. NDT & E International, 110: 102225.

Muchaidze, I., Pommerenke, D., Chen, G. 2011. Steel reinforcement corrosion detection with coaxial cable sensors. Proceedings of SPIE - The International Society for Optical Engineering, 7981: 79811L.

Nahangi, M., Haas, C. 2014. Automated 3D compliance checking in pipe spool fabrication. Advanced Engineering Informatics, 28(4): 360-369.

Natural Resources Canada. 2017. Retrieved from http://www.geomag.nrcan.gc.ca/calc/mfcal-en.php.

Navidi, W. 2010. Statistics for engineers and scientists. McGraw-Hill Science/Engineering/Math.

Ni, C., Hua, L., Wang, X. 2018. Crack propagation analysis and fatigue life prediction for structural alloy steel based on metal magnetic memory testing. Journal of Magnetism and Magnetic Materials, 462: 144-152.

O'Flaherty, F.J., Mangat, P.S., Lambert, P., Browne, E.H. 2008. Effect of under-reinforcement on the flexural strength of corroded beams. Materials and Structures/Materiaux et Constructions, 41(2): 311-321.

Perkins, Ph.H. 2000. Swimming Pools: Design and Construction. Fourth Edition, CRC Press.

Proakis, J.G., Manolakis, D.G. 1996. Digital Signal Processing Principles, Algorithms, and Applications. Third edition. Prentice-Hall International, INC.

Ren, J.L., Song, K., Wu, G.H., Lin, J.M. 2001. Mechanism study of metal magnetic memory testing. In: Proceedings of the 10th Asia-Pacific Conference on Non- Destructive Testing, 17-21 September, Brisbane, Australia.

Perin, D., Göktepe, M. 2012. Inspection of rebars in concrete blocks. International Journal of Applied Electromagnetics and Mechanics, 38(2-3): 65-78.

Rashid, M.H., Khatun, S., Uddin, S.M.K., Nayeem, M.A. 2010. Effect of strength and covering on concrete corrosion. European Journal of Scientific Research, 40(4): 492-499.

Ribichini, R. 2011. Modelling of electromagnetic acoustic transducers. Ph.D. thesis, Department of Mechanical Engineering, Imperial College, London.

Rose, J.H., Uzal, E., Moulder, J.C. 1995. Magnetic permeability and eddy current measurements. Review of Progress in Quantitative Non-destructive Evaluation, 14: 315-322.

Sakai, Y., Unishi, H., Yahata, T. 2004. Non-destructive method of stress evaluation in linepipes using magnetic anisotropy sensor. JFE Technical Report, (3): 47-53.

Saranya, C., Manikandan, G. 2013. A study on normalization techniques for privacy preserving data mining. International Journal of Engineering and Technology, 5(3): 2701-2704.

Shi, Y., Li, Z.X., Hao, H. 2009. Bond slip modelling and its effect on numerical analysis of blast-induced responses of RC columns. Structural Engineering and Mechanics, 32(2): 251-267.

Schober, P., Schwarte, L.A. 2018. Correlation coefficients: appropriate use and interpretation. Anesthesia and Analgesia,126(5): 1763-1768.

Sobieck, T., Atadero, R.A., Mahmoud, H.N. 2015. Fatigue crack propagation of notched steel rebar in RC beams repaired with externally bonded CFRP. Journal of Composites for Construction, 19(5): 04014076.

Stewart, M.G. 2009. Mechanical behaviour of pitting corrosion of flexural and shear reinforcement and its effect on structural reliability of corroding RC beams. Structural Safety, 31(1): 19-30.

Szymanik, B., Frankowski, P.K., Chady, T., Chelliah, C.R.A.J. 2016. Detection and inspection of steel bars in reinforced concrete structures using active infrared thermography with microwave excitation and eddy current sensors. Sensors (Switzerland). 16(2): 234.

Tabrizi, M. 1987. The nonlinear magnetic core model used in spice plus. Applied Power Electronics Conference and Exposition, 2-6 March 1987, San Diego, USA, pp. 32–36.

Tahershamsi, M., Fernandez, I., Lundgren, K., Zandi, K. 2017. Investigating correlations between crack width, corrosion level and anchorage capacity. Structure and Infrastructure Engineering. 13(10):1294-1307.

Takahashi, K., Okamura, S., Sato, M. 2015. A fundamental study of polarimetric GB-SAR for nondestructive inspection of internal damage in concrete walls. Electronics and Communications in Japan, 98(11): 41-49.

Tanel, Z., Erol, M. 2008. Students' difficulties in understanding the concepts of magnetic field strength, magnetic flux density and magnetization. Latin-American Journal of Physics Education, 2(3): 184-191.

Tauxe, L. 2010. Essentials of paleomagnetism. Berkeley. University of California Press, Berkeley, United States.

Taylor, B.K., Johnsen, S., Lohmann, K.J. 2017. Detection of magnetic field properties using distributed sensing: A computational neuroscience approach. Bioinspiration and Biomimetics, 12(3): 036013.

Twumasi, J.O., Le, V., Tang, Q., Yu, T. 2016. Quantitative sensing of corroded steel rebar embedded in cement mortar specimens using ultrasonic testing. Proceedings of SPIE - The International Society for Optical Engineering, 9804: 98040P.

Valipour, M., Shekarchi, M., Ghods, P. 2014. Comparative studies of experimental and numerical techniques in measurement of corrosion rate and time-to-corrosion-initiation of rebar in concrete in marine environments, Cement and Concrete Composites. 48: 98-107.

Vera, R., Apablaza, J., Carvajal, A.M., Vera, E. 2013. Effect of surface coatings in the corrosion of reinforced concrete in acid environments. International Journal of Electrochemical Science, 8(10): 11832-11846.

Verma, S.K., Bhadauria, S.S., Akhtar, S. 2013. Review of nondestructive testing methods for condition monitoring of concrete structures. Journal of Construction Engineering, 2013 (834572): 1-11

Vu, K., Stewart, M.G. 2000. Structural reliability of concrete bridges including improved chloride-induced corrosion models. Structural Safety, 22(4): 313-333.

Wang, Z.D., Yao, K., Deng, B., Ding, K.Q. 2010. Quantitative study of metal magnetic memory signal versus local stress concentration. NDT and E International, 43(6): 513-518.

Wang, Z.D., Gu, Y., Wang, Y.S. 2012. A review of three magnetic NDT technologies. Journal of Magnetism and Magnetic Materials, 324(4): 382-388.

Wilson, J.W., Tian, G.Y., Barrans, S. 2007. Residual magnetic field sensing for stress measurement. Sensors and Actuators, A: Physical, 135(2): 381-387.

Witos, M., Zieja, M., Zokowski, M., Roskosz, M. 2014. Diagnosis of supporting structures of HV lines with using of the passive magnetic observer. Studies in Applied Electromagnetics and Mechanics, 39: 199-206.

Xin, Q., Shu, D., Hui, L., Wei, W., Chen, J. 2012. Magnetic Barkhausen noise, metal magnetic memory testing and estimation of the ship plate welded structure stress. Journal of Nondestructive Evaluation, 31(1): 80-89.

Xu, C., Li, Z., Jin, W. 2013. A new corrosion sensor to determine the start and development of embedded rebar corrosion process at coastal concrete. Sensors (Basel, Switzerland). 13(10): 13258-13275.

Xu, M., Fralick, D., Zheng, J.Z., Wang, B., Tu, X.M., Feng, C. 2017. The differences and similarities between two-sample t-test and paired t-test. Shanghai Archives of Psychiatry, 29(3): 184-188.

Yao, K., Wang, Z.D., Deng, B., Shen, K. 2012. Experimental Research on Metal Magnetic Memory Method. Experimental Mechanics, 52(3): 305-314.

Yuan, J., Zhang, W. 2010. Detection of stress concentration and early plastic deformation by monitoring surface weak magnetic field change. In Proceedings of the IEEE, 4-7 August 2010, pp. 395–400.

Zagorski, P., Bangert, P., Gallina, A. 2017. Identification of the orbit semi-major axis using frequency properties of onboard magnetic field measurements. Aerospace Science and Technology, 66: 380-391.

Zaki, A., Chai, H.K., Aggelis, D.G., Alver, N. 2015. Non-destructive evaluation for corrosion monitoring in concrete: A review and capability of acoustic emission technique. Sensors (Switzerland), 15(8): 19069-19101.

Zhang, H. Liao, L., Zhao, R., Zhou, J., Yang, M., Xia, R. 2016. The non-destructive test of steel corrosion in reinforced concrete bridges using a micro-magnetic sensor. Sensors, 16(9): 1439.

Zhao, J.-M., Tang, J., Zhang, H.-J., Zhang, Ch-K., Yang, J., Jia, Sh-X., Zhang, J.-S., Yang, Z.-X. 2000. Wavelet transform and its application in data processing and interpretation of seismic reflection/refraction profile. Acta Geophysica Sinica, 43(5): 666-676.

Zhao, Y., Karimi, A.R., Wong, H.S., Hu, B., Buenfeld, N.R., Jin, W. 2011. Comparison of uniform and non-uniform corrosion induced damage in reinforced concrete based on a Gaussian description of the corrosion layer. Corrosion Science, 53(9): 2803-2814.

Appendix A: Mesh specifications of the defective rebar in Chapter 2

Table A-1. Different mesh specifications of rebar, with the fixed specifications of box mesh #1.

Rebar mesh #	Maximum element size (mm)	Minimum element size (mm)	Maximum element growth rate	Curvature factor	Resolution of narrow regions	Number of degrees of freedom (in total)
1	2.000	1.000	1.450	0.500	0.600	601773
2	1.340	0.670	1.407	0.450	0.636	1267526
3	0.898	0.449	1.364	0.405	0.674	3324359
4	0.602	0.301	1.323	0.365	0.715	9764894
5	0.571	0.286	1.310	0.361	0.722	10441703
6	0.5605	0.278	1.295	0.3505	0.746	10995911
7	0.550	0.270	1.280	0.340	0.770	11594725
8	0.530	0.240	1.260	0.330	0.780	12877797
9	0.500	0.200	1.250	0.320	0.790	15173763
10	0.460	0.160	1.220	0.280	0.810	19243609
11	0.446	0.141	1.100	0.240	0.830	20879674

Table A-2. Different mesh specifications of box, with the fixed specifications of rebar mesh #8.

| Box mesh #	Maximum element size (mm)	Minimum element size (mm)	Maximum element growth rate	Curvature factor	Resolution of narrow regions	Number of degrees of freedom (in total)
1	8.000	4.100	1.450	0.500	0.600	12877797
2	7.720	3.400	1.330	0.410	0.620	13794957
3	6.820	2.300	1.300	0.400	0.650	14188984
4	5.810	1.400	1.250	0.350	0.680	15058001
5	4.110	1.100	1.190	0.290	0.710	17446126
6	2.840	0.850	1.150	0.250	0.730	22627445
7	2.250	0.820	1.140	0.230	0.730	28481960
8	2.210	0.815	1.130	0.230	0.740	29650862

Appendix B: specifications for fitted non-linear curves (in section 3.3.2.1)

Table B-1. Different mesh specifications of box, with the fixed specifications of rebar mesh #8.


Specifications of the fitted curve on the data related to rebar #1	General model Fourier5:
	f(x) = a0 + a1*cos(x*w) + b1*sin(x*w) +
	    a2*cos(2*x*w) + b2*sin(2*x*w) + a3*cos(3*x*w) + b3*sin(3*x*w) +
	    a4*cos(4*x*w) + b4*sin(4*x*w) + a5*cos(5*x*w) + b5*sin(5*x*w)
	Coefficients (with 95% confidence bounds):
	  a0 = 1.674e+04 (-1.265e+04, 4.613e+04)
	  a1 = 2.002e+04 (1.07e+04, 2.934e+04)
	  b1 = -3.666e+04 (-9.495e+04, 2.162e+04)
	  a2 = -3.745e+04 (-8.744e+04, 1.254e+04)
	  b2 = -2.121e+04 (-2.785e+04, -1.457e+04)
	  a3 = -9867 (-1.619e+04, -3540)
	  b3 = 2.617e+04 (-3571, 5.591e+04)
	  a4 = 1.084e+04 (720.2, 2.095e+04)
	  b4 = 1580 (-3828, 6988)
	  a5 = -150.6 (-1720, 1418)
	  b5 = -2079 (-3513, -645.5)
	  w = 0.004394 (0.003987, 0.004802)
	
	Goodness of fit:
	  SSE: 1.608e+05
	  R-square: 0.9945
	  Adjusted R-square: 0.9945
	  RMSE: 11.7	

Specifications of the fitted curve on the data related to rebar #2 (the first and the second non-linear fitted curves)	General model Fourier5:
	f(x) = a0 + a1*cos(x*w) + b1*sin(x*w) +
	    a2*cos(2*x*w) + b2*sin(2*x*w) + a3*cos(3*x*w) + b3*sin(3*x*w) +
	    a4*cos(4*x*w) + b4*sin(4*x*w) + a5*cos(5*x*w) + b5*sin(5*x*w)
	Coefficients (with 95% confidence bounds):
	  a0 = -1.265e+12 (-4.065e+13, 3.812e+13)
	  a1 = 2.03e+12 (-6.167e+13, 6.573e+13)
	  b1 = 5.785e+11 (-1.568e+13, 1.684e+13)
	  a2 = -1.03e+12 (-3.416e+13, 3.21e+13)
	  b2 = -6.387e+11 (-1.873e+13, 1.745e+13)
	  a3 = 3.08e+11 (-1.013e+13, 1.075e+13)
	  b3 = 3.387e+11 (-9.383e+12, 1.006e+13)
	  a4 = -4.567e+10 (-1.779e+12, 1.688e+12)
	  b4 = -9.211e+10 (-2.789e+12, 2.605e+12)
	  a5 = 1.892e+09 (-1.009e+11, 1.046e+11)
	  b5 = 1.025e+10 (-2.984e+11, 3.189e+11)
	  w = 0.0008543 (-0.001806, 0.003515)
	
	Goodness of fit:
	  SSE: 3.409e+04
	  R-square: 0.9945
	  Adjusted R-square: 0.9945
	  RMSE: 5.671
		Linear model Poly7:
		f(x) = p1*x^7 + p2*x^6 + p3*x^5 + p4*x^4 + p5*x^3 +
		    p6*x^2 + p7*x + p8
		Coefficients (with 95% confidence bounds):
		  p1 = -2.351e-14 (-2.657e-14, -2.044e-14)
		  p2 = 4.707e-11 (4.062e-11, 5.353e-11)
		  p3 = -3.851e-08 (-4.416e-08, -3.286e-08)
		  p4 = 1.657e-05 (1.392e-05, 1.923e-05)
		  p5 = -0.004028 (-0.004748, -0.003307)
		  p6 = 0.5483 (0.4357, 0.6608)
		  p7 = -38.26 (-47.6, -28.91)
		  p8 = 1031 (713.6, 1348)
		
		Goodness of fit:
		  SSE: 2.082e+04
		  R-square: 0.7642
		  Adjusted R-square: 0.762
		  RMSE: 5.217

Specifications of the fitted curve on the data related to rebar #3	Linear model Poly9:
	f(x) = p1*x^9 + p2*x^8 + p3*x^7 + p4*x^6 +
	    p5*x^5 + p6*x^4 + p7*x^3 + p8*x^2 + p9*x + p10
	Coefficients (with 95% confidence bounds):
	  p1 = 3.012e-20 (4.005e-21, 5.623e-20)
	  p2 = -1.704e-16 (-2.406e-16, -1.002e-16)
	  p3 = 3.082e-13 (2.284e-13, 3.879e-13)
	  p4 = -2.745e-10 (-3.244e-10, -2.246e-10)
	  p5 = 1.387e-07 (1.199e-07, 1.574e-07)
	  p6 = -4.172e-05 (-4.603e-05, -3.74e-05)
	  p7 = 0.007454 (0.006853, 0.008055)
	  p8 = -0.7526 (-0.8001, -0.7051)
	  p9 = 38.52 (36.64, 40.4)
	  p10 = -778.8 (-806, -751.6)
	
	Goodness of fit:
	  SSE: 2.407e+05
	  R-square: 0.9598
	  Adjusted R-square: 0.9596
	  RMSE: 13.15	

Appendix C: SG and AG analyses of X component magnetic data recorded at different vertical distances over a rebar with three non-similar cracks (in section 4.4.2)

❖ The vertical distances in this study refer to the distance between rebar and the magnetic sensors in the PMI scanner.
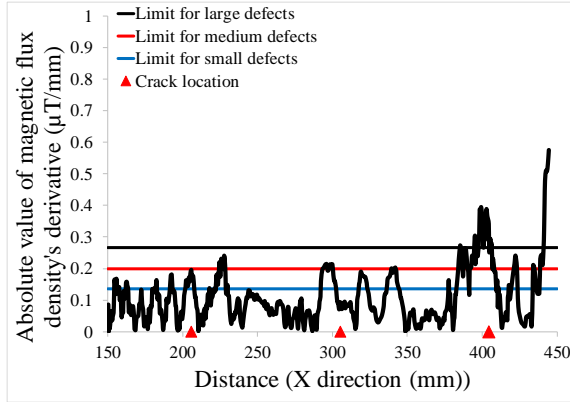
(a)
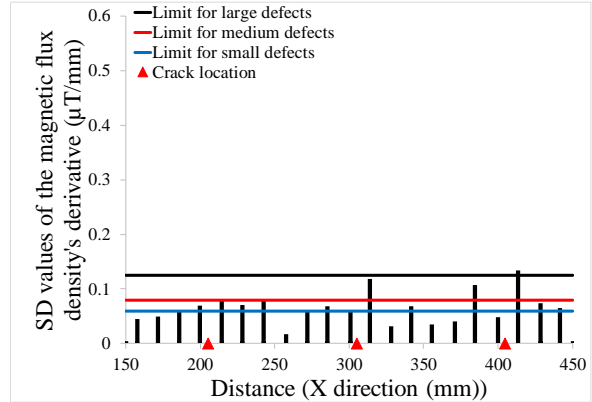
(b)
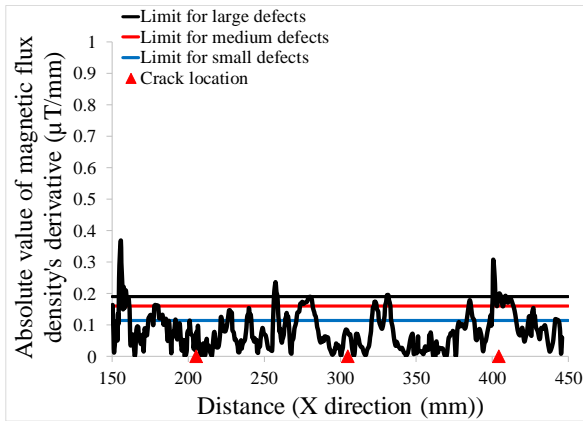
(c)
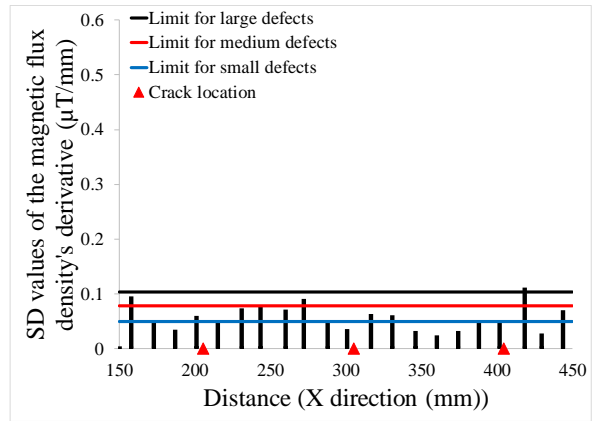
(d)
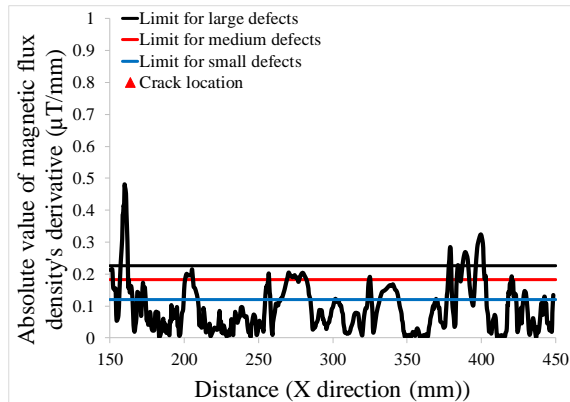
(e)
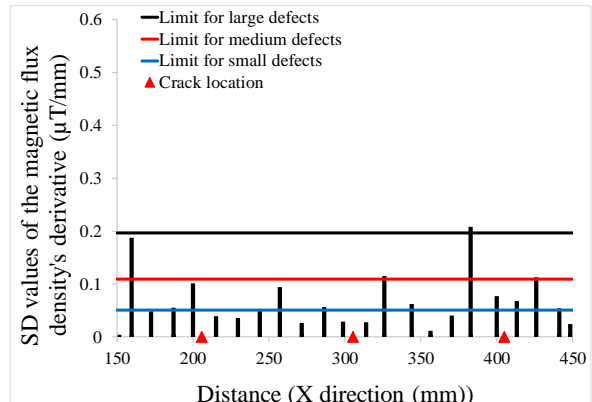
(f)
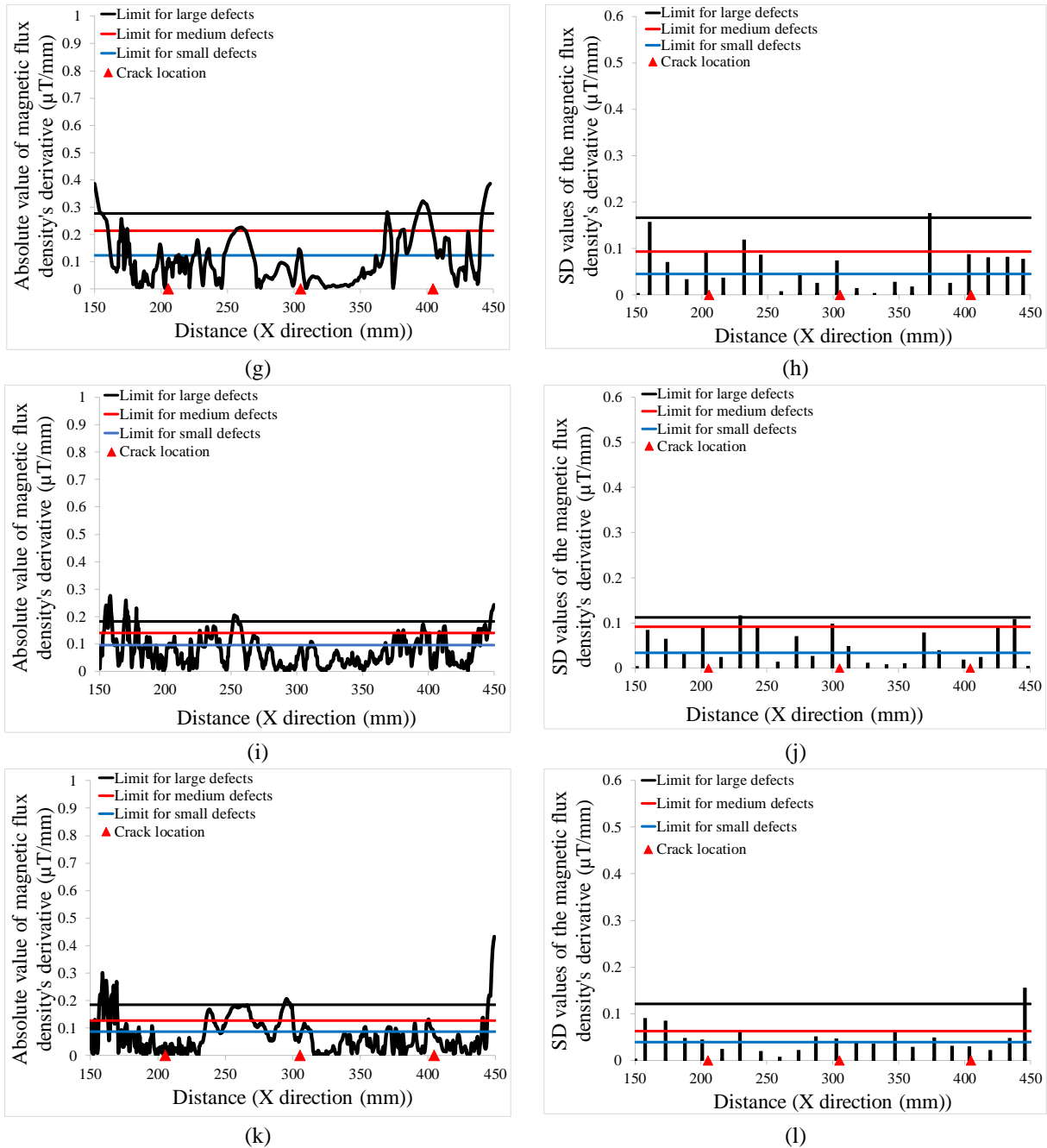
Figure C.1. SG and AG analyses of X component magnetic data recorded at different vertical distances over rebar 5: (a) AG analysis of data recorded at a vertical distance of 2 cm; (b) SG analysis of data recorded at a vertical distance of 2 cm; (c) AG analysis of data recorded at a vertical distance of 3 cm; (d) SG analysis of data recorded at a vertical distance of 3 cm; (e) AG analysis of data recorded at a vertical distance of 4 cm; (f) SG analysis of data recorded at a vertical distance of 4 cm; (g) AG analysis of data recorded at a vertical distance of 5 cm; (h) SG analysis of data recorded at a vertical distance of 5 cm; (i) AG analysis of data recorded at a vertical distance of 6 cm; (j) SG analysis of data recorded at a vertical distance of 6 cm; (k) AG analysis of data recorded at a vertical distance of 7 cm; (l) SG analysis of data recorded at a vertical distance of 7 cm.

Appendix D: Bridge deck PMI scans results and analysis (related to Chapter 7)

Scan #1

(a)

(b)

(c)

(d)

Figure D.1. Results and analysis of magnetic data recorded in scan #1: (a) Magnetic data after being normalized to a range between -1 and 1, (b) Magnetic derivative values after removing secular linear trend and subjection to moving average, (c) Magnetic data subjected to AG analysis approach, (d) Magnetic data subjected to SG analysis approach (all distances are represented from the West wall).

Table D-1. Specifications of defects with a cross-section loss greater than 4% in scan #1.

No.	Distance from West wall (cm)	Based on AG analysis		Based on SG analysis		Average of cross-section loss based on SG and AG approaches
		Abs. gradient value (µT/mm)	Cross-section loss	SD of gradient value (µT/mm)	Cross-section loss	
1	51.05 - 57.2	0.15	4.5%	0.03	5.4%	5.0%
2	65.9 - 78.28	0.37	10.8%	0.04	6.6%	8.7%
3	113.1 - 115.5	0.17	5.0%	0.03	4.1%	4.5%
4	120.9 - 128.1	0.19	5.5%	0.05	7.4%	6.4%
5	181.8 - 186.2	0.16	4.6%	0.03	4.4%	4.5%
6	205.5 - 216.2	0.65	19.1%	0.06	10.3%	14.7%
7	236.2 - 246.9	0.68	20.0%	0.12	20.0%	20.0%
8	257.6 - 265.2	0.29	8.4%	0.03	4.5%	6.5%

Table D-1 (continued).

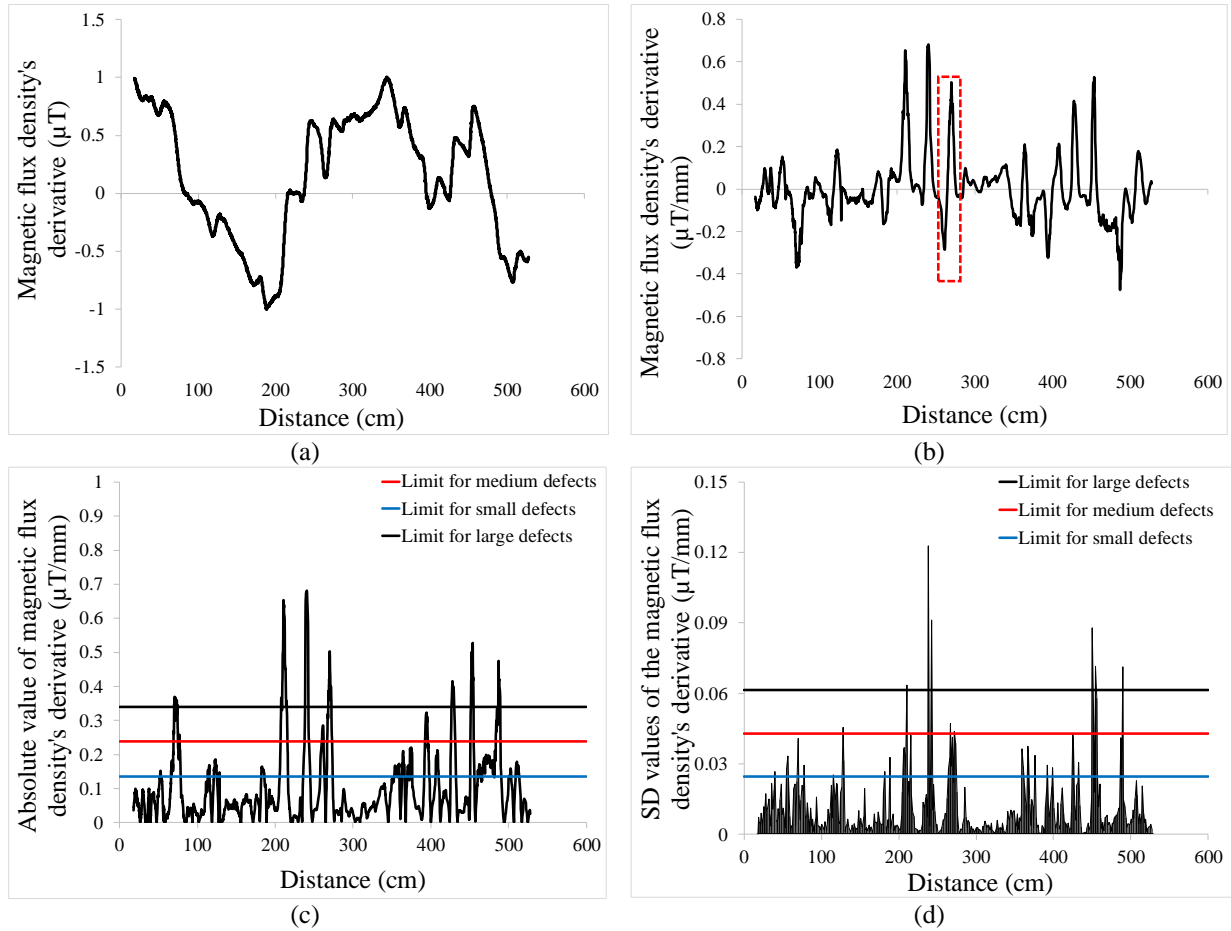| No.	Distance from West wall (cm)	Based on AG analysis		Based on SG analysis		Average of cross-section loss based on SG and AG approaches
		Abs. gradient value (μT/mm)	Cross-section loss	SD of gradient value (μT/mm)	Cross-section loss	
9	266.6 - 273.7	0.50	14.8%	0.05	7.7%	11.2%
10	353.1 - 360.6	0.17	5.1%	0.04	5.9%	5.5%
11	362.6 - 376.2	0.21	6.2%	0.04	6.1%	6.1%
12	391.4 - 398.3	0.32	9.5%	0.03	4.8%	7.1%
13	424.5 - 432.3	0.42	12.2%	0.04	7.0%	9.6%
14	449.7 - 456.1	0.53	15.5%	0.09	14.3%	14.9%
15	481.1 - 490.4	0.44	13.0%	0.07	11.6%	12.3%

Scan #2

Figure D.2. Results and analysis of magnetic data recorded in scan #2: (a) Magnetic data after being normalized to a range between -1 and 1, (b) Magnetic derivative values after removing secular linear trend and subjection to moving average, (c) Magnetic data subjected to AG analysis approach, (d) Magnetic data subjected to SG analysis approach (all distances are represented from the West wall).

Table D-2. Specifications of defects with a cross-section loss greater than 4% in scan #2.

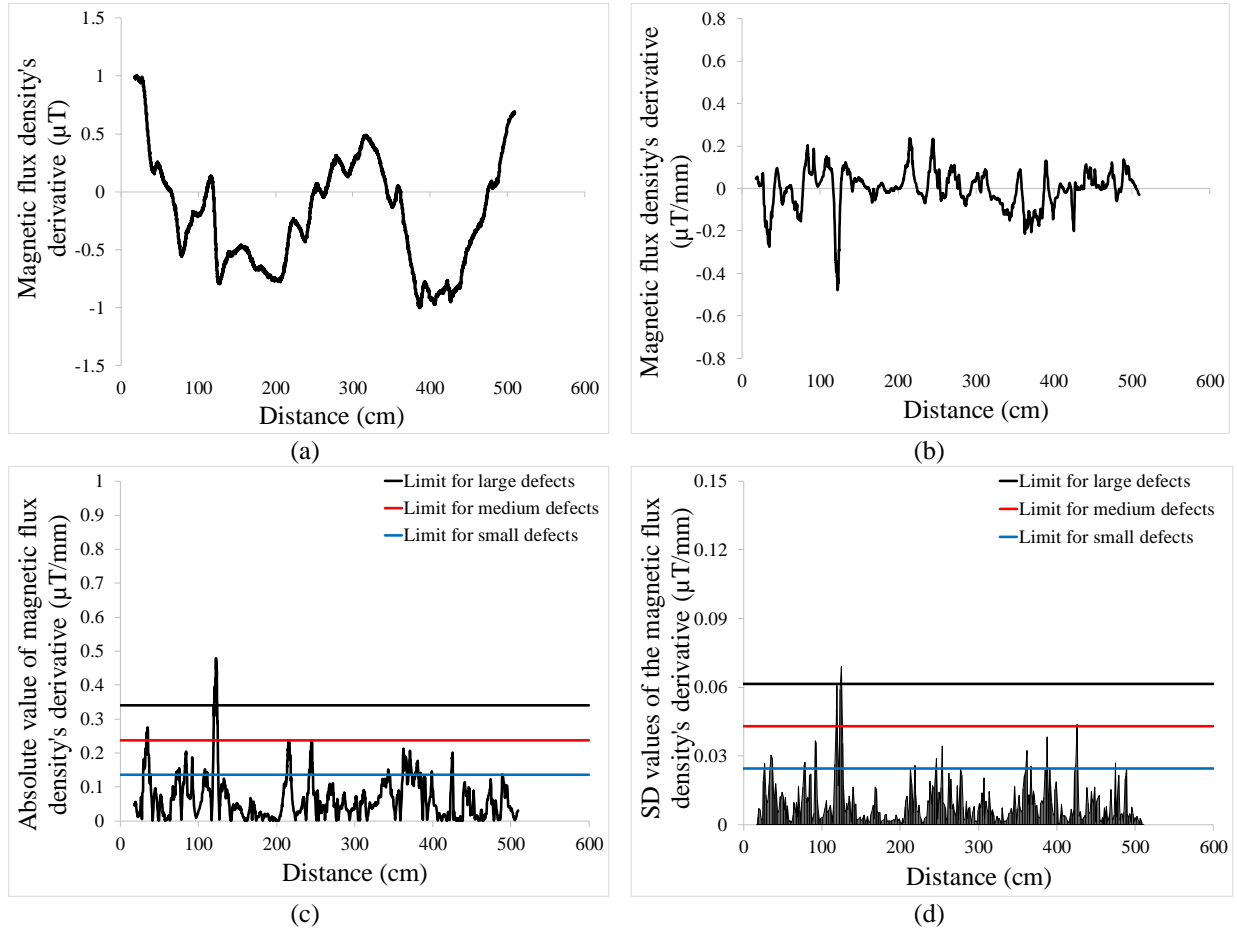| No.	Distance from West wall (cm)	Based on AG analysis		Based on SG analysis		Average of cross-section loss based on SG and AG approaches
		Abs. gradient value (µT/mm)	Cross-section loss	SD of gradient value (µT/mm)	Cross-section loss	
1	28.81 - 38.37	0.03	4.9%	0.28	8.1%	6.5%
2	71.12 - 78.44	0.15	4.3%	0.03	4.4%	4.3%
3	81.9 - 91.22	0.20	6.0%	0.04	6.0%	6.0%
4	118.2 - 125.1	0.48	14.1%	0.07	11.2%	12.7%
5	213.25 - 218.1	0.24	6.9%	0.03	4.2%	5.6%
6	241.49 - 253.4	0.23	6.9%	0.03	5.6%	6.2%
7	361.5 - 373.72	0.20	6.0%	0.03	5.3%	5.6%
8	377.4 - 381.48	0.17	5.1%	0.04	6.3%	5.7%
9	423.7 - 425.9	0.20	5.9%	0.04	7.1%	6.5%

Scan #3

Figure D.3. Results and analysis of magnetic data recorded in scan #3: (a) Magnetic data after being normalized to a range between -1 and 1, (b) Magnetic derivative values after removing secular linear trend and subjection to moving average, (c) Magnetic data subjected to AG analysis approach, (d) Magnetic data subjected to SG analysis approach (all distances are represented from the West wall).

Table D-3. Specifications of defects with a cross-section loss greater than 4% in scan #3.

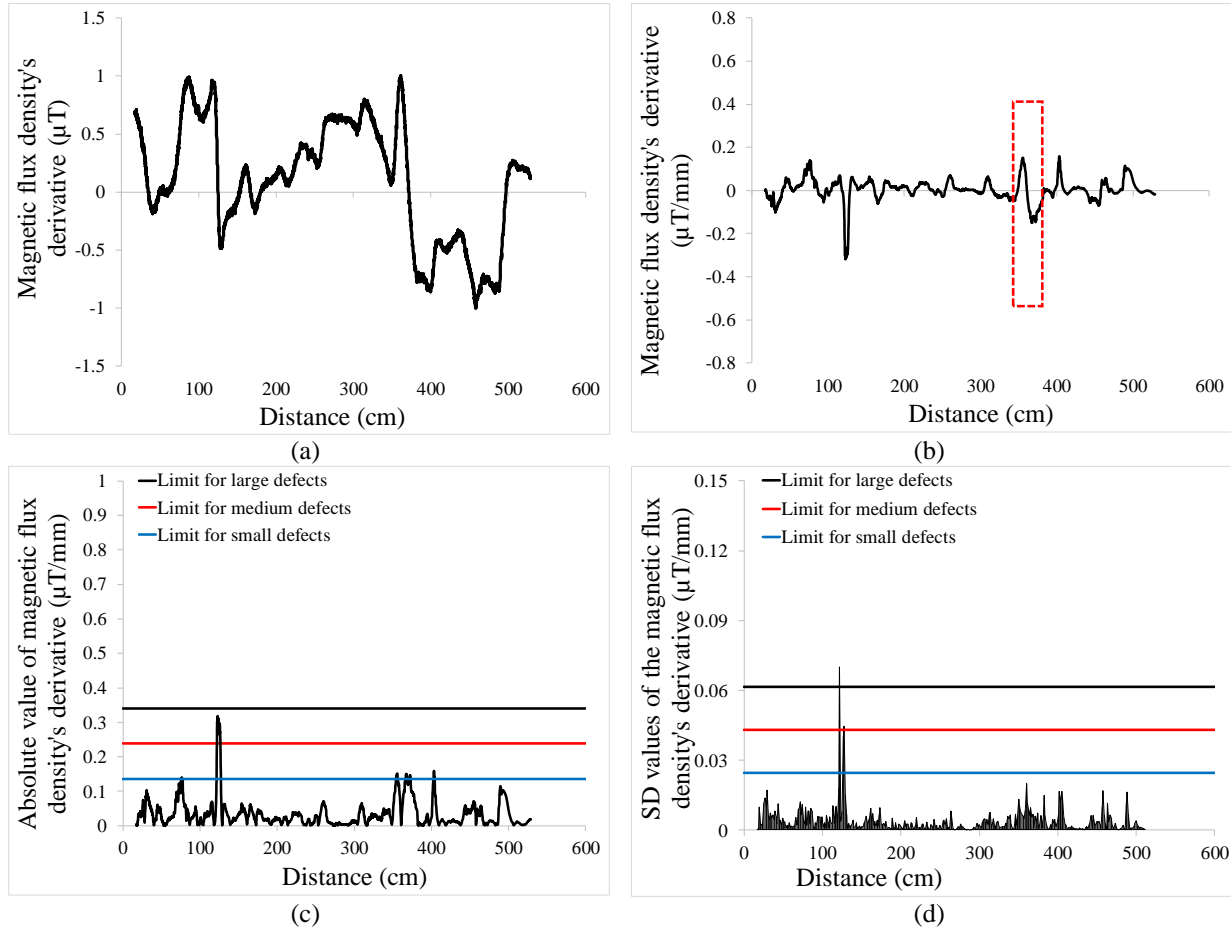| No.	Distance from West wall (cm)	Based on AG analysis		Based on SG analysis		Average of cross-section loss based on SG and AG approaches
		Abs. gradient value (µT/mm)	Cross-section loss	SD of gradient value (µT/mm)	Cross-section loss	
1	121.53 - 127.3	0.32	9.3%	0.07	11.4%	10.4%

Scan #4

Figure D.4. Results and analysis of magnetic data recorded in scan #4: (a) Magnetic data after being normalized to a range between -1 and 1, (b) Magnetic derivative values after removing secular linear trend and subjection to moving average, (c) Magnetic data subjected to AG analysis approach, (d) Magnetic data subjected to SG analysis approach (all distances are represented from the West wall).

Table D-4. Specifications of defects with a cross section loss greater than 4% in scan #4.

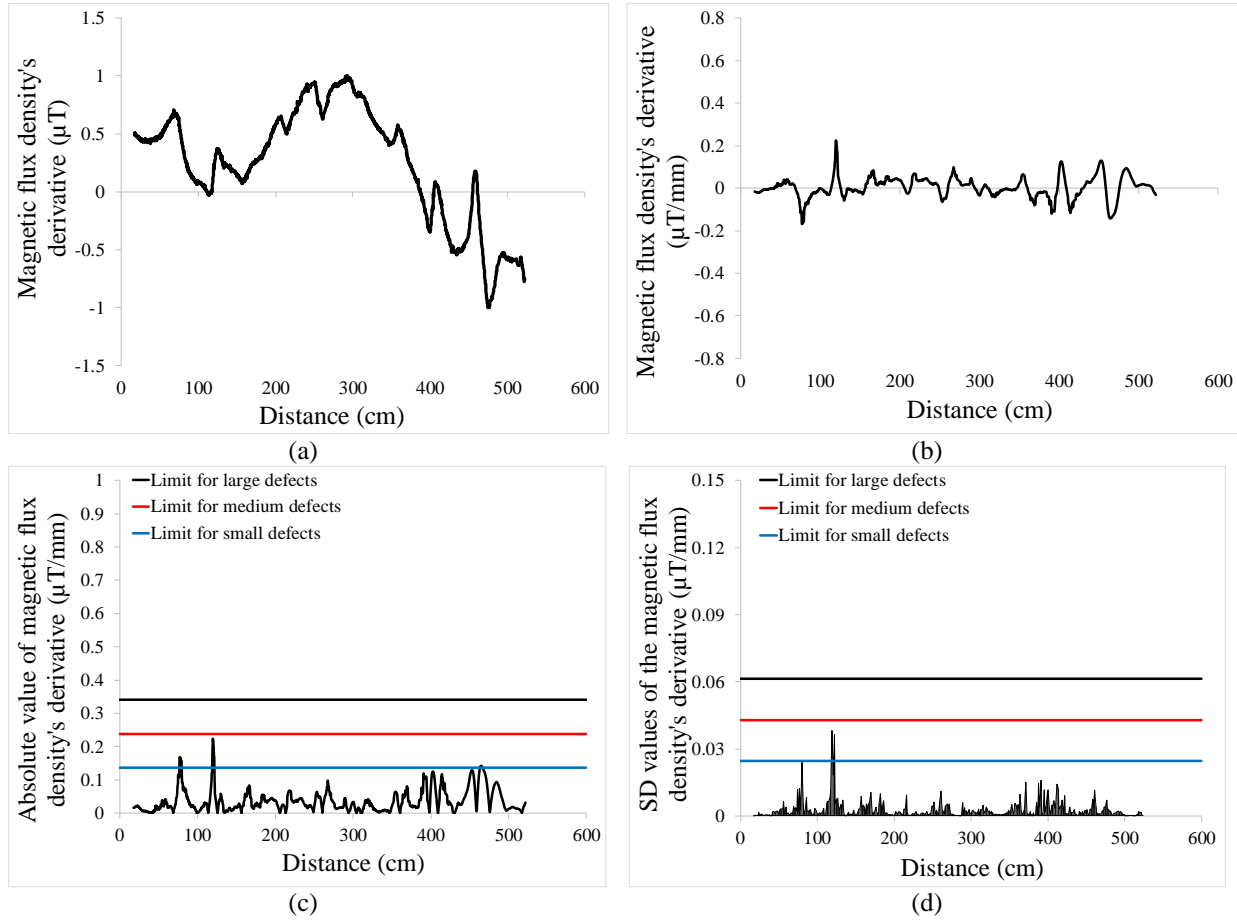| No.	Distance from West wall (cm)	Based on AG analysis		Based on SG analysis		Average of cross-section loss based on SG and AG approaches
		Abs. gradient value (μT/mm)	Cross-section loss	SD of gradient value (μT/mm)	Cross-section loss	
1	76.63 - 79.78	0.17	4.9%	0.02	4.0%	4.5%
2	118.76 - 121.9	0.22	6.5%	0.04	5.9%	6.2%

Scan #5

(a)

(b)

(c)

(d)

Figure D.5. Results and analysis of magnetic data recorded in scan #5: (a) Magnetic data after being normalized to a range between -1 and 1, (b) Magnetic derivative values after removing secular linear trend and subjection to moving average, (c) Magnetic data subjected to AG analysis approach, (d) Magnetic data subjected to SG analysis approach (all distances are represented from the West wall).

Table D-5. Specifications of defects with a cross-section loss greater than 4% in scan #5.

No.	Distance from West wall (cm)	Based on AG analysis		Based on SG analysis		Average of cross-section loss based on SG and AG approaches
		Abs. gradient value (µT/mm)	Cross-section loss	SD of gradient value (µT/mm)	Cross-section loss	
1	120.3 - 124.3	0.18	5.2%	0.04	6.1%	5.7%
2	408.4 - 411.7	0.24	6.9%	0.04	7.0%	7.0%

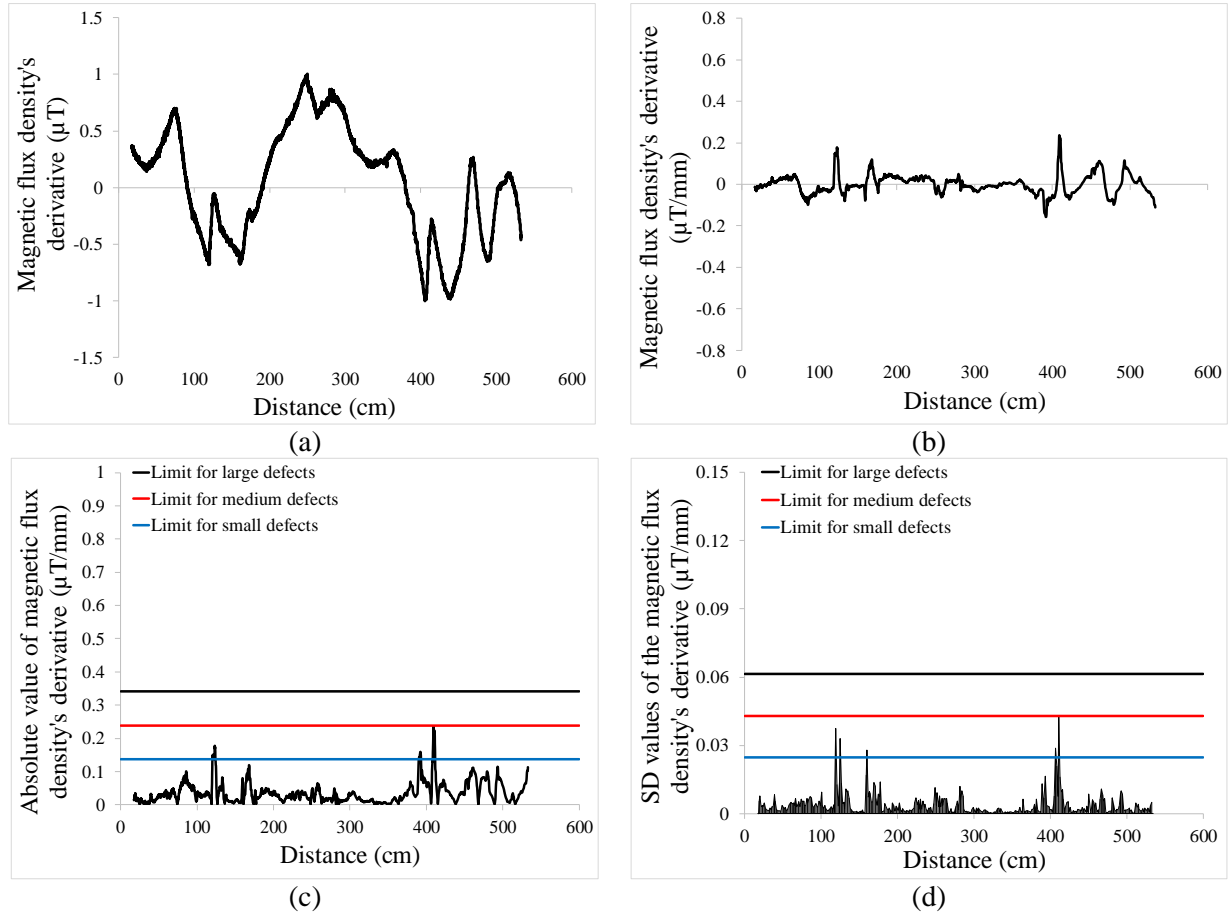# Scan #6

(a)

(b)

(c)

(d)

Figure D.6. Results and analysis of magnetic data recorded in scan #6: (a) Magnetic data after being normalized to a range between -1 and 1, (b) Magnetic derivative values after removing secular linear trend and subjection to moving average, (c) Magnetic data subjected to AG analysis approach, (d) Magnetic data subjected to SG analysis approach (all distances are represented from the West wall).

Table D-6. Specifications of defects with a cross-section loss greater than 4% in scan #6.

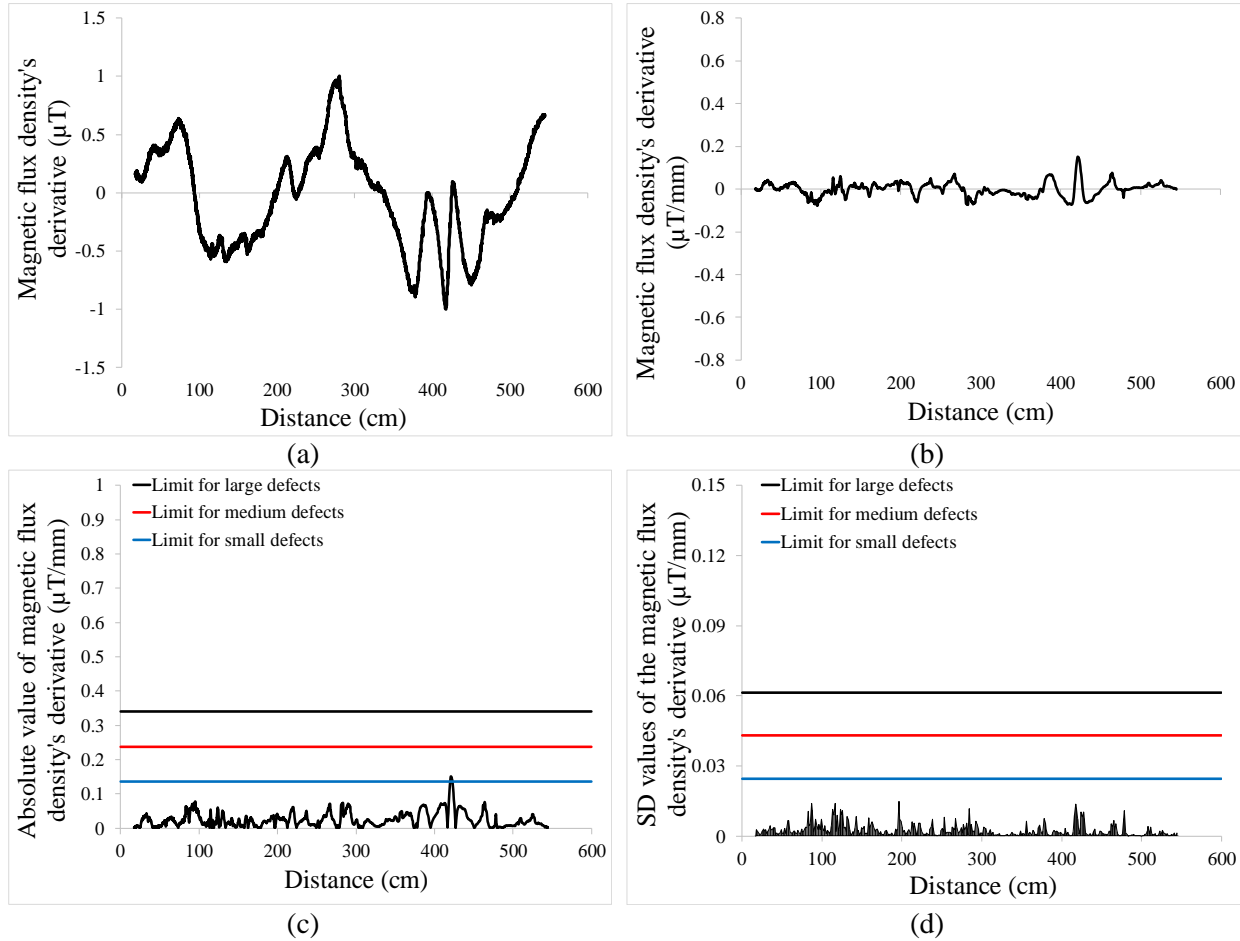| No.	Distance from West wall (cm)	Based on AG analysis		Based on SG analysis		Average of cross-section loss based on SG and AG approaches
		Abs. gradient value (µT/mm)	Cross-section loss	SD of gradient value (µT/mm)	Cross-section loss	
Empty						

Scan #7

(a)

(b)

(c)

(d)

Figure D.7. Results and analysis of magnetic data recorded in scan #7: (a) Magnetic data after being normalized to a range between -1 and 1, (b) Magnetic derivative values after removing secular linear trend and subjection to moving average, (c) Magnetic data subjected to AG analysis approach, (d) Magnetic data subjected to SG analysis approach (all distances are represented from the West wall).

Table D-7. Specifications of defects with a cross-section loss greater than 4% in scan #7.

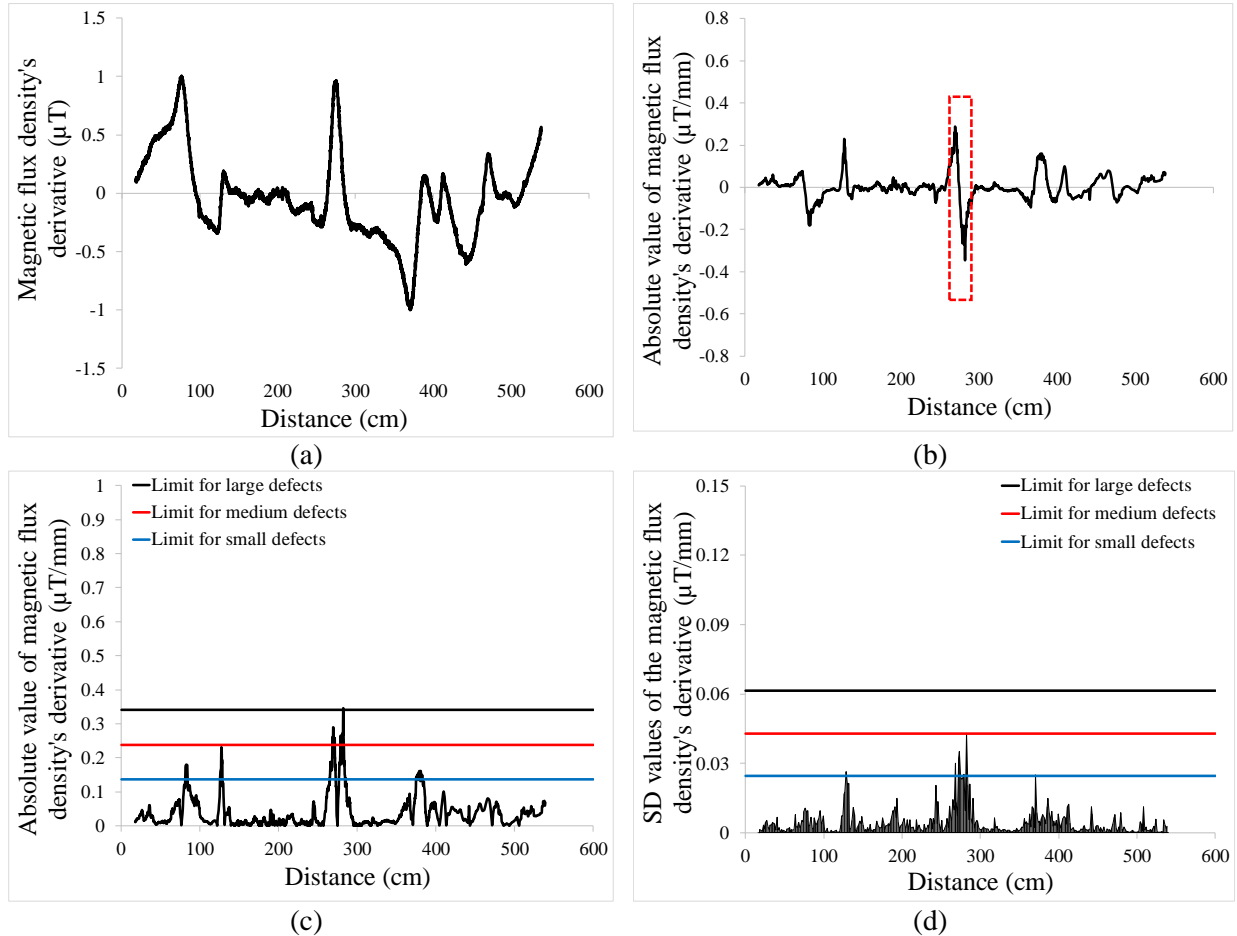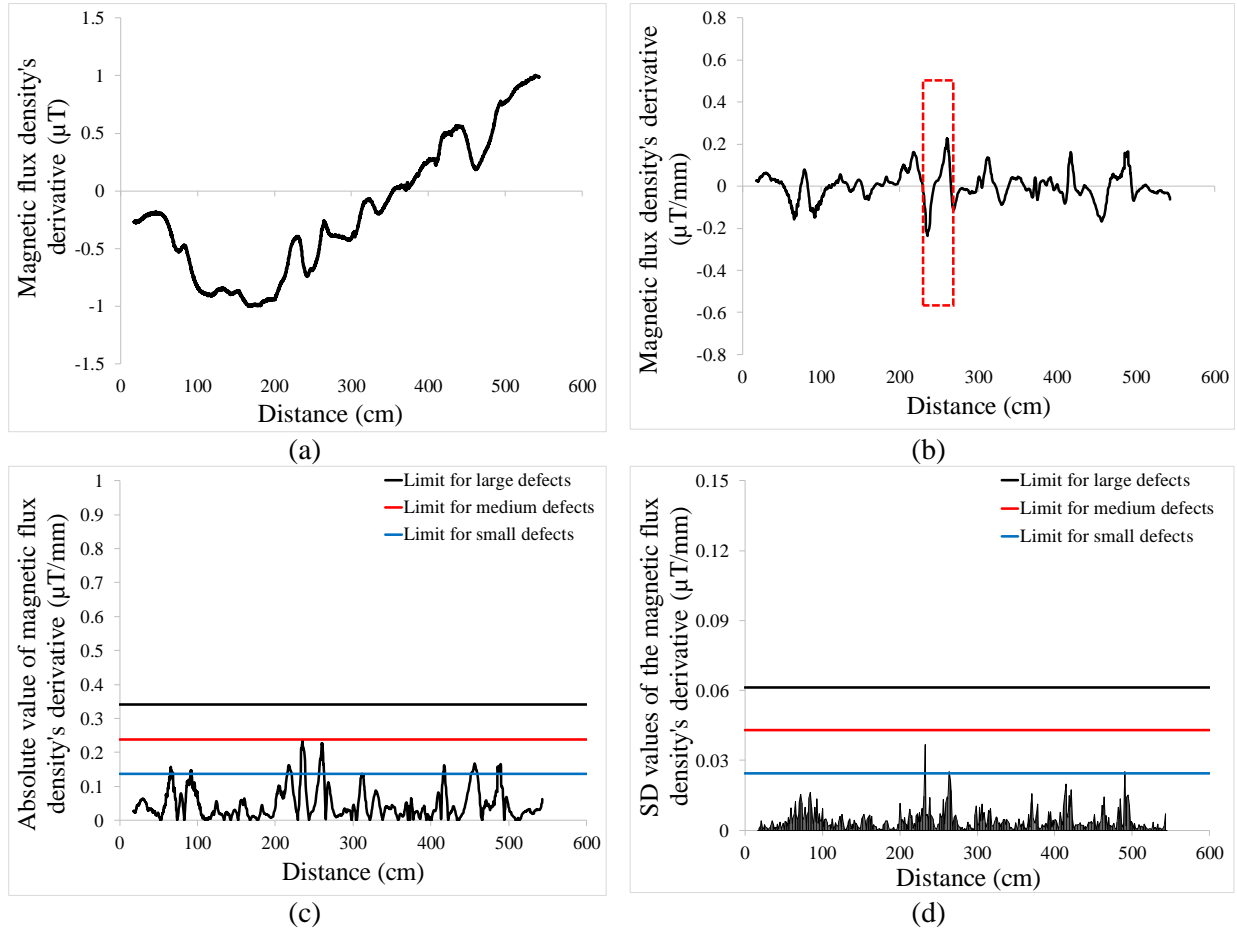| No.	Distance from West wall (cm)	Based on AG analysis		Based on SG analysis		Average of cross-section loss based on SG and AG approaches
		Abs. gradient value (µT/mm)	Cross-section loss	SD of gradient value (µT/mm)	Cross-section loss	
1	125.4 - 128.4	0.23	6.8%	0.03	4.3%	5.5%
2	264.9 - 273.5	0.29	8.5%	0.04	5.7%	7.1%
3	276.5 - 285.2	0.34	10.1%	0.04	7.0%	8.5%
4	370.5 - 382.7	0.16	4.6%	0.03	4.1%	4.3%

Scan #8

Figure D.8. Results and analysis of magnetic data recorded in scan #8: (a) Magnetic data after being normalized to a range between -1 and 1, (b) Magnetic derivative values after removing secular linear trend and subjection to moving average, (c) Magnetic data subjected to AG analysis approach, (d) Magnetic data subjected to SG analysis approach (all distances are represented from the West wall).

Table D-8. Specifications of defects with a cross-section loss greater than 4% in scan #8.

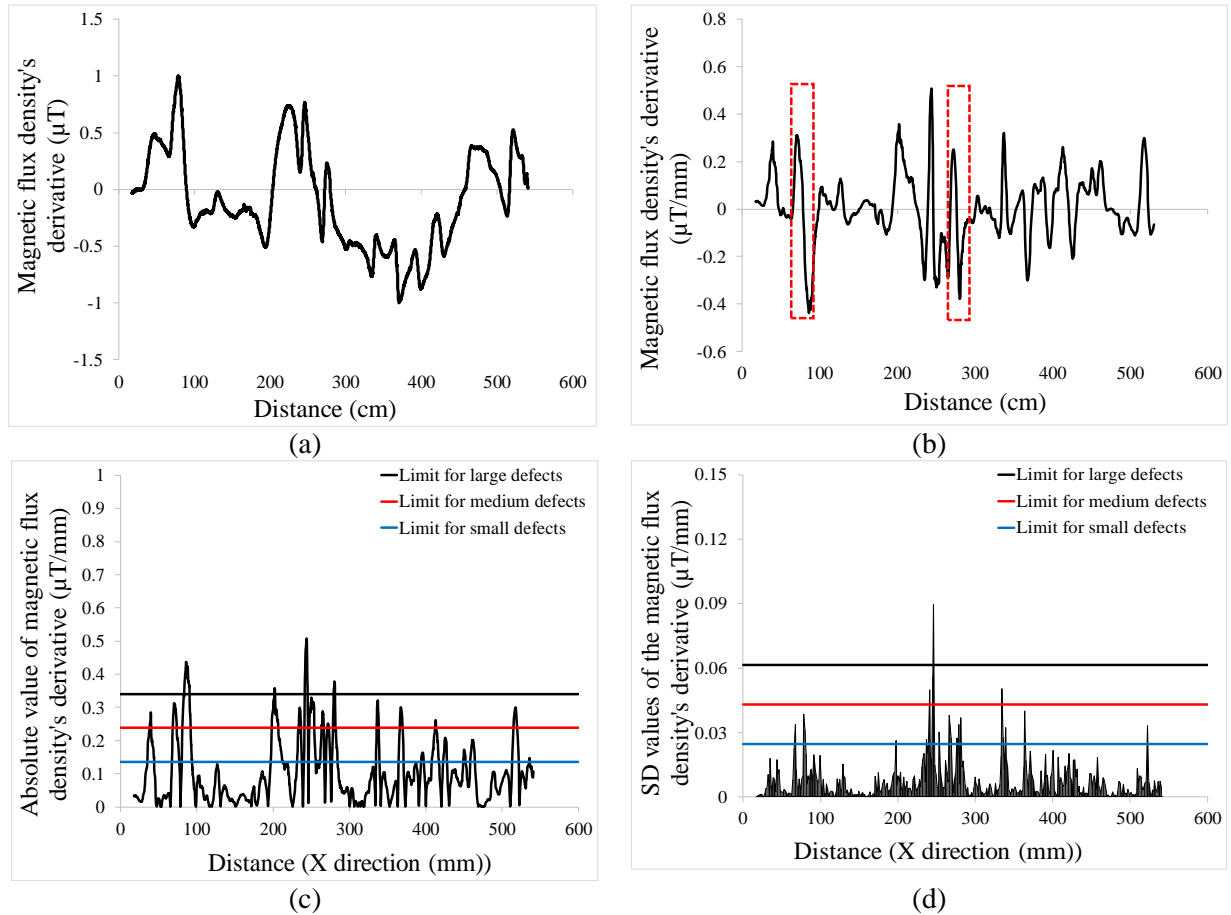| No.	Distance from West wall (cm)	Based on AG analysis		Based on SG analysis		Average cross-section loss (average)
		Abs. gradient value (µT/mm)	Cross-section loss	SD of gradient value (µT/mm)	Cross-section loss	
1	232.6 - 238.6	0.23	6.9%	0.04	6.0%	6.4%
2	256.4 - 263.8	0.23	6.6%	0.03	4.1%	5.4%
3	485.6 - 490.5	0.16	4.8%	0.03	4.1%	4.5%

Scan #9

(a)

(b)

(c)

(d)

Figure D.9. Results and analysis of magnetic data recorded in scan #9: (a) Magnetic data after being normalized to a range between -1 and 1, (b) Magnetic derivative values after removing secular linear trend and subjection to moving average, (c) Magnetic data subjected to AG analysis approach, (d) Magnetic data subjected to SG analysis approach (all distances are represented from the West wall).

Table D-9. Specifications of defects with a cross-section loss greater than 4% in scan #9.

No.	Distance from West wall (cm)	Based on AG analysis		Based on SG analysis		Average of cross-section loss based on SG and AG approaches
		Abs. gradient value (µT/mm)	Cross-section loss	SD of gradient value (µT/mm)	Cross-section loss	
1	67.3 - 76.8	0.31	9.2%	0.03	6.9%	8.0%
2	78.4 - 92.6	0.44	12.8%	0.04	7.9%	10.4%
3	196.9 - 212.7	0.36	10.5%	0.03	5.4%	7.9%
4	231.6 - 237.6	0.30	8.8%	0.03	5.5%	7.1%
5	240.5 - 245.6	0.51	14.9%	0.05	10.1%	12.5%
6	246.41 - 255.7	0.33	9.7%	0.09	18.2%	13.9%
7	261.5 - 266.9	0.29	8.5%	0.04	7.7%	8.1%
8	269.4 - 275.9	0.25	7.4%	0.03	5.6%	6.5%
9	277.26 - 284.3	0.38	11.1%	0.03	6.9%	9.0%
10	334.5 - 339.3	0.32	9.4%	0.05	10.2%	9.8%
11	364.1 - 370.9	0.30	8.8%	0.04	8.1%	8.5%
12	513.6 - 522.4	0.30	8.8%	0.03	6.7%	7.8%